UNIVERSITY OF CALIFORNIA

Santa Barbara

High Strain Rate Loading of Multi-phase Materials

A dissertation submitted in partial satisfaction of the

requirements for the degree Doctor of Philosophy

in Materials

by

Avery Francis Samuel

Committee in charge:

Professor Frank W. Zok, Chair

Professor Irene J. Beyerlein

Professor Tresa M. Pollock

Professor Frederic Gibou

September 2022

The dissertation of Avery Francis Samuel is approved.

Professor Irene J. Beyerlein

Professor Tresa M. Pollock

Professor Frederic Gibou

Professor Frank W. Zok, Committee Chair

July 2022

High Strain Rate Loading of Multi-phase Materials

by

Avery Francis Samuel

ACKNOWLEDGEMENTS

Thank you to all family and friends who have helped and supported me along the way.

VITA OF AVERY FRANCIS SAMUEL

April 2022

Education

Ph. D. — University of California, Santa Barbara
Materials, July 2022 (expected)

M. S. — University of California, Santa Barbara
Materials, 2019

B.S.E. — University of Michigan – Ann Arbor
Materials Science and Engineering, 2016

Publications

Samuel, AF, Christodoulou, PG, Zok, FW. Strain fields around strain-concentrating features in fiber-reinforced oxide composites. *J Am Ceram Soc*. 2020; 103: 1942– 1955. https://doi.org/10.1111/jace.16840

A.F. Samuel, Z.S. Levin, C.P. Trujillo, S.J. Fensin , M.J. Demkowicz, I.J. Beyerlein, F.W. Zok. Quasi-static and dynamic response of a Cu/Nb composite following equal channel angular extrusion. *Submitted 2022.*

A.F. Samuel, S.J. Fensin, J.-W. Zhang, W.-Z. Han, I.J. Beyerlein, F.W. Zok. Low- and high-rate mechanical response of Zr-2.5wt% Nb processed in two ways. *In preparation 2022.*

A.F. Samuel, S.J. Fensin, D.R. Jones, J.-W. Zhang, W.-Z. Han, I.J. Beyerlein, F.W. Zok. Understanding the Effect of Microstructure on Damage and Failure in Zr-2.5wt% Nb with Hierarchical Microstructures. *In preparation 2022.*

A.F. Samuel, I.J. Beyerlein, F.W. Zok. Effects of Constituent Properties on the Nature of Propagating Waves in Elastic Multiphase Composites. *In preparation 2022.*

C.Q. Dong, **A.F. Samuel**, L.A. Kuettner, B.M. Patterson, C. Montgomery, C.A. Britt, F.W. Zok, A.M. Beese, J.S. Carpenter, M.R. Begley. Effective geometry and properties of SLM stainless steel 316L thin struct intersections (nodes) built with different energy densities. *Submitted 2021*.

ABSTRACT

High Strain Rate Loading of Multi-phase Materials

by

Avery Francis Samuel

Multi-phase metal composites have garnered increased attention in recent years. While the mechanical properties of these materials under high strain rate loadings have been found to depend heavily on microstructural heterogeneities, the current understanding of the roles of constituent properties and microstructure on dynamic properties is lacking. The current study addresses the outstanding issues through a combination of experimental measurements under both low and high strain rates, characterization of microstructural changes associated with dynamic loading, and simulations of stress wave propagation in a family of idealized two-phase metal composites.

The experimental work focuses on two classes of materials: a Cu/Nb composite made by equal-channel angular extrusion and a lamellar two-phase Zr-2.5wt% Nb. The Cu/Nb composite was found to exhibit plastic anisotropy similar to that of pure Cu made by the same process, but with greater strength and with compressive failure occurring through a kink banding mechanism. The strengths and localization behavior at low and high strain rates were similar to those obtained in a Cu/Nb nanolaminate. The Zr-2.5wt% Nb material was studied in two conditions, distinguished by a dynamic compression step following heat treatment and upon cooling. The materials were assessed in tension and compression at quasi-static and high-strain rates, and during incipient spall via flyer plate impact at rates $>10^5$ /s. Material

failure in all cases was found to be dominated by prior β grain boundaries. In compression, boundaries normal to the loading direction promote shear banding; in tension, including incipient spallation, they are preferred locations for void nucleation.

Finite element simulations were used to study elastic wave propagation and stress distributions in idealized models of aligned two-phase metal composites. The properties relevant to wave propagation – wave speed and acoustic impedance – were varied through selection of Young's moduli and densities of the constituent phases. Three regimes of wave behavior, characterized by the ratio of the wave speeds of the two phases, were identified. Shear waves were found to arise from purely axial loading, and their magnitude during late-time propagation were found to be reasonably approximated by a shear lag-type model for a subset of the composite configurations examined.

This work provides valuable insight into the role of microstructure on the performance of multi-phase metal composites, including the characteristics necessary for bi-phase interfaces to be a primary strengthening mechanism. It also shows that other microstructural features can dictate response over bi-phase interfaces. The finite element simulations of wave propagation provide a foundational base on which to build a more complete understanding of the evolution of stress distributions during dynamic loading.

Table of Contents

Chapter 1

Introduction

1.1 BACKGROUND ON METAL/METAL COMPOSITES

Composites combine multiple materials of disparate properties to create new materials with properties that either fall between those of the constituents or, in some instances, exceed those of both constituents. The prototypical example is fiber-reinforced polymer composites comprising strong and stiff fibers embedded in a protective and supportive matrix. Composites of this kind are increasingly being used in structural applications due to their high specific strength and stiffness.

Over the past few decades, advances in processing have led to renewed interest in all-metal composites, known variously as multiphase metal composites, in-situ composites, or deformation processed metal-metal composites (DMMCs)[1–7]. Whereas most existing conventional composites combine materials from different material classes (e.g., glass fibers in a polymer or ceramic particles in a metal), multiphase metals consist of phases from the same class. Constituents are often chosen to be for minimal solid miscibility to prevent diffusional microstructure evolution, and to avoid formation of additional phases with undesirable properties. The attraction of all-metal composites stems from their capabilities of achieving extraordinarily high strengths, remarkable microstructural stability and attractive levels of other properties, such as electrical and thermal conductivity, and appreciable ductility[1,2,5,6,8,9].

The most common metal composites are based on copper and a refractory metal such as niobium, tantalum, or chromium. The Cu-Nb system in particular has proven to be amenable to deformation processing and hence has been the most widely studied. Many of the underlying mechanisms have been elucidated through study of this system. A wide variety of other composites of this type have also been developed, such as Cu-Ta, Cu-Ni, Ag-Cu, Al-Cu, Ti-Y and Ti-Sc[1,5,6,10].

1.2 FILAMENTARY METAL COMPOSITES

Two morphological types of metal composites have received the greatest attention to date: filamentary and multilayered. Filamentary metal composites were the first to be actively pursued. They were intended for high-strength, high electrical-conductivity windings for pulsed magnets. They were first produced through extensive drawing of rod-shaped castings of Cu-Nb, eventually reaching true strains of 10-20. Drawing to these strains reduces the diameter by several thousands of times and reduces the spacing between the phases to tens of nanometers[1,5,11–13].

Modifications to the original process have been made to attain larger final dimensions, since practical applications require final wire or rod diameters on the order of millimeters, while wires continuously drawn to such extreme strains have miniscule final diameters for processable starting sizes. The modified process is called accumulative drawing and bundling (ADB) and entails inserting a rod-shaped cast composite into a jacket of the matrix phase, hot extruding, and then drawing to a significantly reduced cross-section. The resulting rod/wire is cut many times along its length (from 55[14] to 823 times[15]), the short pieces stacked together and encased in another jacket of matrix, and the extrusion, drawing, and stacking is repeated

two or three times[15–20]. Additional steps such as hot isostatic pressing can be used to consolidate the bundles between encasement and extrusion[15,20].

In another variation, the initial composite is made by inserting a rod of only one phase into a jacket of another; the same extrusion, drawing, and bundling steps are followed[14,16–18]. The microstructures are not identical to drawn castings – the filaments are continuous, and relatively large (~1 μm diameter) pockets of matrix from the jackets remain – but refinement to nanoscale sizes of both the filaments and the matrix still occurs in a significant fraction of the total volume[14,17,18]. In addition, filaments produced by ADB can be in the form of either flattened ribbons or cylinders, depending on the deformation methods, heat treatments, and draw ratio[18–21]. Despite the morphological differences, the mechanical properties of ADB composites are comparable to those of drawn-only wires that have similar microstructural dimensions. The mechanisms governing properties are also expected to be the same in the two cases.

1.2.1 Microstructure and mechanical properties of filamentary composites

Extensive drawing reduces the minority phase to extremely fine filaments that are elongated along the drawing axis and distributed throughout the matrix of the major phase. When starting with a cast billet, the uniformity of the distribution of filaments increases with draw ratio[12,22]; ADB naturally preserves the arrangement of the filaments[14,17,18]. At lower drawing ratios (<5), the grains of the matrix are refined to around ~500 nm and contain dislocation cells ~300 nm across. The filaments are reduced to tens of nm thick and ~1 μm in length (or continuous for ADB). Further drawing refines both phases with the minimum grain sizes <50 nm.

For FCC/BCC systems, the filaments spread along one non-axial direction into ribbons that are several times wider than they are thick and curl randomly. The width of the ribbons remains small relative to the length in the axial direction[12,14,17,22,23]. When the minority phase is brittle (e.g., Mo in Cu), the initial dendrites formed upon solidification may comminute into smaller particles of only a few grains before being elongated into filaments[24]. Curling of the filaments occurs due to a combination of alignment of the BCC{011} aligns with the drawing axis, at which point only two ⟨111⟩ directions are aligned for slip during subsequent drawing steps, and bending of the ribbon driven by flow of the surrounding matrix material which is still able to accommodate axially symmetric deformation[12,17,22,23,25]. Filaments in FCC/FCC composites form long cylinders instead of flattened ribbons because they do not experience the mismatch in deformability with the matrix[11]. Cu-BCC systems in which the BCC component is much harder than Cu exhibit dissimilar strains in the two phases and a limit to refinement of the harder phase (e.g. in Ta, ribbon thickness decreases to around 20 nm then plateaus)[17,24–26]. Composites with HCP components have received some attention, but substantially less. Their microstructures typically contain flattened ribbons, similar to FCC/BCC composites, brought about by a similar limitation in slip directions as the HCP phase develops a $\langle 10\bar{1}0 \rangle$ fiber texture and subsequently only deforms on two $\{10\bar{1}0\}\langle 11\bar{2}0 \rangle$ slip systems.

At draw ratios of 1-2, strengths of these composites are a few hundred MPa, comparable to the strengths of the constituents alone in the same worked condition. After additional drawing steps the tensile strengths of these wires reach 2 GPa while the electrical conductivity only decreases by ~50% from that of the pure copper standard[1,23,27]. Strengths continually increase with both increasing draw ratio[12,22,23,28] and reduction in filament size at

constant draw ratio (determined by modulating initial dendrite size through cooling of the casting)[13,22].

At draw ratios greater than ~5-10 the ultimate tensile strength strongly deviates from the rule-of-mixtures predictions and can even exceed the strength of the stronger constituent[5,12,22,23,28]. Exceeding the strength of the stronger constituent requires particularly fine filaments. Cu-Nb composites at large draw ratios can have a strength less than that of pure Nb at the same draw ratios when the filaments are "large" (i.e. hundreds of nm). This occurs when the initial dendrites are too coarse to refine to the ~10 nm range at the imparted draw ratio[23,28]. It does not indicate a limit of the material though. Additional refinement, such as through further drawing, would increase their strength. Other composite systems exhibit similar trends: strengths increase as interphase spacing decreases, and rule-of-mixtures predictions are exceeded when strains reach ~5[1,5,17,21,24,26,28–31].

Combinations of FCC and BCC metals have been found to provide greater strengthening than FCC/FCC combinations, because of the formation of curled ribbon-like morphology of the BCC phase which helps further refine the interphase spacing[15,17,24,29]. Strengths and electrical conductivities of FCC/HCP composites can exceed ROM estimates but are generally lower than those of other Cu-based systems[32–34].

TEM studies have revealed that interfaces between Cu and Nb are semi-coherent with a {111}Cu||{110}Nb and ⟨111⟩Cu||⟨110⟩Nb Kurdjumov-Sachs orientation relationship[5,14,35], while Cu and Ag form semi-coherent cube-on-cube interfaces[30,36]. These studies have also shown that the dislocation density first increases with drawing before dramatically decreasing for the largest draw ratios. In Cu-Ag, dislocation densities reach ~10^{12}-10^{14} /cm^2 at 99% reduction in cross-section, but then decrease rapidly such that the fibers appear nearly free of

dislocation at 99.99% reduction (filament sizes of ~50 nm)[11]. In Cu-Nb, final dislocation densities in both phases are[22] ~10^{10} /cm^2. The reduction is attributed to dislocation absorption at the interfaces when the spacing becomes too small and the interfacial area too large for stable internal dislocation arrays[11,22,37].

1.2.2 Strengthening mechanisms in filamentary composites

For filamentary multi-phase metal composites, mechanical response and the governing mechanisms change as the length scales of the microstructure are reduced[5,12,14,17,38]. At the largest scale with the greatest distance between phase interfaces, the primary obstacles to dislocation motion are single-phase grain boundaries and dislocation structures within each phase and the composite behaves like a conventional mixture of the constituent phases. In particular, the strength of the composite follows the rule-of-mixtures prediction found with the strengths of the bulk individual components[14,28].

After some refinement, to the point where spacing between phases is roughly ~100 nm – 1 μm, the ultimate tensile strength scales linearly with the inverse square root of the spacing between filaments[5,12,22,28,38] $\sigma \propto \lambda^{-1/2}$. This is the same scaling as that of the Hall-Petch relationship, and an analogous mechanism is responsible: pile-ups of dislocations at boundaries. The distinction from the traditional Hall-Petch model is that the boundaries are those between two different phases rather than between grains of a single phase[22,28]. Note that the spacing of the Nb filaments is distinct from their thickness. While strength does increase as filament size decreases, this is only because filament size and spacing decrease concurrently. However, composites with equal spacing but unequal filament size have the same strength

whereas the converse is not true[22,23] (Figure 1.1) . This indicates that the dislocations are traveling in the Cu phase rather than the Nb[22].

At finer filament spacings (~5 – 50 nm), the ribbon-like filaments begin to behave like thin films[12]. Strengths in this regime increase dramatically, deviating from both the Hall-Petch relation and the rule-of-mixtures predictions based on bulk material properties, indicating a change in the mechanism of slip transmission[12,14,23,39,40]. Formation and movement of multiple dislocations on a single plane in a single phase becomes impossible due to the restriction by the close boundaries; there is not enough space for pile-ups to occur. Instead, single dislocations nucleate and move on parallel, closely-spaced slip planes and extend from one bi-phase boundary to the next[5,14,38,39,41]. The yield stress dependence changes to a relationship analogous to that for Orowan bowing:

$$\sigma_y = \frac{\beta G}{d} \cdot \ln\left(\frac{d}{b}\right) \tag{1.1}$$

where G is the shear modulus, d is the spacing between Nb filaments (i.e., width of the Cu), b is the length of the Burgers vector, and β is a constant related to the dislocation character[5,18,41]. This mechanism only occurs in the Cu phase; the Nb filaments behave like nanowhiskers, remaining elastic until failure of the wires[14,17,41]. This behavior has been directly observed in TEM for the Cu-Nb system[14].

In the ultimate limit, where both phases begin to act like whiskers, the composite ultimate strength approaches a rule-of-mixtures prediction based on the theoretical strengths of the constituents, rather than their strengths in bulk form[12,14,38]. The greatest strengths therefore are achieved by material combinations that can be refined to the greatest extent, nearest to a collection of nearly-perfect whiskers[5,12,14,17,18,42], not necessarily by combinations of constituents with the greatest bulk strengths.

1.2.3 Effects of temperature on filamentary metal composites

Most evaluations of performance have been conducted at room temperature. However, the potential use-cases for these materials would involve elevated temperatures. Effects of temperature on strength and electrical performance have been investigated through both intermediate heat treatments between drawing steps and post-deformation aging. The results are divided between systems with essentially immiscible constituents and those with some solid solubility.

When the constituents are immiscible, strengths are stable for only short times (a few hours) following moderate temperature elevations (to ~300°C) but dramatically soften at higher temperatures[19,37,43–46]. However electrical conductivity increases following annealing[37,47,48]. Softening is primarily due to coarsening and spheroidization of the minority-phase filaments as well as some recovery in the matrix. At the same time, the coarsening of the filaments benefits conductivity by reducing the interface area scatters electrons[37,44,46–48].

When the constituents exhibit some mutual solubility, aging at low temperatures can increase strength somewhat, but softening sets in for sufficiently high temperatures and long aging times. Electrical conductivity increases after all ageing treatments. Strengthening occurs in these systems through formation of nanoscale precipitates; softening again is due to coarsening and spheroidization of filaments and dislocation recovery in the matrix[15,19,36,44–46,49,50]. Conductivity increases due to reduction in scattering by solute atoms (dissolved by the intense deformation) and also due to reduced interface scattering[15,49–51].

1.3 MULTI-LAYERED LAMINATES

The second common morphology of metal composite that has been extensively studied is nanoscaled multi-layered laminates. These composites comprise a repeating sequence of essentially planar layers. Their microstructures are more regular and defined than the ribbons produced by casting and drawing. They are produced by one of two types of methods, characterized as bottom-up and top-down processes.

Bottom-up processes involve building the composite using deposition techniques such as physical vapor deposition (PVD), electrodeposition, and magnetron sputtering[2,8,52–54]. These processes entail assembling the composite by small clusters of atoms or a thin layer at a time. Bottom-up processes are amenable to use with a wide variety of potential elemental combinations, yield laminates with low-impurity content (though this is more challenging to achieve with electrodeposition), and provide control of phase dimensions to below the nanometer scale, with typical layer thicknesses being on the order of 1-10 nm[38,55–58]. While the precise control and uniformity are significant advantages, the growth rates possible with bottom-up processes are low so that only thin films are feasible to produce[54,57,59,60].

In contrast, top-down processes refine the microstructure of bulk materials. In particular, severe plastic deformation (SPD) processes are employed to refine microstructures to the sub-micron range in bulk quantities. As their name suggests, these processes entail imparting very large strains (usually >4)[38,61,62] and in doing so reduce the bi-phase interface spacing, reduce grain sizes within each phase, strain harden the material, and drive changes to grain morphology and orientation. Numerous SPD processes have been developed, but the most widely studied and the one most amenable to producing laminates is accumulative roll bonding (ARB)[38,61–64].

1.3.1 Nanolaminates fabricated through bottom-up processes

The individual layers of bottom-up laminates are polycrystalline and collectively the grains exhibit one of three morphologies (Figure 1.2)[58,65]. One type is equiaxed with the intralayer single-phase boundaries that are normal to the bi-phase interfaces but generally not aligned between adjacent layers (and hence phases). The other two have in-plane grain dimensions several times greater than the layer thickness with the intralayer boundaries either not aligned between adjacent layers, forming microstructures like random stacks of plates, or very closely aligned, forming columns of alternating layers. The columnar structure is associated with epitaxial growth of the phases on one another and does not occur for all element combinations or all layer thicknesses. In any case, at nanoscale layer thicknesses the layers are typically spanned by a single grain[58,65–72].

Bottom-up techniques are near-equilibrium processes, and the resulting atomic arrangements, both crystal structures and the bi-phase interfaces, are simply those that are thermodynamically favored. The bi-phase interfaces are atomically sharp when the constituents are immiscible[8,57,58,66,73–75] and may be coherent, semi-coherent, or incoherent, depending on the crystal structures and lattice parameter mismatch of the constituents[Nasim20, Misra05, Saenz-Trevizo20]. In addition, the interfaces adopt specific crystallographic orientation relationships, such as the {111}Cu||{110}Nb and ⟨110⟩Cu||⟨111⟩Nb Kurdjumov-Sachs (KS) relationship in FCC/BCC pairings and cube-on-cube in FCC/FCC composites[8,54,58,69,73,76]. The grain rotations about the layer normal direction are random though, rendering these laminates isotropic in-plane[66,77].

Extremely small layer thicknesses can induce changes to the structure of the phases as well. In some systems, such as Zr/Nb and Mg/Nb, one phase undergoes a phase transformation

to match the crystal structure of the other phase when the layers are too thin to permit interface misfit dislocations. The transformed material is called a pseudomorphic phase and, as might be expected from a change in structure, the properties of composites containing a pseudomorphic phase can deviate from those of the usual state, such as greater hardness[53,54,66,75]. Composites with pseudomorphic phases have not been examined as extensively as those with stable phases, but available results show the same active mechanisms as in other metal nanolaminates[54].

Since growing bulk nanolaminates by deposition is impractical, mechanical testing of these laminates has largely been through nano-indentation and micro-pillar compression[58,66,69,76,78–80]. The hardness measured in an indentation test is a measure of the yield strength[58,77,81], although the stress state is not the same as that in standard uniaxial tension or compression tests[78]. In addition, when the laminates are very thin, the measured response may include effects of the substrate. The indentation direction is usually along the growth direction for practicality; the in-plane direction has been only minimally investigated[58]. ("Standard" mechanical tests are possible with thin films but are more difficult and therefore less common. For example, uniaxial tension has been used to study effects on elastic modulus in Cu-Ni thin films[82]. Additionally, Mara et al. measured an ultimate tensile strength similar to that inferred from indentation[78,83].) Despite some of its limitations, indentation is useful for evaluating and comparing the relative performance of various specimens.

The hardness of deposited nanolaminates monotonically increases as layer thickness (h) is reduced. For many bi-metal systems, the hardness scales with $h^{-1/2}$ until ~50 nm layer thicknesses. This is the same scaling as the traditional Hall-Petch relationship. Although this relationship captures effects of bi-phase interfaces, contributions from other strengthening

mechanisms are embedded into the initial or "inherent" strength term[56,66,75]. At smaller layer thicknesses the hardness continues to increase as h decreases, albeit at lower rate. Once h reaches around 1-10 nm (depending on the specific system), hardness either plateaus or begins to decrease[56,66].

The strength and plateau thickness can vary substantially across systems, indicating a role of interface character and material properties: Cu-Nb plateaus at ~7 GPa for 1 nm thick layers while Cu-Cr plateaus at 6.8 GPa starting at 10 nm, and Cu-Ni peaks at 4.5 GPa at 5 nm before decreasing with smaller h. Nevertheless, for all systems, the peak hardnesses are substantial fractions of the theoretical strengths ($\sim G/30$)[56,66,75]. The difference in hardening rates above and below 50 nm layer thickness was found to vary with the nature of the bi-phase interface – the FCC/BCC combinations have a greater large-thickness hardening rate than in the Cu/Ni FCC/FCC system. As discussed in greater detail later (Section 1.3.3), the FCC/BCC systems have bi-phase interfaces that are essentially impenetrable to dislocations, while in the latter with common crystal structures and slip systems, the coherency strains present a weaker barrier[56,66]. Interestingly, the grown laminates have lower hardnesses (by ~20%) and lower Hall-Petch coefficients (by ~80%) compared to the heavily-drawn composites with comparable layer spacings, despite the laminates having greater Nb fractions[75].

1.3.2 Nanolaminates fabricated through roll bonding

ARB has seen particular recent interest due to the larger finished sizes of laminates and the similarity of the layered configurations to laminates made by deposition processes. As with the heavily drawn composites, the majority of work has focused on the Cu-Nb system, which has also seen more success than others[53,58,64,73,77,84]. Although control of the layer thicknesses

is less precise than for bottom-up methods, layer thicknesses can be as low as about 10 nm, allowing close comparisons to nanolaminates made by deposition. Additionally, the final laminates can be much thicker than is practical to produce by deposition, typically several millimeters thick, enabling mechanical characterization by test methods other than nanoindentation[8,53,59,73,85,86].

The intralayer grain structure of ARB laminates is predominantly wide, flat grains. At nanoscale thicknesses, each layer is typically spanned by a single grain[9,77,87–89]. Refractory metals are more commonly reported as being multi-crystalline in the through-thickness direction[9,88,90]. Grain sizes in the in-plane directions are anisotropic – their dimensions in the rolling direction are several times those in the transverse direction. Both dimensions are about 10 times greater than the layer thickness[9,64,77,87,91].

The bi-phase interfaces produced by ARB are distinguished from those of deposited nanolaminates by their orientation relationships and their atomic-scale structures[61,64,73,84,92]. While the interfaces remain atomically sharp after ARB (provided the constituents are immiscible), they take on new configurations with atomic-scale facets[73,84,92]. The crystallographic textures deviate from those of PVD and sputtering and vary with size scale. At layer thicknesses above ~700 nm (in Cu-Nb), the classic rolling texture persists[84,90]. Below this thickness, the orientation relationship for FCC/BCC is again a Kurdjumov-Sachs type, but with an atypical interface plane, {112}Cu||{112}Nb, instead of pairing of close-packed planes, {111}Cu||{110}Nb; regions with twinned Cu can have a variety of other relationships as well[73,84,92–94]. In addition, the crystal orientations aligned with the in-plane directions are not random as they are in PVD laminates – specific directions point along both the transverse and rolling directions[8,59,95]. The factors governing the relationships that form have been determined

to be low formation energy and plastic stability, i.e. the ability to maintain orientations and orientation relationships during straining[73,84]. These suggest that the ARB process could be used to achieve particular interfaces with desired character. Changes to the rolling direction have been found to alter the orientation relationships[73,88]. ARB laminates have also been found to be low in dislocation density compared to rolled single-phase materials[9,96].

In terms of mechanical performance, the hardness of ARB laminates increases as layer thickness decreases, reaching GPa levels, as in thin-film nanolaminates[53,58,73,88,94,97]. However, the values measured for ARB laminates with sub-micron layer thicknesses are consistently ~20% lower than for laminates of the same layer thickness made by deposition-type processes[73,77,88,97–99], which was determined to be due primarily to the different crystal orientations produced by the two methods – the crystal direction aligned normal to indentation in ARB laminates is both elastically and plastically softer than that aligned with the indentation direction in PVD laminates[73,98]. Tensile strengths of ARB laminates parallel to the layers are also somewhat lower than the strengths (converted from hardness) determined by indentation normal to the layers[59]. The strengths along two in-plane directions also differ from each other in tension, compression, and indentation hardness, an effect attributed to the aforementioned crystallographic texture[59,77,95]. Shear strengths have also been found to be highly anisotropic which can lead to dissimilar failure modes for the two directions[77,92,100,101].

1.3.3 Strengthening mechanisms in nanolaminates

The ultra-high strengths of nanolaminates are derived from several mechanisms which are the same regardless of whether the composite was made by bottom-up or top-down methods. The descriptions evolved from the ones developed during consideration of the

filamentary composites discussed previously and so bear similarities to them. One set of mechanisms is related to the size scale or spacing of the phases, while another set is related to the characteristics of the interfaces themselves. Restricting the systems to crystalline constituents, plastic deformation in these composites is due to motion of dislocations and strengthening is related to inhibiting that motion[38,53,79,94].

At the largest length scales, conventional dislocation motion and pile-up at boundaries takes place. This encompasses thicknesses of roughly several microns down to submicron level where there is sufficient space for multiple dislocations to form and collect on a single plane. In multi-layered laminates, pile-ups occur at both grain boundaries and bi-phase interfaces; at small spacings the interfaces become the more common boundary type. The pile-up causes a stress concentration which, once enough dislocations have collected, overcomes the strength of the barrier. Because of the stress concentration from the pile-up, the applied stress necessary to transmit slip is less than the strength of the barrier itself, *i.e.* the material is softer. In this regime, the Hall-Petch scaling of strength applies so that $\sigma \propto h^{-1/2}$, where h is layer thickness rather than grain diameter used in the standard Hall-Petch model[53,66,74,79,94,102,103]. The width L of a dislocation pile-up is given by

$$L = \frac{NGb}{\pi(1-\nu)\tau} \tag{1.2}$$

where N is the number of dislocations, G is the shear modulus, b is the length of the Burgers vector, ν is Poisson's ratio, and τ is the resolved shear stress[39,74,75]. For typical materials, pile-ups of ~5 dislocations require spacings greater than tens of nanometers. Thus, for layers roughly in the range of 50 nm down to 5 nm, the distance between boundaries is too small for multiple dislocations to move on the same plane and back stresses on the source accumulate from the dislocations that do form[56,74,75,94].

In these cases, deformation instead occurs by movement of individual dislocations through a mechanism called confined layer slip (CLS). During CLS, a dislocation expands until it is trapped between bi-phase interfaces that are effectively impenetrable. Further motion of the dislocation occurs through bowing parallel to the interfaces in an Orowan-loop type mechanism. The flow stress still increases as layer spacing decreases, but now follows the scaling relationship $\sigma \propto \frac{1}{h}\ln\left(\frac{h}{b}\right)$ where h is again layer thickness and b is the length of the Burgers vector[53,58,66,74,79,104]. Based on observations that Cu/Nb laminates are generally weaker than predictions from the original model formulation, refinements have been made to the model to account for dislocations left at the bi-phase interfaces by previous CLS glide events and back-stresses from elastic deformation of the interface region, resulting in

$$\sigma = \frac{MGb}{8\pi h}\left(\frac{4-\nu}{1-\nu}\right)\ln\left(\frac{\alpha h}{b}\right) - \frac{f}{h} + \frac{Gb}{\lambda(1-\nu)} \tag{1.3}$$

where M is the Taylor factor, G is shear modulus, ν is Poisson ratio, α relates to the dislocation core size, and f is a characteristic interface stress[58,74,105]. This mechanism has been directly observed using nanoindentation in a TEM for Cu/Nb nanolaminates[104] and is essentially the same as that observed in a layer-like portion of a Cu/Nb filamentary composite[14].

Finally, at even smaller layer spacings (<5 nm), the strength of the laminate is dictated by the stress needed to transmit single dislocations across interfaces[5,53,58,74,79,106,107]. In this regime, the hardness no longer increases with decreasing layer thickness[58,74,108]. Instead, the interface character and the properties of the abutting phases determine the resistance to crossing the interface. Interfacial structure, lattice mismatch, and shear modulus mismatch particularly influence this resistance[56,58,74,94,106,107,109].

Coherent interfaces, where crystal structures and slip systems are continuous across the interface (e.g., Cu/Ni), provide little geometrical resistance to transmission[56,79,94,109].These

composites still exhibit strengths on the order of 1-2 GPa though, indicating substantial strengthening from other sources. The most important has been found to be coherency strains due to lattice mismatch, with an estimate of the upper bound of the strength of this type of interface being the coherency stress of a perfectly coherent interface[56]. The interface is likely not perfectly coherent, lowering the resistance from this mechanism, but additional strengthening can come from Koehler stress when the phases have unequal shear moduli[56,58,107,109].

For composites with multiple crystal structures, like FCC/BCC of Cu/Nb laminates, the interfaces are at least partially incoherent and therefore the coherency stresses are minor. Since the slip systems are not shared across phases, a dislocation cannot directly traverse the interface and slip transmission requires formation of a new dislocation in the adjacent layer[56,74,94,110]. The strengthening effect of semi- and incoherent interfaces are due to relatively low shear strengths of those interfaces. The low shear strength has two roles in impeding slip. First, the stress field of a dislocation near the interface causes the interface to shear, which produces an image force that attracts the dislocation to the interface. Second, once at the interface the core of the dislocation broadens or spreads into a non-planar structure within the interface region. Transmitting the dislocation requires additional stress to re-coalesce the core and bow the dislocation into the other phase[56,94,107,110]. Thus, an interface with a high shear strength may lead to a lower peak composite strength because the core cannot dissociate. At the same time, if the interface shear resistance is too low, it will behave like a free surface and the laminate is expected to behave like a stack of foils[56,74,107].

1.3.4 Effects of temperature on nanolaminates

When deposited Cu/Nb films are subjected to moderately elevated temperatures, the Nb layers decompose and spheroidize[111–116]. The process is similar to the breakdown of lamellar microstructures in traditional multi-phase systems like eutectoid steels and conventionally-processed Al-Ni[117]. The driving force is reduction in areas of interfaces and boundaries that have excess strain and interfacial energy. (Since the two are immiscible and not mixed, there is minimal chemical energy involved.)[111–114,116,118]. Breakup (or pinch-off) of the layers occurs by deepening of grooves at the single-phase grain boundaries that are aligned normal to the layer planes[111,113,114,116,119]. Roughness of the interface also appears to reduce the time to break up the layers[116,120,121].

Typically, for layers <15 nm thick, the time for spheroidization varies from 1-3 hours at temperatures of ~500°C[115,116]; in contrast, for layers >35 nm thick, the layered structures remain stable for more than an hour at 700°C[111,115]. The latter stability appears to be associated with the formation of a zig-zag array of triple-points. The 15 nm layers are unstable essentially because they are too thin relative to the in-plane grain size to form this type of array. During the rearrangement from the layered structure to the zig-zag configuration, a vertical translation is required. For the thinner layers, the vertical offset is greater than the layer thickness, and so they are split (pinched off) with ends of layers terminating in the layers of the opposite phase[111,115]. These ends are unstable due to capillary forces and the layers decompose into spheres through "edge spheroidization"[111,117]. Degradation of the layered morphology, even if not carried to completion, is accompanied by a drastic reduction in strength[115,122].Other systems of immiscible metals behave similarly: ~15-20 nm thick layers of Cu/Ta decompose in less than an hour at 800°C[123] while 5 nm layers of Cu/W are completely degraded in less than 2

hours at 800°C[121]. In the latter case, structure evolution has been found to be governed by transport of W along boundaries[121].

In other studies, non-Cu systems with refractory components (Hf-Ti, Mo-Au, W-Cr) were found to completely recrystallize after annealing for 96 hours at 1000°C. In contrast, a Ta-Hf nanolaminate was found to retain evidence of layers even after this treatment[114]. Cu/Ag laminates with layers of ~100 nm completely spheroidize after several hours at >500°C and lose their strength (though the same system also lost nearly all significant strengthening after 6 hours at 150°C without spheroidization[124]). Cu/Ag also shows a size effect to stability like that exhibited by Cu/Nb, with layers below 20 nm being far less stable than those with thicker layers[70].

ARB laminates with nanoscale layers tend to be more stable at elevated temperature than the PVD laminates discussed previously[9,64,91,96]. During annealing at temperatures up to 900°C for ~2 hours, the main KS texture of ARB Cu/Nb has been found to sharpen rather than weaken, indicating no recrystallization and also elimination of other less-favorable interfaces[9,89]. Texture sharpening is opposite the response of bulk single-phase materials or large-thickness laminates. The texture strengthens because the dominant orientation relationships present have the lowest energy in the deformed microstructure and lower energy interfaces cannot be formed by the coarsening mechanisms[89]. The lack of recrystallization is due to a combination of lower driving force – the density of dislocations decreases in the nanoscale regime as they are absorbed at bi-phase interfaces – and impeded movement of grain boundaries in thin layers[9,89,96]. While there is no recrystallization, the layers coarsen significantly, nearly tripling in thickness after 1 hour at 700°C. However, the layered structure remains intact and few pinch-offs occur[9,91,119]. The layers can also develop waviness as the

intra-layer boundaries move; the degree of waviness is greater for larger starting layer thicknesses[91]. (Recall, for comparison, that PVD laminates with comparable initial layer thickness completely spheroidize after half as long at 700°C[9,111,115].)

The combination of layer coarsening and sharpening texture suggests removal of interfaces that do not have the main texture[9]. Pinch-off before widespread layer breakdown has been occasionally observed away from grain boundaries when the Cu/Nb interface deviates from the main {112}Cu||{112}Nb Kurdjumov-Sachs relationship[9,84,119]. The reduced layer breakup may be due to the lower density of single-phase grain boundaries in ARB laminates, precluding the mechanisms that degrade the microstructure in PVD laminates[9,111,115,119]. In agreement with this, thermal stability was further enhanced when the density of single-phase boundaries was reduced by using cross-rolling ARB instead of always rolling in the same direction. In addition, the interface orientation relationship changed from the typical KS type and the morphology became flat (instead of stepped), though the effects of these changes were not separated from the grain boundary effect[64].

The ARB laminates do still decompose at sufficiently high temperatures though, and faceting at unstable bi-phase interfaces causes perturbations and ultimately Rayleigh instabilities have been suggested as a mechanism that does not require triple points like in deposited laminates[119]. The hardness of annealed ARB Cu/Nb is comparable to as-rolled material of the same layer thickness. Loss of the lamellar structure is accompanied by a substantial loss of hardness[9,91]. The Hall-Petch coefficient increases after annealing up to 700°C, an effect attributed to the layer waviness developed during the treatment[91].

Thermal studies of other laminate systems reveal microstructure evolution mostly by the same decomposition mechanisms[88,97,125–127]: cross-rolled ARB Cu/Ta and Cu/V laminates

exhibit both grain boundary grooving and waviness/Rayleigh instabilities, although their strength remains stable until the lamellar structure degrades; cross-rolled ARB Cu/Fe exhibits an increase in strength at low annealing temperatures and a sharp decrease beyond 400°C. The latter is due to the typical breakdown of the lamellae while the increase is attributed to a relaxation of an interfacial zone that is not present in most typical nanolaminate systems[125]. A reduction in coherency stresses and attendant slight increase in hardness was also noted after annealing of sputtered Cu/304 stainless steel[128]. The Cu/Fe system has also demonstrated increasing stability with layer thickness like that noted for PVD Cu/Nb laminates, with layers 30 nm thick spheroidizing after times that produce only minor grooving in composites with 90 nm layers[126]. When the components are miscible, intermixing occurs and the system evolves toward either solutions or intermetallic compounds. The layer thicknesses affected the rate at which precipitates form and the composition of the compounds. Dissimilar solubilities of the components in each other and disparities in diffusivity are thought to control the initial phases (and subsequent sequence, if multiple phases are possible)[112,120,129]. Due to the ability to form new, nanoscale precipitates, some of these can increase in strength after thermal excursions[130].

1.3.5 Localized deformation in nanolaminates

Nanolaminates produced by both bottom-up and top-down methods have been found to exhibit strain localization which often limits their ultimate ductility[55,98,106,131–133]. (Shear bands are also observed in some nanoindentation measurements[99].) During micropillar compression normal to the layers, PVD laminates with sufficiently small layers form a small number of concentrated shear bands. Following formation of the shear band, flow stress gradually softens before rapidly decreasing as the pillar shears completely[55,76]. Meanwhile,

ARB laminates form a large number of shear bands spread along the height of the pillar, termed "diffuse shear banding", and no global softening occurs prior to failure[73,98]. The manifestation of the localization was linked to the interface structure of each type of composite[73,98]. For PVD laminates, layers remain intact within the shear band but initially are only reoriented. As they rotate, the shear stress increases until the layers slide past one another due to the low interfacial sliding resistance of flat interfaces and the Kurdjumov-Sachs relationship[55,76,98]. Calculations show that the ARB interface is more resistant to sliding, due to the orientation relationship and the atomic-scale faceting, so that instead the individual copper layers shear on crystallographic planes[86,98]. More generally, interfaces that do not transmit dislocations lead to tilting of layers and non-crystallographic shear banding (e.g., PVD Cu/Nb and heterotwin interface Cu/Ag), while interfaces that do permit dislocations to cross lead to shearing on crystallographic planes (e.g., ARB Cu/Nb)[94,131].

Recent work has focused on producing nanoscaled metals which achieve exceptionally high strengths and microstructural stability while mitigating other aspects such as the proclivity for shear banding and anisotropic behavior. A general philosophy which has emerged is to form microstructures that are nano-scaled in 3 dimensions, meaning structures that are non-planar, hierarchical, and/or stabilized by nano-scale second phases[2,60,79,134–136]. Thin films fabricated by concurrently depositing Cu and Mo via sputtering can be used to produce hierarchical microstructures containing Cu islands and regions of co-continuous, intertwined Cu and Mo. After micro-/nano-pillar compression, no shear bands were observed; Cu-Mo nanolaminates of similar length scales *do* exhibit shear bands. The prevention of shear banding is attributed to the misalignment of slip systems in ligaments of the tortuous structure and the presence of Cu islands that may strain harden[60,79,134,137].

The co-deposition technique has been expanded to other immiscible systems which have also proved to form hierarchical, tortuous microstructures of various modulation directions and length period that are currently under investigation[136,138]. For example, co-deposited Cu-Ta films with non-uniform hierarchical microstructures can achieve GPa hardness like nanolaminates without shear bands[139]. As with laminates, techniques other than deposition are used to produce bulk quantities of material. Cryogenic ball milling of copper/refractory systems Cu-(1-10)at% X (X = Nb, Ta, Mo, or W) followed by thermal aging has been shown to nanocrystalline phases with dispersed, nanoscale particles and nano-lamellar structures of the refractory elements as well as mechanically alloying the constituents to produce supersaturated solid solutions. (The solute concentration is only a few percent, but this is high as the Cu-X systems are essentially completely immiscible at low temperatures.) Thermal aging studies show that these systems can remain nanoscaled even after annealing at ~700-1000°C for several hours (note that copper melts at 1085°C). Initial microhardnesses can reach ~4-5 GPa, and after additional aging remains at ~1-2 GPa[140–146]. The stability is due primarily to kinetic hindrance as the nanoscale insoluble particles inhibit grain boundary motion with additional thermodynamic stabilizing effects as solute refractory atoms near the grain boundaries reduce the driving force for grain growth[140,143,144]. Mechanical testing of these materials did not produce shear bands even at strain rates of ~10^5 /s[7,141,147].

An additional type of localized deformation called kink banding has been observed in metal laminates[77,85]. Kink bands are a region where the microstructure is misoriented at a constant angle relative to the initial configuration. This phenomenon occurs when loading parallel to the interfaces in materials that are anisotropic and have aligned planes of low shear stress. Other examples of systems where kink bands have been observed are continuous fiber-

reinforced composites and single crystals of metals. The process of kink band formation bears some resemblance to the shear bands described above: a slightly misaligned portion of the material yields and begins to rotate, which produces a geometric softening that promotes further rotation in a relatively narrow region. In metal laminates, kink bands propagate without a decrease in the macroscopic stress (unlike shear bands) and without cracking or delamination. A localization somewhat like kink banding has also been found in eutectic Ag-Cu material compressed at strain rates of 2500-6000 /s. Colonies of alternative Ag and Cu layers kinked or folded while maintaining continuity of the layers through the corner, though delamination occurred above ~25% strain[148,149]. While some models for kink formation have been developed based on the quasi-static results for the Cu-Nb system[77,150], additional studies of the high strain-rate behavior are needed to understand the competition between the mechanisms like confined layer slip, shear banding, and kink banding.

1.4 ALTERNATIVE COMPOSITE PROCESSING METHODS

The multiphase metals studied in the present work were fabricated through two other methods which have received less attention for producing composite materials than those discussed previously. The first, used for the material of Chapter 2, is equal channel angular extrusion (ECAE). ECAE is a severe plastic deformation technique in the same vein as the accumulative drawing and bundling and accumulative roll bonding processes used to produce filamentary composites and laminates, respectively. The second, used for the material of Chapters 3 and 4, is phase transformation and decomposition, whereby sequences of thermal and mechanical treatments are used to induce formation of a particular morphology of stable microstructure.

1.4.1 ECAE processing of metals

In the case of ECAE, a billet of initial material is forced through a die consisting of two channels (the same dimensions as the billet) which meet at a corner defined by the full angle between their axes 2Φ (Figure 1.3)[3,151,152]. The outer corner of the channels is typically smoothed into an arc which subtends an angle Ψ to reduce extrusion pressure needed to overcome friction[153,154]. When passing through the corner, the billet deforms in the intersection plane of the channels, imparting a significant amount of strain. Assuming that the deformation is simple shear, the shear strain γ imparted by a single pass through a die with channel half-angle Φ (and neglecting the outer curve through angle Ψ) is:

$$\gamma = 2\cot(\Phi) \tag{1.4}$$

With the consistent billet orientation, distortion of material elements is progressively increased between passes so that after N passes of path A the shear accumulated is simply[3] $\gamma_{total} = N \times \gamma$. To compare with other forming processes, converting to effective strain is more useful and for ECAE is given by[3]:

$$\varepsilon_{eff} = \frac{\gamma}{\sqrt{3}} \tag{1.5}$$

As a point of reference, 4 passes with a die angle of 90° gives an effective strain of ~4.6 compared to true strains of ~10 for ARB nanolaminates[77].

Despite the intense deformation, the billet geometry and dimensions are nearly unchanged by the extrusion, which allows further extrusions with the same tool[3,152,155,156]. Maintaining the billet dimensions also means that ECAE can be used to produce bulk quantities of material. Common billet cross-sections are square or circular and, between passes, the billet can be rotated around the extrusion axis (or not rotated). Rotating the billet alters the strain path between passes and thereby the final microstructure. Several sequences of rotations, called

"paths", have become standard: A (0°, i.e., no rotation), B_A (alternating ±90°), B_C (90° in same direction every pass), C (180°), and E (180°, then 90°, then 180°)[151,154,156,157]. Paths A and B_A progressively elongate and thin material elements, with A causing thinning in one dimension while B_A thins in two[157,158]. Meanwhile, paths B_C, C, and E ultimately reverse deformation of preceding passes and return elements to their original shape for multiples of 2 (path C) or 4 (B_C and E) passes[154,156,157,159].

The deformation mode when passing around the corner has been shown to be similar to the assumed simple shear, but slightly altered by the presence of friction, the rounding of the external corners of the channel, and material that is not perfectly plastic[3,151,160–162]. After a single pass, the texture can be simulated reasonably well by assuming simple shear but the measured texture is not uniform throughout the billet due to variation in material flow from the top of the billet to the bottom[151,160,161]. For multiple passes, texture continually strengthens for path A, become highly pass-dependent and difficult to characterize for paths B_A and B_C, and for path C overall strengthen the first-pass texture but even-number passes produce weaker textures than after odd-numbered passes as there is partial recovery for every other pass[151,156,161,162].

The texture changes are indicative of the microstructure evolution occurring. The extrusion deforms grain shapes, reduces their size, and forms subgrain dislocation cell structures[161,163–166]. With repeated extrusions, these cell structures gradually increase in misorientation angle until they essentially become grain boundaries after a large numbers of passes[151,156,163,164,166,167]. Grain refinement is most rapid during the first pass then continues more slowly afterward[155,163,165,168]. Grain size distributions and morphologies stabilize after ~4-8 passes to average diameters of ~0.1-1 μm for a variety of materials, with variation due to

rotation path, processing conditions (e.g, temperature, extrusion rate, alloy), die geometry, and the specific combination of these factors[154,156,162,164,165,168–170]. In general, paths C and B_C have been found to produce more equiaxed grains while A and B_A give greater aspect ratios and less homogeneous microstructures[156,157,163]. Recrystallization during extrusion or intermediate annealing steps can form abnormally large (and dislocation-lean) grains for all paths[151,156,160,163].

1.4.2 Strengthening in ECAE-processed materials

Most of the materials processed by ECAE are single-phase, and therefore the primary strengthening mechanisms are due to the grain refinement Hall-Petch effect and strain hardening which cause yield and flow stresses to generally increase with each pass for the first several passes[163,165,171]. The stresses stabilize though, as grain sizes reach their minimum and dislocation densities saturate[163,164,170,172]. In some cases, additional passes cause a reduction in flow stresses by inducing recovery and recrystallization[164]. Most ECAE-processed materials exhibit little work hardening after yielding, which is understandable since the effective strains are usually on the order of 5-10 and dislocation densities accordingly are high[163,164,169,170,173]. The significant non-random textures also lead to anisotropic plastic responses when subsequently loaded, regardless of processing path similar[174–176]. The anisotropy is due to the change in strain path as the slip systems activated by the loading are different from those during processing, the processing-induced subgrain structures are not encountered equally for all systems, and the active systems differ between loading directions. The anisotropy is typically transient though –the flow stresses and hardening rates (usually softening by this point) of

different directions are similar once the processing dislocation structures are sufficiently dissolved[174–177].

1.4.3 ECAE processing of multi-phase materials

Despite some of the earliest work on ECAE processing being with metal/metal composites[3], most interest in multi-phase metals made by ECAE has focused on improving the properties of conventional alloys. The strain hardening and grain refinement imparted can greatly increase the flow stresses relative to the standard materials[154,178–182]. For precipitate-containing alloys, the precipitates are often fragmented, and some then dissolve[154,180,183–185]. Supersaturated solutions formed by ECAE-induced dissolution are unstable and can form precipitates dynamically during extrusion or afterward even at room temperature for low melting point alloys[180,185–187]. Precipitation in this condition is driven by strain and chemical energy and the transport of atoms to form nuclei is potentially assisted by the defect structures formed by the extensive deformation[185,187,188]. Some metal matrix/ceramic particle composites have also been explored. The matrix experiences the typical grain refinement and strain hardening while the particles become more uniformly distributed. The particles may fragment but are not refined as significantly as the matrix[154,189,190].

Recently, new attempts have been made to use ECAE in the production of metal/metal composites[141,157,158,180,191,192]. Of the few studies that have been performed, most begin with phase dimensions in the range of 10-100 μm. Unlike ceramic-particle composites, the ductile particles are deformed during extrusion. Their shape changes follow the transformations of material elements described above for the theoretical analysis of ECAE. For example, path A elongates the particles[157,158,180], and paths E and B_C leave them relatively unchanged[157,180].

While the grains within each phase were refined to a few hundred nanometers in diameter, the phases themselves remained above the size needed for the anomalous strengthening observed for wire-drawn and laminated metal composites. Thus, with strengthening primarily due to grain refinement and strain hardening as in single-phase materials, the strengths were still modest at best, albeit increased over as-cast material[157,158,180,191].

A recent (perhaps only recent) result of a nanoscaled microstructure used ECAE to consolidate powder, induce precipitation of a supersaturated solution, and refine grain size. The starting powder particles were supersaturated Cu-10 at% Ta achieved through extensive cryogenic ball milling which mechanically alloyed the metals. The ECAE processing then caused nanoscale inclusions of Ta to form and kept grains below 100 nm in both phases. This composite exhibited high thermal stability, high flow stresses, and significant ductility[7,140,141,147]. The microstructure was also stable under dynamic compression loading and no shear banding was reported[147,193]. However, the flow stresses, though high relative to the starting materials, did not reach the same magnitudes as those achieved for other metal/metal composites. The strengthening was attributed primarily to the typical dislocation interactions with nano-scale precipitates and not the single-dislocation mechanisms of filamentary and laminated metal composites[7,147,193]. The microstructure is also not like that which would be achieved by extensive ECAE processing in a top-down type of approach, which makes leaves open the question of the influence of ECAE processing on mechanical behavior of nanoscale metal composites.

1.4.4 Strain localization in ECAE metals

Strain localization during testing of ECAE-processed materials does occur, but in most cases requires dynamic loading rates[169,170,194–196], whereas in nanolaminates shear bands formed during quasi-static compression. One exception is magnesium alloys, although these also form shear bands at low rates after conventional processing as well; ECAE processing of these alloys does not cause a new deformation mode to become active. However, ECAE processing has been argued to increase propensity for strain localization as the extensive grain refinement may prevent twinning so that slip becomes more favored[197]. ECAE processing may also affect the tendency toward forming adiabatic shear bands, which are shear bands formed at high strain rates where the name indicating the role of temperature rise and thermal softening on their formation. This thermal influence distinguishes ASBs from the geometric instability that initiated shear bands in nanolaminates. ASBs are discussed in greater detail in Section 1.6. The formation of ASBs is not uncommon in nanocrystalline and ultrafine-grained materials, regardless of processing, due to the reduced capacity for hardening and increased flow stresses that come with the grain refinement[171,195,198,199]. SPD methods such as ECAE exhaust strain hardening capability in addition to reducing grain size. This may further increase the propensity for shear band formation, but also may not as nano- and ultrafine-grained materials typically exhibit little capacity for strain hardening[171,200]; SPD-processed materials have not been conclusively shown to be more or less prone to forming ASBs.

Localized deformation formed during the ECAE processing have been noted, but these are not reported to grow or otherwise affect mechanical response during subsequent testing[3,166,201]. (Though in some cases such localizations can cause cracking of the billet before extrusion can be completed[202].) Levin et al. did report shearing deformation during quasi-static

compression of some ECAE Cu-Ta composites but noted that this may have been related to poor bonding between the phases[157]. Meanwhile, compression of the particulate-type Cu-Ta composites (made by ECAE processing after ball-milling) did not produce shear bands even at strain rates up to 700,000 /s[7,141,147,193]. Both of these studies used Cu as a primary component though, and Cu seems to be resistant to shear band formation; Cu typically only forms shear bands for forced shear conditions even after ECAE[203–206]. The stability has been attributed to the relative ease of recovery processes and high stacking fault energy[203,204]. The dearth of metal/metal composites made by ECAE processing precludes general conclusions about the role of the microstructures produced by ECAE on tendency for flow localization.

1.4.5 Multiphase metals through phase decomposition

For a given bulk composition, multi-element systems often exhibit a single phase that is stable at higher temperatures and multiple stable phases at low temperature. By subjecting the material to various thermal and mechanical processes, such as annealing, cooling, and deformation, a variety of microstructures can be produced[207–211]. One early area of interest in this field was eutectic alloys. Their microstructures are broadly similar across many systems, frequently lamellar and continuous throughout large regions or discontinuous with discrete particles of one phase distributed in a matrix of the other[209,210,212–214]. The phases typically exhibit well-defined crystallographic orientation relationships and the interfaces can be coherent, semi-coherent, or incoherent[207,209,210,212,214–216]. In addition to lamellar microstructures, multi-modal and hierarchical microstructures have recently been receiving attention as a way to achieve high strengths as well as higher ductility than is usually found in nanostructured materials. On one hand, the strength of these materials is attributed primarily

to well-known mechanisms such as boundary blocking, solid solution effect, and dislocation storage[207,209,210,212,213]. For example, strengths are generally found to increase as length scales of the microstructure decrease; in fully lamellar microstructures, flow stresses scale with phase spacing λ as $\lambda^{-1/2}$, analogous to the Hall-Petch relationship[209,210,212,213] and the scaling found for nanolaminates.

Unlike traditional eutectic materials, multi-modal materials can have both lamellar and non-lamellar regions, as well as features which span length scales. One design principle that has arisen in this area is to incorporate multiple morphologies to promote non-homogeneous plastic deformation through multiple mechanisms as this can improve overall plastic response[2,217–219]. For example, in a Ti-based composite, a combination of micro-scale shear banding and dislocation mechanisms was found to enhance ductility and hardening without sacrificing strength[220]. Furthermore, these microstructures can be made without the symmetry found in the nanolaminates discussed previously, which produces a more isotropic response. Multi-modal microstructures, and therefore deformation, can also help to avoid the detrimental features of nanolaminates such as shear banding[2,218,220]. The initial results are promising but the response of hierarchical materials is still relatively unexplored for more demanding conditions such as high strain rates, temperatures, and radiation exposure.

1.5 STRAIN RATE SENSITIVITY OF STRESS

At strain rates in the range of ~10^{-3} – 10^{4} /s, flow stress during plastic deformation is primarily linked to interactions between dislocations and obstacles such as grain boundaries, interfaces, and other dislocations. These interactions have an associated time scale: an obstacle

may be overcome at a lower stress with more time or a larger stress in less time, or temperature can be increased to reduce the mechanical stress needed. Thus, many materials exhibit an increase in flow stress with increasing strain rate due to the reduced time for dislocation motion to occur[221,222]. The two parameters typically used to relate flow stress and strain rate are the strain rate sensitivity parameter m and the activation volume V^*, together given by[223–227]:

$$m = \frac{\partial ln\sigma}{\partial ln\dot{\varepsilon}} = \frac{\sqrt{3}k_B T}{V^*\sigma} \tag{1.6}$$

where k_B is the Boltzmann constant, T is absolute temperature, and σ is flow stress. The rate sensitivity and activation volume describe the effects of thermally-activated mechanisms such as dislocation motion on plastic deformation in metals. In the case of a dislocation-mediated mechanism, the activation volume represents the size of the region swept by a mobile dislocation in a single event. When dislocations do not travel far, pile-ups near the source exert stress that inhibits slip of new dislocations, and rate sensitivity is increased[223,224,226,228,229]. For FCC metals, grain boundaries and dislocation structures produced by deformation provide the major portion of the strength of the material. The strain rate sensitivity of these materials is therefore primarily in the post-yield response. In contrast, for BCC metals the intrinsic lattice resistance is high compared to other strengthening effects so that overcoming the lattice remains the rate-limiting process, and therefore the rate sensitivity primarily occurs in the yield point. HCP metals can behave either way depending on the element[171,221,222,227,230].

Reducing grain sizes to the nanocrystalline regime has been found to cause enhanced strain rate sensitivity in many single-phase FCC and HCP metals (relevant examples including Cu, Ni, Mg, and Zn). Meanwhile, BCC and some HCP metals (e.g., Nb, Fe, Ti) exhibit reduced strain rate sensitivity, to being almost rate-*in*sensitive[170,171,195,222,224,229,231]. In terms of the activation volume, for FCC metals, the distance between grain boundaries is decreased and so

V^* decreases, and thus m increases. For BCC metals, the lattice still provides most of the resistance and is unchanged by the reduction in grain size, so V^* and m remain relatively unchanged[224,230]. Strain rate sensitivities for these mechanisms cover the range of $m \approx 0.01$-0.1. Much higher rate sensitivities, $m \approx$ ~0.5-1, have been reported from some nanocrystalline FCC metals and are associated with different rate-controlling plasticity mechanisms, assumed to be mediated by grain boundary motion[39,171,229].

As covered above, in the realm of nanostructured metal composites, the mechanisms mediating plasticity at low rates in nanostructured metal composites are distinct from those of single-phase metals (Sections 1.2.2 and 1.3.3), and so trends with rate sensitivity are potentially uncorrelated from those of the constituents. To date, most measurements of rate effects in nanostructured composites have consisted of nanoindentation and micropillar compression covering a range of quasi-static strain rates. For nanolaminates, the only consistent trend to have emerged seems to be that there is no unusual increase in rate sensitivity of strength. Comparing nanoscaled FCC/BCC composites to the single-phase nanocrystalline form of the component elements, the rate sensitivity of the composite has been found to be greater than that of the BCC component but less than that of the FCC component[232–234], comparable to both components[106,228], or lower than both[235,236]. Other crystal structure combinations have not been widely explored but also do not display extraordinary behavior: HCP/HCP Mg/Ti and FCC/HCP Cu/Zr had rate sensitivities between those of the nanocrystalline components[106,231], and FCC/FCC Cu/Ni had an SRS lower than that of the constituents[69,232]. An added complication for the HCP materials is their anisotropic flow stresses and strain rate sensitivities due to the large variation in critical shear stress for the different slip systems[237,238]. Thus, strongly textured composites with HCP components will likely exhibit anisotropy in strain rate

sensitivity if slip within the HCP phase contributes significantly to the plastic response[237–239]. In addition, for HCP/cubic composites the hexagonal vs. square symmetry means that slip planes of the two crystal systems may be aligned by an interface orientation relationship, but only some of the slip directions on those planes, exacerbating anisotropy in rate sensitivity as the aligned directions transmit slip more easily[240,241].

The few studies using dynamic strain rates (~10^3 /s) show little deviation from the quasi-static results: a nanolayered Ag/Cu eutectic (with many randomly-oriented grains) was found to be relatively rate-insensitive[148] while a Cu/Ta composite with Ta nanoprecipitates had rate sensitivity comparable to that of the Cu matrix[141].

The effect of layer repeat period size or thickness (i.e., the combined thickness of the two layers in a bi-metal composite) on rate sensitivity seems to be mixed. Some composites do show an increase in m with decreasing layer thickness, as would be expected to occur if activation volume decreased with h[233,235]. However, other composites show a stable m across the same range of layer thicknesses[228,231], others a stable m followed by an increase below a critical thickness[236], and yet others a decrease through much of the nanoscale range before stabilizing against further layer thinning[232]. The variation in thickness may depend on the type of interface: copper layers with nanoscale twins have a higher rate sensitivity than nanocrystalline Cu layers for layers thicker than ~30 nm. That sensitivity decreases with layer thickness as the density of twins decreases[242]. In turn, this may be related to the bi-phase interface relationship within the twinned regions, or blocking effects of the twin lamellae, since enhancement of strain rate sensitivity in nanotwinned single-phase Cu has also been observed[229,232]. In another instance, an incoherent interface is associated with increased SRS

with decreasing h, but the same material with coherent interfaces exhibits decreasing SRS with decreasing h[232].

While some of these variations are consistent with the activation volume being limited by the bi-phase interfaces, others suggest that another feature is dictating the behavior. One possibility is that the absorption and spreading of dislocations at non-coherent interfaces effectively increases the distance a dislocation can travel, i.e., increases the apparent activation volume and thus reduces rate sensitivity. Alternatively, if dislocations can pass through the interfaces instead of being stopped at them, which may occur if the interface transitions from semi-coherent to coherent, the activation volume could increase as well[228,232,236].

Specimen-scale deformation of nanolaminates and multilayers are not always covered in these investigations of rate sensitivity, so it is assumed that modes are generally unchanged over the small range of strain rates of these studies. When discussed, the deformation type is reported to change with layer thickness but not with strain rate. For some composites, shear banding occurred below a critical layer thickness[242], while others do not exhibit these[231]. Kingstedt et al. did report kinking and delamination in their Ag/Cu eutectic, but these occurred at both low and high strain rates; shear bands were not mentioned[148]. Meanwhile the Cu/Ta particulate composite was explicitly reported to not shear band at quasi-static strain rates[141], though there was no mention of localization at higher strain rates[147].

1.6 FORMATION OF ADIABATIC SHEAR BANDS IN METALS

When loaded at high strain rates and to high strains, the deformation of many materials becomes nonuniform, localized along narrow bands of high shear oriented at an angle to the loading direction[199,243,244]. (As a minor point – these features are actually thin, usually non-

planar, *surfaces* which appear as bands only in cross-section.) These bands are of great engineering importance because voids and cracks may form within them and ultimately lead to fracture and failure of the material[198,244–246]. They are referred to as adiabatic shear bands (ASBs), owing to the localized accumulation of heat associated with their formation[198,199,243,246]. The "high" strain rates necessary to form ASBs are material-dependent and need not be dynamic strain rates of ~10^3 /s – the first reports of ASBs, by Tresca around 1878, were in alloys possessing unusually low thermal conductivity and heat capacity rather than after exceptionally rapid deformation[198,246,247].

Careful experiments have revealed the macroscale formation and progression of ASBs. First is an initial period of homogeneous deformation which can extend to substantial strains; then deformation proceeds inhomogeneously for a brief period while the flow stress remains relatively high; and finally the deformation begins to occur only within a very narrow region, reaching very high levels (hundreds of %), while the surrounding material is not deformed at all[198,199,248,249]. Often the flow stress collapses during this final stage as well, but most likely due to void coalescence and formation of a macroscopic crack within the shear band rather than the formation or propagation of the shear band itself[198].

Computational analyses have been used to determine the conditions required for strain localizations. In a general sense, material softening effects must exceed hardening effects, and the imbalance must lead to further softening in excess of hardening. Nearly all materials have hardening rates that decrease with strain so that at some point the hardening rate equals or falls below the softening rate (or the material fails). Localization sets in when a small deviation in the deformation field increases the net softening rate only within a small volume. The small deviation can then grow (deform more) than material elsewhere and it propagates across the

body. To initiate the localization, the initial site must contain some form of non-uniformity that causes local softness, such as a particular texture, a spot of locally elevated temperature, or a geometric deviation; in the case of ASBs, elevated temperature and thermal softening is the assumed cause. Note that net softening alone does not cause localization: if the body softens uniformly, deformation should remain homogeneous. That is, softening is necessary for localization, but not sufficient[198,199,244,246,250,251].

Based on the general picture of ASB progression, theoretical analyses have been used to study the effects of various factors on their formation[198,199,246,250,252]. Onset of localization is delayed by greater hardening effects such as strain hardening, strain rate hardening, strain rate sensitivity, phase transformations, and inertial effects (depending on strain rate). Localization due to thermal effects is enhanced by low thermal conductivity, low heat capacity, greater thermal softening rate ($d\sigma/dT$), and higher flow stress (due to the greater amount of heat from plastic work and therefore temperature change induced). Texture or change in texture can either prevent or promote localization, depending on the texture and the loading conditions[199,244,250,251,253–255]. These findings provide some insight into the behavior that might be expected though: since nanostructured materials generally possess higher flow stresses and limited strain hardening, they might be more prone to form ASBs. ECAE materials, even if not nanostructured, also have very little strain hardening capacity, and composites by their nature, have a high density of microstructural heterogeneities which could potentially serve as shear band initiation sites. However, as discussed in Section 1.5, nanoscaled grains can increase strain rate sensitivity and hardening rate; these can offset the negative effects of refinement. To date, no broadly-applicable analytical criteria for the formation of ASBs employing some

combination of these have been found, although various researchers have found criteria for their own sets of data[198,199,246,250,252].

The microstructural processes by which shear bands form is still unclear. Some researchers favor formation tied to sudden movement ("avalanches") of large numbers of dislocations causing rapid a local temperature increase. These models assume that a very large number of dislocations accumulate against a barrier (e.g., grain or twin boundary), then suddenly move together either by overcoming the barrier or when the barrier breaks down. Temperatures calculated assuming this type of mechanism are broadly in-line with measured and implied experimental values[227,244,256]. Geometric softening arising from localized rotation has also been proposed. Essentially, a grain or group of grains rotate to an orientation that is favorable for cooperative slip which leads to inhomogeneous accumulation of strain and drives deformation in neighboring grains[252,254,255,257,258].

Recently, the base assumption of adiabatic shear failure has been called into question as well: rather than a reduction in flow stress due to temperature, softening due to dynamic recrystallization has been suggested[259–262]. While recrystallization has long been known to occur at some point during shear banding, it is largely thought to occur after formation and concurrently with deformation[198,199,259,262]. Through sets of interrupted tests, dynamic recrystallization progressively increased prior to ASB formation in several alloys. Due to the interruptions between loading events, the temperature increase, and hence thermal softening, was negligible[259–261]. Simulations were used to show that shear bands could result from these conditions[261,263]. An independent work investigated initiation of ASBs in a single system with both dynamic recrystallization and thermal softening active. The dominant mechanism

depended on the initial state of the microstructure and varied continuously from recrystallization-controlled, to a combined role, to control by thermal softening[262].

As summarized by Walley, a number of groups have found evidence that localization in various steels is associated with ultrafine second-phase particles that drive microvoid formation. These voids, as well as those that form through coalescence of vacancies, could serve as nuclei for shear bands[246]. In various other multi-phase materials, the size of inclusion particles, grains, and lamellae colonies has been found to affect propensity for shear banding, though clear mechanistic causes for these effects are still lacking[252,255,264–266].

1.7 SHOCK AND SPALL OF MULTI-PHASE METALS

A further broader interest is the performance of multi-phase metals under extreme loading conditions, where deformation behavior may substantially differ from that at quasi-static or lower dynamic strain rates. To this end, the response of these materials to shock and/or spall conditions been studied to some extent both experimentally and through simulations. The plasticity mechanisms of layered Cu/Nb during shock loading normal to the layers was found to strongly deviate from the pure materials for both PVD and ARB composites. For the PVD laminate, the frequency of deformation twins in Cu layers was much higher than in shocked pure Cu, while the dislocation density was insignificantly increased from the deposited state[57]. ARB nanolaminates showed no increase in twin density but also minimal increase in dislocation density, whereas the pure metals formed many dislocation tangles. Reduced twinning compared to the PVD laminates was attributed to the faceted interface compared to the atomically-flat structure of PVD layers and much larger layer thicknesses of the ARB laminates, which can suppress twinning[267]. Simulations show that the stresses required to

transmit dislocations are much higher for flat interfaces of PVD laminates than for the faceted interfaces of ARB laminates[268,269], which may reduce generation of new dislocations. On a macroscopic scale, the layered structure remained intact. The orientation relationship at the bi-phase interface remained as well, though twinning in the Cu changed the interface plane locally[57,267]. Only immediately at the failure plane of a sample completely spalled the layers were destroyed, transforming to equiaxed grains due to intense plastic deformation[267]. Spall voids were found only in the Cu layers, mostly in the center (measured parallel to the shock direction) and occasionally near the interface, but not by separating the bi-phase interfaces[57,267].

An analogous result was obtained for particulate-type Cu/Nb and Cu/Ag composites, where voids formed in the softer phase (Cu matrix in the former, Ag dendrites in the latter) near – but not at – the bi-phase interfaces[270]. In contrast, spallation seems to occur by decohesion of interfaces in other two-phase alloys such as titanium alloys[271–273] and some brasses[274]. This latter set of composites had microstructures larger than nanoscale, and the effect of this on behavior is unclear; simulations with large enough length scales and experiments bridging to smaller length scales are missing. Void formation in the interior of one phase contrasts with the conventional notion that the interfaces themselves are relative weak sites where voids preferentially form, as observed for single-phase materials where grain boundaries serve as the interfaces[267,268,270].

These results also illustrate the effects of distribution and morphology of the phases on resistance to failure. In the layered Cu/Nb, the spall strength was lowered compared to the pure materials as the physics of stress wave interactions with the materials of differing properties across the interfaces produced higher local stresses[57,267]. Simulations have shown that

modifying the interface spacing and orientation relationship in bi-metal laminates can shift void nucleation into either phase or to the interface, and concurrently alter the stress required[268,269,275]. At a sufficiently small spacing, the strengths are reduced as dislocation nucleation changes from homogeneous in the layers to an interface-assisted heterogeneous mode, and failure initiation also moves to the interfaces[268,275]. The particulate Cu/Nb and dendritic Cu/Ag composites had slightly greater spall strengths as their morphologies did not induce these concentrating effects[270]. In these and other non-laminate multi-phase metals, incompatibility of deformation across particular boundaries has been suggested as the way stress increases enough that voids can form[272,276,277]. Other studies have shown that texture and heterogeneous microstructures (e.g., regions or strings of small grains) can produce preferential sites for void initiation. In these cases, the features may lead to local increases in stress or be relatively weak compared to the rest of the material[277–279]. Additional material deformation mechanisms, such as what appears to be shearing between spall voids, has also been observed in Ti alloys due in part to the void morphologies[271,272]. Such unexpected modes illustrate that the response of multi-phase materials to extreme loading conditions warrants further study.

1.8 UNRESOLVED ISSUES WITH METAL COMPOSITES

To date, much of the work on metal/metal composites has been conducted at low loading rates[2,3,10,12,47,60,74,78,85]. However, in their use as structural materials they may be subject to dynamic (high-strain rate) loadings. For materials controlled by conventional plasticity mechanisms, it is considered that at sufficiently high rates, the times associated with the mechanisms governing material response to deformation are comparable to the rate at which

the deformation is being applied, and additional effects such as material inertia also become important[199,280–282]. The mechanical response of nanoscaled metal composites can be governed by mechanisms which do not operate at larger length scales, and their operation at higher strain rates has not been thoroughly investigated. The strain rate sensitivity studies which have been conducted primarily involve a range of quasi-static rates, which cannot necessarily be extrapolated to dynamic rates[69,228,232,234]. The higher loading rates can inhibit thermally-activated processes, contributing to rate hardening and higher stresses in the material. Alternative deformation mechanisms such as twinning may become active[281], and twinned regions are known to behave differently in metal composites[8]. Rapid deformation can also lead to a temperature rise which in turn can lead to thermal softening and failure modes that deviate from those at lower strain rates. For example, steel undergoes a ductile-to-brittle transition as strain rate is increased[199], and many materials exhibit an increased propensity for localized deformation in the form of shear banding when dynamically compressed[171,198,199,244]. The latter is particularly important during dynamic events since shear bands are often precursors to fracture and, as was discussed above, metal composites have proven to be susceptible to shear banding at low rates[198,199,244].

Despite considerable work on the subject, the role of microstructure in the formation and propagation of localized deformation are not well understood. In general, strain localizations are known to occur when a heterogeneity in an otherwise uniform deformation field starts to grow unstably, i.e., at a falling stress level. Effects such as strain hardening and strain rate hardening inhibit localization by increasing the stress required to continue deformation, while thermal and geometric softening promote localization[198,199,244,282]. Some have suggested that microstructural changes (e.g., recrystallization) instead of temperature is

the primary cause of softening that induces shear bands[259,262]. Microstructural heterogeneities that concentrate stress have been shown capable of promoting localization in some cases as well[283]. The microstructures of multi-phase metals contain numerous features which may affect their tendency to localize deformation. In the high strain rate research that is available, heterogeneities have been found to dictate their dynamic mechanical response. However, the complex microstructures and atypical source of the performance of these composites complicate the task of predicting their performance from measurements at low rates and of only their constituents. It is therefore important to study these types of materials under the conditions of interest to develop an understanding of relationships between their structure, properties, and performance.

1.9 EXPERIMENTAL METHODS OF ACHIEVING HIGH STRAIN RATES

One challenge in studying high strain rate behavior is simply in attaining such rates in a controlled setting. Typical mechanical test load frames can only reach strain rates of ~10 /s at the highest, whereas dynamic rates are roughly 1000 /s and higher[199,284]. In the present work, rates on the order of 1000 – 5000 /s were achieved using a Split Hopkinson Pressure Bar (SHPB) (Figure 1.4). SHPBs allow for loading in uniaxial compression and tension and for determining the dynamic stress/strain response based on the theory of one-dimensional elastic wave propagation.

In the typical setup, a short striker bar is launched axially into the end of the incident bar to produce an elastic stress wave pulse in the incident bar. This wave passes into the specimen, likely plastically deforming it, and then into the transmitted bar where it again propagates as an elastic wave. Because the specimen has different properties than the bars, a

portion of the incident wave is reflected instead of passing through. Strain gauges are used to capture the elastic strains of the three waves in the bars (incident and reflected in the incident bar and the transmitted wave in the transmission bar). These signals are then integrated over time using Equations 1.6 – 1.8 to determine the (engineering) strain rate, strain, and stress in the sample[284].

$$\dot{\varepsilon}_s = \frac{2C_b\varepsilon_r}{\ell_s} \tag{1.6}$$

$$\varepsilon_s = \int \dot{\varepsilon} dt \tag{1.7}$$

$$\sigma(t) = \frac{A_s E_b}{2A_s}(\varepsilon_i + \varepsilon_r + \varepsilon_t) \tag{1.8}$$

where E is Young's modulus, A is cross-sectional area, C is elastic wave speed, ℓ is length, ε is strain, and subscripts b, s, i, r, and t indicate the SHPB bars, the sample, and the incident, reflected, and transmitted waves respectively. The stress produced is uniaxial in nature, the same as that used for characterizing materials at low strain rate tests.

A second method of dynamic loading used in this work is flyer plate impact (Figure 1.5). This technique entails launching a flat flyer plate at a second plate that holds the target sample. The velocity of the flyer is commonly on the order of 100-500 m/s, producing strain rates of 10^5 /s and higher. While the impact obviously induces compression in the target, these tests are often designed to generate high tensile stresses within the target and thus probe spall response (as is the present work). This is achieved by making the flyer plate thin enough that a wave reflected off the back face will overlap with a wave reflected from the back of the target (schematically shown in Figure 1.6). For reflection from free surfaces, both waves are tensile since the incident wave was compressive. If the tensile stress is large enough, voids nucleate, grow, and coalesce within a region known as the spall plane. Unlike the SHPB tests, the resulting loading state induced by flyer impact is one of uniaxial *strain*. The key measurement

on the sample is the velocity of the back face (opposite the impact). From this, the stress in the sample throughout the pulse duration can be calculated by assuming one-dimensional wave propagation (see equations in Chapter 4).

1.10 ON COMPUTATIONAL METHODS

A drawback of experimental methods is the inability to monitor the material response at the length scales of constituents and in the entirety of the specimen. Numerical methods enable such analysis and thereby allow for additional insight into dynamic deformation. Finite element simulations grant control that is impossible to achieve in real experiments. Material properties and loading conditions can easily be varied throughout the range of realistic values to determine fundamental response. The value of simulation results rely on relevant material descriptions. The present work was intended to gain general insight into effects of material properties (Young's modulus and density) and the associated derived dynamic properties (wave speeds and impedances) on the propagation of stress waves. For this, simple linear elasticity was sufficient for initial work. Countless other more complex constitutive laws have been developed, all of which are essentially curve fitting to better capture measured response using various parameters[199]. Introducing these other terms, ranging from strain hardening plasticity to the Johnson-Cook equation with strain, strain rate, and temperature will provide additional insight, though deconvoluting the roles of the parameters becomes increasingly difficult.

1.11 OBJECTIVES AND ORGANIZATION OF THE DISSERTATION

The overall objective of the present work is to expand the understanding of the relationships between microstructural heterogeneities and the dynamic mechanical response of multiphase metal composites. High strain rate tests are used to investigate the behavior of

several multiphase metals. Connections are made between microstructural features and the observed deformation modes, namely strain localization methods. Finite element simulations are used to elucidate roles of material properties on wave propagation in idealized version of elastic composites.

The remainder of this dissertation proceeds as follows. Chapter 2 concerns the high strain rate compressive behavior of Cu/Nb composites produced by equal channel angular extrusion. The mechanical performance and deformation modes are compared to a more extensively-studied Cu/Nb composite made by accumulative roll bonding. Chapters 3 and 4 examine two types of Zr-Nb materials in both tension and compression at rates ranging from quasi-static to very high ($>10^5$ /s). Attempts are made to connect behavior across strain rate regimes. Chapter 5 describes numerical simulations of stress waves propagating in simplified and idealized composites. The focus is the effects of material properties and their mismatches across phases on the nature of elastic stress waves during dynamic loading. Finally, Chapter 6 contains suggestions for future research.

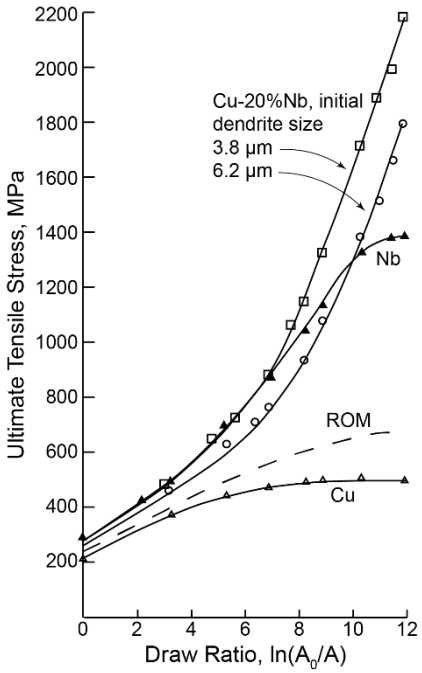

Figure 1.1. Ultimate tensile strengths of highly drawn Cu, Nb, and Cu-20wt% Nb composites. Both composites exhibit greater strengths than predicted by the rule of mixtures (ROM) and, at large enough drawing strains, greater than the stronger component of the composite. From Raabe et al.[23]

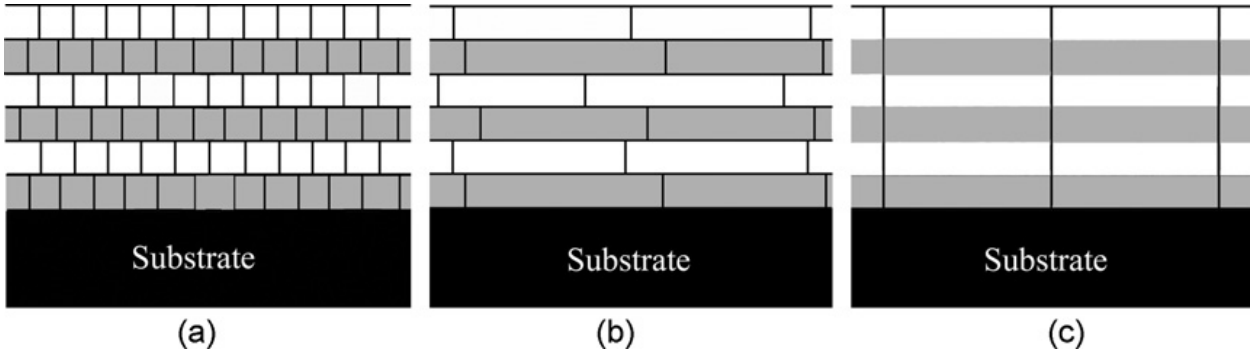

Figure 1.2. Schematic of three types of grain morphologies observed in metallic nanolaminates: a) equiaxed grains with intralayer boundaries not aligned between phases; b) wide, plate-like grains with intralayer boundaries not aligned between phases; and c) columnar structure formed by wide grains with intralayer boundaries aligned between phases (from Wen et al.[65]).

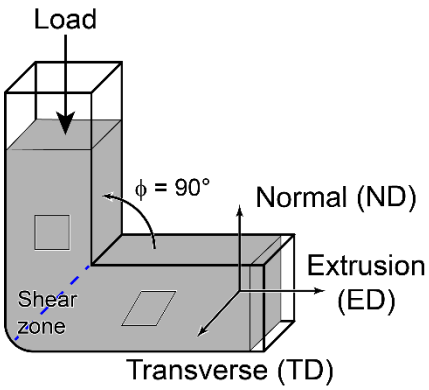

Figure 1.3. Schematic of the equal-channel angular extrusion process[3]. A billet inserted into the vertical channel is pressed through by an applied load and is extruded out of the horizontal channel. Insets show that an initially square material element is transformed into a parallelogram. The die angle Φ need not be 90°.

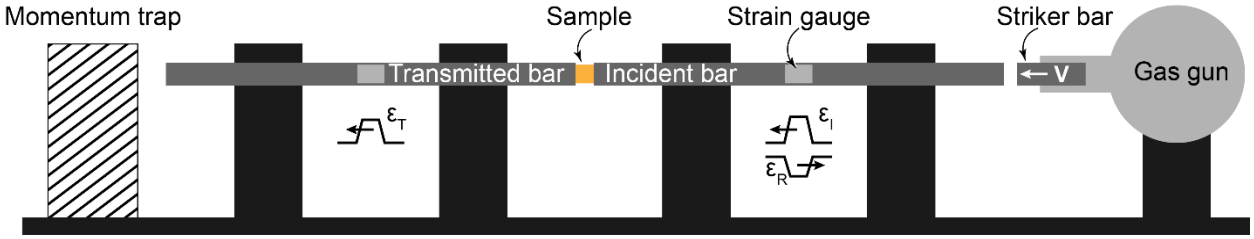

Figure 1.4. Schematic of a Split Hopkinson Pressure Bar. Adapted from Gray[284]

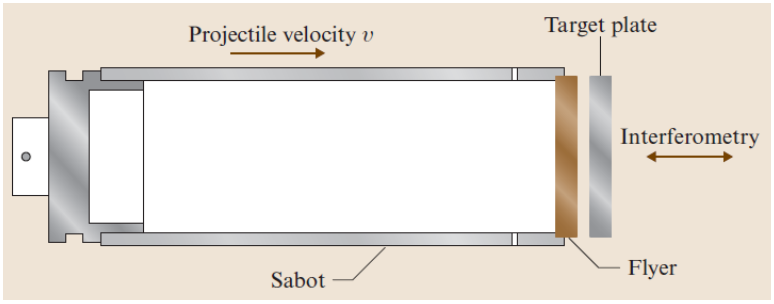

Figure 1.5. Schematic of a flyer plate impact setup designed for normal impact[285]

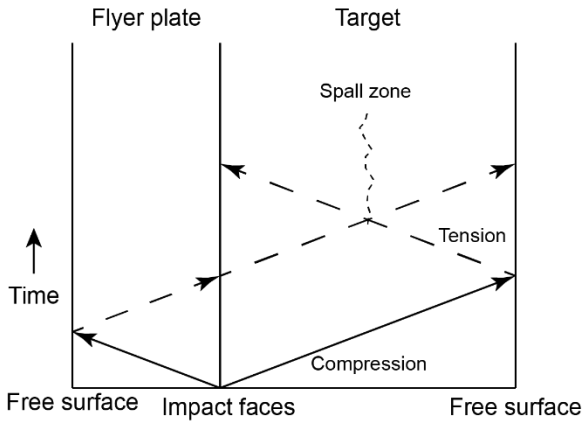

Figure 1.6. Schematic of wavefront positions over time for a flyer plate impact test configured to induce spallation in the target.

Chapter 2

Quasi-static and dynamic response of a Cu/Nb composite following equal channel angular extrusion

2.1 INTRODUCTION

Materials exhibiting combinations of high strength and high thermal and/or electrical conductivity are required for applications in windings for pulsed field magnets, the conductive rails of railguns[286]; advanced electronics including electrical contacts and sputtering targets for film deposition[10,287]; turbocharger and landing components in aerospace[10,287]; cables and contact wires in robotics and high-speed rail[6,10]; and combined structural and functional materials for energy generation such as heat exchangers[6,38,288]. Copper is attractive as the principal component for these applications due to its workability and high thermal and electrical conductivities. However, in pure form, copper exhibits modest strength[19,288–290]. While its strength can be improved by strain hardening or alloying, these modifications can have detrimental effects on conductivity and can reduce microstructural stability at elevated temperatures[64,171,288,291]. Copper-based composites containing immiscible refractory metals have proven to yield interesting property combinations in this regard. These composites can be made with sub-micron microstructural features, providing size-effect benefits in strength yet retaining substantial ductility and stability uncharacteristic of typical ultrafine or nanoscale metals[9,19,27,38,85,98,171,290,292,293]. In some cases, the strengths of bi-phase metal composites exceed those of the constituents, surpassing the limits of linear rule-of-mixtures

predictions[4,12,23]. The mechanisms and microstructural features that enable such capabilities are under active investigation[4,10,16,38,141,293,294].

The most common production processes for copper-based composites involve severe plastic deformation (SPD)[38,47,290,292]. SPD processes involve imparting large plastic strains (≥4) which work hardens the material while also intermixing the constituents and refining their microstructures[38,63,154,292,295]. A number of SPD processes have been employed, including extensive drawing of wires[12,44,290], accumulative roll bonding (ARB) of multilayer laminates[64,77], accumulative drawing and bundling (ADB) of large-diameter wires[18,296], high-pressure torsion (HPT) of thin disks (for hard-to-process metals such as Mg)[295], and equal-channel angular extrusion (ECAE) or pressing (ECAP) of square or round billets[3,62]. ECAE is attractive when the billet geometry is to be retained, is amenable to large billet sizes, and exhibits potential for upscaling to industrial capacities[3,62,287,295].

The current work focuses on the quasi-static and dynamic compressive response of a Cu-18wt% Nb composite processed by ECAE. This composition has attracted attention for its potential use in high-electrical current applications such as pulse magnets and superconductors. With appropriate processing, it can attain strengths that are higher than those of competing alloys, such as those based on Cu-Ag and Cu-Fe, while retaining electrical conductivity that is only about 30% lower than that of pure copper[6,12,19,21,290]. A greater Nb fraction might provide more strength but this would inevitably come at the cost of conductivity[27,47,48].

Despite the potential of such composites for structural applications, the strain-rate sensitivity of their mechanical properties under dynamic loading conditions has received relatively little attention. While dynamic loading is known to promote deformation and structure evolution modes not seen at lower rates (e.g. strain localization and dynamic

recrystallization)[171,198,199], the manifestations of these modes depend on microstructural characteristics like grain size as well as prior work hardening[171,224]. For example, the strain rate sensitivity of ultra-fine grained pure Cu has been shown to be greater than that of corresponding coarse-grained materials[171,297] and exhibits a dramatic upturn as grain sizes are reduced below ~100 nm[226]. In contrast, nanostructured composites of Cu-10at% Ta have been found to be rate *in*sensitive up to strain rates approaching 10^6 /s[7,147].

The present article is primarily concerned with the mechanical response and deformation behavior of the ECAE Cu/Nb composite at quasi-static and dynamic strain rates. The results are compared to those of a Cu/50 vol% Nb laminate made by accumulative roll bonding. Contributions of various strengthening mechanisms of each composite are estimated.

2.2 MATERIALS AND TEST METHODS

2.2.1 Materials

Two Cu/Nb composites materials were used in this study. The first is Cu/18 wt.% Nb. An ingot of this material 250 mm in diameter and approximately 1500 mm long was cast by consumable arc melting (this initial casting was performed by H.C. Starck, Inc., circa 1994; the ingot has remained with Texas A&M University since then). These elements exhibit negligible miscibility in one another in the solid state (temperatures below ~1080°C) and the significant difference in melting points suggests that dendritic structures will form (Figure 2.1)[23]. The as-cast microstructure was not examined here, but specimens from this same ingot had dendrite-like Nb with a fairly uniform 15-25 μm diameter dispersed in a Cu matrix[3]. The distribution of Nb in the Cu was *not* uniform in the ingot though[3], due to agglomeration of the Nb during cooling. Preventing this agglomeration is highly impractical to prevent[298,299]. A

smaller billet was extracted from the ingot and subjected to 8 passes of equal channel angular extrusion (ECAE) following path A (*i.e.*, no rotation of the billet around the extrusion axis between passes). The extrusion was performed at a rate of 0.1 in/s at room temperature using a sliding-wall die tool with a 25 mm square cross section and angle between extrusion channels of $2\Phi = 90°$. The die was lubricated with Loctite 8150 Anti-Seize grease. The resulting extruded billets were approximately 110 mm long (along the extrusion direction, ED) and 25 mm in the two other directions (vertical, labeled the normal direction, ND; and horizontal, labeled the transverse direction, TD – see inset of Figure 2.5a). Only the central 50 mm along the length was used for this work.

With the consistent billet orientation, distortion of material elements is progressively increased with each pass. The shear γ accumulated during each pass of path A is given by[3] Equation 1.4 (copied here)

$$\gamma = 2\cot(\Phi) \tag{1.4}$$

and the Mises effective strain is given by[3] Eqn. 1.5

$$\varepsilon_{eff} = \frac{\gamma}{\sqrt{3}} \tag{1.5}$$

Thus, after 8 passes this material has experienced a total shear of $\gamma = 16$ and an effective strain of $\varepsilon_{eff} \approx 9.2$.

The microstructure within ~5 mm of the central axis of the extruded billet was deemed sufficiently uniform for further analysis. Compression specimens were machined from this region via electrical discharge machining. These were right cylinders, 5.0 mm in height and 5.0 mm in diameter. The specimens were cut in three orientations, each with the loading axis parallel to one of the processing axes (ED, ND, and TD). Two specimens were tested at each rate; a third ND specimen was tested at high-rate to verify that a late-test ringing feature in the

measurements was caused by the strain-limiting collars. Even in the center of the billets, some of the Nb particles were agglomerated into bands. Agglomeration in the initial ingot was an unavoidable consequence of the casting process[298,299], and ECAE processing refines and distorts these features rather than break them apart[3]. These bands were identifiable with the naked eye as dark surface streaks. Specimens were divided for testing such that one specimen at each rate contained these bands and one did not.

To provide a basis for comparison, a 50/50 vol.% Cu/Nb laminate produced by accumulative roll bonding (ARB) was also tested. Details of the processing can be found elsewhere[85,300]. Due to material quantity limitations, mechanical tests were only performed parallel to the rolling direction (RD). All samples were removed from the center of the plate to avoid near-surface effects arising from the ARB process. Cuboidal compression specimens were prepared via EDM with dimensions of 5.1 mm along the RD, 3.9 mm along the ND (perpendicular to the layers and equal to the plate thickness), and 5.0 mm along the TD (in the layer plane, perpendicular to RD). Prior to testing the ARB specimens were annealed for 30 minutes at 400°C in gettered Ar with heating and cooling rates of 10°C/minute. This treatment has been shown to enhance bonding between the most recently bonded layers and thus inhibits delamination during mechanical loading[300]. One specimen was tested at low strain rate (to confirm similarity to previously-reported properties of similar material[59,85,300]) and two tested at high rate.

2.2.2 Mechanical testing

Compression specimens were tested both under quasi-static (QS) conditions, at a strain rate of $\sim 3\times10^{-4}$ s^{-1}, and under dynamic conditions, at $\sim 3\times10^{3}$ s^{-1}. Low rate tests were performed

on a servohydraulic test frame (Material Test System 810, MTS, Eden Prairie) with SiC blocks between the samples and the metal platens to prevent fixture damage. High rate tests of the ECAE material were performed on a split-Hopkinson pressure bar (SHPB) system at Los Alamos National Laboratory. The bars were 350 grade maraging steel with a diameter of 12.7 mm. Momentum trapping was used to preclude multiple hits on the sample, ensuring that all deformation was the result of the measured pulse. The strain rate was ~3.6×10^3 s^{-1} for all of these tests. Hardened steel collars were used to limit the strain to a maximum value of ~0.3. The high rate tests of the ARB material were performed at UCSB on a different SHPB system. The bars in this system were also made of 350 maraging steel but had a larger (19 mm) diameter. Momentum trapping was again used to prevent multiple hits. Strain-limiting collars were not used; instead the striker bar was sized to impart a strain of ~0.3. The strain rate of these tests was ~3×10^3 s^{-1}. The loading faces on all specimens used for high-rate tests were lapped to remove machining burrs and ensure flatness and parallelism to within about 0.01 mm.

2.2.3 Microscopy

Microstructures were examined through a combination of scanning electron microscopy (SEM) and electron backscatter diffraction (EBSD). Specimens for microscopy were prepared from both the pristine material and tested specimens using a combination of wire EDM and a low-speed saw with a diamond wafering blade. The sections were parallel to the loading axis and in orientations selected to reveal localization features visible on the exterior surfaces. The specimens were cold-mounted in epoxy, ground and polished down to 1 μm with diamond suspensions. For imaging with SEM, final polishing was by flat-milling

on a broad-beam ion mill (Leica EM TIC 3x) in two steps: 1.5 hours at 8 kV to remove the near-surface regions affected by mechanical polishing and 30 minutes at 4 kV as a final polish. Because Cu is removed more rapidly than Nb, ion milling produces surface relief between the phases. Shadowing effects were minimized by continuous rotation of the specimen during milling. The resulting surfaces were free of polishing media and provided sharp edges and contrast between phases. It was also possible to discern orientation contrast (by electron channeling) in the Cu matrix when imaged in backscattered mode with SEM.

The slight surface relief from ion milling interfered with EBSD pattern collection. Therefore, for EBSD measurements, the ion-milled surfaces were repolished with 0.020 μm colloidal silica. EBSD was performed on a ThermoFisher Apreo C SEM with an EDAX EBSD camera using an accelerating voltage of 15 kV, current of 6.4 nA, step size of 40 nm, and 8×8 pattern binning. The patterns were indexed by a dictionary method using EMSphInx[301]. The indexed datasets were subsequently cleaned and analyzed using OIM Analysis (AMETEK, Inc.); data cleanup consisted of a single iteration of grain dilation which affected <5% of points of each dataset.

The EBSD data were used to determine the pertinent grain dimensions. Grains contain at least 4 pixels and a misorientation angle of at least 2° from neighboring points. These grains were characterized by the major and minor axis dimensions in the viewing plane as well as the aspect ratio, s (minor/major). Texture was analyzed through pole figures. The convention for ECAE materials is to use the TD plane whereas the section planes here were chosen based on localization features. Therefore, the EBSD scans were mathematically rotated to the typical axes using MTEX[302].

2.3 RESULTS

2.3.1 Texture and microstructure of as-extruded composite

The ECAE composite comprises Cu as a continuous matrix and Nb in the form of isolated, pancake-shaped particles, as evidenced by the optical micrographs of the ND and the ED planes (Figure 2.2). The Nb particles are arranged into strings or layers aligned within the ND plane.

The IPFs constructed in the ND and ED planes (Figures 2.3 and 2.4) reveal rather broad Cu grain size distributions. In the ND plane, most Cu grains are roughly equiaxed, with $0.3 < s < 0.5$, and sub-μm in size (Figure 2.5). Also evident are occasional large (>10 μm) grains, presumably formed through partial re-crystallization. The area-averaged grain size is about 500 nm. Similar distributions are obtained in the ED plane, albeit with a great fraction of elongated grains ($s \approx 0.1$).

The Nb particles are polycrystalline with similarly-broad grain size distributions. Most grains are sub-μm while a small number of large grains comprise the majority area fraction of the Nb phase. In the ND plane the grains are roughly equiaxed with $0.3 < s < 0.5$. In the ED plane, however, the grains are far more elongated, many with $s \leq 0.2$.

Figure 2.4 presents the textures of the Cu and Nb phases in the form of pole figures in the TD plane. The Cu-phase textures are similar in many respects to those measured previously in single-phase Cu after 8 passes of ECAE route A[303]. The main texture components in both the ⟨110⟩ and ⟨111⟩ pole figures exhibit symmetry about the shear plane, which lies approximately 45˚ from the ED and about the TD. As is common for shear textures, the intensity is relatively weak, being four times random for most of the texture with the few peak maxima reaching around five times random[151]. While the texture of the single-phase Nb

counterpart has not been reported to date (to our knowledge), we note that the Nb-phase textures are very much like those in IF-steel, another BCC metal, after four passes of route A[155]. The symmetry in and average intensity of the shear components about the 45˚ shear plane in these ⟨110⟩ and ⟨111⟩ pole figure Nb-phase textures are comparable to the reported IF-steel ECAE textures. The consistency implies that most of the Cu and Nb phases in the composite deform as they would when deformed alone and that, in every pass, the deformation can be reasonably described as simple shearing along the plane where the entry and exit channels of the ECAE die intersect.

The ARB laminate consists of continuous layers of pure Cu and Nb (Figure 2.6). The layers have an average thickness of about 200 nm, though in some regions they are as thin as 100 nm and in others almost ~1 μm thick. Orientation (electron channeling) contrast visible after ion milling shows that the copper grains span their layers in the ND and are about 0.25-0.75 μm in the ND plane. These values are consistent with those measured previously on other batches of the same material[77]. Orientation contrast in Nb was insufficient to determine grain size. Nevertheless, previous studies of comparable materials using TEM have shown that the Nb grain size is 1-10 μm along RD, <1 μm along TD, and equal to the layer thickness (~0.2 μm) along the ND. Extensive analysis of textures in ARB Cu/Nb had been performed previously and can be found elsewhere[77].

2.3.2 Mechanical response

The inelastic portion of the compressive response of the ECAE Cu/Nb is distinct for each test orientation at both low and high loading rates (Figure 2.7). The following trends are obtained:

(i) The response is softest along the ED. Under QS loading, yielding occurs at ~400 MPa and, with slight subsequent hardening, the flow stress rises to reach 500 MPa at a plastic strain $e_p \approx 0.2$. Similar behavior is obtained at high rate, albeit at higher stress levels. Here yielding initiates at about 600 MPa and, with continual and constant hardening, the flow stress rises to 680 MPa at $e_p = 0.25$. The dynamic yield and terminal stresses are about 30% greater than the corresponding QS values.

(ii) The response along the ND is intermediate to those in the other orientations. Under QS loading, the response is essentially elastic-perfectly-plastic, at a stress of 500 MPa. At high rate, yield occurs at a stress of about 575 MPa with subsequent hardening up to 700 MPa at $\varepsilon_p = 0.3$. The dynamic yield and terminal stresses are, respectively, 15% and 40% greater than the QS values.

(iii) The response along the TD is strongest, at least at low strains. Under QS loading, yielding occurs at about 525 MPa with rapid hardening to 550 MPa. This is followed by strain softening to $e_p = 0.2$ where the flow stress reaches a plateau at about 500 MPa, 5-10% below the initial yield stress. The terminal flow stress is comparable to those in the other orientations at the same strains. Under high loading rate, yielding occurs at about 625 MPa, followed by hardening to 750 MPa, then slight softening to a flow stress of about 700 MPa at $e_p = 0.3$. This yield stress is 20% greater than at the QS rate, while the peak and terminal flow stresses are ~40% greater.

(iv) The responses in all orientations (nearly) converge and attain a plateau at a common point on their respective stress/strain curves at each loading rate. At the low rate, this point occurs at ~500 MPa at $\varepsilon_p \approx 0.15$ while at high rate it would occur at ~725 MPa and $\varepsilon_p \approx 0.28$.

(v) The response of the ARB laminate closely resembles that of the ECAE material along the TD. Under QS loading, yielding begins at about 450 MPa with rapid hardening to 550 MPa and, following a period of slight softening (to ~500 MPa at $e_p = 0.13$), strain hardening gives rise to a flow stress of 575 MPa at $e_p = 0.3$. At high rate, the response is essentially elastic-perfectly-plastic at 650 MPa up to a strain of $e_p = 0.2$, and then exhibits softening.

(vi) The average hardening rate at intermediate strains increases for all directions of the ECAE material but decreases, to the point of softening, for the ARB composite (Figure 2.8). The order of hardening rate with ECAE direction is reversed relative to the order of yield stresses. That is, ED has the highest hardening rate and the lowest yield stress while TD has the lowest hardening rate and the highest yield stress. In the case of TD, the material exhibits strain softening (i.e., a negative hardening rate), although the softening rate at high strain rate is considerably lower than that at low strain rate.

2.3.3 Deformation behavior

Micrographs of the specimen cross-sections (Figures 2.9 – 2.12) show that deformation eventually becomes localized in all but one case: that of the ECAE material along the ND. Thus, localization occurred for all cases where the load was applied parallel to the oriented microstructure, namely both alignment directions of the Nb particles in the ECAE composite and along the layers in the ARB laminate. The localizations take the form of bands in which the material has been visibly misoriented in a coordinated manner relative to the surrounding material. The orientation of the surrounding material is largely unchanged from the initial state. Each band has one end at the corner of the specimen and the other end either at the opposite

corner or within the bulk of the specimen. For the ECAE composites, when multiple bands are present, one crosses the entire width of the specimen while the other(s) end in the bulk; no sample has bands ending in the bulk without one spanning the width and only the ARB composites have full-width bands crossing each other. No bands bifurcate or act as sources for bands at other angles. The degree to which the bands develop is affected by specimen orientation and terminal plastic strain. These deformation bands pass through the bands of agglomerated Nb aligned parallel to the loading direction (when present).

Metrics used to characterize the bands are the orientation angle φ of material inside relative to that outside the bands (schematic in Figure 2.10), the orientation of boundary between deformed and undeformed material β, and the widths of the bands in the direction parallel to the layers within them; the measured values are given in Table 2.1. For both rates, the boundaries of the reoriented material are less distinct and the corner radii larger in the ECAE material than in the ARB material. The angle φ is uniform across the width of each band but can vary along the length; it is highest near the specimen corners and lower near the specimen center, most noticeably in the near-tip regions of partially-developed bands. The β angles are broadly consistent along the length of each band, even in the presence of bands of agglomerated Nb. In the ARB material, the β values are ~42° and φ values are ~60-80°. For the ECAE material, the measured β angles span a wider range but typical values are $\beta \leq 45°$ and $\varphi < 90°$. The sole exception is the sample tested at high rates along TD, where β reaches nearly 50° near the tip of a band of agglomerated Nb (Figure 2.10, above scale bar). Note that deformation bands that impinge on the side of the Nb bands (as opposed to passing near the end of one) cross through with no apparent effect on the deformation band. Band widths are

lower when more bands are present. For cases with multiple bands, the ones that cross the full width of the sample are wider than the partial bands.

In contrast, compression along the ND direction of the ECAE material does not produce localization bands at either loading rate. Instead, the specimens exhibit barreling. The barreling is non-uniform in regions containing Nb-rich agglomerates because of the plastic incompatibility between phases (the Nb being stronger than the Cu) (Figure 2.11). Where these Nb-rich bands meet a free surface, the adjoining Cu extrudes laterally beyond the ends of the Nb bands. Macroscopic mechanical response was not noticeably affected by the presence of these Nb bands at either rate.

2.3.4 Texture and microstructure evolution

To gain insight into the mode of deformation, the texture and grain evolution in the samples with the most fully developed localization bands (TD compression, Figure 2.10) were further examined via EBSD both inside the bands and in adjacent (non-reoriented) material (Figures 2.13 and 2.14). In material deformed at low strain rate, the crystallographic texture, as well as the morphological texture of the grains in the Cu and Nb phases, are much like those of the starting ECAE material (Figure 2.3). They comprise mostly fine (sub-μm) grains with a high aspect ratio and aligned closely along the TD. The Cu phase contains a small fraction of re-crystallized twinned grains, again as seen in the as-ECAE processed material. In contrast, in the banded regions, the textures and grain morphologies have noticeably changed. The Cu-phase texture has weakened substantially. The ⟨111⟩ poles have dispersed and the ⟨110⟩ pole figure displays signs of evolving from the initial ECAE texture towards a TD compression texture expected for an FCC metal, i.e., TD||⟨110⟩. The aspect ratio of the Cu grains within the

shear bands has reduced and the long axes have morphologically reoriented nearly normal to the TD, which are signatures of TD compression. The Nb-phase textures and grains within the bands have augmented in similar ways, indicating that the Cu and Nb phases co-deformed within the bands. The ⟨111⟩ pole figure suggests evolution towards TD||⟨111⟩, a compression texture for BCC. Taken together, the analysis suggests that the localized bands predominantly accommodated the TD compression deformation.

The phase textures and grains in the material deformed at high rate exhibit differences that are not seen in the material deformed at low rate. The Cu phase textures outside the shear bands has weakened but nonetheless retained most of the starting ECAE texture components. Most of these grains remain elongated along the TD, with occasional pockets of re-crystallized material. The Cu-phase within the shear bands, however, is characterized by a much higher fraction of large re-crystallized Cu grains (>10 μm). as evidenced by the number of large grains and annealing twins in Figure 2.14. This is consistent with the high propensity for Cu to undergo re-crystallization and grain growth at even ambient temperatures[203,304,305] coupled with the temperature rise associated with adiabatic heating. Rudimentary analysis based on mass density, heat capacity and the measured stress-strain curves yields a predicted average temperature rise of about 50 K[203]. The texture is nearly random, with a few sharp peaks, likely corresponding to the few relatively large grains in the scan. For both low and high strain rates, the pole figures for the Nb within the deformation bands are rotated about the surface normal with the relative arrangement of peaks essentially unchanged. The aspect ratios of the Nb platelets within and just outside the bands are the same. This indicates that the Nb platelets have simply rotated along with the surrounding material rather than deforming through lateral

flow. There is no evidence of recrystallization of the Nb: an unsurprising result, given the high melting point of Nb.

Despite the large reorientation angles and high local strains, there is virtually no evidence of cracking in the ECAE specimens. In contrast, the ARB specimens exhibit cracking at the center of the TD faces on the outer surface (Figure 2.15).

2.4. DISCUSSION

The following discussion focuses on comparisons of the anisotropic flow response of the ECAE Cu-Nb composite with that reported earlier for pure Cu and pure Nb and that obtained from crystal plasticity models as well as the nature of the strain localizations. While establishing equivalence between the test conditions associated with the available literature data and those of the current test results is challenging, the flow properties of both Cu and Nb are known to plateau at large plastic strains, comparable to those of interest in the ECAE materials, and thus minor differences in test conditions are not expected to change the key conclusions. The comparisons thus provide useful insights into the properties of the Cu-Nb composite.

The anisotropy in yield stress and hardening behavior of the ECAE composite at low strain rates is broadly consistent with previous experimental studies on ECAE of pure Cu and pure Nb as well as predictions based on crystal plasticity models for polycrystalline metals that incorporate texture and grain microstructure[175–177,306]. In pure Cu, among the three principal directions, the yield stress in the TD is predicted to be greatest; the subsequent plasticity is characterized by transient softening (to strains of about 0.1) followed by gradual hardening. In the ED and ND, the yield stresses are predicted to be somewhat lower than that in the TD but

without a significant transient softening domain. The disparities are due to differences in the orientations of the strain paths caused by the ECAE processing and subsequent compressive loading. When the strain path is changed between two processes, transients in the response from the second loading can arise due to a "cross effect" and "reversal effects". The former is caused by dislocations activated by the second loading interacting with the dislocation structures formed by the first loading; reversal effects are dislocations moving in the opposite direction during the second event as in the first, and their motion may be aided by internal stresses caused by the first loading (the first stage of this is the Bauschinger effect). The extent to which cross effects and reversal effects are activated varies with the change in orientation between the initial strain and subsequent loading events[175–177]. Crystal re-orientations and removal of the prior dislocation structures by the new mobile dislocation populations in the three respective loading directions eventually bring the stress-strain curves to a common point[175,177]. These predictions, although made for only one of the pure constituents, are in accord with the present test results for the composite. Some pertinent comparisons are shown in Figure 2.15.

The degree of anisotropy of the extruded composite on a relative basis appears to be rate-insensitive. At low strain rates, the maximum difference in flow stress of materials in the strongest and weakest directions (TD and ED, respectively) is about 80 MPa (at about 2% plastic strain). Relative to the average strength (500 MPa), this represents a range of about 18%. At high rates, the maximum difference in the extruded composite rises to over 120 MPa. Relative to the average strength at the same strain rate (680 MPa), the range is again about 18%.

Additional comparisons are made of the flow stress achieved in both the Cu-18% Nb composite and pure Cu and Nb following ECAE. Some of the available data on low and high rate tests are plotted on Figures 2.7 and 2.16. At low strain rates, test results on pure Cu after 8 passes of ECAE show a flow stress in the ED of about 430-460 MPa (with almost elastic-perfectly plastic response), about 40 MPa lower than that of the Cu-Nb composite. Additionally, low-rate tests on pure Nb show a flow stress of about 540 MPa, 60 MPa above that of the composite. The fact that the composite flow stress is between those of the pure components after similar straining histories suggests that the composite strength can be rationalized (roughly) on the basis of a rule-of-mixtures predictions. Additionally, in light of the fact that the plastic properties of Cu and Nb are not very dissimilar, the prospect for achieving large strength gains by addition of Nb in its current form is not great. Similar conclusions are reached upon examining the high-rate test data in Figure 2.7[170,176,203].

For the ARB laminates, the measured strength (in the RD) is greater than that of the ECAE composite in the comparable direction (ED), by about 100 MPa. This difference is attributable to the fine scale of the constituent layers (ca. 200 nm). Previous studies have shown that the strength increase associated with layer thickness is attributable primarily to dislocation blocking at bi-phase (Cu-Nb) interfaces and that it follows a Hall-Petch type relationship, notably $\Delta\sigma_y = K_y h^{-1/2}$ where K_y is the Hall-Petch coefficient of the boundary (≈0.08 MPa-$m^{1/2}$) and h is layer thickness[59]. Thus for the ARB material with 200 nm average layer thickness, the corresponding strength increment is predicted to be about 170 MPa: comparable to, though slightly higher than, the increment inferred from the strengths of the current laminate and of corresponding coarse-layered (>10 μm) ARB laminates. That is, the strength of coarse-layered Cu-Nb laminates made the same way is 440 MPa[59,77], about 110 MPa below that of the

current laminate. The differences may be attributed to the non-uniformity in layer thicknesses, as evident in Figure 2.6.

The hardening characteristics of the ARB laminate fall mid-way between the two limiting cases for the ECAE composite. At low strain rate, the ARB laminate exhibits almost no capacity for hardening after yield; by comparison, the hardening rate of the ECAE material spans the range from about 100 MPa in the ED to -250 MPa in the TD. At high strain rate, the hardening rates of the ECAE material in all orientations increase somewhat while that of the ARB laminate remains the same. In both ECAE and ARB materials, the strain rate sensitivity is similar to that of the pure constituents in bulk form. From grain size alone, no effect would be expected as the constituents and other laminates do not exhibit increased rate sensitivity at these length scales either. However this also indicates that there is no special effect on rate sensitivity due to these materials being bi-phase composites, i.e. the thermally-activated mechanisms are unaffected by the presence of the second phase. This fits with the distances between the various types of barriers present in these materials: the grain boundaries and dislocation cells are submicron whereas the distances between bi-phase boundaries are roughly on the scale of 1 micron.

Despite the localized deformation within the ECAE composites, no signs of the onset of localization are evident in the stress/strain curves. In contrast, other materials that exhibit similar forms of strain localization, including fiber composites, metal single crystals, and geological minerals, exhibit stress drops due to localization[307–310]. This is also distinct from other types of strain localizations, such as shear bands, which are also accompanied by decreasing flow stress[198,199].

The strain hardening behavior of pure Cu has been studied extensively. The processes involved include generation of a high density of dislocations, the formation of cellular structures and low- and high-angle boundaries, and, in some cases (especially in very pure Cu), re-crystallization. The effects are manifested in an increasing strength with accumulated plastic strain and, at sufficiently large strains, attainment of a plateau in strength. In Cu, the plateau strength at low strain rates is 400-450 MPa. By comparison, assuming that the dislocations are randomly arranged, the predicted strength of Cu once the dislocation density has reached saturation ($\rho_d = 2\times10^{15}$ /m^2, after 8 ECAE passes[163,173]) is $\Delta\sigma = M G \alpha b \sqrt{\rho_d}$ where G is shear modulus (45 GPa), α is a constant (≈ 0.3), b is the length of the Burgers vector (0.256 nm), and M is the Taylor factor (about 3). Combining these results yields a strength of 460 MPa. Similar processes occur in pure Nb, although its higher melting temperature renders the material less prone to re-crystallization[170]. The strengths of the current ECAE Cu-Nb composite can be attributed to the same processes.

Based on the prevailing understanding of strengthening mechanisms in metal composites, the present ECAE material should not be expected to achieve extraordinary strengths. Throughout most of the material, the distance between Nb particles is at least an order of magnitude larger than required for transition from bulk behavior of the constituents to the interface spacing playing a significant role in blocking dislocations[5,74]. In addition, the Nb particles have not been significantly distorted from their initial shape into long, thin filaments, especially not to the extent that they might begin to ask like whiskers[12,14,38]. Thus, further improvements would require significant refinement in microstructural length scales. Ostensibly, continued ECAE processing could be used to transform the Nb particles into extremely fine ribbons. Assuming the deformation of material elements and the Nb particles

follows the geometric relationships for ideal ECAE, the ratio between final (δ) and initial (δ_0) particle "diameters" is given by[3]

$$\frac{\delta}{\delta_0} = \left(1 + \left(2N\cot(\Phi)\right)^2\right)^{-1/2} \tag{2.1}$$

for N passes of ECAE path A in a die with angle 2Φ. Performing the required number of extrusions is likely prohibitive in both time and cost though: a reduction from $\delta_0 \approx 10$ μm of the current particles to $\delta \approx 10$ nm requiring roughly $N = 500$ passes. Further, it is not clear whether even this many passes of ECAE would sufficiently reduce the *spacing* between Nb filaments, which is a critical factor in transitioning to single-dislocation mechanisms and achieving extraordinary strengths (see Sections 1.2.2 and 1.3.3). One alternative strategy that has shown promise involves ECAE of mechanically alloyed powders made by extensive cryo-milling of the constituent powders (rather than using a cast product as the starting material). In one case, a Cu-10%Ta composite achieved strengths of almost three times that of the Cu itself[141,147]. This type of composite benefits from a combination of nanoscale precipitates and spacing between them, grain refinement in the matrix, and strain hardening.

Several types of deformation modes involving strain localization are possible. The localizations observed here in the ECAE composite appear to be kink bands. Fully-developed kink bands (as defined by Nizolek et al.[300]) are localizations in which (i) the deformation band is either microstructurally or crystallographically misoriented with respect to the surrounding material, (ii) the misorientation angle, φ, is approximately uniform across the width of the band, and (iii) the orientation of the plane of the boundary of the band nominally bisects the angle between deformed and undeformed material. (To exclude twins from this definition, the plane of the band boundary cannot be restricted to a specific crystallographic plane.) Kink bands have previously been observed in a range of anisotropic materials including fiber

composites, geological minerals, and engineered laminates. The bands in the ECAE material appear to meet the criteria for kink bands. The bands are clearly microstructurally misoriented from their surroundings and the bands are not restricted to a single crystal plane. The misorientation angles are approximately uniform across the width of the bands, although they vary somewhat along the band length. Finally, the misorientation angles are close to but typically somewhat less than 2β (i.e., the angle is not exactly bisected). One possible implication is that the kink bands observed here are not yet fully developed and that further deformation would cause further rotation. Deviations from ideal values may be due in part to the microstructural heterogeneities of the ECAE material, evident in the micrographs in Figures 2.2 and 2.9 – 2.11.

Kink bands that extended across the width with nearly-constant misorientation can be wider and exhibit larger misorientations very near the specimen corners while the tips of the bands (residing in the bulk) appear to be wedge-shaped. These features suggest propagation from a starting location (typically a corner) followed by additional rotation and spreading rather than simultaneous uniform shearing across the entire width. They are also consistent with lower values of φ in the near-tip regions and the development of wedge-shaped bands. Analyses of kink band formation and propagation suggest that the strains that accommodate the reorientation are primarily elastic in the ECAE material (whereas the corresponding strains in the ARB laminate are likely plastic)[300]. Additionally, initiation of kink bands at corners is consistent with findings that such bands initiate at stress concentrations[77,170,300].

2.5 SUMMARY AND CONCLUSIONS

The current study has examined the plastic properties of a Cu-18% Nb composite following equal channel angular extrusion under both low- and high-strain rate loadings. Textures and microstructures were characterized by optical and scanning electron microscopy as well as electron backscatter diffraction. Comparisons were also made with a Cu-50% Nb laminate made by accumulative roll bonding. The key conclusions follow.

(i) Crystallographic textures obtained within the respective phases in the extruded composite closely mimic those previously found for the pure components alone (Cu and Nb).

(ii) Grain sizes and shapes of the major phase (Cu) exhibit broad distributions, due to a combination of grain refinement associated with the extensive plastic straining and partial non-uniform recrystallization during the extrusion process.

(iii) While the degree of anisotropy, the work hardening characteristics, and the strain rate sensitivity of the composite are similar to those of pure Cu after extrusion, the strength levels of the composite are somewhat greater, falling broadly between those obtained in the pure components after extrusion to comparable plastic strains. The strength of the extruded composite can be attributed primarily to refinement in Cu grain size and a high dislocation density resulting from the extrusion process. Further improvements in strength would require refinement of the pertinent microstructural length scales.

(iv) The deformation modes of extruded composite depend on loading orientation and resemble the deformation experienced by other anisotropic composites. Notably, compression parallel to the plane containing Nb platelets leads to localized deformation by kink banding while compression normal to this plane leads to more uniform

deformation, followed eventually by barreling at high strains. Kink band formation during high strain rate loading gives rise to a temperature elevation that induces further (though not complete) recrystallization of Cu within the kink bands and, in turn, a further increase in the non-uniformity of the Cu grains.

Acknowledgements

The authors thank Prof. Tresa Pollock for providing the Cu/Nb ARB material. The work was supported by the Department of Energy, National Nuclear Security Administration under Award no. DE-NA0003857. Microscopy was performed at the UCSB Materials Microscopy Facility, an MRL shared facility. The MRL Shared Experimental Facilities are supported by the MRSEC Program of the NSF under Award No. DMR 1720256, a member of the NSF-funded Materials Research Facilities Network (www.mrfn.org).

Table 2.1. Characteristics of localization bands.

	ED		TD		ARB
Loading rate	Low	High	Low	High	High
Width (mm)[§]	0.16-0.21	0.29	0.80	0.20-0.34	0.23-0.46
β (°)	30-40	30	40	19-50	42-43
φ (°)	20-45	15-30	90	60-130	60-80

[§] Measured parallel to the layers within the bands.

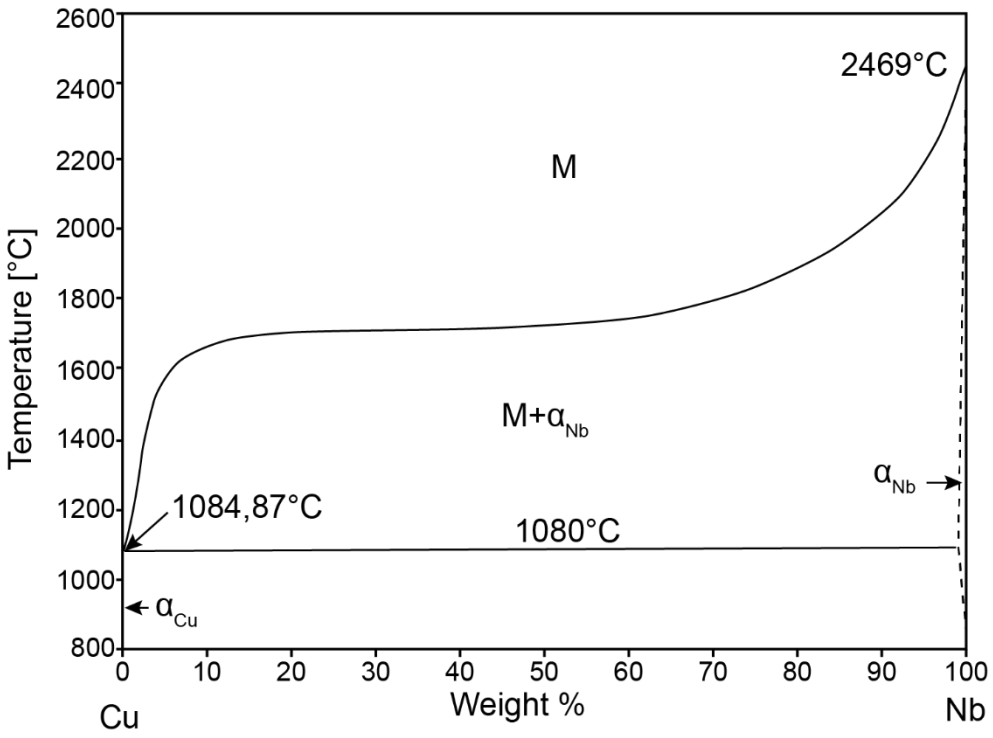

Figure 2.1. Binary phase diagram for the copper-niobium system, after Raabe[23], Neither element has significant solubility in the other at temperatures below 1080°C.

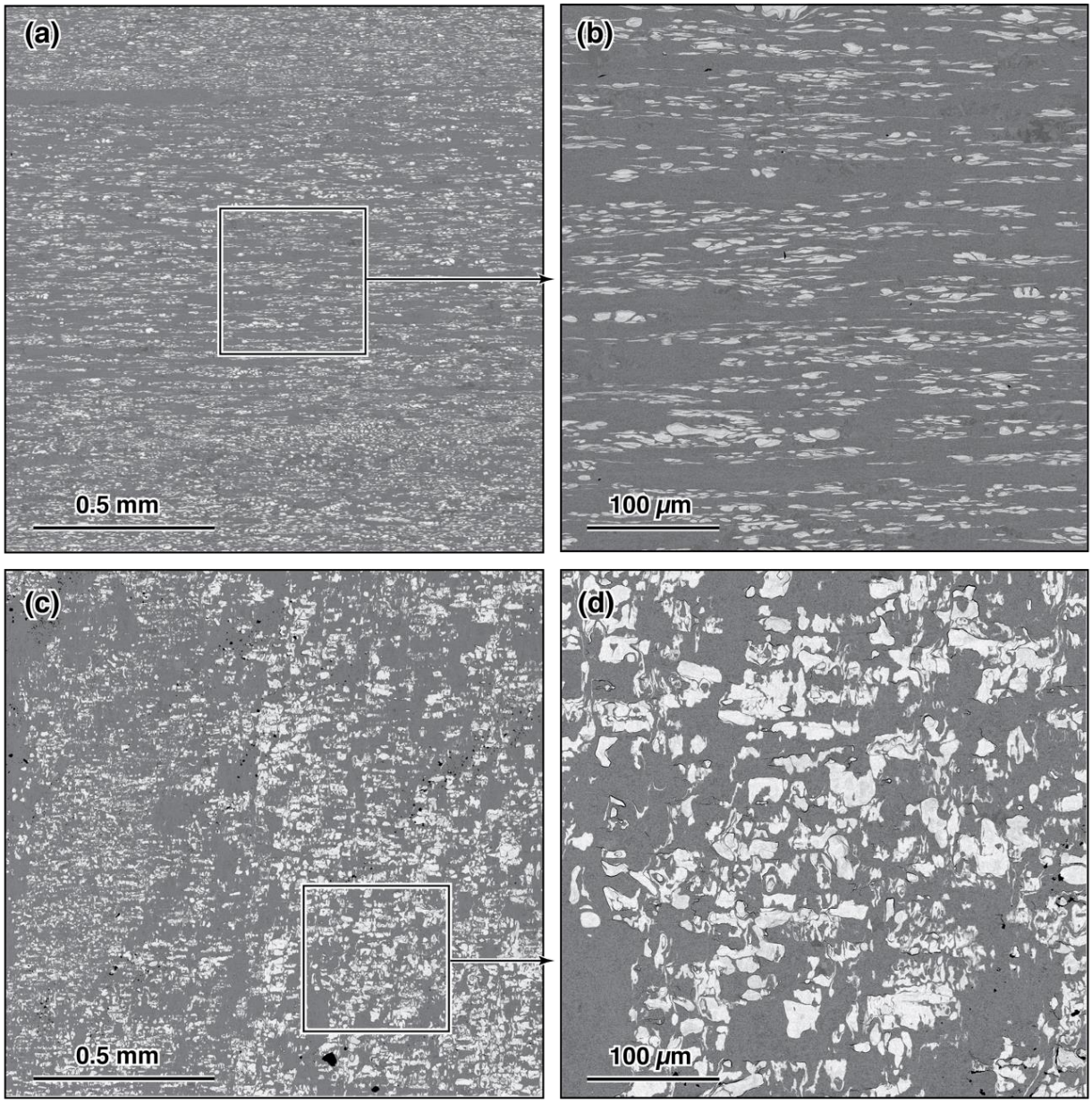

Figure 2.2. Low magnification optical micrographs of the ECAE composite viewed (a, b) in the plane normal to the ED and (c, d) in the plane normal to the ND, showing the morphology of the Nb platelets.

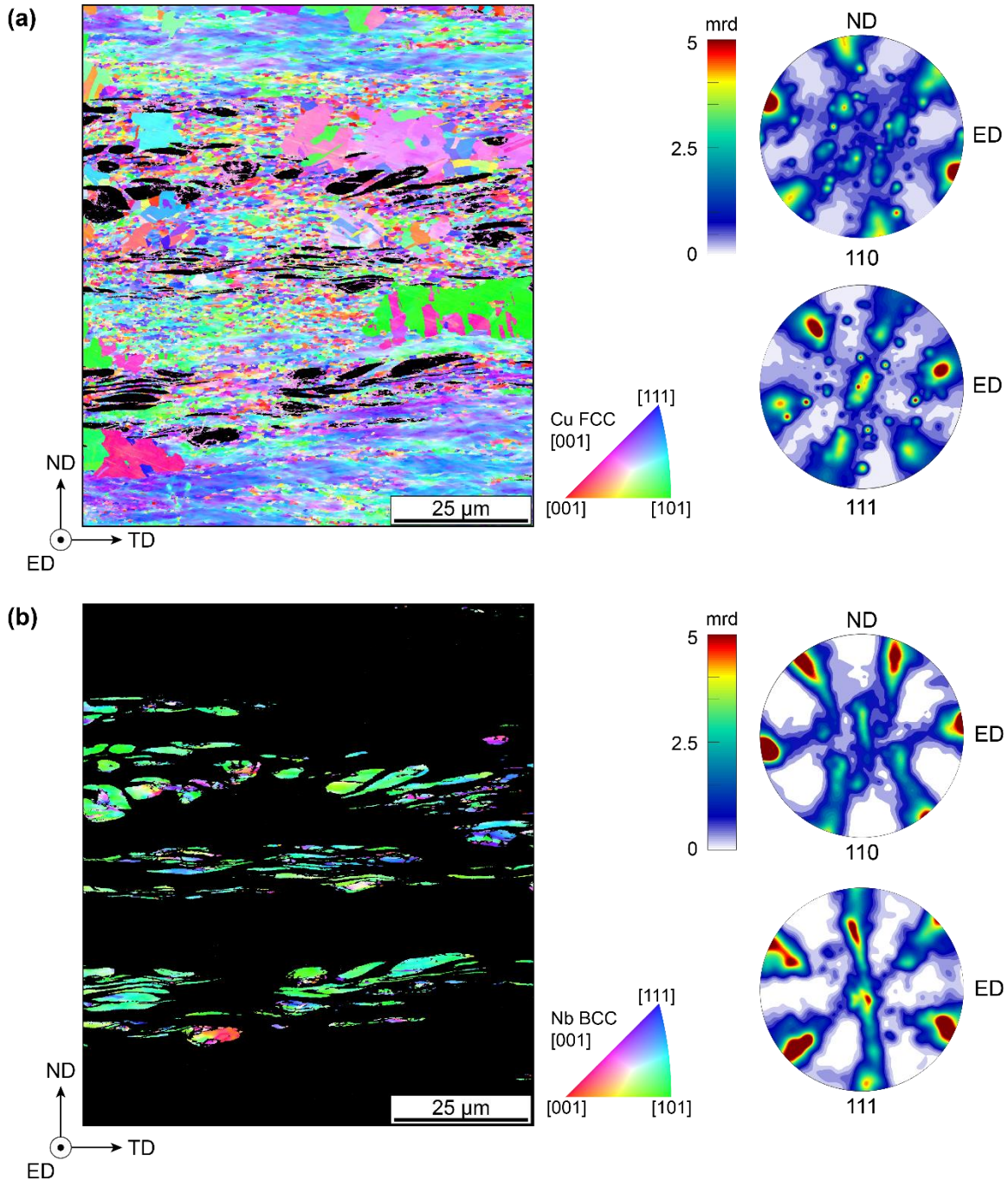

Figure 2.3. (a) EBSD IPF map of Cu in the as-extruded composite reveals mostly sub-μm grains with occasional large grains. There is no evident crystallographic effect of the Nb particles on the adjacent Cu. (b) EBSD IPF of the Nb phase shows that some of the particles are polycrystalline. (EBSD scans performed on ED plane; IPFs referenced to scan plane normal.) The corresponding TD pole figures for Cu and Nb are on the right side.

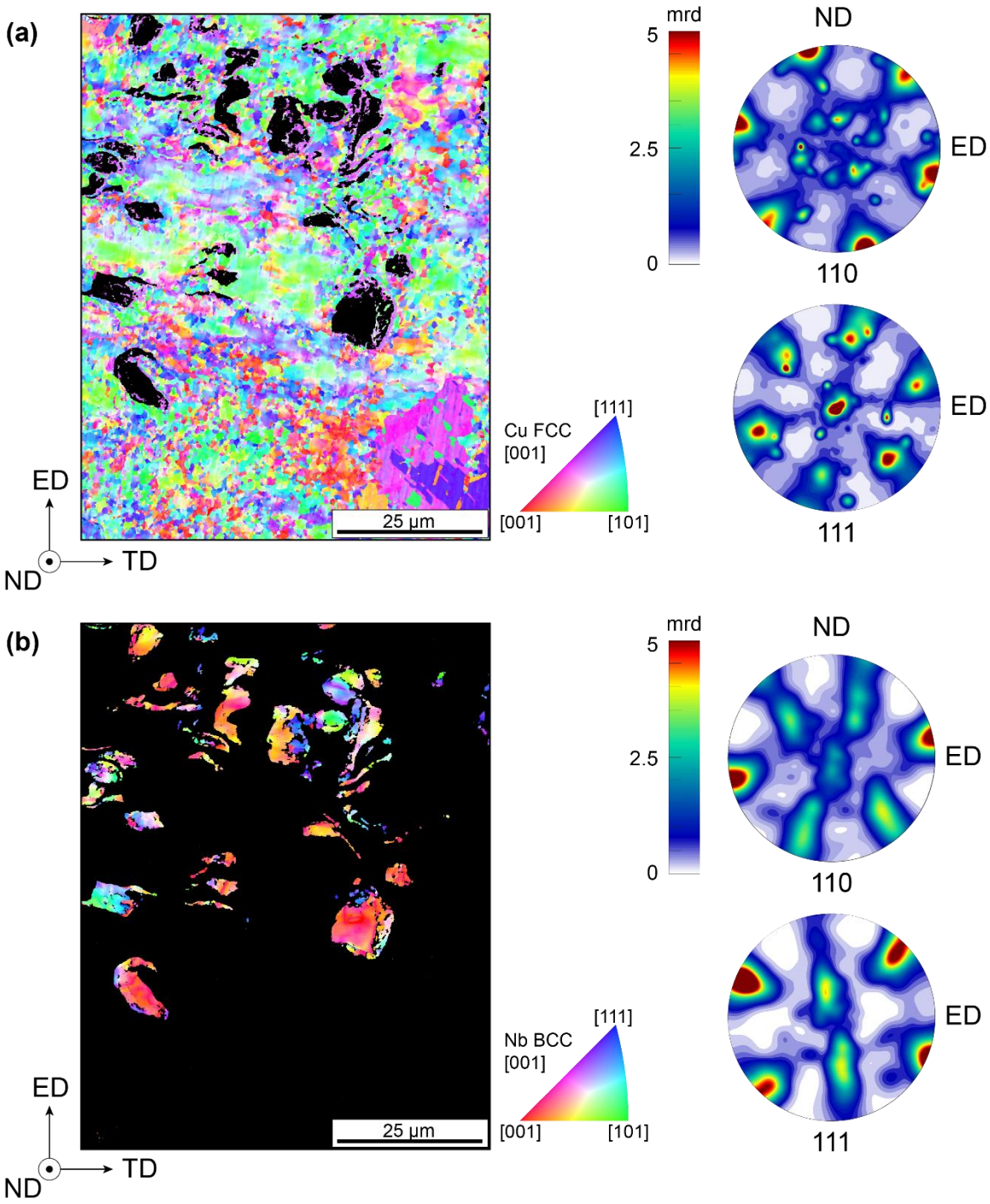

Figure 2.4. EBSD IPF maps and pole figures obtained from scans on the as-extruded composite in the ND plane. As in Figure 2.2, IPFs are referenced to the scan plane normal (ND in this case) while the pole figures are in the TD plane.

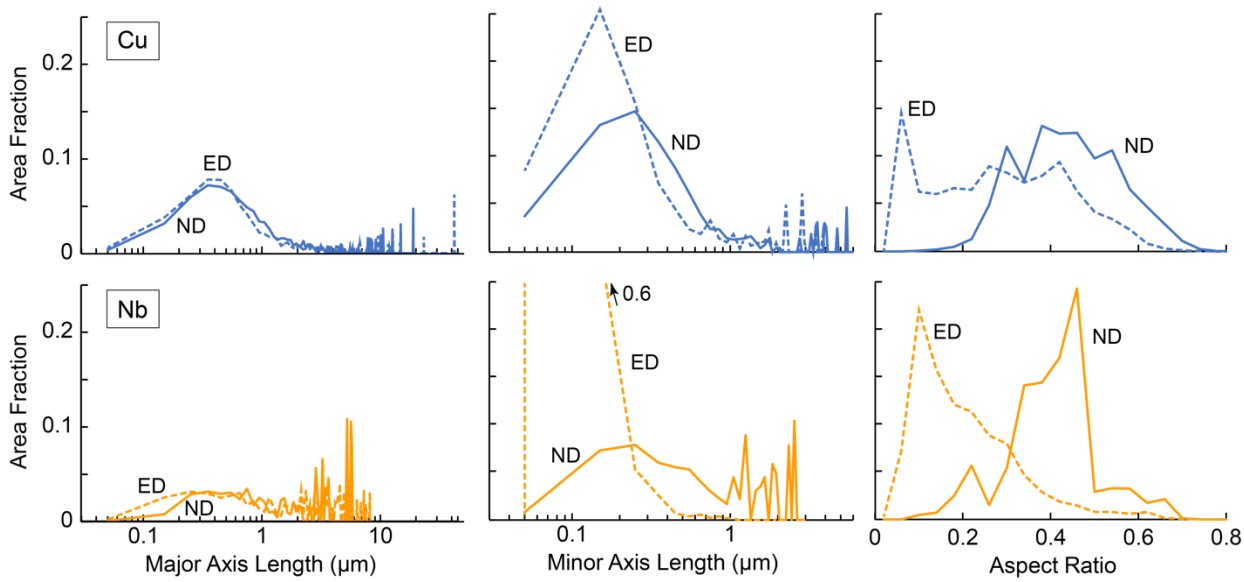

Figure 2.5. Grain size characteristics from EBSD analysis of Cu (top) and of Nb (bottom), on two orthogonal imaging planes (ED and ND). (Bin sizes are 50 nm for axes lengths and 0.05 for aspect ratio.)

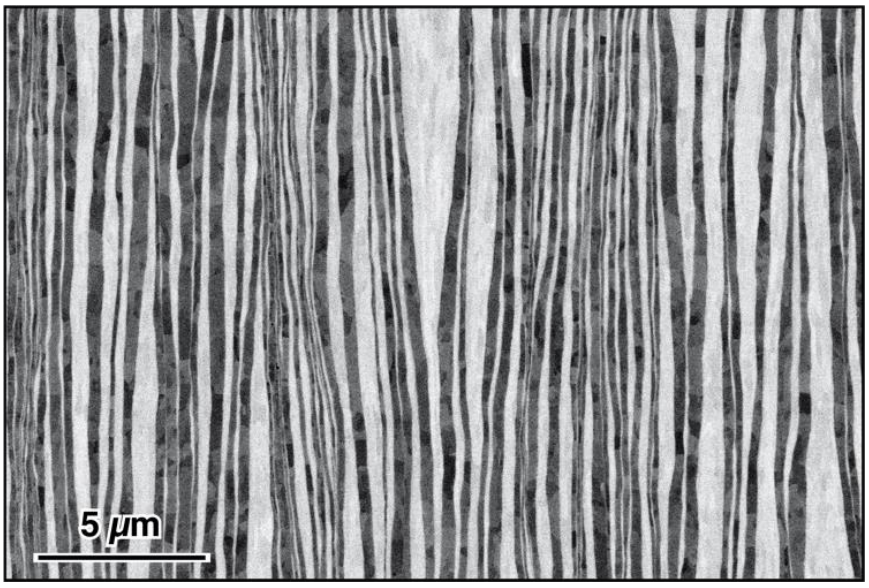

Figure 2.6: BSE image of ARB Cu/Nb laminate showing somewhat wavy layers.

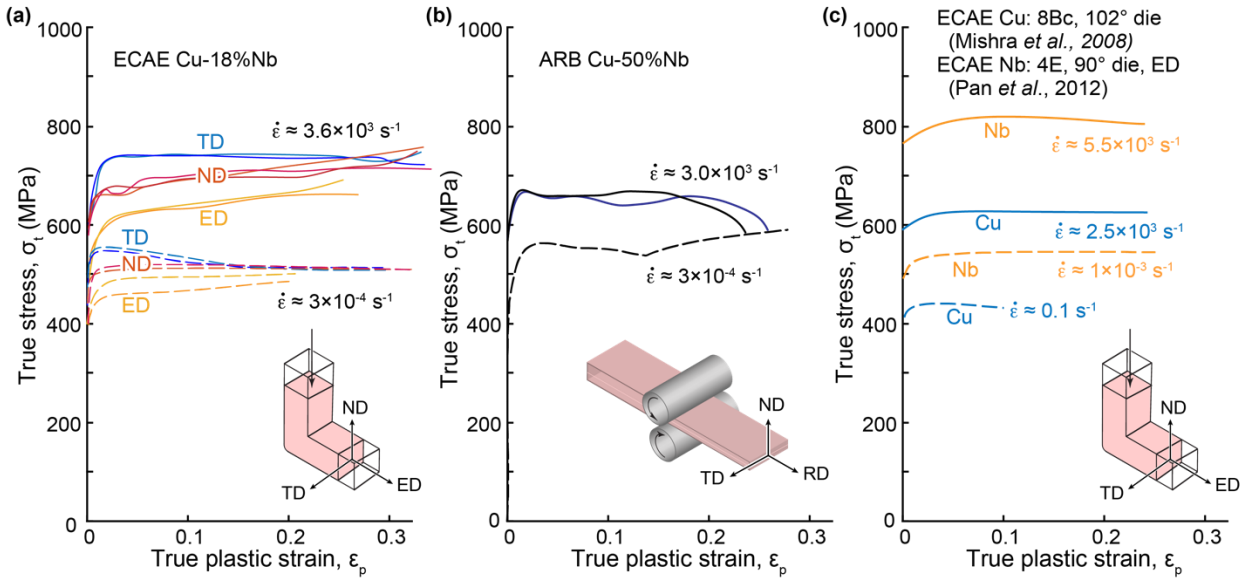

Figure 2.7. Plastic stress/strain response of (a) ECAE and (b) ARB composites at both quasi-static (dashed lines) and high-rate SHPB (solid lines) compression. (c) Reported properties of the composite constituents, Cu and Nb, after similar ECAE processing.

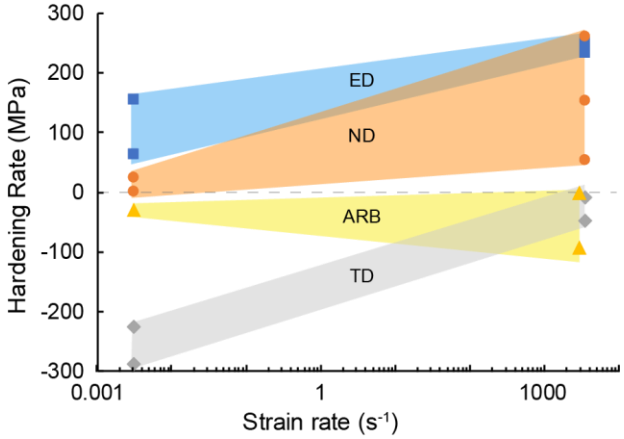

Figure 2.8. Average hardening rate over the plastic strain range 0.05 – 0.15 increases with strain rate for the ECAE material in all loading orientations. In contrast, it either decreases with strain rate or remains the same for the ARB composite. Note that the ECAE material in the TD orientation exhibits softening at both rates, but less at the high rate.

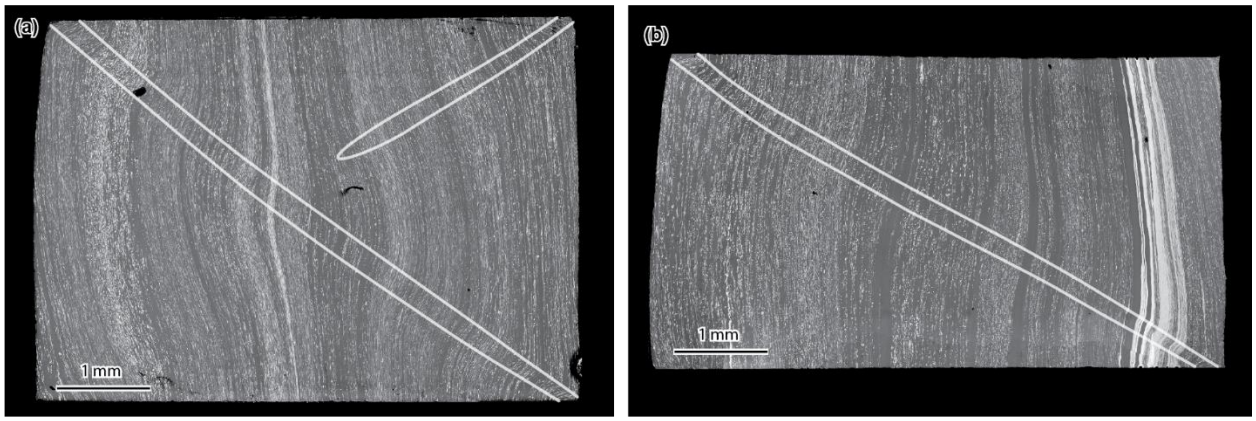

Figure 2.9. Cross-section of ECAE composite compressed along ED (a) at low strain rate, to a strain of 0.20 and (b) at high strain rate, to a strain of 0.3. TD is into the page. White lines indicate approximate boundaries of incipient kink bands.

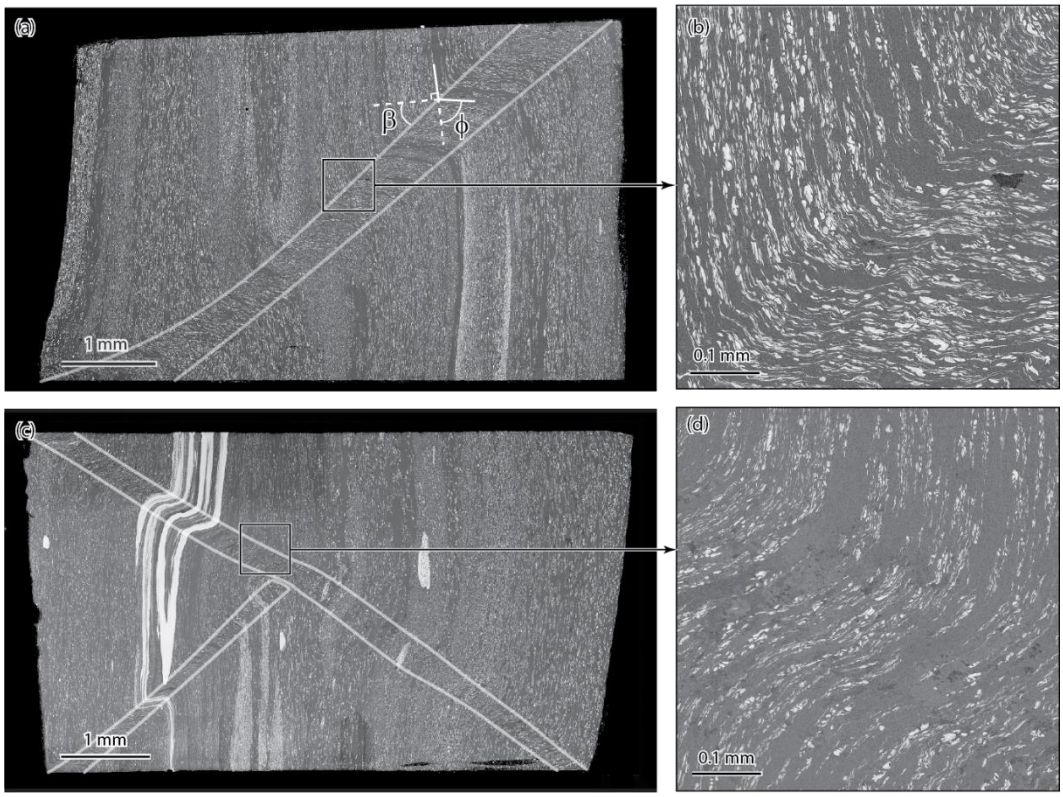

Figure 2.10. Cross-section of ECAE composite compressed along TD at (a, b) at low strain rate, to a strain of 0.25 and (c, d) at high strain rate, to a strain of 0.35. ED is into the page. A single well-defined kink band is evident in (a) while three kink bands are seen in (c).

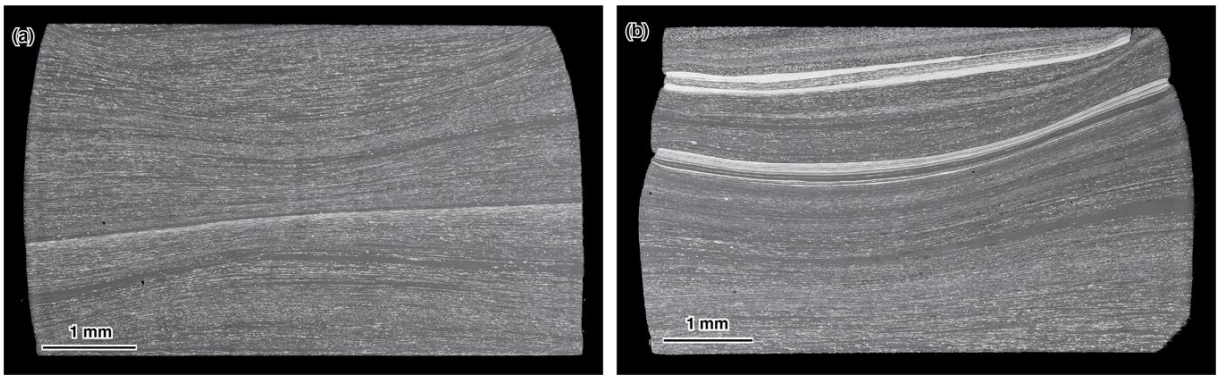

Figure 2.11. Cross-section of ECAE composite compressed along ND at (a) low strain rate to a strain of 0.25 and (b) high strain rate to a strain of 0.35. Specimens both without Nb-rich bands (as in (a)) and with Nb-rich bands (in (b)) were tested at both rates; no difference in deformation modes was obtained.

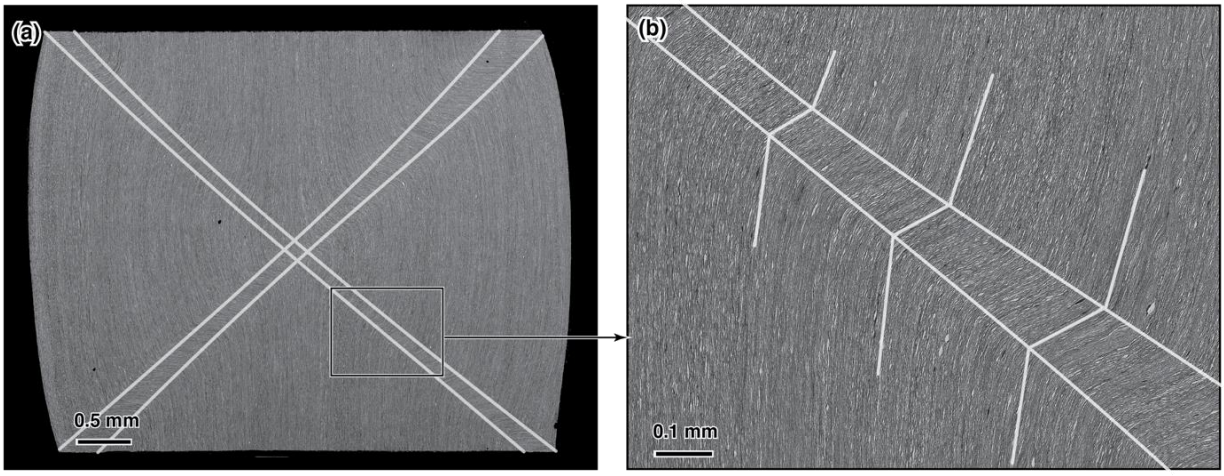

Figure 2.12. Cross-section of ARB composite compressed along RD at high strain rate, to a true strain of 0.30. TD is into the page. Deformation is accompanied by two distinct crossing kink bands.

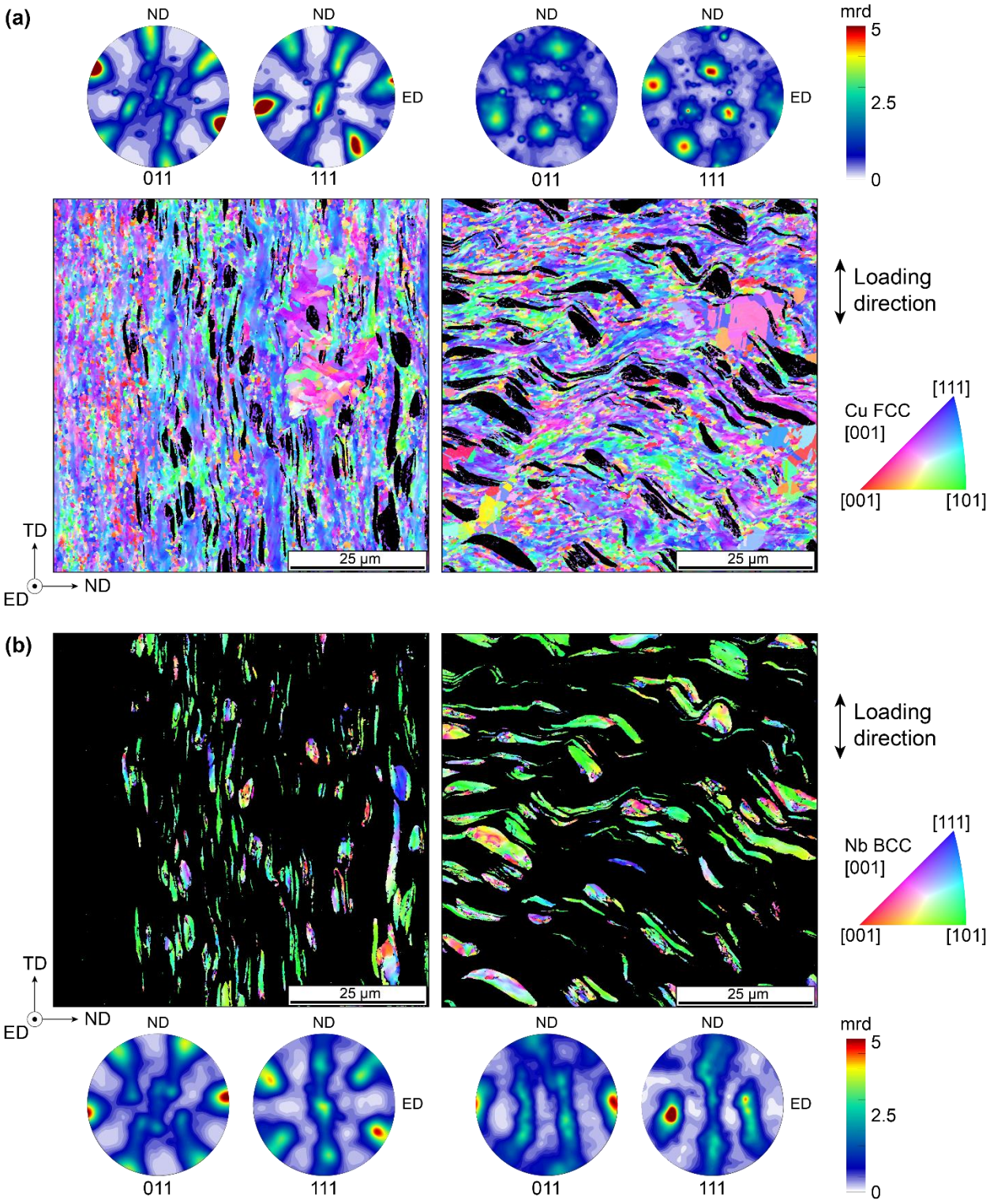

Figure 2.13. IPFs and pole figures of the ECAE composite after QS compression along TD. (Scanned on ED plane; pole figures in TD plane.)

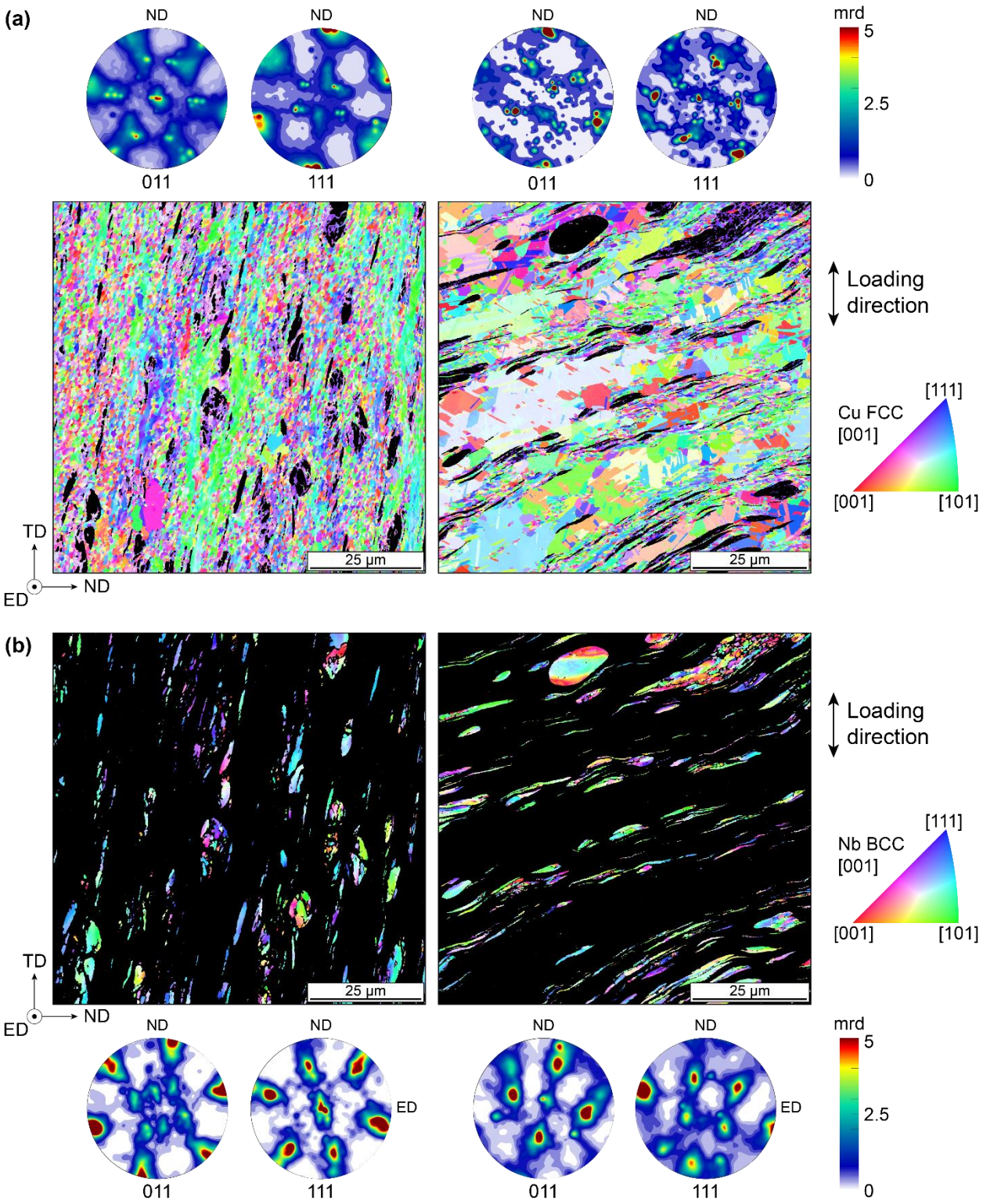

Figure 2.14. IPFs and pole figures of the ECAE composite after dynamic compression along TD. (Scanned on ED plane; pole figures in TD plane.)

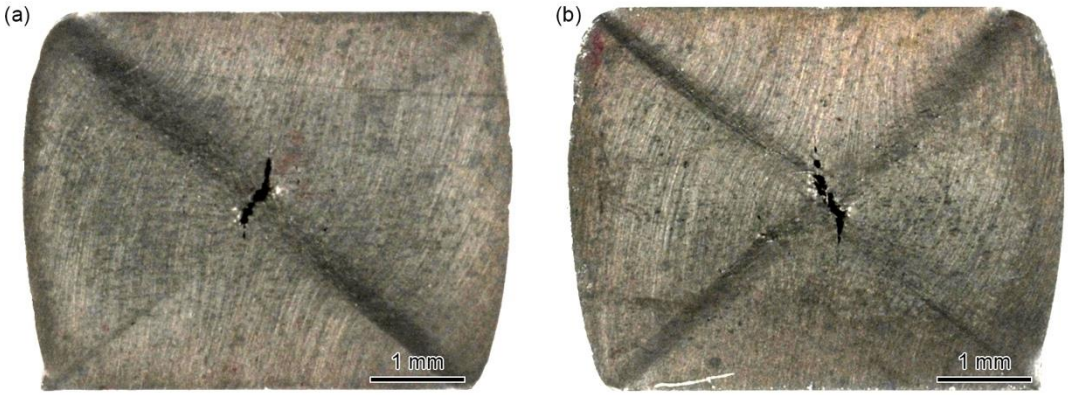

Figure 2.15. ARB specimens tested at high rate exhibit cracks near their centers where kinkbands intersect. The images show front and back faces of the same specimen, illustrating that the crack extends through the entire thickness. (RD is vertical, TD is into the page.)

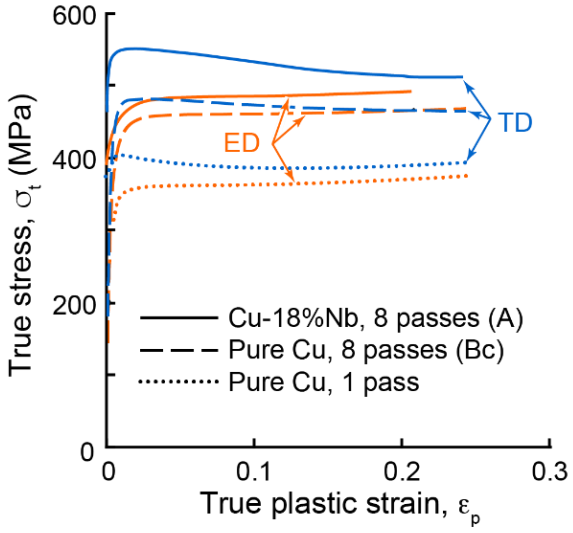

Figure 2.16. Comparisons of quasi-static responses of current ECAE Cu-18% Nb composite in ED and TD orientations (from Figure 2.7, averaged accordingly) with those of pure Cu after 1 pass[177] and 8 passes (following route Bc[175]).

Chapter 3

Low and high strain rate mechanical response of Zr-2.5 Nb processed in two ways

3.1 INTRODUCTION

Zr and its alloys are attractive for use in the nuclear industry as structural materials due to their strength, corrosion resistance, and small thermal neutron scattering cross-section. These materials are widely used for fuel element claddings, structural guide tubes, and waste fuel containers. In these applications, the materials may experience simultaneous exposure to high stresses and temperatures as well as chemical and radiation effects[277,311–316]. Demand for increased mechanical performance has motivated research into new processing paths to tune the microstructures of these materials. Numerous strategies involving alloying and processing of Zr have been developed to produce a variety of phases, microstructure morphologies, and textures which in turn allows tailoring of properties. Nb is particularly important as an alloying addition for improved corrosion resistance as well as improving strength[208,313,316–322]. In particular, Nb is a β stabilizer and Zr-Nb alloys can be processed to produce various lamellar α+β as well as duplex microstructures which exhibit improved performance over single-phase α materials[208,314,317,323,324].

One potential strategy for achieving greater performance involves microstructure refinement. When grain sizes are reduced to the nano-scale, strengths may be much greater than that in the coarse-grained state. The strength elevation, however, comes at the cost of reduced ductility and hardening capacity[171,200,291,325]. Recent findings suggest that the reduced

ductility can be mitigated while retaining strength through the use of "heterogeneous" microstructures, such as multi-modal, hierarchical, and gradient microstructures. In such materials, interactions between microstructure features at various length scales promote enhanced local hardening. The principle has been applied to many systems already and has potential to improve performance for others[2,200,217,323,325–328]. Recently, Zr-2.5 wt% Nb with microstructure spanning several length scales was produced via a novel processing method termed dynamic thermal-mechanical phase transformation (DTMPT or DT processing). The material contains stacked α/β lamellae at the submicron scale, colonies of laths several microns wide, and collections of colonies at yet larger scales[329,330]. In addition to the benefits of microstructure refinement and hierarchy, this material is partially motivated by the possibility of exploiting recent findings for nanolaminates and metallic multilayers[329]. The high density of bi-phase interfaces and very thin layers has proved to impart exceptional strength and stability relative to the constituents[2,329,331–333]. Like other multilayers, this lamellar Zr-2.5 wt% Nb comprises two alternating layers of distinct crystal structure and composition: namely, HCP α of essentially pure Zr and BCC β of Zr with up to 20 wt% Nb[329,334]. However, unlike composite metal laminates, the lamellae are arranged randomly in all orientations, rather than having the same orientation. This arrangement is expected to produce a more isotropic response than that obtained in metal laminates. Thus far, the material has been reported to exhibit quasi-static tensile properties that exceed those of conventionally-processed alloys of the same composition[329,330] as well as high thermal stability[330].

In structural applications, components may experience impacts which cause loading at high strain rates. The material response at high strain rates can differ dramatically from that obtained under low strain rate loadings[199,265,312,335,336]. For example, while UFG materials such

as those considered here are stronger than their coarse-grained counterparts, they tend to be more prone to strain localization and particularly shear banding[171,337,338]. Shear banding is a critical phenomenon to understand because it often precedes cracking that leads to catastrophic part failure. Microstructure refinement can increase the propensity for this deformation type, by reducing strain and strain rate hardening capabilities, both of which are needed to balance the local softening that ultimately leads to strain localization. Higher flow stresses may also be detrimental by increasing the amount of heat generated, thereby exacerbating thermal softening effects[171,245,336,337].

Investigations of shear banding in HCP materials have primarily involved Ti alloys (not Zr) with microstructures that are not fully lamellar (e.g., single phase α or bi-modal with large equiaxed domains)[265,266,335,336,338–344]. The limited data for Zr precludes identifying expected behavior, and even for the more-studied Ti system are not entirely clear. For example, in Ti-6Al-4V, the lamellar structure has been found to be more prone to shear banding than a bimodal microstructure[341–343], and within bimodal structures a large lamellar thickness has been associated with a *lower* propensity for shear banding[266]. On the other hand, in a fully lamellar material large lamellae and colonies have been associated with *higher* occurrence of shear bands[343]. While there are often similarities in the behavior of Ti and Zr, it is not yet clear whether such trends hold for the present Zr materials, where variations in lamella size, colony size, and colony arrangements naturally emerge from the various thermomechanical histories[329].

The present study is concerned with evaluating two types of Zr-2.5 wt% Nb materials in terms of mechanical response and connecting the behavior to the respective microstructures. One was processed through a conventional heat treatment route and the other produced using

the recently DTMPT method described above[329]. Two general strain rate regimes are considered, quasi-static (~10^{-4} /s) and dynamic (~10^{3} /s), and two loading conditions, uniaxial compression and uniaxial tension. Additionally, the microstructure and development of shear bands formed during dynamic compression are examined.

3.2 MATERIALS AND METHODS

3.2.1 Materials

This study used two materials of a single nominal composition, Zr-2.5 wt% Nb, with impurity concentrations of 2 wt% Hf and 0.04 wt% Fe (composition analysis in Table 3.1)[345]. Zr and Nb have essentially no solubility for the other element at room temperature but the two form a continuous BCC solid solution at higher temperatures with a monotectoid point at 620°C and ~19 wt% Nb (Figure 3.1)[346]. The materials came from the same initial casting and were then processed in the two ways. The first method consists of annealing the as-cast alloy for 15 minutes at 1000°C to homogenize the material in the β-Zr phase field and then air cooling to room temperature. Cooling to the monotectoid temperature was completed in around 20 s. Hereafter this material is denoted "AC". The second method involves annealing the cast material for 12-13 min at 950°C and then compressing it axially at temperature at a strain rate of 1/s to a total strain of 0.7 before cooling in air[345]. This material is denoted "DT". Cooling to the monotectoid temperature took around 12 s. The DT processing method is nearly the same as that described by Zhang et al.[329,347], but the cooling times for the material used here were ~3× longer. The prolonged time at high temperature likely caused additional defect recovery and therefore reduced phase transformation nucleation sites compared to the material discussed previously[345].

For quasi-static and high strain rate compression and tension, the AC material was supplied as a cuboidal block roughly 31 mm × 30 mm × 29 mm. Tension specimens were dogbone-shaped with gauge dimensions of 6.7 mm long × 4.9 mm wide and 1.9 mm thick; compression specimens were right circular cylinders, 3.1 mm in height and 3.1 mm in diameter. Both tension and compression specimens were made with their loading axis aligned to two of the three axes of the block, designated the horizontal and vertical directions. These directions are arbitrary as no preferred orientation of the block was evident and the material was expected to be isotropic given its processing history. All specimens were taken at similar distances from the exterior surface to reduce effects of variation in cooling rates.

The DT material began as a roughly cylindrical billet with diameter ~37 mm and thickness of ~7.3 mm. Prior to machining test specimens, the billet was thinned and both faces flattened using a surface grinder with an Al_2O_3 grinding wheel; this operation left surface pits, several tens of μm in diameter, which were subsequently removed by polishing. Compression specimens were made with the loading axis parallel to the processing direction (the out-of-plane direction) and perpendicular to this processing direction (in-plane direction). Tensile specimens were of the same dogbone geometry employed with the AC material and oriented in-plane with the front and back faces parallel to the top and bottom surfaces of the initial billet. The gauge sections are from the center of the billet and as a result the loading axis is neither parallel nor perpendicular to the radial direction of the billet. For the tension specimens, faces with surface grinding pits were ground and polished to 1200 grit SiC sanding paper. Using the same process for the compression specimens while maintaining parallel faces proved to be infeasible. Nevertheless, parallelism and flatness (apart from surface pits) were maintained within 0.013 mm through the machining and grinding operations alone.

Shear band progression was investigated through dynamic compression tests performed on AC material from one other billet and on DT material from two other billets. The second billet of AC material was in the form of a square plate, 30 mm × 28 mm × 6 mm. The two additional DT billets were both roughly cylindrical and 38 mm in diameter; one was ~4 mm thick and the other ~7.3 mm thick. All of these billets were thinned to final specimen height by removing material from both the top and bottom faces before machining test specimens; for these billets all machining was by wire EDM. Compression specimens were right circular cylinders with dimensions 5.0 mm height × 5.0 mm diameter (AC), 3.7 mm height × 3.0 mm diameter (DT billet 1), or 5.0 mm height × 5.0 mm diameter (DT billet 2). The loading direction was parallel to the thin direction of the billet (i.e., out-of-plane loading); for the DT billets this amounted to a direction parallel to the processing direction. Here again parallelism and flatness of the loaded faces were maintained to within 0.013 mm. Although the two additional DT billets were supposedly processed in the same manner as the DT billet used for the tension/compression study, their low and high-rate mechanical properties proved to be noticeably different from those of the other DT billet. The nature of shear banding, however, was qualitatively similar among all DT billets.

3.2.2 Quasi-static and SHPB testing

For the compression/tension study, both materials were tested in quasi-static (QS) compression and tension at a rate of ~3×10^{-4} /s, in high strain rate compression at ~$3\text{-}4\times10^{3}$ /s, and high strain rate tension at 3×10^{3} /s. Quasi-static tests were performed on a servohydraulic test frame (Material Test System 810, MTS, Eden Prairie). For the compression tests, samples were placed between lubricated SiC or WC blocks atop standard steel platens. Strains were

measured using a laser extensometer with retroreflective tapes placed on the blocks immediately adjacent to the sample. For the tension tests, samples were loaded using hydraulic grips and strains were measured over the entire straight-sided portion of the gauge length using a laser extensometer.

The high strain rate compression tests were performed on a Split Hopkinson Pressure Bar (SHPB) system utilizing an air-propelled striker bar (REL, Inc., Calumet, MI). For the compression tests, the bars employed were made from 350 maraging steel and had a diameter of 19 mm. The ends of the bars were greased before each shot to reduce friction against the sample. A thin Cu pulse shaper (0.5” diameter × 0.020” thick) was used to mitigate dispersion effects and smooth the pulse. The striker bar was 152 mm long and impacted the incident bar at velocities of 24-25 m/s. A momentum trap on the incident bar was used to prevent multiple impacts on the sample. (There were two exceptions: one test was performed with a longer (229 mm) striker bar, and another was performed without the momentum trap.)

The dynamic tension tests were performed on the same system but with a different set of bars. The bars were made from Al 7075 T6 and were 19 mm in diameter. The striker was a hollow aluminum tube, 305 mm long and of the same cross-sectional area as the incident bar; the inner diameter of the striker bar is marginally greater than the diameter of the incident bar to give a sliding fit. In this setup, the striker impacts a flange on the end of the incident bar. In this case, a copper washer (0.75” ID, 1” OD, 0.05” thick) was used as a pulse shaper. The washer was held against the flange of the incident bar using a thin layer of grease to reduce signal noise. Samples were held in toothed wedge-shaped grip faces inside aluminum collets that thread onto the incident and transmitted bars. To reduce slipping upon loading during the test, the samples and grip faces were pressed into the collets using a hydraulic jack.

Strains in the high-rate tensile tests were measured by 2D digital image correlation (DIC). Images were captured using a Shimadzu Hyper Vision HPV-X2 FTCMOS2 camera with a Nikon AF-S VR Micro-NIKKOR 105mm f/2.8G IF-ED Lens. The interframe time was 1.25 or 1.5 μs (equivalently, 800,000 or 667,000 fps) and exposure time was 0.5 μs with an aperture of f/4. The images were 400 px × 250 px with a linear scale factor of approximately 50 μm/pixel. The sample was illuminated using a continuous duty cycle high-intensity LED array arranged in a ring concentric with the camera lens (Sure-Bright, REL Inc. MI, USA). The constant output obviates the need for synchronizing lighting and camera triggers and precludes temporal and spatial variation to lighting during the test that can occur with flash-lamp setups. For DIC in both dynamic and quasi-static tests, the surfaces of the gauge sections were first coated with a flat white acrylic paint using an aerosol can and then speckled with a black acrylic paint using either an airbrush (for the quasi-static tests, to achieve smaller speckles) or an aerosol can (for the SHPB tests). DIC analysis was performed using Vic2D 2009 (Correlated Solutions Inc.) with a subset size of 11 px and step size of 2 pixels, consistent with recommended practice[348].

The interrupted dynamic compression tests were performed with the aforementioned SHPB setup or one at the Los Alamos National Laboratory. The latter employed 12.5 mm diameter bars of 350 maraging steel. In both cases the bar ends were greased before each shot and strain was limited using steel collars. Momentum traps were not used as the collars limited the deformation to prescribed amounts. The strain rates employed with both systems were $\sim 3.5\times10^3$ /s. In all cases the striker bar lengths were selected to ensure that the samples were fully compressed to the collar length. For the tests with final strains of ε_{final} = 0.1 and 0.2, the collars were placed on the incident bar rather than the transmission bar. (In the latter location,

the collars interfered with the recording of the stress pulse.) The stress data beyond small strains for these tests is not representative of the stresses experienced by the sample. This did not affect the stress, strain, or strain rate imparted to the samples. Baseline quasi-static compression tests were also performed on a small number of samples to cross-check properties of the various billets used in this work.

3.2.3 Microscopy

The microstructure was characterized in the pristine and as-tested states through a combination of light optical (LOM), scanning electron (SEM) and transmission electron microscopy (TEM), as well as electron backscatter diffraction (EBSD) and STEM electron dispersive spectroscopy (EDS). SEM was performed on a Nova Nano 650 FEG SEM with the concentric backscatter detector or through-lens detector. EBSD was performed on a ThermoFisher Apreo C with an EDAX EBSD detector at an accelerating voltage of 15 kV and current of 13 nA with 4×4 binning and a step size of 0.07 μm. Scans were reindexed in OIM Analysis (AMETEK EDAX) using Neighbor Pattern Average Reindexing (NPAR)[349]. TEM and STEM were performed on a ThermoFisher Talos G2 200X TEM/STEM with ChemiSTEM EDS at 200 kV.

Specimens were prepared for LOM and SEM through standard metallographic preparation procedures down to 1 μm diamond suspension. Final polishing was performed by either flat milling on a broad-beam ion mill (Leica EM TIC 3x) or vibratory polishing with 0.05 μm colloidal silica. Ion milling parameters varied with specimen size and shape; a typical procedure involved 1-2 hours at 6 kV and 4 kV with a beam incident angle of 6° while the specimens were continuously rotated and translated. Ion milling was found to give the sharpest

phase edges for high-magnification SEM imaging and measuring microstructural features but also had two undesirable effects. First, the glancing incident angle of the ion beams produces shallow scallops on the surface that interfere with low-magnification LOM imaging; these scallops are generally nearly unnoticeable in higher magnification LOM and in backscatter SEM. Second, ion milling induces an unknown change to these alloys that apparently persists some distance below the surface. This change manifests as a darker coloration in LOM and BSEM that greatly increases contrast between patches of seemingly identical microstructure but yields poor quality EBSD patterns and eliminates variation in reflection of polarized light with HCP crystal direction. While the scalloped surface texture from ion milling could be removed by vibratory polishing for a few hours, thereby improving optical image quality, the near-surface affected layer remained and the EBSD results remained poor without further polishing. Thus, for EBSD, polishing with the 1 μm diamond slurry was followed by extended vibratory polishing with 0.05 μm colloidal silica until the lamellae were distinguishable, typically 2 or more days.

STEM imaging was also used to examine microstructure while TEM selected area diffraction was used to evaluate crystallinity and orientations. TEM foils were prepared by focused ion beam milling on an FEI Helios Dualbeam NanoLab 600 with a Ga^+ ion source. The average final thickness of the foils was approximately 200-300 nm.

3.3 RESULTS

3.3.1 Pristine Microstructure

Both AC and DT materials exhibit a hierarchical microstructure spanning length scales from nearly a millimeter down to sub-micron. Both reveal distinct former β grains. Within the

transformed grains, the microstructure comprises either a basketweave or a parallel plate colony microstructure. At the largest length scales, boundaries of prior β grains formed during annealing are evident as bands up to ~30 μm wide and ~100-500 μm long. In the AC material, the material within the prior boundaries is randomly orientated relative to the sample axes. The prior β grains are approximately straight-sided polygons, 100-700 μm wide (Figure 3.2). In the DT material, the arrangements of the prior grain boundaries are anisotropic with respect to viewing direction. In sections viewing down the axis of the billet (out-of-plane direction, Figure 3.3a), the boundaries are at random orientations and occasionally follow tortuous paths. In through-thickness sections (viewing direction in-plane, normal to the billet axis, Figure 3.3b), the boundaries are roughly perpendicular to the billet axis and slightly curved to enclose high-aspect ratio lenticular regions. Note that the billet axis is parallel to the direction of the compression imparted during processing. Per Zhang et al.[329], the β grains were deformed while at temperature (prior to transformation) and the α lamellae nucleated afterward once cooling had started; the lamellae and colonies were not deformed by the DTMPT process and hence their orientations were not influenced by the deformation.

At intermediate scales of ~10-100 μm, the prior β boundary regions comprise colonies of lamellae extending from the edge of the prior β grain at a constant angle. This angle is fixed along a given boundary segment but may differ between boundary segments and between prior grains on either side of a boundary. Many prior boundaries also exhibit a central core of non-lamellar α (often called boundary α in Ti literature). Note that the prior β boundary region comprises material in two adjacent prior β grains. In each former grain the α colony at the boundary has a single spatial and crystallographic orientation over a relatively large area. The spatial and crystal orientation may differ in each prior grain for a given boundary and also

differ from the variants comprising the majority of the interior of the former grain (Figure 3.4). The DT material has some regions that are entirely enclosed by non-lamellar α and contain only a single colony of lamellar α (Figure 3.3b, lower right panel). These are roughly 10-30 μm across and approximately equiaxed. They cover a minor fraction of the section area.

The interiors of the prior β grains exhibit either basketweave microstructures or parallel plate colonies, both comprising α plates separated by very thin β laths. The basketweave structure consists of a repeating array of bundles of a few parallel lamellae at several distinct orientations. Parallel plate colonies comprise lamellae of the same spatial and crystallographic orientation. In general, the interior regions of prior β grains contain almost solely either basketweave or colonies. Occasionally, non-aligned lamellar arrangements overlap with colonies. Similarly, colonies are occasionally present in basketweave regions. Each grain typically contains only a few variants of α, differentiated by their spatial orientation.

Statistics on the prevalence of colony and basketweave arrangements were measured using a point count on 15-20 regions for each material (Figure 3.5). The colony count includes the collections of α lamellae that line the prior β grain boundaries as well as those in grain interiors. The AC material contains primarily basketweave microstructure in both billets, at several times the frequency of the colony morphology. In both materials, colonies are most commonly near or at prior β boundary regions. When viewed along the in-plane direction, the DT material also displays primarily a basketweave structure, although the relative fractions of the two are comparable to one another. The DT material along the out-of-plane direction shows a greater fraction of colonies with typically greater in-plane size. In both orientations, the colonies in the DT material are again typically situated near prior β grain boundaries.

At the nano/submicron-scale, both AC and DT materials comprise two types of alternating lamellae, one thicker and one thinner. The phases had been previously identified via TEM diffraction[329]: the thicker one is HCP α phase and the thinner one is BCC β phase. The α lamellae are 300-700 nm wide and ~3-10 μm long while the β lamellae are <50 nm wide and ~3-10 μm long (or possibly continuous). The average width of α/β repeat units in the current materials were determined from SEM and TEM images by drawing straight lines perpendicular to the lath direction and dividing the length of the lines by the number of α/β pairs. (For SEM images, this amounted to counting α laths as the β layers are too thin to accurately measure at most magnifications used.) The α/β layer thicknesses of material used in the tension vs. compression study fell in the range 0.35-0.78 μm (average 0.54±0.11 μm) and 0.37-0.76 μm (average 0.52±0.11 μm) for the AC and DT materials, respectively. The corresponding thicknesses in the billets used for the interrupted compression tests fell in the range 0.30-0.79 μm (average 0.53±0.10 μm) and 0.22-0.55 μm (0.35±0.07 μm) for the AC and DT materials.

3.3.2 Mechanical Properties

The quasi-static (QS) response of both materials in tension and compression is shown in Figure 3.6. In compression, the DT material yields at stresses of about 500 MPa and 550 MPa in the in-plane and out-of-plane orientations, respectively, and then monotonically hardens at a progressively decreasing rate. The flow response of the AC material falls essentially midway between those of the DT material in the two orientations.

In tension, the DT material (in-plane) yields at 475 MPa and hardens to 550 MPa at $\varepsilon_{eng} \approx 0.07$ before gradually softening; softening is associated with the formation of a diffuse

neck. Similarly, the AC material yields at ~500 MPa and then harden to ~580 MPa at $\varepsilon_{eng} \approx 0.07$ at which point a neck forms and the material exhibits softening. Post-peak behavior varied substantially between samples. The vertical orientation sample formed a crack beginning at low strain (by $\varepsilon_{eng} \approx 0.15$) while the horizontal sample withstood nearly twice that strain without failure (test terminated at $\varepsilon_{eng} \approx 0.25$).

Dynamic responses in both compression and tension are shown in Figure 3.7. In compression, the AC material yields at $\sigma_{eng} \approx 825$ MPa and then hardens at a nearly-constant rate. The DT material yields at 825 MPa and 875 MPa in the in-plane and out-of-plane orientations; both then harden at near-constant rates until the out-of-plane direction experiences sudden dramatic softening beginning at $\varepsilon_{eng} \approx 0.16$ ($\varepsilon_{true} \approx 0.18$). Increasing the strain rate to 6700 /s (increase of 67%) for loading along the out-of-plane DT direction increases the yield stress to 900 MPa but has minimal effect on hardening rate and delays the sudden softening until $\varepsilon_{eng} \approx 0.22$. For the AC material, increasing striker bar length led to the sudden softening behavior beginning at $\varepsilon_{eng} \approx 0.28$. During high-strain rate tension, both materials yield at $\sigma_{eng} \approx 650$ MPa, reach a peak stress of ~700 MPa, then soften at similar rates to complete rupture at $\varepsilon_{eng} \approx 0.22$ (AC) and 0.25 (DT). Softening rates increase with strain for both materials but there are no abrupt decreases in flow stress.

Assuming that the flow stress follows a power law with strain rate, the strain rate sensitivity index m was calculated using

$$m = ln\left(\frac{\sigma}{\sigma_R}\right) / ln\left(\frac{\dot{\varepsilon}}{\dot{\varepsilon_R}}\right) \tag{3.1}$$

where σ is true stress, $\dot{\varepsilon}$ is strain rate, and subscript R indicates the reference state. The quasi-static loading case was used as the reference. The index was calculated at the yield point in both tension and compression tests and at a true strain $\varepsilon_{true} = 0.13$ for the compression tests (the

latter being the strain at the peak stress for the DT material loaded out-of-plane at 4000 /s) (Figure 3.8). The rate sensitivity indexes computed at the yield point in compression are essentially the same in both the in-plane and out-of-plane directions the DT and both directions of the AC material (m = 0.025±0.002). The corresponding values in tension are similar, though slightly lower, by ~30% (m = 0.019 and 0.023 for the AC and DT materials, respectively). The sensitivity indices at a strain of ε_{true} = 0.13 (m = 0.012±0.002) are roughly half those at the yield point.

True stress/strain curves for the dynamic compression with strain limited by collars and for quasi-static compression are shown in Figure 3.9. Curves for dynamic compression to strains other than 0.25 are omitted for clarity as misplaced collars interfered with the measurements. At QS rates, both materials yield at ~575 MPa and then smoothly harden to 950 MPa at $\varepsilon_{true} \approx 0.28$ at practically the same rate. All stresses monotonically increased throughout loading.

At dynamic rates the AC material yielded at ~975 MPa and reached a peak stress of ~1075-1100 MPa at $\varepsilon_{true} \approx 0.15$. A sample not limited by a collar experienced a sudden decrease in stress beginning at $\varepsilon_{true} \approx 0.28$; the sample with the ε = 0.25 collar softened only slightly after the peak stress. The DT material yielded at ~900 MPa and hardened to 1075 MPa. One ε = 0.25 collar sample reached this peak stress very near the end of the deformation ($\varepsilon_{true} \approx 0.24$) while the other peaked earlier at $\varepsilon_{true} \approx 0.2$ and then rapidly softened. However, note that the sample which did not show drastic softening may still have experienced it – effects of the collar obscure a portion of the signal and hinder accurate identification of the response at the end of the loading. (And since both samples showed extensive shearing and cracking, it is almost certain that the second sample would have shown such softening at that strain had the

collar been absent.) The sample without collars reached the same peak stress at $\varepsilon_{true} \approx 0.25$ as well, then begin to soften rapidly at $\varepsilon_{true} \approx 0.28$.

3.3.3 Deformation and Failure Modes

During the quasi-static compression tests, all specimens exhibit uniform straining at low strains and some barreling at higher strains with no external signs of localized deformation. During dynamic compression tests, however, the test specimens show one of two types of behavior. The first (again) involves uniform straining followed by some barreling. This was obtained in the AC material and the DT material in-plane as well as the DT material out-of-plane when the strain was restricted through the use of a shorter (152 mm) striker bar. The other is shear localization accompanied by cracks at inclined angles relative to the loading direction (Figure 3.10); this behavior was evident for the DT material in the out-of-plane orientation at strain rates of 4000 /s and 6700 /s (using a 152 mm striker bar) and for the AC material in the vertical orientation (using a 228 mm striker). The shear cracks were oriented between about 35° and 55° relative to the loading direction. One of the specimens also exhibits markings that suggest a second shear event parallel to the main crack.

In tensile loading, both the AC and the DT materials exhibit a peak (nominal) stress and begin to neck at global axial strains of about 0.05; the subsequent deformation is accommodated within a diffuse neck. The DIC strain maps from a QS tension test (Figure 3.11) on the AC material reveal that, despite the low strain at the stress maximum, the local axial strains exceed 0.4 near failure. The highest strain was found on one side of the gauge section; the region grew toward the center, thus appearing to fail by tearing from one side to the other.

The strain magnitudes reported by DIC very near the failure site are potentially faulty; a crack would present as very large strains even if it cannot be visible distinguished. High local strains were also obtained in the DT material (at least 0.5), although cracking of the DIC paint precluded measurement of the strains up to fracture. In this case the concentration is near the center of the gauge section. One face of the interrupted DT sample was polished with 1200 grit SiC paper prior to testing (to remove pits left by surface grinding). After removing the DIC paint, 2 cracks near the center of the gauge are visible on the polished face. Also present are numerous "sunken" line features which enclose regions of varying surface roughness (Figure 3.12). All other surfaces were in EDMed state and no features could be conclusively identified. In dynamic tension the peak magnitudes of local strains are lower, at ~0.5 for both materials. In addition, for AC the band of elevated strain grows across the gauge section at an angle of ~75°. The concentration near the top corner increases and spreads along the band; this band is ultimately the rupture location. For DT, the location and shape of the concentration matches the corresponding QS test (Figure 3.13).

Tensile fracture surfaces of AC samples at both strain rates exhibit facets on the order of 500 μm width with larger voids evident at the base of several of the valleys (Figure 3.14). Meanwhile the DT surface has few facets on nearly a chisel-tip appearance that is broadly typical of moderate ductility metals. A few large voids elongated in the gauge-width direction are visible. Both materials have round dimples corresponding to tensile necking between voids as well as some elongated dimples from shearing. No inclusion particles are present in the dimples.

3.3.4 Microstructure Changes Due to Deformation

Quasi-static compression led to uniform compression with no external signs of localized deformation for all cases. After dynamic compression the AC material strained to $\varepsilon_{true} \approx 0.25$ and the DT material strained to $\varepsilon_{true} = 0.1$ or 0.2 exhibited uniform deformation with no external evidence of localizations. However, both of DT specimens limited to $\varepsilon_{true} = 0.25$ had a crack at a diagonal spanning between the loaded faces. One specimen remained connected immediately after the test but separated upon handling while the other survived cross-sectioning for further analysis. All specimens which did not have collars were sheared completely in two along a diagonal. Cross-sections of the QS-tested samples show microstructures apparently unchanged from the pristine material (Figure 3.15). Evidence of localized deformation was absent for both materials.

The cross sections from the AC strained to $\varepsilon_{true} = 0.25$ and the DT strained to 0.1 likewise show microstructures essentially indistinguishable from the pristine materials with no localized deformation. However a DT in-plane sample deformed to $\varepsilon_{true} = 0.2$ has one corner which appears to contain an incipient shear band (Figure 3.16): stemming from the corner is a lighter streak at an angle uncommon for prior grain boundaries. The typical lamellar microstructure is not discernible within the streak at higher magnifications in BSEM.

In the DT sample strained to $\varepsilon_{true} = 0.25$ are two cracks opposite each other extending diagonally from the external surfaces toward the center of the sample with the crack tips connected by a thin band of lighter material (Figure 3.17). Like the cracks, the band is inclined relative to the roughly horizontal prior β boundaries that are common in the DT material. The band and cracks intersect many of those boundaries with little apparent effect, though near the center of the specimen is a segment that may follow a prior β boundary mostly normal to the loading direction (horizontal in the image). The band also bifurcates adjacent to this segment.

A few small cracks extend from the shear cracks roughly normal to the loading direction as well; these appear to follow nearby prior β boundaries more closely. Higher magnification of the crack tip (Figure 3.19) shows that some of the edges near the tip are jagged with sharp teeth separated by rounded spaces rather than being flat and straight. Backscatter SEM and STEM imaging (Figures 3.17 and 3.18) reveal that the band comprises many approximately equiaxed nanoscale grains. TEM diffraction at locations within the shear band contain nearly complete circles indicating the presence of many grains that are randomly oriented. Diffraction patterns from near the shear band exhibit streaking of the spots resulting from small rotation changes. Patterns from other regions, all of which show alternating α/β lamellae in STEM in both AC and DT materials, show only a few populations of spots that indicate a single crystal orientation for a given lath packet.

3.4. DISCUSSION

3.4.1 Microstructure

The microstructures observed here are, in many respects, like those found in other Zr alloys such as Zircaloy-2 and -4 and many Ti alloys. Common microstructural features of fully lamellar (β-processed) versions of these alloys include large prior β grains, continuous α along the prior β grain boundaries, and lamellar α in basketweave and colony configurations[350–355]. The α phase is HCP and the lamellae are separated by thinner laths of BCC β phase; the two phases are known to exhibit the Burgers Orientation Relationship (BOR) as in other Ti and Zr lamellar alloys[329,350,354–357]. As a result of this OR, the basal plane of a given α lath is parallel to the (110) planes of the β, and one of the $\langle 11\bar{2}0 \rangle$ directions of the α is parallel to one of the $\langle 111 \rangle$ directions of β. Although there are 12 possible orientation combinations, in most cases

variant selection causes only a few to be present in a particular prior β grain[355,358]. Variant selection appears to occur for the Zr-2.5wt% Nb of this work, with usually only 3-5 orientations being observed for a given prior β grain. The large fraction of basketweave microstructure and most of the colony-type lamellae arrangements being near or attached to the prior β grain boundaries indicates a relatively fast cooling rate[350,355]. The larger fraction of colony microstructure observed for the DT material appears due to the greater density of prior β grain boundaries rather than additional plate nucleation sites in grain interiors as proposed previously[329]. Colonies may be more prevalent when viewing the DT material in the out-of-plane direction because of the orientation of the section plane and the broadening/flattening of the prior boundaries created by the compression step during processing.

3.4.2 Stress/Strain Mechanical Response

The variations in yield strength and flow stresses between materials and orientations do not reflect the vast dissimilarities in configuration of the prior β boundaries. The strain hardening rates and strain rate sensitivities in compression are also similar (likewise for softening rates in tension), suggesting that common mechanisms operate in both materials regardless of those boundaries. Additionally, although the DT material is anisotropic with the out-of-plane orientation being stronger than AC material and in-plane orientation weaker, the disparity between the two directions is only moderately greater than the experimental variation of the AC material. The presence of some anisotropy in the response of the DT material (and lack of it in the AC material) are unsurprising, but evidently the large-scale prior β grain boundaries have relatively little effect on the flow stresses of these alloys. Given that the measurements for the two DT orientations are the same material simply loaded in a different

direction, the strength disparity between the materials is likely due to anisotropy in the structure of the DT material.

These results can be rationalized by considering the material response mechanisms. While many HCP materials deform by twinning instead of or in combination with slip, twinning has been shown to be suppressed at room temperature and low rates for the alloys used here[329,359], as well as in general for Zr with sub-micron α phase[360]. Furthermore, yield stress is constant with strain rate when twinning is the dominant deformation mode[361,362], whereas here the yield stress clearly increases with strain rate for both materials. The primary deformation mechanism is therefore assumed to be dislocation slip.

When controlled by slip, the flow stress and deformation response of metals depend on movement of dislocations and their interactions with obstacles, meaning slip length (i.e., the mean free travel distance or mean free path of mobile dislocations[357]) and resistance to slip are critical factors in determining mechanical performance. Greater resistance leads to higher strength while greater slip lengths lead to lower ductility due to greater strain accumulation[319,350,357,363,364]. In the lamellar materials like the present alloys, the primary unit controlling slip behavior has been found to be the packets of similarly-aligned laths. This is because adjacent laths have similar (identical) crystallographic orientations and hence deform together. And while phase boundaries are typically dislocation barriers, in these Zr-2.5wt% Nb alloys the α and β phases have one set of slip direction nearly exactly aligned and another only ~10° misaligned due to the α phase growing out of the β in the Burgers Relationship[329,354–356,365]. Thus, slip transfer between phases and into adjacent parallel lamellae likely is not a primary strengthening mechanism[343,366] But neighboring colonies (or basketweave lath packets) have significantly different crystallographic orientations, and therefore propagating

slip from one to the next is difficult[207,319,342,343,357,366]. Consequently, the size of colonies is correlated with strength through a Hall-Petch type argument.

In the alloys studied here, the type and size of "slip units" are more or less the same in the AC and DT materials: large colonies along the prior grain boundaries and predominantly small packets and basketweave α laths in interiors. The AC material had a greater fraction of basketweave and small-packet microstructure than the DT (Figure 3.5), but the sizes of packets and basketweave structures were qualitatively similar across materials. In light of this, the similarities in stresses are more understandable. Nevertheless, the AC and DT materials are not equal; there must be another factor influencing the response. One possibility is the change in slip orientation between adjacent prior β grains and the orientation of their boundaries with respect to the applied load. If these boundaries serve as meaningful barriers to dislocations, having adjacent prior β grains that are closely aligned should permit easier slip transmission and hence lower strength. An alternative is texture in the DT material. Texture can occur in the final product even without deformation of that material through the possibility of inheritance during the $\beta \rightarrow \alpha$ transformation. In addition, variant selection is influenced by applied stresses and by the texture in the high temperature β phase[356,367–369], and texture in the β phase can be either formed by processing or inherited from the initial α phase[356,358,367,368,370]. The compression during processing of the DT material could have induced a texture in the β phase or the stress state during cooling could have caused a non-random selection of α variants during transformation. Whole-sample x-ray diffraction or extensive EBSD would reveal whether this is the case.

To match the measured results, the texture would be one that is difficult to deform along the axial direction and easy to deform perpendicular to that. This appears plausible given the

known details of the processing. The DT compression step occurred while the material was in the BCC phase. Assume that the DT compression aligned the {111} planes of the BCC β phase to be perpendicular to the loading axis, as tends to occur for BCC crystals[371]. On cooling, the β transforms to HCP α following the Burgers Orientation Relationship, meaning that the basal planes of the α phase form parallel to the {110} planes of the prior β BCC grains and two of the $\langle\bar{2}110\rangle$ HCP directions align with the ⟨111⟩ type directions of the prior BCC directions[365]. As a result, one of the $\langle\bar{2}110\rangle$ directions in the α would become parallel to the deformation axis. These directions in the basal plane have the lowest critical resolved shear stress and are usually most active in slip[372]. However, the direction parallel to the loading axis would have no resolved shear stress. Thus, deforming the DT material in the out-of-plane orientation (the same direction as the compression during processing) might require activating a greater fraction of high-CRSS slip systems or additional hardening of the remaining low-CRSS systems, both of which would increase the flow stress. Conversely, none of the low-CRSS directions are parallel to the in-plane direction and so that direction could have an accordingly a lower flow stress. Currently this series of events is speculative; it is not clear whether the compression during processing could have produced sufficient texture for this, and as noted above, an existing texture that was not removed by annealing could have been inherited in the final product.

The similarities in rate sensitivity are further suggestive that the nature of the deformation mode does not change (e.g., twinning does not take over for slip) with either rate or strain, and the same type of slip systems are active in both materials and orientations. Even within the ⟨a⟩-type slip systems (basal and prismatic) with low CRSS, the rate sensitivity is likely different if the present materials behave like two-phase Ti[237,373]. The magnitude of the

strain rate sensitivity is similar to those reported for many other metals deforming by thermally-activated mechanisms (see Chapter 1.5). Thus, the length scales of the phases are not small enough to produce the increase in SRS found in nanoscale materials, and also the lamellar and hierarchical microstructural features do not have a meaningful effect either (or there are counteracting effects that cannot be identified).

3.4.3 Compression Deformation Behavior

The deformation behavior during low-rate compression was practically identical across the materials and orientations, implying that the differences in microstructure had relatively little effect in this strain and strain rate regime. There were also no deformation or failure mechanisms that would suggest material limitations related to the microstructure. During high-rate compression, deformation up until shortly prior to complete failure is seemingly independent of material again. However, failure was observed for both materials at this rate. While the mode was the same (shear localization) the conditions required to initiate failure were varied. Samples loaded along the DT out-of-plane orientation were the most prone to shear banding, with an onset strain ~60% of that required for the AC material.

The appearance of the cracks on the external surfaces suggests the formation and propagation of the shear bands could be affected by microstructural effects. For example, note the change in angle on a single side in the DT out-of-plane sample compressed at 4000 /s and the AC sample and the change in angle that occurred for the AC sample. Theoretical considerations of the shear localization phenomenon (specifically adiabatic shear bands, ASBs) have shown that the critical point for initiation depends on several material properties (e.g., density, heat capacity), a temperature-dependent shear stress/strain relationship, and the

"strength" of the initial "defect/heterogeneity"[198,199,243,249]. The material properties are presumably identical for the AC and DT materials and therefore do not affect the relative propensity for shear banding. In the shots with the 152 mm striker bar, the higher flow stresses mean the thermal energy from plastic deformation for the AC and DT in-plane specimens is comparable to or greater than that for the DT out-of-plane specimens and yet only the last sheared. Assuming the same degree of thermal softening, this implies that the ASB-forming defects are "more severe" for the DT out-of-plane orientation than for the AC or DT in-plane samples.

Somewhat unexpectedly, increasing strain rate for compression along the DT out-of-plane direction to 6700 /s *increased* the strain at which the stress collapsed. Since the higher strain rates is accompanied by an increase in flow stress, thermal softening presumably also increases (heat generated is proportional to $\int_{\varepsilon_0}^{\varepsilon_f} \sigma d\varepsilon_p$, so a greater flow stress increases heat over a given strain increment) which in turn would cause shear bands to form at lower strains[251,374], and then the cracks within the shear band would form and cause flow stress to drop all at lower total strain. The increase in critical strain indicates a delay in formation of either the shear band or the cracks. Formation of the shear band itself is thought to not cause an insurmountable decrease in load-bearing capacity[198], but the shear bands seem to give rise to voids and cracks. The exact cause is unclear, and modeling of shear band initiation has shown that the effect of strain rate depends on the interplay between many material parameters[251,374,375]. Interestingly, the same phenomenon of increasing strain to failure with increasing strain rate was also observed for a Ti-6Al-4V alloy[265], though the only commentary addressing that result specifically was to note that the adiabatic shear bands were more

branched at the higher strain rate. Another group has also reported formation of adiabatic shear bands without failure or significant softening and similarly negligible commentary[335].

3.4.4 Tension Deformation Behavior

In tension at both low and high rates, the only localization phenomenon is diffuse necking, standard for ductile metals. The failure strains during QS tension vary widely. Of these, the AC tension sample that reached high strain and was interrupted may be the anomaly. The fracture surfaces of all other AC samples show angular intergranular fracture with facets of similar size to prior β grains, indicating failure at prior β grain boundaries. But polished sections from the gauge region of the interrupted sample show only a small number of large prior grains, and their boundaries were oriented predominantly parallel to the loading direction. This is more comparable to the DT material than what is typical of the AC material and could have limited the locations at which failure could initiate.

In high-rate tension, necking initiated at lower strains and the ultimate elongations were reduced for both materials compared to the lower strain rate. The DT material still reached a larger strain than the AC samples though. In addition, the DIC strain maps show that the local strains under dynamic loading reach only half as large as during QS loading. While at the high strain rate the AC material failed along an inclined band, the angle of the band (~75°) is inconsistent with the 45° associated with a shearing type failure[351]. The fracture surface exhibits large facets with ductile dimples, further indicating that the angled propagation of the strain concentration was not due to shear localization in the manner reported for some other HCP materials[351,376]. The fracture surface of the DT specimen is consistent with a microstructure lacking the roughly equiaxed polyhedral prior β grains that comprise the AC

material. The DT specimen may still have failed at prior β boundaries that were normal to the loading direction, but the facets would be smaller and sharper because the boundaries are more closely spaced and the prior grains flatter than in the AC material. The fracture surfaces of both materials and rates contain large voids at locations that appear to correspond to prior grain boundaries as well, further supporting the notion of these as weak points where failure can initiate.

Recall from the above discussion of stresses, the deformation of metals is associated with slip through their microstructure. A region which experiences easy slip and a has larger slip length due to a lack of barriers will experience greater strain accumulation. In the present alloys, this corresponds to regions where the α laths are parallel with similar crystallographic orientations; the longest such regions are the continuous non-lamellar α phase and wide colonies that line the prior β grain boundaries. Following this reasoning, one would expect the prior β grain boundaries to accumulate strain more rapidly than the interiors of former grains and ultimately dictate fracture. Others have indeed reported that the interiors of grains deform less than the boundary regions because the colonies at the latter act as large grains and slip together[342,343,366].

Additionally, grain boundary α has been extensively implicated as the limiting factor in tensile elongation for Ti[319,350,377,378]. Peters et al. found that low ductility in a lamellar β-processed alloy was due to large equiaxed β grains surrounded by a soft layer of continuous α[378]. Luan states that grain boundary α is the site of early crack nucleation and leads to decohesion and intergranular type fracture at boundaries[379]. The deleterious effect increases with the strength difference between the hard and soft zones[319,350]. Despite the ruinous effect on elongation, there is relatively little impact on strength properties[319,350,377] while reducing the

size of α colonies increases yield strength by reducing slip length[319,364].The α near grain boundaries has also been identified as a one of several preferred types of site for void nucleation (along with colony boundaries and α/β lamellae interfaces). With increasing strain rate, the grain boundary regions became even more favored for void nucleation[342,343] and the number of voids formed increased with the number of sites available[342].

3.4.5 Tension/Compression Asymmetry

Tension/compression asymmetry (TCA) in yield stress is present at both loading rates and for both materials. The magnitude of the effect is independent of processing but roughly doubles with the increase in strain rate (which may be slightly exacerbated by the dynamic compression strain rate being higher than the dynamic tension rate.) A common cause of TCA is activation of twinning, where tension twins have a lower critical resolved shear stress than compression twins[380,381]. In addition, high strain rates have been shown to increase propensity for twinning in other HCP metals including pure Zr[361,382]. However, twinning is likely to be minimal given the submicron scale of lamellae in both AC and DT materials as deformation twinning is observed to decrease as grain size is reduced[359,360,382]. The tensile samples were not inspected for twinning though, so it cannot be definitively ruled out though.

Texture can also result in asymmetric response as different slip systems are activated[382]. However, the isotropic response of the AC material shows that it has a random texture. Therefore, an inherently asymmetric cause is needed, specifically one which permits deformation along the ⟨c⟩ direction to permit general deformation and meet compatibility requirements[380,383]. Pyramidal ⟨c+a⟩ type slip has been shown experimentally[380,381,384] and through simulations[321,384] to have a greater critical resolved shear stress in compression than in

tension. Given the lack of evidence for other deformation modes, it is cautiously assumed that pyramidal slip is causing the asymmetry observed here.

3.4.6 Shear Band Development

In both cases the shear bands begin near corners and appear to propagate across the sample rather than shearing the entire width and widening – the band in Figure 3.16 seems to terminate a distance into the bulk and the complete shear band in Figure 3.17 changes direction near the center of the sample suggesting two bands that grew toward each other. For neither is the direction of shearing noticeably affected by the local microstructure.

The equiaxed, randomly oriented and ultrafine microstructure of the fully-formed shear band is distinct from the microstructure elsewhere in both AC and DT materials. Although the appearance can be similar to prior β boundaries at low magnifications, the microstructures at smaller length scales are clearly dissimilar. This is consistent with recrystallization within that localized region. The boundary between the recrystallized band and the surrounding material is sharp in terms of grain morphology but the streaking in the diffraction pattern from near the band implies grain rotation. Rotation may be to accommodate the sheared material but these features may also point to a rotational recrystallization mechanism that has been postulated to occur in shear bands[385,386]. The nascent shear band in Figure 3.16 similarly appears to lack the typical lamellar structure but without TEM and STEM it cannot be determined whether it consists of random nanoscale grains. The presence of grains smaller than the initial lamellae but not yet randomly oriented would be consistent with the recrystallization model as well[386].

The toothed appearance of the crack faces are a result of crack growth by coalescence of voids ahead of the crack tip. Void growth appears to have been limited by the width of the

shear band. The lack of voids outside of the shear band indicates that the stress for void nucleation was much lower inside the band and their near-sphere shape shows the shear band was ductile[387].

3.4.7 Discrepancy vs. Reported Results

The observed microstructures are inconsistent with the observations reported previously for similarly-processed materials[329,347]. The average α lath thicknesses in the present DT material are ~50-100% larger than previously reported, and the present DT material cannot be said to comprise "nearly equiaxed coarse grains filled with microscale colonies"[329]. Rather, the prior β grains are large and elongated and many, if not most, contain substantial volume fractions of basketweave microstructure. Further, prior β grain boundaries also have a central rib of non-lamellar grain boundary alpha and extensive arrays of aligned alpha that potentially act as (very) large colonies. A closer inspection of Figure 1 (e) and (f) of Zhang's results[329] suggests that even those materials contain large regions of basketweave microstructure.

Regarding performance, the disparities in flow stresses between the AC material and the two orientations of the DT material, both in tension and in compression, are lower than previously reported for tension of AC material vs. the in-plane direction of the DT material[329]. Additionally, the magnitudes of the yield and flow stresses in tension are lower for both of the present materials.

The variation in between these billets may be due to the greater cooling time in these materials which allowed recovery mechanisms to operate for longer and accordingly affected the final microstructures. In addition, there is the possibility of dissimilar microstructures in the starting materials or slight variations in the processing such as time at temperature which

may have carried through. The initial texture before heat treating, residual and applied stress, and especially peak temperature during treatment also can influence the final variants[356,388,389]. Texture of α/β Zr alloys has been found to depend on the β grain size during the high-temperature steps of processing, with larger grains reduce variant selection and can lead to more random textures[358,389].

3.5 SUMMARY AND CONCLUSIONS

The current study investigated the mechanical properties and deformation behavior of a Zr-2.5wt% Nb alloy that was processed in two different ways. Both versions were tested in quasi-static and high-strain rate loading in tension and compression. A series of interrupted high-strain rate compression tests were used to study progression of strain localization. The resulting microstructures were characterized using optical, scanning electron, and transmission electron microscopy. Key conclusions are:

- AC material is isotropic in tension and compression at both quasi-static and dynamic rates while DT material is anisotropic in compression at both rates; the in-plane orientation is softer than the AC material while the out-of-plane orientation is stronger.
- Strength of both alloys is primarily dictated by the colony or lath packet size, not α lamella width.
- Both AC and DT exhibit tension/compression asymmetry, likely resulting from an asymmetric slip mode while other deformation mechanisms (e.g., twinning) are suppressed.
- Failure of these alloys is strongly affected by prior β grain boundaries. In dynamic compression, boundaries oriented normal to the loading direction increases propensity

for shear band formation and thereby limits straining capability. In tension, at both low and high rates, failure occurs through intergranular fracture initiated at the α phase lining these boundaries.

- The adiabatic shear bands initiate at specimen corners and propagate into the sample with minimal influence by microstructure. Failure occurs when cracks subsequently form along the sheared/recrystallized band through nucleation and coalescence of voids.
- Microstructure outside of strain localizations is relatively unchanged from the pristine state.

Acknowledgements

This work was supported by the Department of Energy, National Nuclear Security Administration under Award no. DE-NA0003857. Microscopy of this work was performed at the UCSB Materials Microscopy Facility, an MRL shared facility. The MRL Shared Experimental Facilities are supported by the MRSEC Program of the NSF under Award No. DMR 1720256; a member of the NSF-funded Materials Research Facilities Network (www.mrfn.org).

Table 3.1. Composition of the initial casting used to make the AC and DT materials studied in this work[345].

Element	Zr	Hf	Nb	Fe	Cr	C	H	N	O
Content (wt.%)	93.68	1.97	2.48	0.042	<0.01	0.0061	<0.0010	0.014	0.079

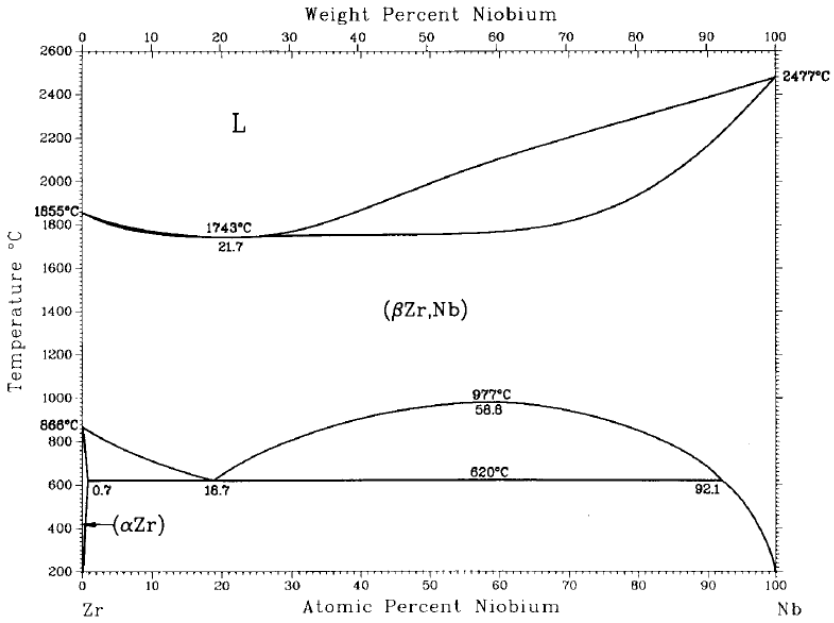

Figure 3.1 Zr-Nb binary phase diagram, from Okamoto[346].

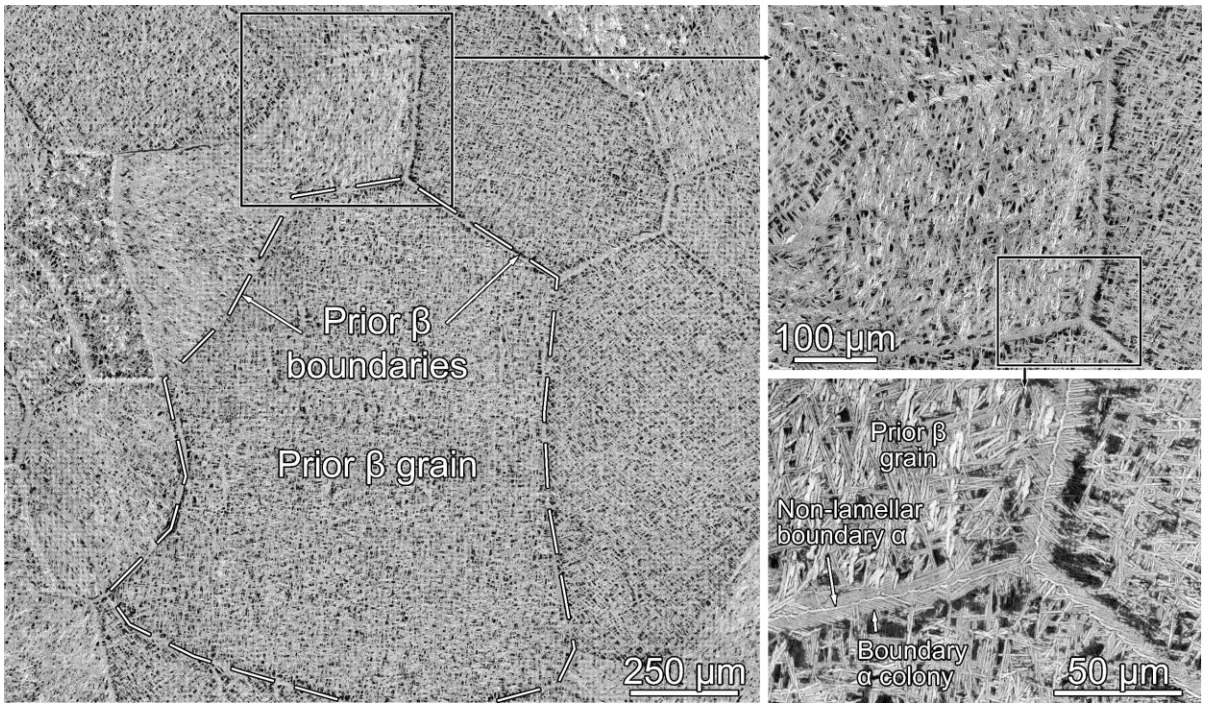

Figure 3.2. (a) Optical micrographs of a representative region of pristine AC material showing several prior β grains and their boundaries. (b, c) Higher magnification images reveal the lamellar structure along the boundaries and former grain interiors.

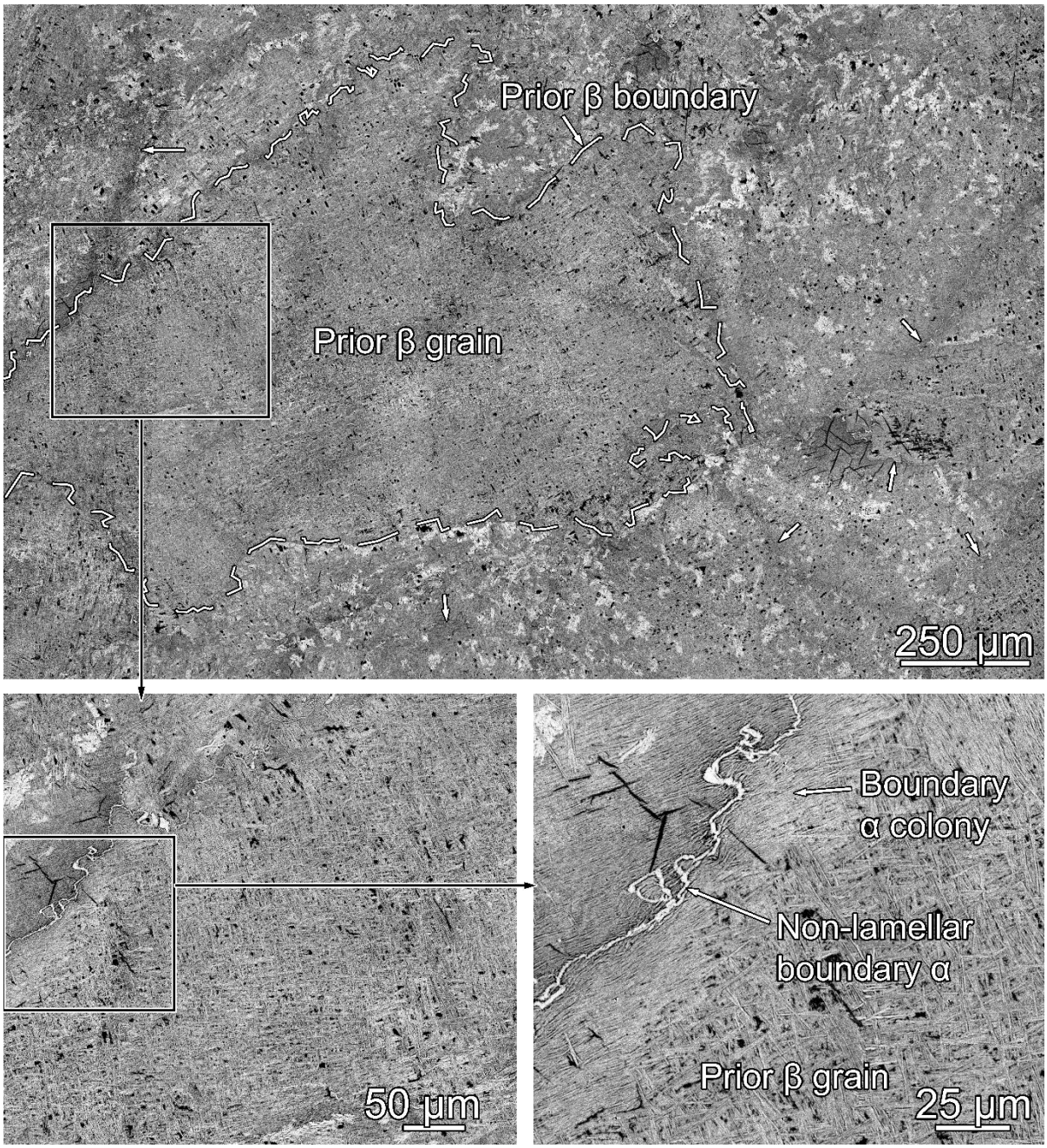

Figure 3.3a. Optical micrographs of pristine DT material viewed parallel to the DTMPT processing axis. One prior β boundary is traced with a dashed line in the top panel; several others are indicated by small arrows.

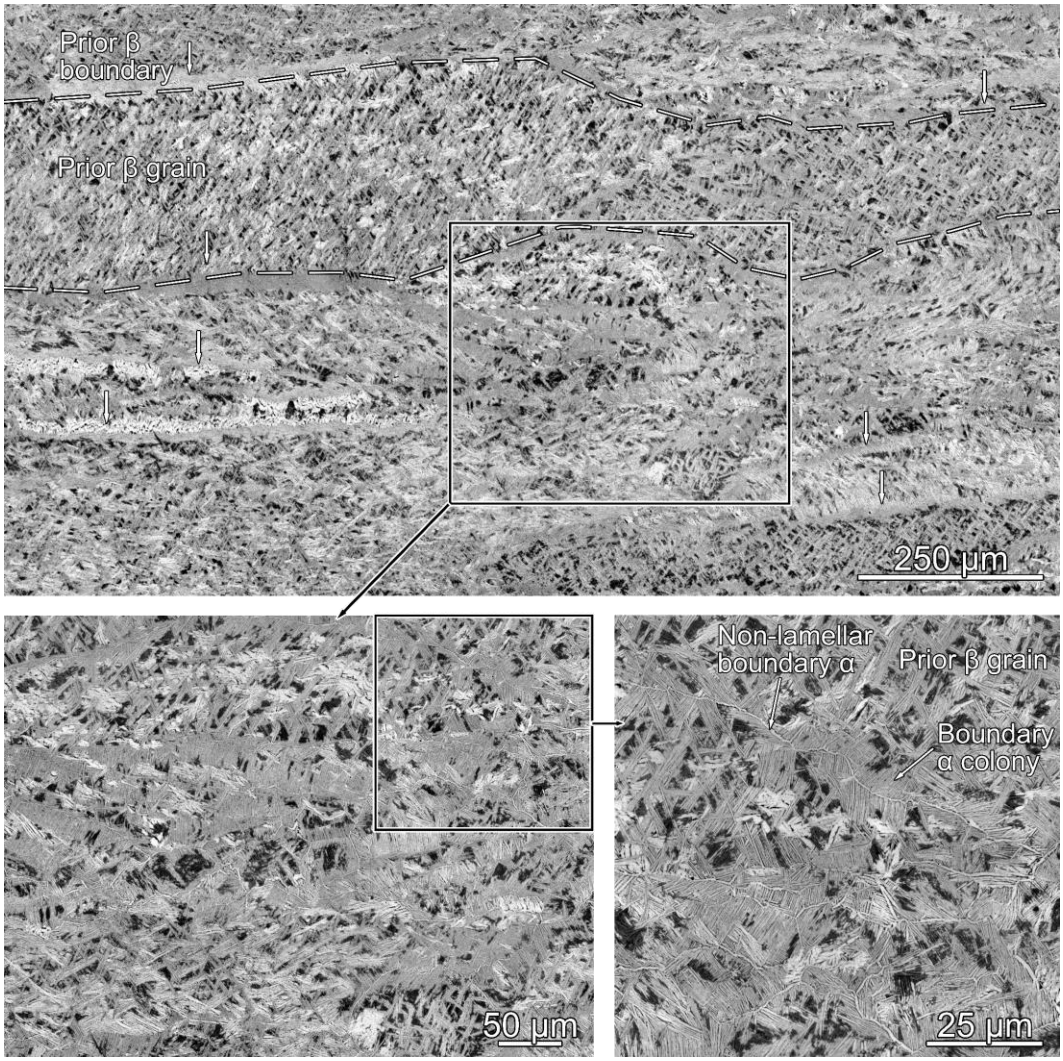

Figure 3.3b. Optical micrographs of pristine DT material viewed normal to the DTMPT processing axis. One prior β boundary, spanning the width of the field of view, is traced with a dashed line in the top panel; several others are indicated by small vertical arrows.

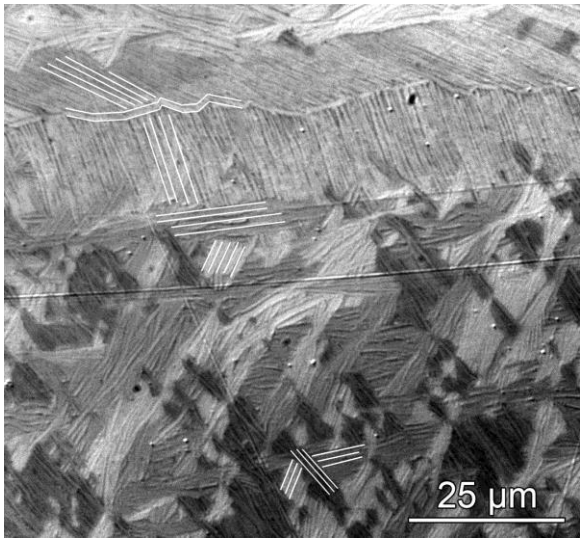

Figure 3.4. Optical micrograph of DT material imaged with differential imaging contrast mode. The polarized light causes each crystallographic orientation to appear as a different shade, thereby revealing that the prior β boundary (at top of image) has α variants which differ in spatial and crystallographic orientation from the neighboring prior β grain and from the α variants within the prior grain. The orientations of several α colonies and the non-lamellar α along the prior β boundary are indicated with white lines.

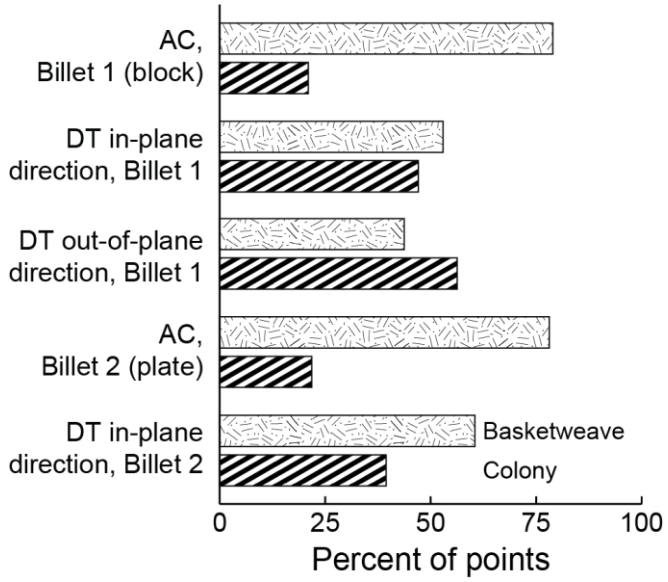

Figure 3.5. Relative fractions of lamellae arrangements for both materials and billets from both sets of experiments in this study. Directions for DT material are normals to the surface of the imaged section.

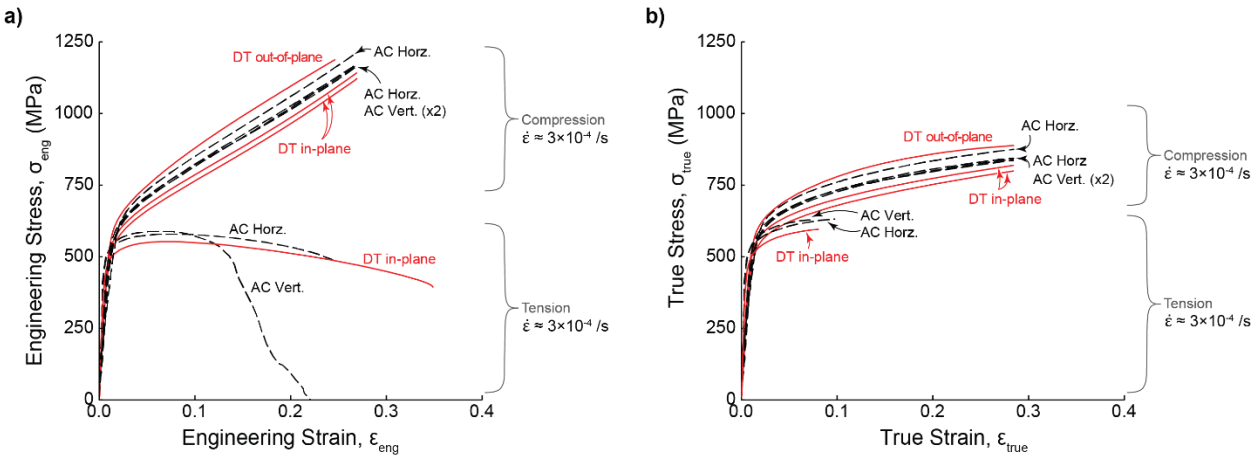

Figure 3.6. Engineering and true stress-strain curves obtained from low strain rate tests in uniaxial compression and uniaxial tension of both AC and DT materials.

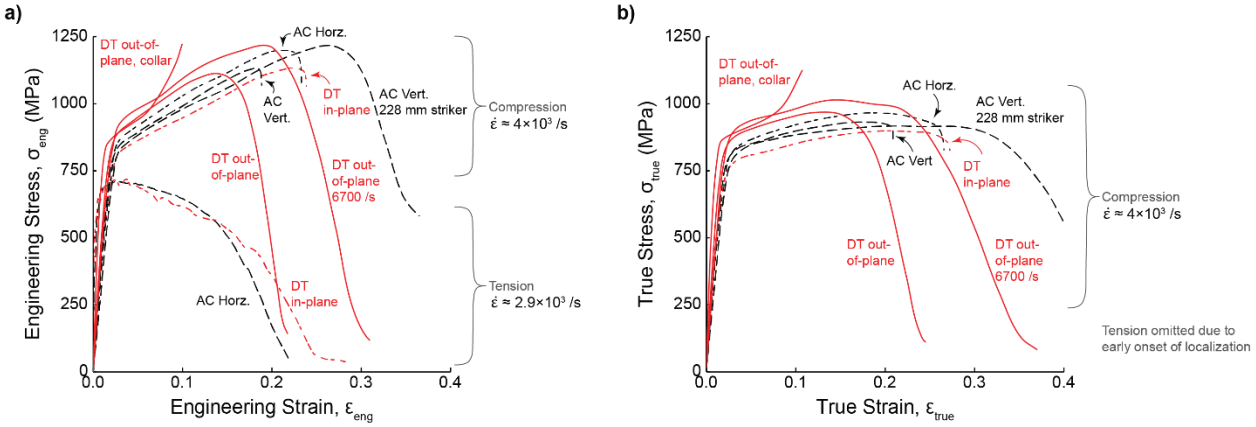

Figure 3.7. Engineering and true stress-strain curves obtained during high strain rate loading in uniaxial compression and uniaxial tension of both AC and DT materials.

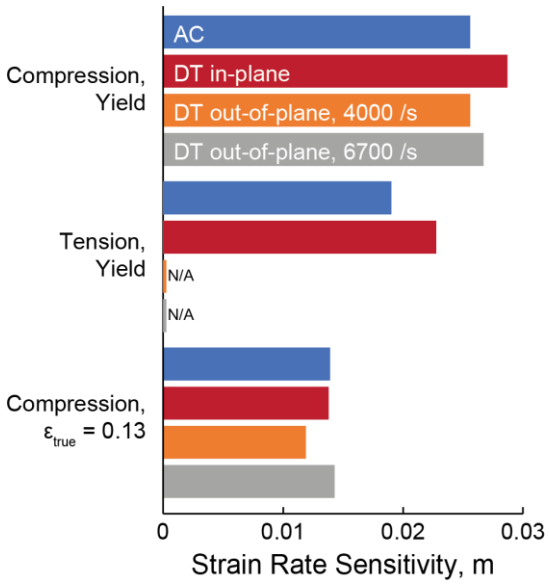

Figure 3.8. Strain rate sensitivity of yield stress is greater than the sensitivity at intermediate strain. There is little change in sensitivity with strain rate or between AC and DT materials. DT out-of-plane could not be tested in tension and true strains could not be determined for $\varepsilon_{true} = 0.13$ as this was beyond onset of necking.

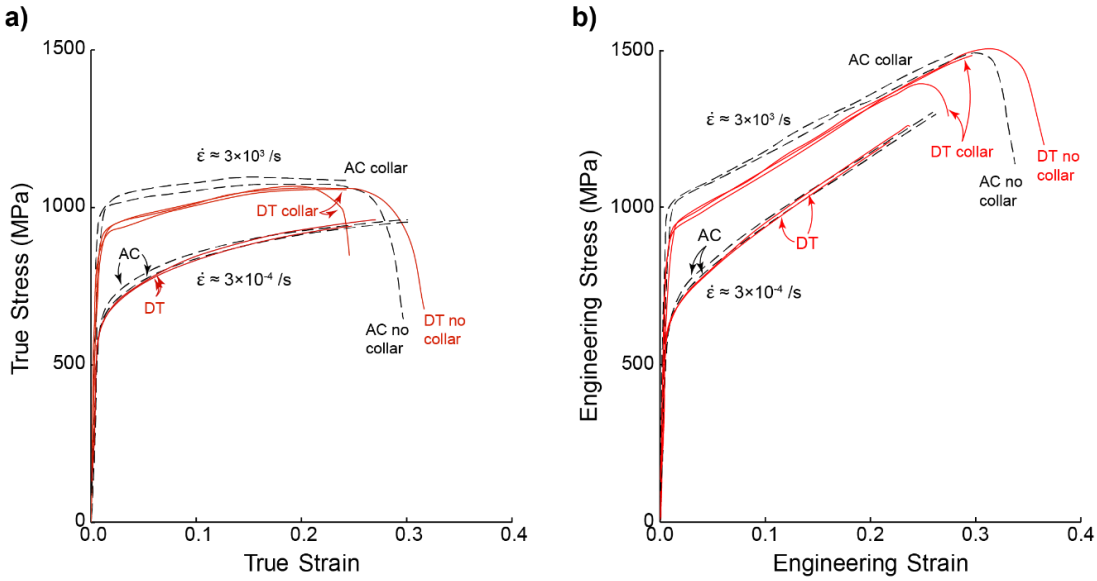

Figure 3.9. Quasi-static and dynamic compression response of AC and DT materials (out-of-plane orientation only) that were limited in strain using steel collars. Curves for DT material that were limited to strains less than 25% are omitted for clarity.

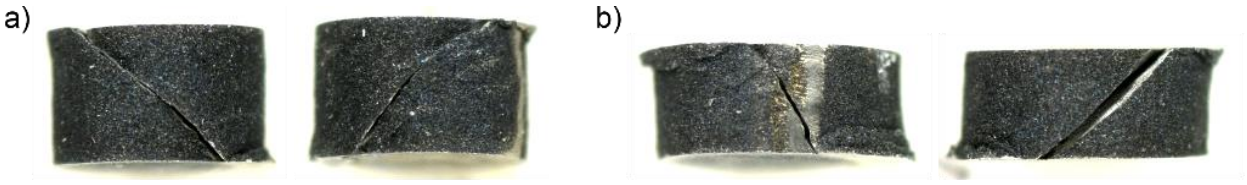

Figure 3.10. External surfaces of samples exhibiting shear failure: (a) DT material, compressed out-of-plane at strain rate of 4000 /s and (b) AC material compressed at 4000 /s using a 228 mm striker bar.

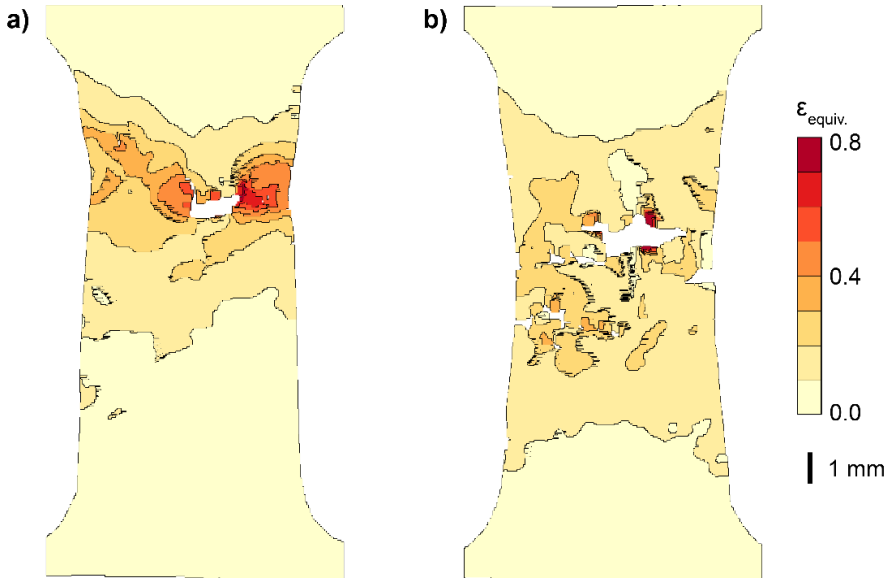

Figure 3.11. DIC maps of in-plane Mises equivalent strain during low strain rate tension of AC material (left) and DT material (right).

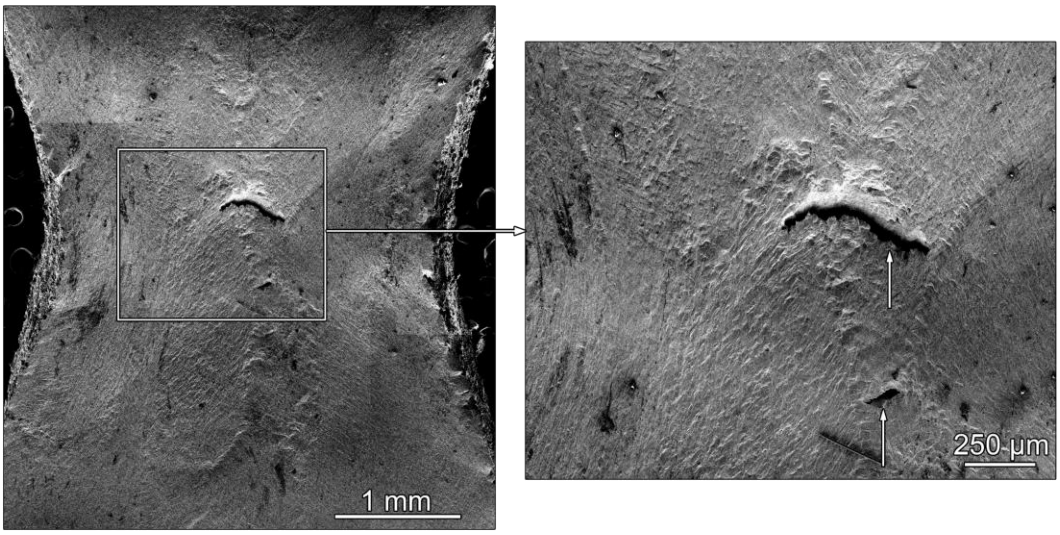

Figure 3.12. SE SEM micrograph of external surface of the gauge section of DT specimen after interrupted QS tension. Two cracks in the center of the necked region and are indicated by arrows.

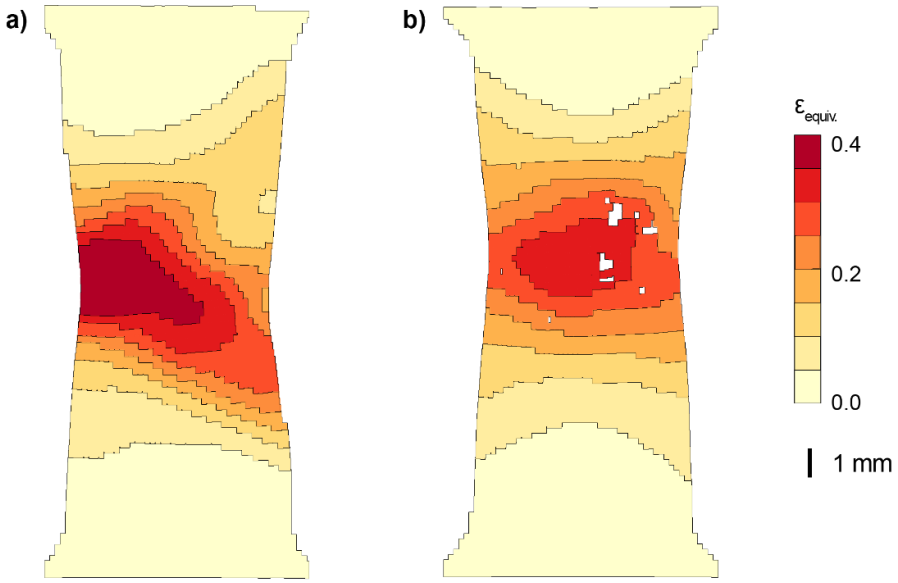

Figure 3.13. DIC maps of in-plane Mises equivalent strain during high strain rate tension of AC (left) and DT (right). The strain concentrations show locations of initial cracks believed to cause final failure.

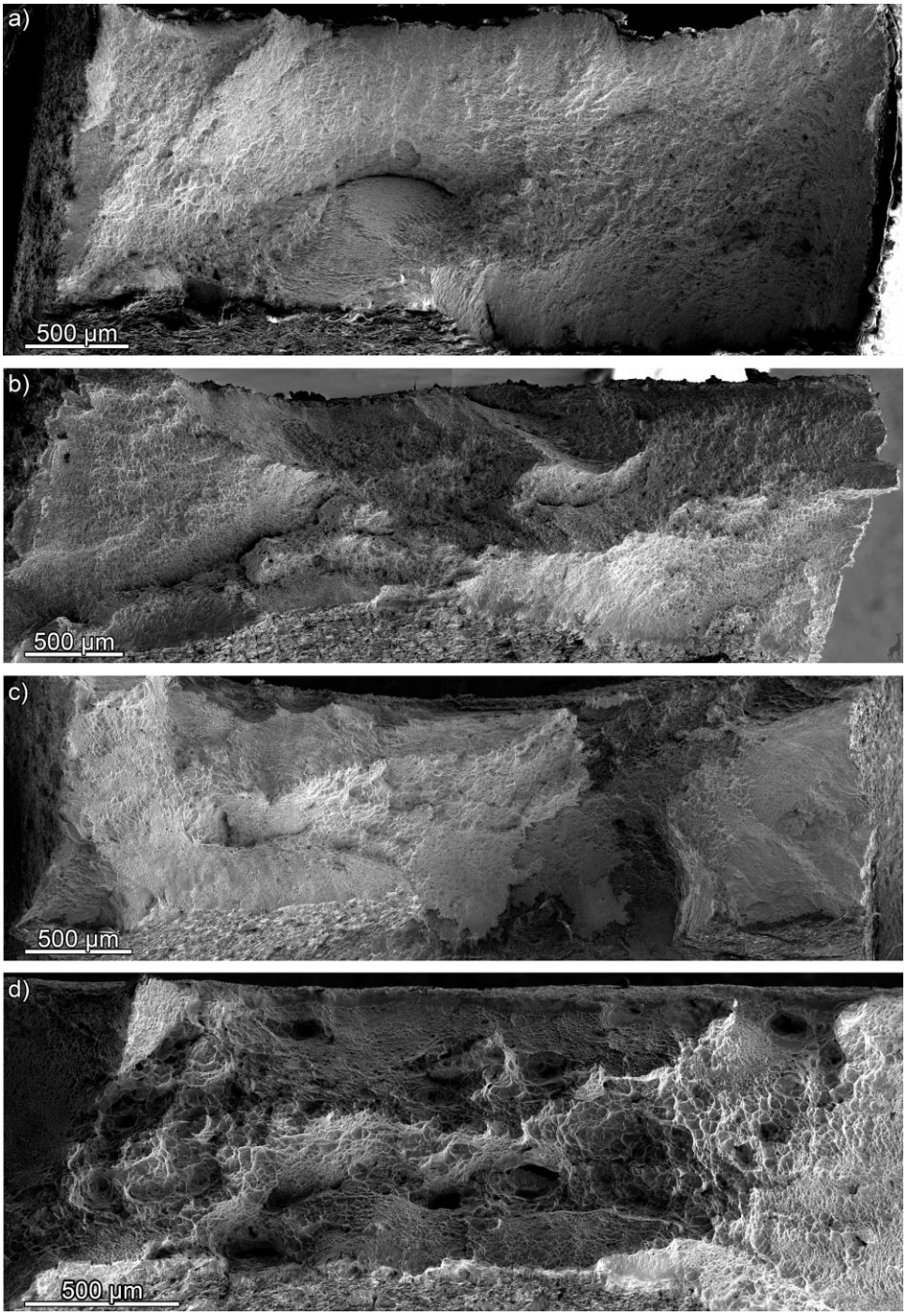

Figure 3.14. Tensile fracture surfaces of AC material at (a) quasi-static and (b, c) dynamic rates show large facets while (d) the surface of the DT material at dynamic rates has a single main ridge in the center of the gauge thickness. (a) corresponds to the strain map in Figure 3.10 (a); (b) and d) correspond to the maps in Figure 3.12.

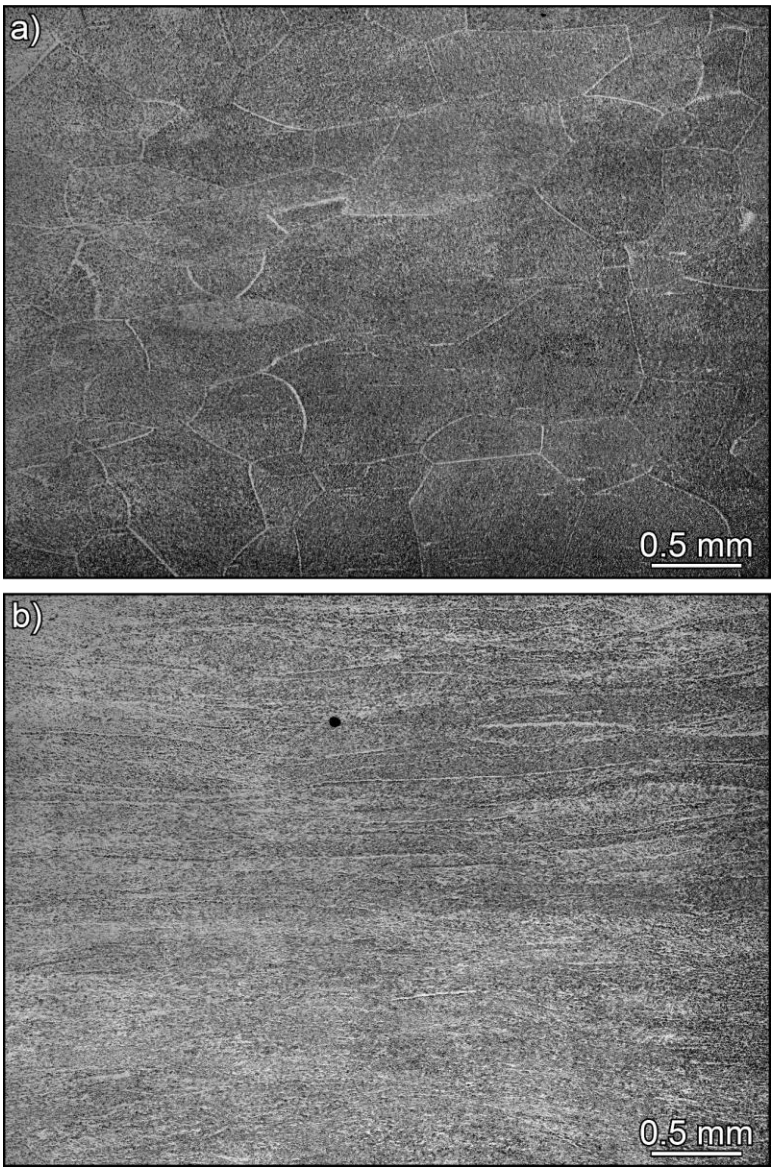

Figure 3.15. Sections after QS compression of AC (left) and DT materials (right) show that the microstructures are essentially unchanged from the pristine state. (Loading direction is vertical.)

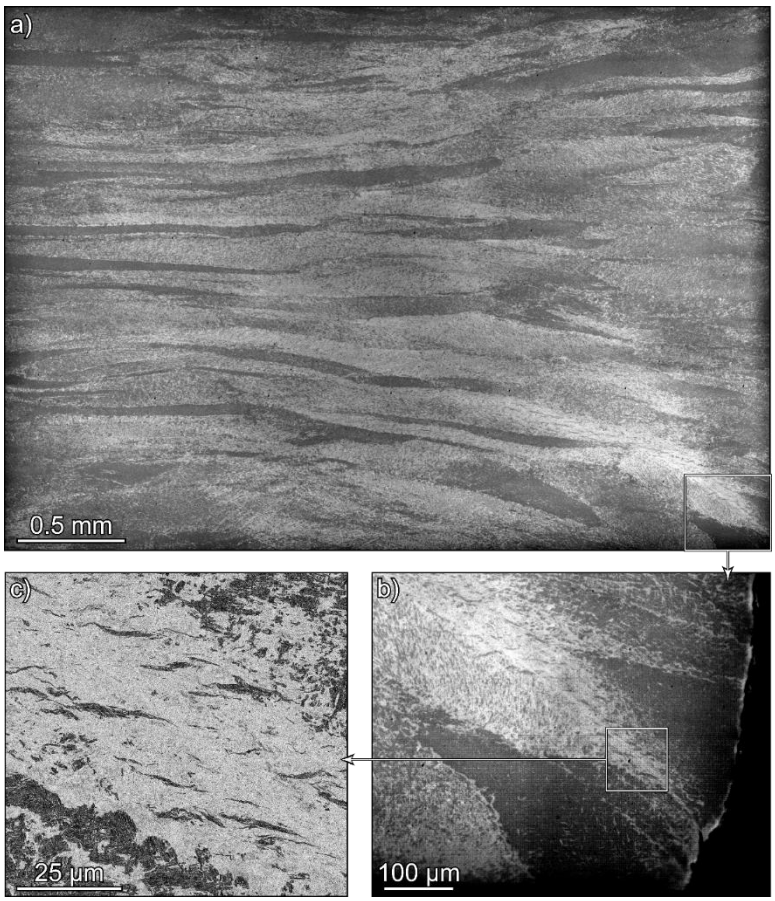

Figure 3.16. Optical micrographs (top and bottom right) of DT sample strained at high rate to $\varepsilon = 0.2$ show a light streak in one corner (top right). BSEM of the band (bottom left) does not show the lamellar features typical of this material. (Loading direction is vertical.)

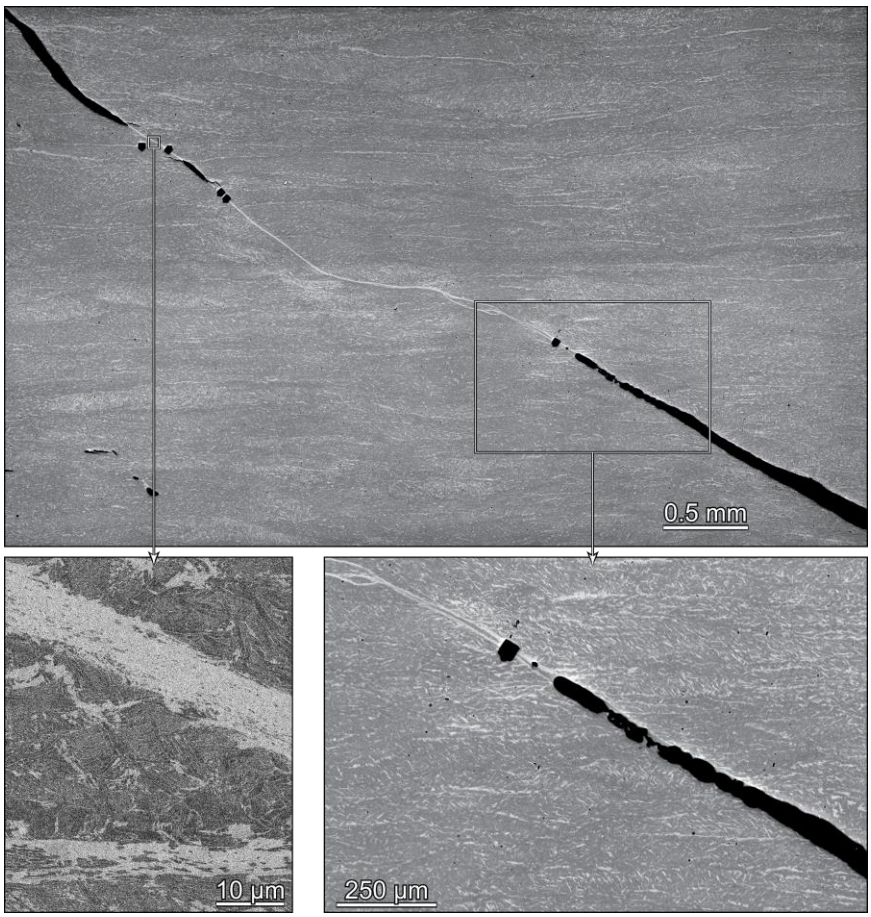

Figure 3.17. Optical micrographs of a DT sample dynamically compressed to $\varepsilon_{true} = 0.25$ reveal a shear band and a pair of shear cracks. The inset on the right shows the tip of the bottom right crack. (Loading direction is vertical. Note that several FIB sites are visible, including the squaring top-left-most "void" in the inset at right.). BSEM of the shear band shows that the band does not have lamellar structure of the pristine material while regions adjacent to the band retain that structure.

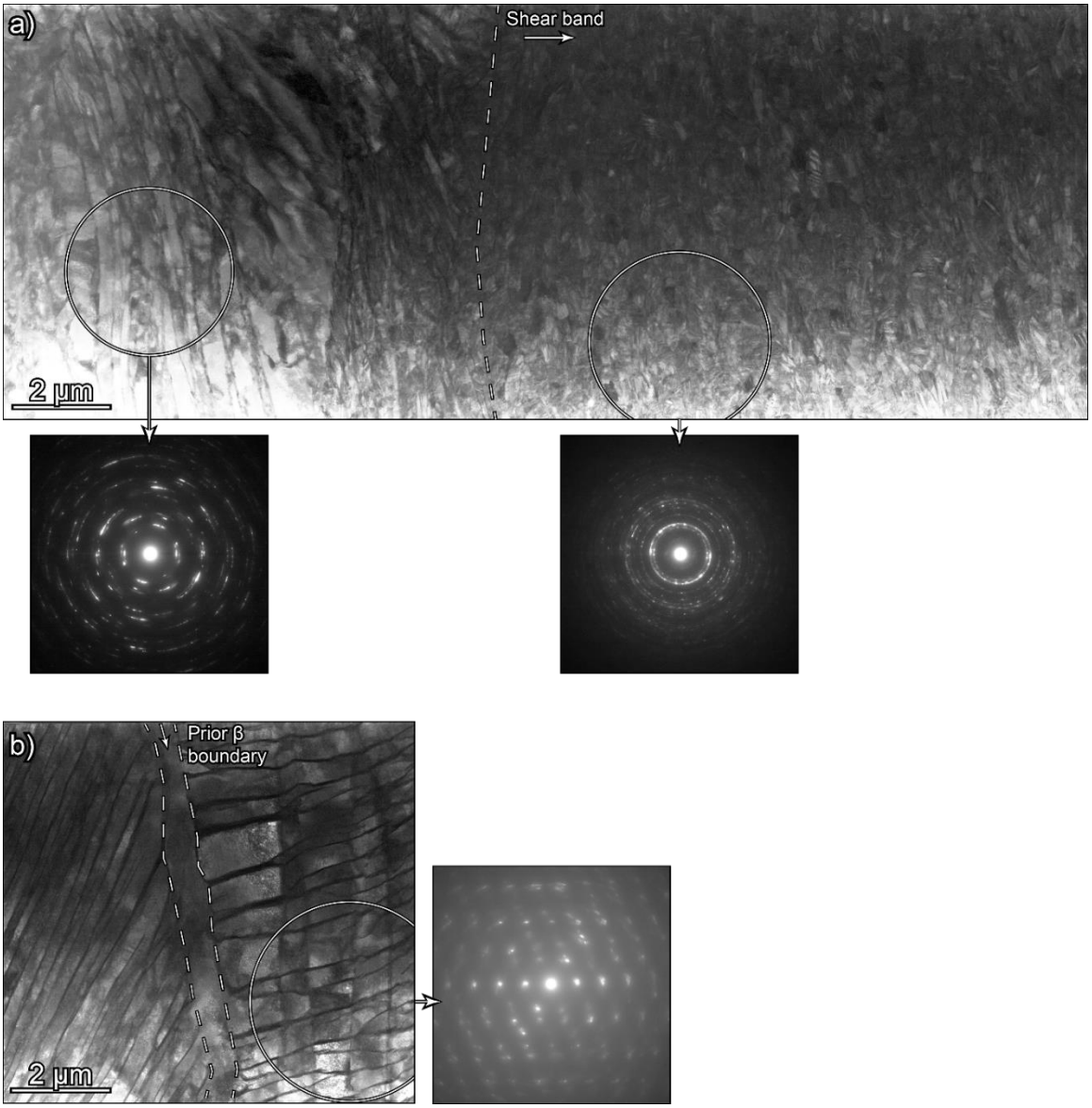

Figure 3.18. (a) Brightfield STEM micrograph of the edge of the shear band reveals the transition from lamellar to highly-refined non-lamellar microstructure. The TEM diffraction patterns show that the interior of the shear band has many randomly oriented grains while material outside of the band have aligned crystal orientations. Streaking in the latter pattern indicates some relative rotation near the shear band. A location far from the shear band (b) has a similar lamellar structure but the diffraction pattern lacks streaking, indicating almost a single crystal orientation within the lamellae.

Chapter 4

Effects of Microstructure on Spall Damage and Failure in Zr-2.5wt% Nb with Hierarchical Microstructures

4.1 INTRODUCTION

Advances in engineering systems depends in large part on the discovery and development of materials with superior performance in harsh environments. Nanostructured materials have been shown to exhibit numerous interesting and attractive properties. However, the features which enhance the capabilities of nanostructured materials often come with tradeoffs, such as strength for highly limited ductility, and also contribute to lower microstructural stability, especially at elevated temperature[73,171,291,325]. Recent work on bi-phase nanostructured materials, and in particular laminates or multilayers, have shown promise in ameliorating these deficits while still exhibiting attractive combinations of properties[2,332]. For example, layered materials have demonstrated[73,332] exceptional strength[59,73,78,85], stability at temperature[2,9,73] and after radiation exposure[73,333,390], and in some cases to extreme strain rates[73,267]. More recently, similar or even more promising performance has been reported for so-called hierarchical materials[2,60,134,391]. In this case, "hierarchical" indicates that multiple phase morphologies exist over several length scales, which might span from nanometer to potentially hundreds of micrometers[2,60,329].

The enhanced performance of the multiphase nanostructured materials is generally attributed to the high density of bi-phase interfaces since, with such small phase dimensions, the interface regions are a significant or dominant fraction of the total volume[73,332]. To produce

phase sizes at sub-micron or nanoscale dimensions, two general categories of processing are used: “bottom-up”, such as physical vapor deposition (PVD) wherein growth of the phases is strictly controlled[78,102]; and “top-down” where a coarser microstructure is refined to a smaller scale, typically through severe plastic deformation processing such as accumulative roll bonding (ARB)[85,332].

Several recent reports describe hierarchical Zr-2.5wt% Nb material with two types of microstructures, with sub-micron and nano-scale lamellae organized into large collective structures. Findings to date indicate that one of the processing methods offers improved strength for quasi-static strain rates and that the lamellar microstructures are thermally stabile to ~700°C[329,330,359]. However this alloy system is of interest for applications which might subject it to elevated strain rates and the performance under these conditions has yet to be assessed. The present interest is in the response during shock loading, including the role of the microstructure on spallation behavior. Much of the spallation work with Zr to date has largely focused on the single-phase metal with equiaxed microstructures. Crystallographic texture was found to significantly affect the dynamic elastic limit while only minimally changing the spall strength. Despite not affecting spall resistance, the presence of harder and softer orientations was manifested in the morphology of damage[277,278,392]. In addition, pure zirconium has been found to undergo a phase transformation from HCP α to hexagonal ω at high pressures; greater impurity content (interstitial oxygen) was found to increase the pressure required to cause the transformation[393,394]. In a titanium alloy (Ti generally exhibits similar behavior to Zr), the presence of the analogous ω phase was associated with a 12% decrease in spall strength[395].

The roles of other microstructural features in spall response have been studied in other (primarily cubic) materials including effects of grain size, grain boundary structure and

misorientation[396–400], the presence of hard[125,399,401] and ductile second phases[270,402], and processing effects such as layer structures from additive manufacturing[363,403–405] and texture. Yet, an adequate understanding of the fundamental mechanisms governing this high strain rate behavior is still lacking. This is exemplified by seemingly counterintuitive and contradictory observation of opposing trends of spall strength, either increasing with grain size or decreasing with grain size[406,407], as well as the disagreement over the influence of polycrystal boundary characteristics on void nucleation and growth[277,398,406–410].

The present paper covers flyer impact tests designed to study spallation behavior in Zr-2.5wt% Nb processed to produce two distinct microstructures. The deformation mechanisms and spall response, including void nucleation and growth behavior, are investigated and linked to microstructural features. The remainder of this article proceeds as follows: (write when finished).

4.2 MATERIALS AND METHODS

4.2.1 Materials

The materials used in this work have the same nominal composition of Zr-2.5wt%. Nb but two processing methods, as described previously in Chapter 3 and in detail by Zhang et al.[329,347]. Briefly, for the material hereafter referred to as "AC", a cast alloy was annealed for 15 minutes at 1000°C in the β-Zr phase field and then air cooled to room temperature. For the second material, referred to as "DT", a cylinder of cast material was annealed for 12-13 minutes at 950°C, compressed at temperature at a strain-rate of 1/s to a strain of 70%, then air cooled to room temperature. Two billets of DT material were used here. The targets used for the spall experiments are from the same billets as those used for studying shear band

development in Chapter 3. The sets of material of this study were nominally equivalent to the ones used in the tension/compression portion of that chapter. Comparison to the DT material of the previous work revealed that the failure behavior and microstructures are broadly similar, although there are disparities in their flow stresses and failure strains.

For the AC material, specimens were obtained from a plate initially 30 mm × 30 mm × 7.3 mm, and for the DT material from two different cylindrical billets roughly 38 mm in diameter and 7.3 mm thick. All billets were thinned and flattened using wire EDM prior to machining. Compression specimens were made from these billets as well to evaluate comparability to the other billets. All compression specimens from these billets were right circular cylinders, 5.0 mm in height and 5.0 mm in diameter and with the loading axis parallel to the thin direction of the billet (out-of-plane orientation for DT, arbitrary for the AC).

4.2.2 Quasi-static and SHPB testing

Baseline performance for both materials was evaluated through quasi-static and high strain rate compression. While the plate impact which is the primary focus of this work causes failure by net tensile loading, material limitations precluded performing these lower rate experiments in tension. The quasi-static (QS) tests were performed on a servo-hydraulic test frame (Material Test System 810, MTS, Eden Prairie) at a strain rate of 3×10^{-4} /s. The samples were held between hard WC blocks atop the standard steel platens. Strain in the compression tests was measured using a laser extensometer with retroreflective tapes placed on the WC immediately adjacent to the sample. High strain rate compression was performed on a Split Hopkinson Pressure Bar (SHPB) system which used 0.5” diameter bars of 350 maraging steel. The strain rate was ~3×10^{3} /s for all shots. The bar ends were greased before each shot and for

some specimens strain was limited using steel collars to preclude complete failure. The striker bar was 10 inches long, sufficient to produce complete failure or to fully compressed the sample to the height of the collar.

4.2.3 Plate Impact Experiments

To examine dynamic failure in these microstructures plate impact experiments were conducted using a 80-mm bore gas launcher and soft-recovery techniques. The details regarding the sample loading configuration are shown in Figure 4.1.

All three specimens were press-fit into a 44.5 mm diameter zirconium target plate/assembly with individual Zr rings. The surface was then lapped to ensure the impact face was completely flat. Additionally, the target plates were designed specifically such that the recovery of the shocked samples enabled post-mortem examination. The target plate consisted of three 3 mm thick cylinders 9 mm in diameter with a 7-degree taper, press-fit into two momentum trapping rings to ensure intimate contact of all the components. The ring diameters were calculated such that the spall process would not be perturbed by edge release waves i.e., the samples were effectively loaded and unloaded under 1D conditions[411]. For this experiment, a Zr impactor 1.59 mm in thickness and 50.89 in diameter was accelerated to 284 m/s. The key parameters for the experiments are listed in Table 4.1. The compressive peak shock stress in this table is calculated using the expression $\sigma = \rho_o u_s u_p$, where ρ_0 is the sample density, u_s is the shock velocity for calculated using $u_s = c_0 + s u_p$ and u_p is the particle velocity obtained from the free surface velocity data. Since there was no equation of state data available of Zr-2.5%Nb, u_s, c_0 and s were taken from the LASL Shock Hugoniot compendium for pure Zr.

Longitudinal and bulk sound speeds were measured with the pulse-echo ultrasound technique for each sample.

Free surface velocities were measured in each experiment using Photon Doppler Velocimetry (PDV)[412]. Collimating probes provided by AC Photonics (Part #: 1CL15P020LC-C01) were positioned to collect the free surface velocity data at the center of each sample with a LANL-built 4-channel frequency-shifted PDV system. One additional PDV probe (not shown in Figure 4.1) was placed in the target mounting plate, imaging down the barrel, to measure the projectile velocity to a high degree of accuracy. A single piezo-electric trigger pin (Dynasen, Inc.) was also placed in the target mounting plate with a typical standoff distance of a few millimeters to provide a trigger signal to the digitizer used to collect the PDV data. While spall strength calculated from the free surface velocity traces provides an estimate of the stress required to nucleate voids, it provides no information regarding the total damage morphology in the material. Hence, following impact all the samples were "soft recovered" by decelerating them in low-density foam[411].

4.2.4 Post-impact Microstructural Characterization

The microstructure in pristine and tested samples was characterized using a combination of light optical (LOM) and scanning electron microscopy (SEM). Optical microscopy was performed with a Leica inverted microscope. A differential imaging contrast filter was occasionally used to increase contrast and reveal orientation variation in the HCP phase. SEM was performed on a Nova Nano 650 FEG SEM with a concentric backscatter detector or through-lens detector (TLD). EBSD was performed on a Thermo Fisher Apreo C with an EDAX EBSD camera and TEAM software. Patterns were collected at 15 kV and 13

nA at 4×4 binning with a step size of either 0.070 μm (larger fields of view) or 0.030 μm (smaller fields of view). Larger accelerating voltages reduced pattern clarity, possibly due to interaction volumes with the small lamellae widths. The scans were analyzed in TSL OIM Analysis after partitioning with CI > -0.05 then reindexing with NPAR (Neighbor Pattern Average & Reindexing); some scans were cleaned with 1 iteration of grain dilation to remove occasional spurious pixels omitted by the partitioning step. Cleanup affected <2% of points. Twins were identified using the axis/angle pairs included as defaults in OIM Analysis.

The recovered targets were diametrically sectioned and mounted in an epoxy resin and prepared following standard metallographic techniques down to 1 μm diamond suspension, then 0.30 μm alumina, and finished by vibratory polishing with 0.05 μm colloidal silica. Some samples were also flat milled with a broad-beam ion mill (Leica EM TIC 3x) as these surfaces provided the clearest boundaries between phases and introduced contrast that aided in measuring lamellae thickness and identifying some features. However, this contrast is now believed to be not representative of the underlying microstructure but did not change metrics such as phase dimensions or introduce new features. The underlying cause of the contrast change is unknown, but it seems to completely preclude EBSD measurements on surfaces prepared this way; patterns are indistinct except at impractically long dwell times. Thus, all surfaces for which EBSD was performed were repolished starting with 9 μm diamond suspension and ultimately finished with colloidal silica. A second undesirable effect of ion milling is shallow scallops on the surface due to the glancing incidence of the ion beams. This surface roughness does not interfere with general SEM imaging but can obscure features when viewed in an optical microscope. Vibratory polishing was used for samples with voids to retain sharp edges and prevent apparent size increases due to preferential ion milling around edges.

Colloidal silica was removed by sonicating in 5 vol% microorganic soap for 30 minutes, rinsing with methanol, then gently drying with a cotton swab to avoid residues and to remove silica particles that may have wicked into voids.

Damage was quantified using the Particle Analysis tool in FIJI with stitched optical micrographs of the polished sections taken at 100× total magnification. A threshold was applied to the images to highlight voids and cracks. Only the regions ~3 mm × 1 mm in the centers of the samples were used; the surrounding area was excluded because release waves may have caused additional damage in this area. This approach has been used previously to analyze incipient spall on other materials subjected to similar loading conditions[270,402,403].

4.3 RESULTS

4.3.1 Pristine Microstructure

Both AC and DT materials exhibit a multiscale microstructure spanning lengths from roughly one millimeter down to sub-micron. In both, the largest features are former β grains and their boundaries. The boundaries of prior grains are 100-500 μm long, ~10-30 μm wide, and have a distinct structure at smaller length scales. In the AC material (Figure 4.2) the prior grains are roughly equiaxed polygons up to ~700 μm wide. The boundaries are randomly oriented relative to the sample axes. In the DT material, the boundary configuration depends on viewing direction. Viewed along the processing compression direction (out of plane direction, parallel to the billet axis) the former grains have tortuous boundaries that rarely form polygons. Viewed normal to the processing direction (in-plane direction, Figure 4.3), the boundaries are roughly perpendicular to the billet axis and enclose highly elongated, lenticular prior grain regions, with roughly millimeter-scale widths and <250 μm thickness in the

processing direction. Some smaller (~50 μm in width) enclosed regions are present, seemingly cut off corners of larger former grains; these small regions comprise a minority of the total section area.

The interiors of the prior β grains in both materials contain a mix of basketweave microstructure and parallel plate colonies with a colony or packet width typically on the order of 10 μm in AC and for DT viewed along an in-plane direction. In the out-of-plane direction, the colonies in DT can be up to ~100 μm wide. At this length scale, prior β boundaries are seen to comprise colonies of α lamellae extending from the edge of the prior β grain into the interior at a constant angle. Many boundaries also exhibit non-lamellar α (often called boundary α in Ti literature). Occasionally there are non-aligned laths within colony regions and large packets/small colonies within basketweave regions. The majority phase in both colonies and basketweave packets is high aspect ratio lamellae previously identified as HCP α[329]. These lamellae are separated by very thin laths or films of the BCC βphase. The average width of α/β lath repeat units were determined from BSE SEM images by drawing straight lines perpendicular to the lath direction that span across many layers and dividing the length of the lines by the number of α/β pairs (for SEM, this essentially amounted to counting α laths because the β layers are too thin to sufficiently resolve at most of the magnifications used). The α lath thicknesses fall in the range 0.22-0.55 μm (average 0.35±0.07 μm) and 0.30-0.79 μm (0.53±0.10 μm) for the DT and AC materials, respectively.

4.3.2 Baseline Compressive Mechanical Properties

The quasi-static (QS) and dynamic mechanical response of both materials is shown in Figure 4.4. At quasi-static rates both materials yield at ~600 MPa and then smoothly and

monotonically strain harden at the same rate, reaching ~950 MPa at $\varepsilon_{true} \approx 0.3$ before being unloaded. At the higher strain rate, the AC material yields at $\sigma_{true} \approx 975$ MPa then hardens to ~1100 MPa by a true strain $\varepsilon_{true} \approx 0.14$, after which the stress remains relatively constant for the remainder of the loading to $\varepsilon_{true} = 0.25$. Samples not strain-limited with collars experienced sudden decreases in stress beginning at strains of $\varepsilon_{true} \approx 0.27$. The DT material yields at a lower stress of 925 MPa then hardens until either a sudden drop or reaching the strain limit set by the collar. Sudden drops occurred both without a collar and with a collar; in the latter case the drop occurred prior to reaching the limit strain of $\varepsilon_{true} = 0.25$. The hardening rate of the DT material during dynamic compression is greater than that of the AC material and for both the average hardening rates at high strain rates are lower than during quasi-static compression.

After quasi-static compression, all specimens of both the AC and the DT materials exhibit uniform deformation with no signs of strain localization, matching the lack of softening in the stress/strain response. Specimens compressed via SHPB show one of two types of behavior. The first is uniform deformation and barreling, exhibited only by the AC material that was limited by the collar. Like after QS compression, no signs of localization were evident on the external surfaces or in polished cross-sections, and the flow stresses show no decrease. The other observed behavior is shear failure along an angle of ~40-45° from the loading direction. This occurred for the AC samples without collars as well as for all DT samples to varying degrees. DT specimens that were limited by a collar sometimes halted prior to complete separation, but others were fully sheared apart; all samples without collars, both AC and DT material, separated fully. All samples with complete failure exhibit a rapid decrease in flow stress. Specimens without obvious stress decreases in their measured response may still have experienced them but had the effect obscured by reverberations of the collars against the

bars. The failure mode was determined to be adiabatic shear bands (ASBs) which subsequently formed cracks. Apart from occurring earlier in the DT material, the ASBs were not noticeably affected by the microstructure of the two materials. Additional post-mortem analysis of these samples is presented in Chapter 3 Section 3.4.6.

4.3.3 Free-surface Velocity Measurements

The free-surface velocity profiles (Figure 4.5) contain features typical of incipient spallation. First, all samples show an initial elastic precursor with a slope change at 78-84 m/s. These velocities are converted to the Hugoniot elastic limit (HEL) using[199]:

$$\sigma_{HEL} = \frac{\rho_0 C_L u_{el}}{2} \tag{4.1}$$

where ρ_0 is the material density, C_L is the longitudinal wave speed given earlier, and u_{el} is the free surface velocity of the elastic precursor. The resulting HELs are 1.22-1.30 GPa. Following the HEL is a continued rise of the plastic compression wave up to the peak state. Two samples (from the AC and DT-B materials) show a slightly increasing shock top instead of a flat plateau; the third (from the DT-A billet) has a leading hump then decreases to the same level as the other samples. This non-uniformity in the peak stress could be due to varying accommodation of the strain by the heterogeneous microstructure. Peak free surface particle velocities in the plateau were 270-276 m/s. The peak shock stresses, calculated using the equations in the Methods above, are 3.48 GPa for the AC material and 3.53 GPa for both DT samples (Table 4.2).

The plateau in velocity is followed by a pullback to a minimum and then rebound to a peak corresponding to the arrival of a tensile wave and growth and coalescence of spallation

voids. The spall strength (σ_{spall}) which is a measure of the stress required to nucleate voids, is estimated from the FSV profiles using the relationship[413,414]:

$$\sigma_{spall} = \frac{1}{2}\rho_0 c_B\left(\Delta u_{fs} + \delta\right) \tag{4.2}$$

where

$$\delta = \left(\frac{h_{sp}}{c_B} - \frac{h_{sp}}{c_L}\right).\frac{|\dot{u}_1|.|\dot{u}_2|}{|\dot{u}_1|+|\dot{u}_2|}, \tag{4.3}$$

where ρ_0 is the initial density, c_B is the bulk sound speed, Δu_{fs} is the pullback in the free surface velocity, h_{sp} is the distance from the spall plane to the rear free surface and $\dot{u}_1$ and $\dot{u}_2$ are the gradients of the deceleration and acceleration phase of the spall pullback signal, respectively. The corrected spall strengths calculated using Eq. (4.2) are 2.3 GPa, 1.87 GPa, and 1.66 GPa for the AC, DT-A, and DT-B materials, respectively (Table 4.2). Thus, the (incipient) spall strength of the AC material was 20% and 40% greater than of the DT-A and -B materials. The curve for the AC material also has a greater slope following the pullback minimum. Despite the DT samples having been processed identically to one another, their pullback velocities values differ by 10% and the average slopes during reloading differ by ~50%. Also during the rise after the minimum, the traces for the specimens from the AC and DT-A materials exhibit steps prior to reaching the spall peak. That is, the slope momentarily decreases to 0 (for AC even becoming negative) before continuing to rise. The reloading for the specimen from the DT-B billet is comparatively smooth beyond a broader minimum.

4.3.4 Microscopy Analysis

In the recovered AC sample, the main damage feature of the spall region is a string of large voids across the center of the sample. Smaller voids are also scattered throughout the area. For both DT specimens, the spall region is spread over a larger fraction of the target

thickness with multiple strings of large voids aligned roughly normal to the impact direction. Again smaller-scale damage is found throughout this region away from the main void strings (Figure 4.6). Within these spall damage regions, five types of damage are distinguished. One is voids that have low aspect ratio and are often rounded or a series of rounded segments that are connected in the direction normal to the impact direction. These appear to cut across lamellae in addition to spreading and distorting adjacent intact laths. Qualitatively they appear predominantly in prior β grain boundary regions, both within and immediately adjacent to the α colonies lining the boundaries (Figure 4.7 and schematically in Figure 4.8).

The second damage mode is also void-like but with high aspect ratios. These are generally associated with the edges of lath packets and colonies (e.g., Figure 4.9 b and c) found away from the prior β grain boundaries. They spread adjacent lamellae without dividing them. It is not possible to determine whether these voids formed within a single lath or by delaminating an α/β interface. They also do not exclusively follow parallel to the lamellae directions – voids or cracks of similar appearance but perpendicular to the laths can also be found (Figure 4.10). This latter case may be due in part to damage outside of the imaged plane.

The third type of damage is “streaks” which appear bright in backscatter SEM (Figure 4.11) and connect neighboring voids, mostly the larger ones of the first damage type. These streaks can track in any direction, change direction between voids, and even double-back on themselves. In the AC specimen they typically follow a direction that is not perpendicular to the loading direction while in DT material they are most often parallel to the loading direction. The local trajectory of these paths is not clearly related to the surrounding microstructure. At smaller scales, the streaks have no discernible lamellae microstructure and instead appear to comprise many small grains. These streaks contain the fourth damage mode of shear-like

cracking. These cracks present as tears parallel to the local shearing rather than spheres or ellipsoids typical of nucleation and growth.

The fifth (final) type of damage encompasses microvoids and cracks at sub-lath scale. The distinction between the two is made based on whether the feature shape: when roughly spherical with a low aspect ratio, it is referred to as a microvoid (Figure 4.12); when long and thin with a high aspect ratio, they are termed microcracks (Figure 4.13). Although distinct in this morphological aspect, the two are grouped together because of their size scale and because they appear to form largely in the same types of locations: namely, within the α phase. However they are too small and scarce to conclusively determine whether void nucleation occurs predominantly in α, β, or at the interface between the two.

Damage quantification was performed using the regions indicated on the cross sections in Figure 4.7 and the results of are given in Table 4.3. The DT samples were similar to each other in all metrics and significantly different from the AC material. The AC target has the most voids, nearly twice as many as either DT sample; the smallest average void size, at 40-50% of the DT targets; and the smallest area occupied by voids, ~2/3 the area of either DT specimen. The large standard deviations, in all cases greater than the average void size, indicate that the void size distributions are heavily skewed. In fact, plotting the distributions reveals that all have a large number of voids smaller than ~50 μm^2 and a long tail to larger sizes. As described above, the largest voids for all samples tend to be on or near prior β grain boundary regions while smaller damage tends to be between lath packets in the former grain interiors. Also note that this analysis does not include the outermost portions of the samples.

4.3.5 EBSD Analysis

Several voided regions were scanned using EBSD. The first scan is in the AC sample and encompasses two voids near a prior β grain boundary (Figure 4.14). Between the two prior β grains is a typical region with a line of non-lamellar α flanked by colonies of lamellar α. All of the α along the boundary has a nearly constant crystal orientation while the material in each of the prior β grains contains several orientations. Each former grain shares one orientation with the boundary region. Additionally, the orientations in each of the prior β grains are distinct from the other. The spatial orientations of the lamellae away from the boundary do not appear to follow those of the boundary colonies. There is significant intra-colony change in crystal orientation only within the prior boundary region adjacent to the void; lamellae in this area are also spatially distorted. Lamellae surrounding the void in the left prior grain show little misorientation within the packet and also remain close to one of the orientations of that prior grain. The Schmid factors are similar and large for most orientations throughout the scanned region for both prismatic and basal slip. The void on the left side of the region is intragranular, away from prior β boundary and the boundary α colony. It is roughly parallel to one of the spatial orientations of the laths in this grain which is also near perpendicular to the impact direction (the impact direction is vertical in the image). The void on the right side is at the transition between the colony lining the boundary and is elongated parallel to the boundary; thus it is parallel to the impact direction and near parallel to one of the lath spatial directions on that side. Both voids follow an orientation of low prismatic Schmid factor. However there is no clear variation in distribution of Schmid factors in the area around either void.

Next is an analogous scan from sample DT-B of a void within a prior β grain boundary region (Figure 4.15). The IQ (band contrast) map shows that a rib of non-lamellar α runs along the center of the prior β boundary and lamellar α colonies extend from the rib above and below.

The laths of the top colony are vertical in the image plane while those in the bottom colony are angled at ~60° from horizontal; the top laths are therefore parallel to the impact direction. A void extends from the non-lamellar α rib upward into the non-boundary material. The void is parallel to both the α lamellae and the impact direction. Several diagonal lines cross through the entire width of the boundary region. The lines do not change direction at edges of laths and have only a small change when crossing the center rib but terminate at the ends of the boundary region colonies. These lines are neither parallel nor perpendicular to the α lamellae in the prior boundary region. The IPF maps show that the boundary region has a single c-axis direction, namely parallel to the surface normal. This orientation is rare in both of the transformed β grains outside of the boundary region. In addition, the [010] IPF map shows that the top boundary colony is misoriented from the lower around this axis by ~10°. The Schmid factor maps show that only the prior β boundary region is oriented for slip on the prismatic systems and not for basal slip while the surroundings are oriented for basal slip but not for prismatic slip. The void is widest near the non-lamellar α rib, which coincides with where a basal-oriented lath packet extends deep into the boundary region. The diagonal line features cannot be resolved in the lower magnification scan, but higher magnification shows that they have near constant crystal misorientation of about 33° relative to their surroundings.

A region inside a single prior β grain of AC material was scanned to compare with the boundary region (Figure 4.16). The region also contains a deformed shear streak (damage mode 3 described above). Most of the scan comprises typical packets of a few lamellae and a single orientation each. Several voids are within the sheared zone and another is unconnected but nearby in the top left corner. No large α colonies are present. The shear streak could not be indexed and the IQ map suggests that it comprises many domains that are much smaller than

the lamellae that constitute the rest of the microstructure. Twinning appears to be present in several lath packets near the sheared region. Two parent crystal orientations that lead to twinning were found. The Schmid factor maps show that nearly the entire region is well aligned for either of the easy slip modes with no obvious clustering or partitioning that might affect deformation.

A second scan from the DT-B sample (Figure 4.17) was taken at a location inside a prior β grain. There are several α colonies and two sets of voids. One void, in the top left of the scan, is approximately aligned with the laths of the main central colony. In the right void, which consists of three branches/arms, the top branch is parallel to the lath edges; the right-side branch is perpendicular to the lamellae, and the final branch is not obviously aligned with any microstructural feature though it is close to the direction of the surrounding laths. The crystal orientations are of the α colonies are varied but largely similar with the c axis parallel to the surface normal and the [2-1-10] direction near the image horizontal (parallel to the sample radial direction). Despite this, the Schmid factor maps show a stark division in preferred slip systems like that found in the boundary region above. A given colony is well-aligned to the impact direction for either prismatic or basal slip and very poorly aligned for the other mode. Both voids are centered at edges between regions oriented for prismatic and basal slip. In the IQ and IPF maps there are diagonal features that are not α laths crossing the central colony. The direction of the diagonal lines changes slightly at several changes to crystal orientation visible in the IPF maps. As with the lines in the boundary region, they do not extend into lamellae of other orientations. These lines are qualitatively similar to those seen in the boundary region.

4.4 DISCUSSION

4.4.1 Low-rate Mechanical Response

In quasi-static compression, the AC material is at least as strong as the DT material in terms of both yield and subsequent flow stress; during SHPB compression the flow stresses of both are increased and AC material reaches higher stresses. The hardening rates during QS compression were nearly identical. The hardening rates under SHPB compression were lower than at the low strain rate, but the rate for DT material was greater than for the AC material. This may indicate that at least one of the two materials has a nonrandom crystallographic texture. The α zirconium phase which comprises the vast majority of both AC and DT materials is HCP and has significant mechanical anisotropy related to activation of its limited slip systems, so dissimilarity in texture would manifest as a disparity in flow stresses[208,415].

However, the flow stresses at QS rates are effectively identical; thus, there would have to be a change in active slip mode with loading rate as well. This is not completely unrealistic since strain rate sensitivity varies with slip system[365,416]. For Zr, prismatic ⟨a⟩ type slip is the most easily activated at room temperature, often being the only type operative at low rates[329,365,383]. For the DT material in particular prismatic slip has been found to be the dominant system at low rates[329]. The basal systems have the next lowest activation stresses (in pure Zr, approximately 30% larger than prismatic slip[372]) and also have greater rate sensitivity than prismatic systems[365,383,416,417]. The disparity when compressed via SHPB could indicate activation of more basal ⟨a⟩ slip for the AC material than the DT material. In other words, this could indicate that the DT material has less volume oriented for basal slip, perhaps with more configured for ⟨c+a⟩ pyramidal slip than the AC material. There would likely be little activity on these planes given their substantially greater critical resolved shear stress (~3.5× greater

than prismatic slip in pure Zr)[365,372,383]. The greater hardening rate of DT material during SHPB loading also fits with activation of fewer systems. Although not a statistically significant number of scans, the EBSD scans of the flyer samples suggest easy prismatic slip orientations for at least the prior boundary regions that comprise a larger volume fraction in the DT material, consistent with the above conclusion.

Many HCP materials, including α Zr, will twin instead of activating the harder slip systems, especially to accommodate deformation along the ⟨c⟩ direction[360,365,383,415,416,418]. However, twinning in the DT material for low strain rates has been found to occur only at cryogenic temperatures[359]. This is likely due to the small scale of the α lamellae as the presence of neighboring layers can suppress twinning, an effect that becomes stronger as the size of the α is reduced[359,360,419]. Twinning in AC material is presumably similarly prevented by the size of the α phase since the typical lath width is comparable to that in the DT material. Therefore, no twinning is expected for any of the quasi-static tests. But twinning becomes more prevalent with increasing strain rates as dislocation motion is a thermally-activated event, and so twinning should still be considered for the dynamic tests[416,418,420]. Strain hardening resulting from twinning also is roughly linear[418,420], which qualitatively matches the appearance of at least the DT material response during Hopkinson bar compression. Possible twinning has been found after compressing this material by SHPB normal to the billet axis (Figure 4.19) as well as in EBSD scans from the present flyer targets, suggesting that this mechanism may indeed be active. In both instances the twins are thin and appear to constitute a small fraction of the sample though.

The observed failure mode, adiabatic shear bands (ASBs), is a form of strain localization that occurs when the balance between softening and hardening is lost on a local

scale and then propagates. As described in Chapter 1.6, for ASBs, the softening is typically attributed to reduction in flow stress caused by temperature increases which are in turn due to rapid plastic deformation in combination with insufficient time for thermal dissipation through conduction[198,199,336]. The greater susceptibility of DT material to ASB formation points to an earlier loss of this balance between hardening and softening. A typical estimate of temperature rise[203,336] would predict a later loss of balance for the DT material though, since the flow stresses are lower than for the AC material while the heat capacities, conduction rates, and global strains are similar. For softening to overcome hardening in the DT material then, one possibility is greater localization of deformation, and hence greater local temperature increase. Confining this deformation to grain boundary colonies or a relatively small number of prior β grains is plausible based on the EBSD scans and would be consistent with explanations for the mechanical response. Neither slip nor twinning is necessarily preferred for this deformation; twinning has been shown to dissipate energy as heat as effectively as slip does[382].

Alternatively, the DT material could experience a faster reduction in hardening rate that is more easily countered without needing *additional* softening compared to the AC material. The decrease in hardening rate might happen through earlier exhaustion of strain hardening capability on the fewer active slip systems or a greater temperature sensitivity of the active deformation modes.

Other possible sources of softening or "effective softening" that promote shear banding have been suggested, such as dislocation pileup and release, collective rotation of crystals or slip planes, and sliding between phases[336]. Some have also suggested that dynamic recrystallization is a softening mechanism which precedes and causes ASBs rather than a consequence of their passage[259,262]. There are conflicting reports on whether the α phase can

rotate within the β "matrix"[421,422] but recrystallization has been found in nascent shear bands in the present material (see Chapter 3.4.6 – Shear Band Development) and potentially contributes here.

The present results are at odds with those found for ostensibly identical material produced at a different time (Chapter 3). There, the AC material had lower yield and flow stresses than the out-of-plane orientation of DT material. Hardening in those other SHPB tests was not as linear either. However, the deformation and failure modes were found to be similar, including the greater susceptibility of DT material to shear banding during SHPB compression. Given the similar deformation behavior, some comparisons of present findings to prior tensile results will be made on the assumption that the current billets would exhibit equivalent behavior.

4.4.2 Dynamic Mechanical Response

The similarity in HEL between the AC and DT materials indicates a common mode by which plasticity begins. This contrasts with the disparity in yield strengths during SHPB compression and corresponds to a reduced role of the dissimilar microstructures in controlling the dynamic compressive yield (at least for these loading directions – DT material has been shown to have anisotropic response (Chapter 3)). One implication is that yielding under dynamic loading is not the same as that at lower rates. This could indicate that the loading during plate impact is sufficiently rapid that relaxation from activation of the low CRSS deformation modes is not communicated soon enough to prevent other types of deformation. Alternatively, the unequal rate sensitivities of the modes may simply lead to similar required stresses despite different active deformation modes or activation of more modes that reduces

disparities between the samples. As described later, although twinning is observed for both materials, it does not appear to have occurred during yield. In addition, the disparity in prevalence of twinning does not support similar yielding behavior if controlled by twins. In any case, the values of effective yield stress from the impact tests vs. the QS and SHPB tests are of similar order, suggesting that the deformation mechanisms during impact are still within the thermally-activated regime like in the lower rate tests. Additional yield vs. strain rate data is required to make a more definitive determination though[423].

Although both correspond to initial yielding, the HEL is not directly comparable to the yield stresses in QS and SHPB tests as the HEL is obtained during uniaxial strain conditions while the others are uniaxial stress conditions. Therefore, the HEL is converted to the von Mises effective stress. The relationship for uniaxial strain is[424]

$$\sigma_y^{\varepsilon} = \sigma_{HEL} = \frac{2Y}{3-\frac{1+\nu}{1-\nu}} = \frac{1-\nu}{1-2\nu}Y \tag{4.5}$$

where σ^{ε}_y is the uniaxial strain yield stress, Y is the effective stress (at yield), and ν is Poisson's ratio. Using Zr's Poisson's ratio ν = 0.34 and the HELs listed above gives effective dynamic compressive yield strengths of Y = 0.59, 0.63, and 0.60 GPa for the AC, DT-A, and DT-B materials respectively. For uniaxial stress states, the relationship is simply $Y = \sigma_y$ with σ_y being the yield values listed in Chapter 3.3.2 – Mechanical Properties. These dynamic yield strengths are on par with the values from QS loading and ~30-40% lower than the compressive strengths measured by SHPB.

One could also compare the axial stress components across loading conditions. For uniaxial *strain* loading this is given by $\sigma_{axial} = C \times \varepsilon_{axial}$ where the uniaxial strain elastic modulus $C = \frac{E(1-\nu)}{(1+\nu)(1-2\nu)}$, with E being Young's modulus (= 95-100 GPa for Zr) and ν being Poisson's ratio. Using the Poisson's ratio for Zr of ν = 0.34, the correction factor to stiffness is thus 1.54.

This gives axial stresses of 0.79, 0.84, and 0.81 GPa for AC, DT-A, and DT-B materials respectively. For the other tests, being uniaxial *stress* states, the axial stress is simply the measured stress. Thus, the axial component from plate impact is still lower than the SHPB compression values by ~10-20% but is now greater than QS compression by the same amount.

4.4.3 Damage and Deformation Characterization

While the elastic yield points are similar across materials, the failure strength, i.e., spall strength, is found to vary significantly. Spall strength is correlated with the ease of void nucleation. With the highest spall strength, the AC material is therefore expected to have the fewest voids. In addition, the rate of FSV increase from the pullback minimum up to the spall peak has been shown to be correlated with the rate of void growth[406]. Thus, the faster rise for the AC implies a higher void growth rate and hence large, isolated voids that have not coalesced, while the low reloading rate for DT suggests an earlier transition to void coalescence as this is a slower process than growth[402,404,406]. Taken blindly, the quantitative damage analysis is generally at odds with these inferences though – AC target has *more* voids than either of the DT samples, not fewer (though the area fraction of voids is smaller), and the average void size in AC target is smaller, not larger. However, these inconsistencies are due to skewed statistics from the extensive joining of small voids in the DT samples: the large "single" voids found in these are often strings of smaller voids that are connected in the direction perpendicular to the loading. Counting void nucleation sites rather than the entire connected set would increase the number and decrease the average size of voids in the DT samples. The same coalescence may be absent from the AC because the voids are less likely to be near one another and growth is more hindered for voids that are within the basketweave regions than in large colonies

The steps during the reloading noted for the FSV traces of the AC and DT-A specimens may correspond to nucleation of many voids on secondary planes, analogous to the stepped reloading observed for layers of AM Ti-6Al-4V[404] but at a smaller scale. Chen et al. also found slope changes during the reloading for spall of Al alloys but did not perform a detailed investigation, only postulating that there was an undetermined change in mechanism[425]. The broad minimum for the DT-B target could have the same cause: nucleation of voids on multiple planes is "communicated" to the free surface at different times and one instance overlapped with the reloading. Thus, these features in the traces are essentially further indication of non-uniform or non-random void formation, presumably at various boundaries and similar regions.

A preference for void nucleation at various types of boundaries and interfaces has been observed in a variety of other materials, including titanium alloys[271,273,276,366,426], Mg[266,401], Cu[406,427,428] and Cu composites[270,402], and wrought Ta[403,408]. The specific mechanisms are still being investigated. Fensin et al. found no relation between nucleation stress to grain boundary energy or free volume[429]. Decohesion at inclusion/matrix interfaces has also been implicated[401,407,408], though there are no inclusion particles in the present material. Other evidence from both experiments and simulations point to the primary cause being deformation incompatibility that concentrates stress[407,408,410]. One outcome of incompatible deformation is that failure at grain boundaries is predicted even when they are not assumed to be weakened at all[407] (which is not to say that relative weakness has no effect on nucleation, only that it is not a necessary condition).

This notion of incompatibility at grain boundaries is appropriate for any boundaries where deformation propensities differ. In a hierarchical material like that being studied here, there are numerous locations where this might occur. Neighboring prior β grains are an obvious

choice; their crystal orientations differed when still in the β phase, and those orientations dictated the current orientations of the transformed phases. The α and β phase interfaces might also be considered. However, in the present material these interfaces follow the Burgers Orientation Relationship[329,430] and several of the slip systems of α are near parallel to those in the β phase, permitting relatively easy slip transfer between phases[358,431,432]. In addition, the variant selection upon cooling means that adjacent α laths which are spatially parallel also share crystallographic orientations[329,358,430]. However, neighboring lamellae that are *not* spatially parallel necessarily have a different crystal orientation, meaning that colony edges are barriers to slip and sites of incompatible deformation[366,431]. In other words, the "effective grain" in these materials is the colony/packet size, not the prior β grain size or the lath size, and neighboring packets may have dissimilar deformation preferences. Incompatibility stresses could therefore explain the observation that voids prefer to form in prior β boundary regions and between lath packets in the prior grain interiors.

Nucleation at prior β grain boundaries may be further exacerbated by localized weakening associated with non-lamellar α that lines the interface between prior grains (Figure 4.8). The presence this continuous boundary α is strongly associated with early failure and reduced ductility in quasi-static loading many titanium alloys, to the extent that processing paths have been designed specifically to prevent it. The layer may be weaker because it is larger than the lamellae and lacks the α/β interfaces, for whatever strengthening those provide[350,377,378]. The deleterious effect of the continuous α worsened with increasing strain rates to the order of 10^3 /s[426].

Void nucleation may also be influenced by the orientation of the boundary or interface with respect to the loading direction. Reports on the relevance and importance are conflicting

though. Francis et al. reported little influence of boundary orientation on void nucleation[408], in contrast to findings that perpendicular boundaries have greater normal strains which increase nucleation on such boundaries[409,410]. In addition, impact tests of additively manufactured materials can show significantly lower strengths when the stress is applied normal to the build layer interfaces than parallel[404]. In the present material, the distribution of voids on prior β boundaries in the AC material appears to suggest (though not strongly) that orientation *does* matter. The voids in that sample are arranged roughly perpendicular to the loading direction even though there are prior β boundaries in the same region. However, those boundaries are oriented parallel to the tension direction. Instead of forming on these parallel boundaries, voids are found within the center of former grains is even though prior boundary regions are highly prone to damage across all of the samples.

Regardless of their location, the non-spherical shape of large scale (above micro-void) damage and void groups indicates an influence of the surrounding microstructure on their growth. Voids in the α colonies that line the prior β grain boundaries often span the long axis of the α lamellae (i.e., extend from the central non-lamellar rib out to the non-boundary regions) while their extent normal to this is more varied (for example, Figure 4.7 and Figures 4.14 – 4. 17). For the prior boundaries that are perpendicular to the loading direction (at least qualitatively the most common case), this means that the voids are often longest *parallel to* the loading direction. Meanwhile coalescence typically occurs through connection perpendicular to the impact. The EBSD scans for the DT material also show a stark transition in preferred slip system for the prior boundary colonies and the former grain interiors.

In contrast, the Schmid maps for the AC material show that the material around voids is essentially isotropic with respect to slip preference even though those voids are non-

spherical, indicating some preference in growth direction. Considering the region in Figure 4.14, the void on the right side of the prior grain boundary region is elongated parallel to the loading direction. On the other hand, the void ~50 μm to the left is elongated perpendicular to the impact direction. In both cases the void is roughly parallel to the α laths in that location. Extensive 3D analysis of voids in shock-loaded Ta suggested that voids nucleated at grain boundaries subsequently grew into whichever adjacent grain was plastically softer[408]. Similarly, EBSD of incipiently-spalled Ti-6Al-4V showed that voids grew into or along plastically softer grains[276].

Considering these previous findings, it is postulated then that here the voids formed in the boundary colonies spread first in the "soft" direction which is parallel to the lamellae regardless of the crystallographic direction. They then expand normal to this when/if hindered by the basketweave material, to continue elongating, as opposed to changing direction. Coalescence may result from a ductile necking type effect normal to the lamellae once the ligaments separating voids are sufficiently thinned despite this being the "hard" direction. In contrast, voids in the interior of prior β grains are often long and narrow although they are found to exhibit both behaviors, spreading along boundaries between lath bundles as well as halting and either widening or cutting perpendicular to adjacent α laths. Widening may be less favored because of constraint by the surrounding packets (the dissimilar orientations mean the two packets prefer to deform in different directions) or because there is typically another boundary nearby. There is no obvious preference for boundaries parallel, perpendicular, or at any other orientation with respect to the loading, pointing to influence by the local microstructure rather than being dominated by the loading condition. Some micrographs suggest that the "spreading" along boundaries is more nucleation of many voids along the same

boundary (Figure 4.9 c and d). Once a first void forms, its presence may elevate the local stresses and thus promote further void formation. It is also possible that these voids are a single void/crack connected outside the image plane.

The micrographs of the early stages of damage formation indicate that two mechanisms likely occur. The spherical voids (Figure 4.12) point to a ductile void nucleation and growth mechanism, whereas the crack-like features (Figure 4.13) are more reminiscent of a brittle fracture mode[272,280,433]. Both modes appear to prefer initiation within the α phase; decohesion of the α/β interfaces is absent and the only damage found in the β phase is from cracks propagating through β to other α laths. Initiation within a single phase is due to homogeneous nucleation at internal defects such as dislocation networks and vacancy clusters[280,433]. This is somewhat unexpected since heterogeneous nucleation typically has a lower required stress[280]. There also is no clear correlation between microvoid/crack appearance and local lath arrangement or loading direction. For example, the microcracks of Figure 4.13 are both parallel and perpendicular to lath edges, directions which also correspond to perpendicular and parallel to the impact direction. Evidently other properties of the microstructure are significant in the damage formation.

Interestingly, the nascent damage found here is in stark contrast to that observed after spall tests of Ti-6Al-4V alloys, which did exhibit heterogeneous void formation. In a fully-lamellar microstructure, i.e. the same morphology as the Zr-2.5wt% Nb alloys examined here, microvoids were found to prefer the α/β boundaries and triple points of α grains[272]. There was also a change in mode with the orientation of the lamellae with respect to the loading direction – perpendicular to the load was associated with decohesion in the center of interfaces while inclined led to voids near junctions of β layers. Meanwhile, a duplex type Ti-6Al-4V exhibited

debonding at α/β interfaces at room temperatures, but increasing the test temperature shifted nucleation to α grain interiors. In the latter case, strain incompatibilities at phase interfaces were decreased as barriers to plastic deformation were lowered by the temperature[434]. Lack of heterogeneous nucleation or interface debonding in the present materials may therefore indicate a large surface energy of the β phase relative to the α, or substantial ductility of the β phase that reduces the plastic incompatibility stresses.

The OIM analysis of the DT material also reveals twin activity throughout the large colonies that are oriented for prismatic slip. At the same time, there is little or no twin activity found in the adjacent material that is oriented for basal slip. Given the different orientations, the colonies which did twin could have simply had larger twin system Schmid factors. But in addition, the larger colonies comprise nearly a single crystal orientation, so twinning may have been necessary to accommodate deformation of the large colony without forming additional voids. This would not be the case for the non-boundary material because the multitude of orientations meant there was always nearby material which was able to deform by the relatively easier slip and relieve stress on the packets which would have twinned. Twinning may be more common in the colonies because of the larger "effective grain size" since smaller grains of Zr are known to be less prone to twin formation[360].

Along those lines, for the AC material, where no large "effective grain" regions oriented for only a single slip mode were found, twinning was also nearly nonexistent. For the small amount of twinning which is found, it is unclear why those few packets would twin. A statistical analysis of twinning in unalloyed Zr found that the local stress state was a significant driver for twin formation and the average applied stress was not necessarily sufficient to make

predictions[435], so presumably the local deformation altered the stresses enough for twinning for a few packets.

It is impossible to determine whether that occurred before or after the shear band-like feature formed though. However, the EBSD scans from the DT targets provide evidence that the twinning may have happened relatively late. Namely, in none of the scans do twins cross voids (in other words, no twins appear to have been split by voids propagating through them). And in Figure 4.18, the lamellae of the colony at the prior boundary are clearly sheared while the twins edges remain straight. Since the shearing was probably associated with material movement for void growth, twinning would have occurred after void nucleation and growth. In this case, the twins could not have acted as sites for void nucleation as has been suggested for some systems[436]. Also note that twins extend across multiple α laths in both AC and DT materials, meaning that neither the α/β interfaces nor the (cubic) β phase itself are strong enough barriers to prohibit twin propagation. This is similar to observations for cryo-rolling of the DT material wherein twins were found to bypass the β layers and grow into several adjacent α lamellae. Crystal plasticity simulations were used to determine that ductility in the β phase reduces the backstress that typically hinders twinning in nanoscale microstructures[359].

The streaks or paths that connect are qualitatively like adiabatic shear bands described for this material after dynamic compression (Chapter 3.4.6) and numerous other materials[163,171,199,259,265,276,336,338] loaded to SHPB compression. Similar features also are found after plate impact of many Ti and Zr alloys where they have been considered shear zones linking voids nucleated on separate planes[271–273,392,395,403,434,437]. In those cases, these features (called shear bridges) were thought to have formed after substantial void coalescence left only

relatively narrow ligaments to bear the tensile load, thereby converting tension stress to shear[271,273,434].

This description is plausible for the DT material where voids formed on distinct planes, but for the AC material certain characteristics seem inconsistent with this explanation: many of the apparent shear zones are tortuous, reverse direction, and have segments perpendicular to the impact direction, even between voids that are close to each other. The surrounding microstructure (e.g., prior β grain boundaries) is not distorted, indicating that these streaks were not straight before being deformed by a later reverberation. This would seem to require a stress state other than uniaxial strain, at least on a local level. Apart from the locations of the voids there is no clear association with the surrounding microstructure that would drive this variation though. Despite these caveats, in all cases there are commonalities between these streaks and those previously reported and identified as being sheared, for example highly-refined, non-lamellar grains and the fact that they link voids.

These characteristics are also consistent with adiabatic shear bands, suggesting that these streaks are formed by a similar mechanism. It is plausible that these shear features similarly are important for ultimate failure, for example by reducing the need for spallation across a single plane. However, the lack of consistency with the uniaxial strain state may indicate that these features form well after the initial spall peak and therefore would not be involved in failure for a longer or larger magnitude pulse.

4.4.4 Comparison to Existing Zr Spall Results

A comparison to previous work on plate impact of Zr materials reveals potential effects of either alloying or microstructure. For a clock-rolled high-purity Zr, the through-thickness

(TT) direction (analogous to out-of-plane direction of the DT material) was found to have an HEL of 1.18 GPa, similar to the values for both current alloys. Meanwhile, in-plane direction (IP) of the same material had an HEL of only 0.61 GPa[392]. The anisotropy is attributed to a strong basal texture (c-axes parallel to TT direction) produced by the clock-rolling procedure. A commercial-purity Zr rod impacted along the extrusion direction also had an HEL of 0.60±0.02 GPa[277,438]. In both the clock-rolled and rod material the grains were equiaxed and of ~25 μm. However, no strong texture was described for the latter. Spall testing of other materials has shown anisotropic HEL measurements such as in textured Mg[439] and single-crystal Mg[440] and Be[441]. Both experiments and simulations have shown that the anisotropy is associated with the activation of different deformation mechanisms depending on orientation, including separate slip systems and twinning modes. The present EBSD results suggest that there might be some texture differences, with a consistent alignment in the prior β boundary regions of the DT material. At the same time, the consistency in HEL between AC and DT materials implies the same mechanism in both materials, which limits the possibilities and suggests that some aspect of the microstructure or alloying is responsible for the relatively high HEL.

In terms of spall response, pullback velocities in the prior studies were ~165 m/s (TT direction) and ~180 m/s (IP direction)[392] and ~200 m/s for the CP rod[277,438]. For both of those studies, achieving a spall response required impact velocities 10+% higher than here though, and Hazell noted a decrease in pullback magnitude with increasing impact rate. For the CP rod, impact at 279 m/s (2% lower than the velocity as used here) did not produce a pullback signal though some voids were formed. Regardless, the pullbacks are comparable to the AC material and more than 10% larger than the DT material tested here. (The DT material is only that

similar with the most favorable comparison of the IP direction vs. target DT-A; other combinations are 50+% larger.) Evidently, the DT material is more susceptible to spall than unalloyed material.

A comparison of the spall plane void distributions shows that both present materials have some similarity to the TT direction of the clock-rolled Zr in that voids often join laterally. In the clock-rolled material this was attributed to the relative softness of that direction and a preference for cleavage on the aligned basal planes[392]. For the DT material, the lateral direction corresponds to spreading across α/β boundaries. However, voids in both prior studies were essentially round/spherical whereas here they are often nonuniform and angular, reflecting influence of the local lamellar microstructure on their formation and growth. It is unclear whether grain (or colony) size plays a role as all of increasing[407,442], decreasing[400], and no effect on[406] spall strength of grain size have been reported. Alloying typically reduces spall strength by introducing additional sites where void nucleation is particularly easy[125,442].

4.5 SUMMARY AND CONCLUSIONS

Two types of Zr-2.5wt% Nb were tested via plate impact to induce incipient spall. The material processed via the DT method has a greater number and density of prior β grain boundaries along the impact direction. The size of lamellae was minimally affected compared to air-cooled material. The differences in microstructure primarily affect response to the tension portion of the plate impact test.

- The dynamic elastic compression response is unaffected by the additional compression step of the DT processing method. HEL for both AC and DT materials was ~1.22-1.30 GPa.

- Examination of microvoids and microcracks suggest that voids initiate primarily in the α phase; neither decohesion of phase boundaries nor small voids within β phase were observed.
- Prior β grain boundaries are preferred regions for void formation. The number, frequency, and distribution of these boundaries is dictated by the processing method.
- Void nucleation is driven primarily by stress concentrations related to deformation incompatibility across boundaries, both of prior β grains and between lath packets of dissimilar crystallographic orientation.
- Spatial orientation is a secondary contributing factor to the ease with which voids nucleate along a boundary, not a main driver; voids grow along any orientation relative to the loading direction.
- Twinning occurs during impact loading but is a minor contributor to deformation response in both materials.
- DT processing is detrimental to dynamic tensile performance when loaded perpendicular to prior β boundaries. Dynamic tension parallel to these boundaries is expected to exhibit less of a deficit compared to the AC. It is not clear whether that orientation would offer advantages over AC though.

Acknowledgements

This work was supported by the Department of Energy, National Nuclear Security Administration under Award no. DE-NA0003857. Microscopy of this work was performed at the UCSB Materials Microscopy Facility, an MRL shared facility. The MRL Shared Experimental Facilities are supported by the MRSEC Program of the NSF under Award No.

DMR 1720256; a member of the NSF-funded Materials Research Facilities Network (www.mrfn.org).

Table 4.1. The peak free-surface velocities and corresponding peak compressive shock stresses in each sample, calculated from the measured velocity data.

Sample	C_L Longitudinal Sound Speed (mm / μs)	C_B Bulk Sound Speed (mm / μs)	Density (g/cm^3)	Peak Free-Surface Velocity (mm / μs)	Peak Shock Compressive Stress (GPa)
AC	4.730	3.891	6.608	0.276	3.48
DT-A	4.713	3.878	6.572	0.272	3.53
DT-B	4.745	3.916	6.436	0.270	3.55

Table 4.2. Calculated results for plate impact tests of Zr-2.5 wt% Nb AC and DT materials. The flyer plate was pure Zr.

Sample	u_{HEL}, km/s	HEl, GPa	u_{FS}^{Max}, km/s	Peak Stress, GPa	u_{pb}^{min}, km/s	ΔFSV, km/s	Spall Strength, GPa	Tensile strain rate (10^4 s^{-1})
AC	0.078	1.22	0.276	3.48	0.097	0.179	2.30	8.48
DT-A	0.084	1.30	0.272	3.53	0.125	0.147	1.87	8.51
DT-B	0.081	1.24	0.27	3.55	0.138	0.132	1.66	8.43

Table 4.3. Results of quantitative analysis of spall voids produced by the plate impact tests.

Sample	Area fraction of voids (%)	Number of voids	Average void area (um^2)	Standard deviation of void area (um^2)
AC	1.90	964	64.69	327.24
DT-A	2.50	519	154.97	588.55
DT-B	2.36	517	139.54	506.08

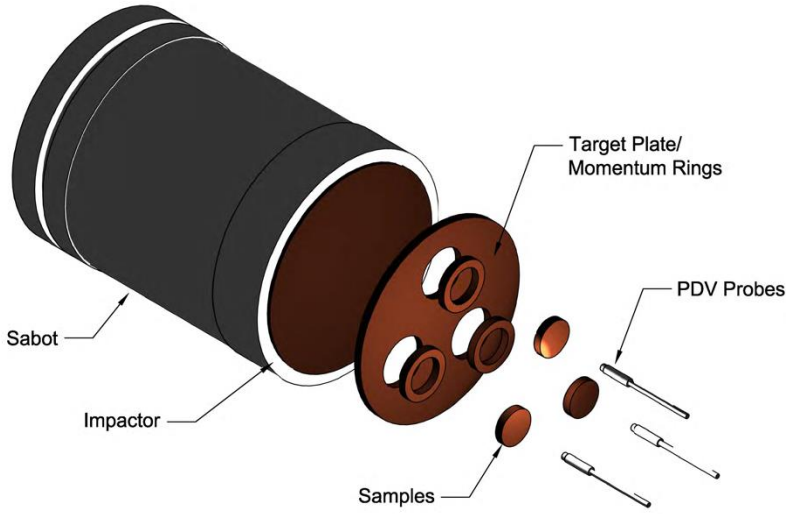

Figure 4.1: Experimental configuration used to produce incipient damage in multiple samples simultaneously. Pure Zr impactors were accelerated in an 80 mm bore gas gun and impacted onto the target. Photon Doppler Velocimetry (PDV) probes were positioned over the center of each sample to provide velocimetry data from the rear free surface.

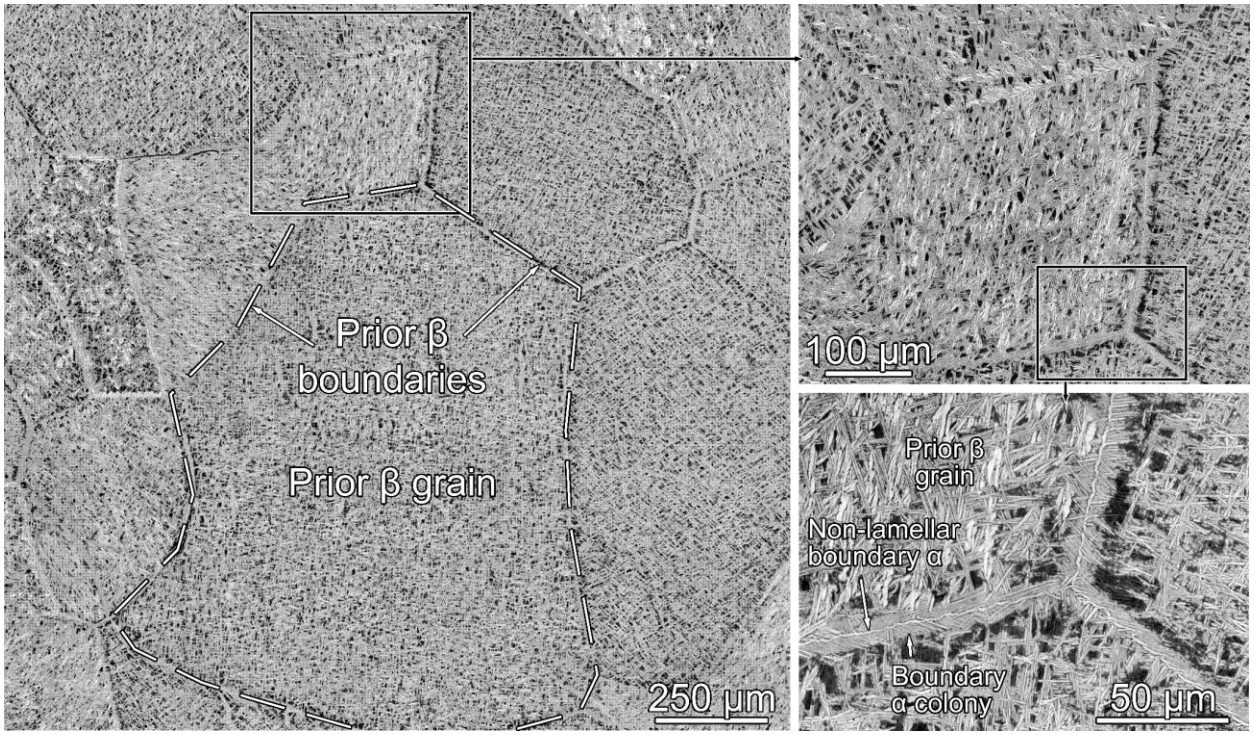

Figure 4.2. Optical micrographs of a representative region of pristine AC material showing several prior β grains and their boundaries. Higher magnifications (b) reveal the lamellar structure along the boundaries and former grain interiors.

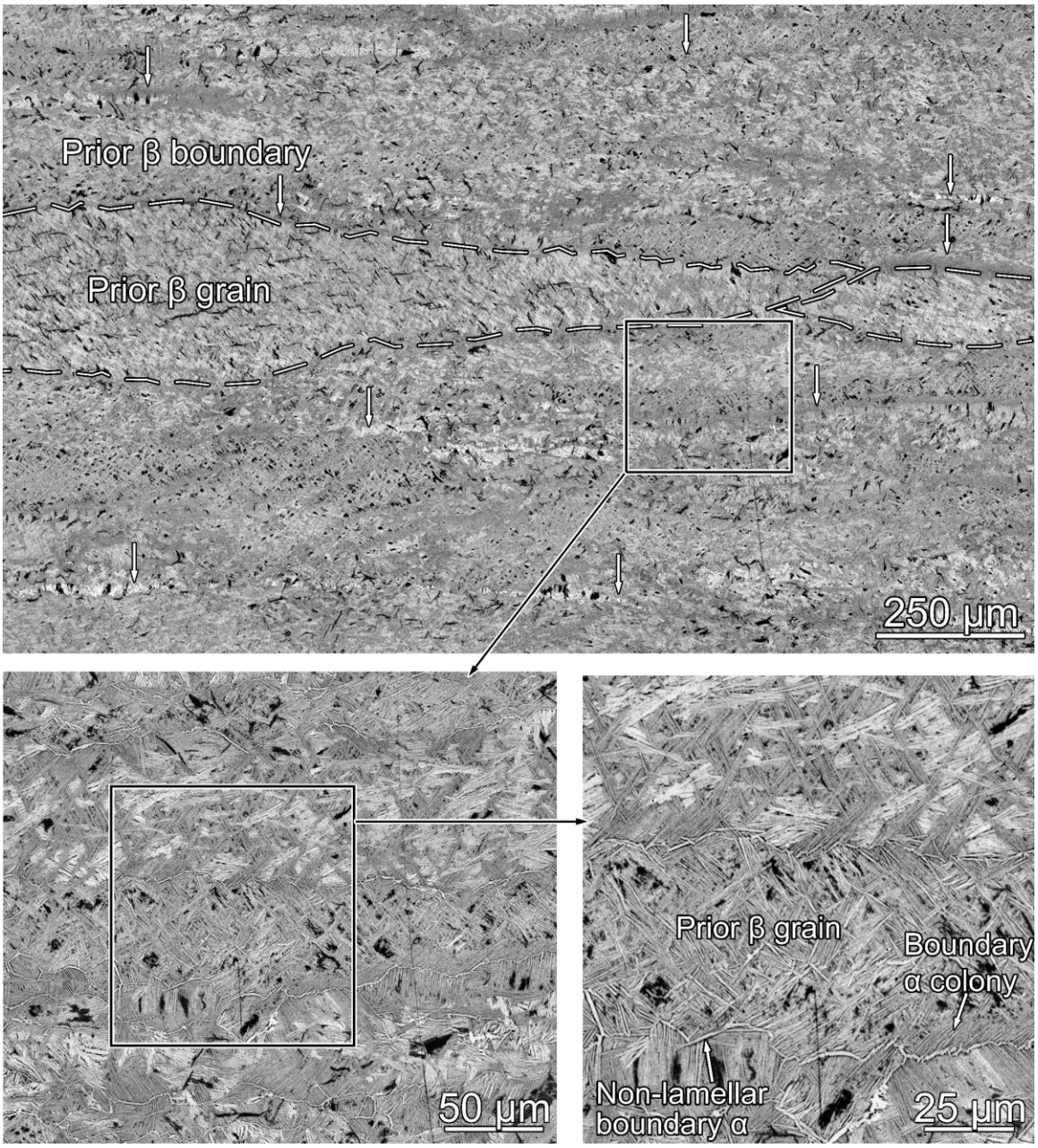

Figure 4.3. Backscatter SEM of pristine DT material viewed normal to processing axis. The processing direction is vertical; the impact was parallel to the processing direction.

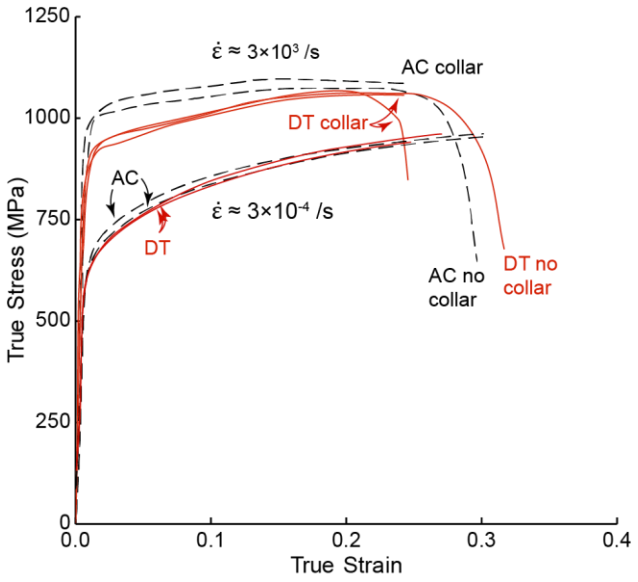

Figure 4.4. Stress/strain response of both AC and DT materials measured during QS and SHPB compression.

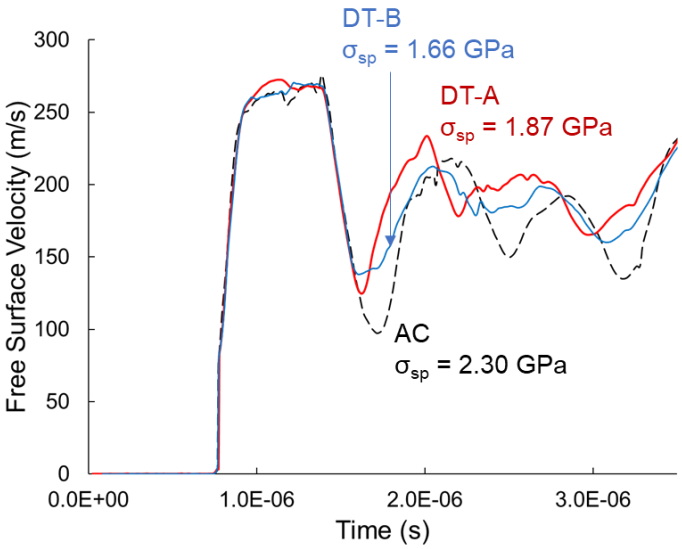

Figure 4.5. Free surface velocity profiles for impact loading of the AC and DT Zr-2.5wt% Nb samples.

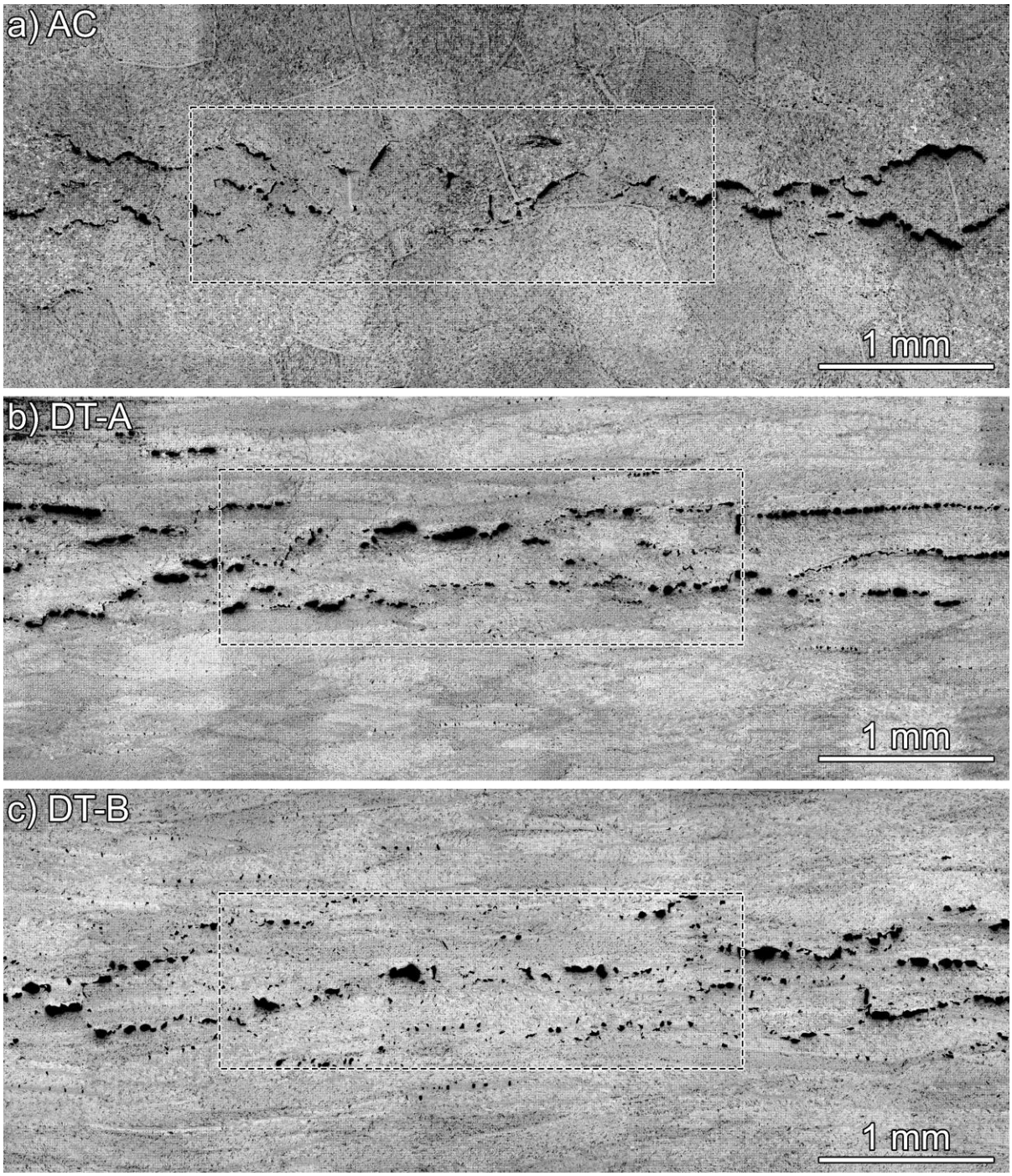

Figure 4.6. Cross-sections of the targets after flyer plate impact show incipient spall in all cases. For the AC material (a), damage and the largest voids are near the midplane; for the DT material (b, c) the damage is spread over several millimeters of the specimen thickness. The dotted boxes indicate the region used to quantify the damage.

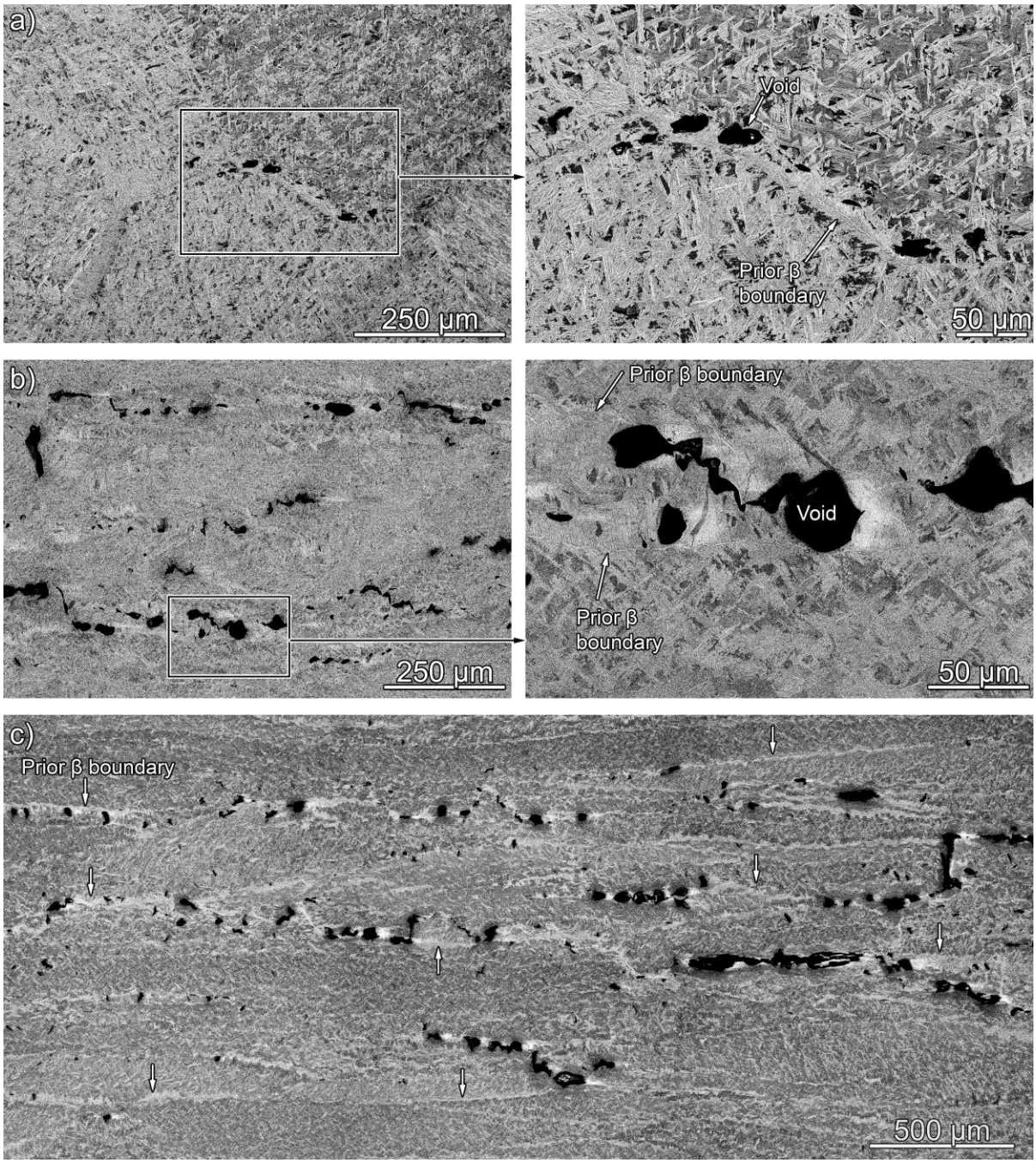

Figure 4.7. Voids frequently formed along prior β boundaries in both a) AC and b) DT materials. c) shows voids formed strings along boundaries in DT at a larger scale; prior β boundaries, lighter bands which are essentially horizontal in these images, are marked with arrows. All images taken in backscatter SEM mode; the impact direction and the DT processing direction are vertical in the image plane.

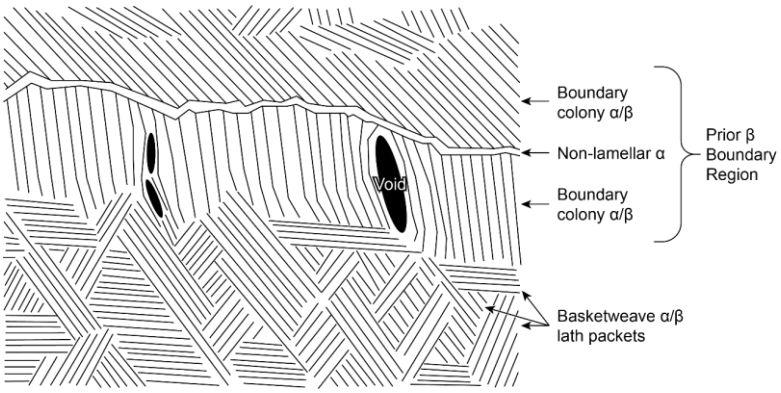

Figure 4.8. Schematic of locations of voids within prior β boundary regions.

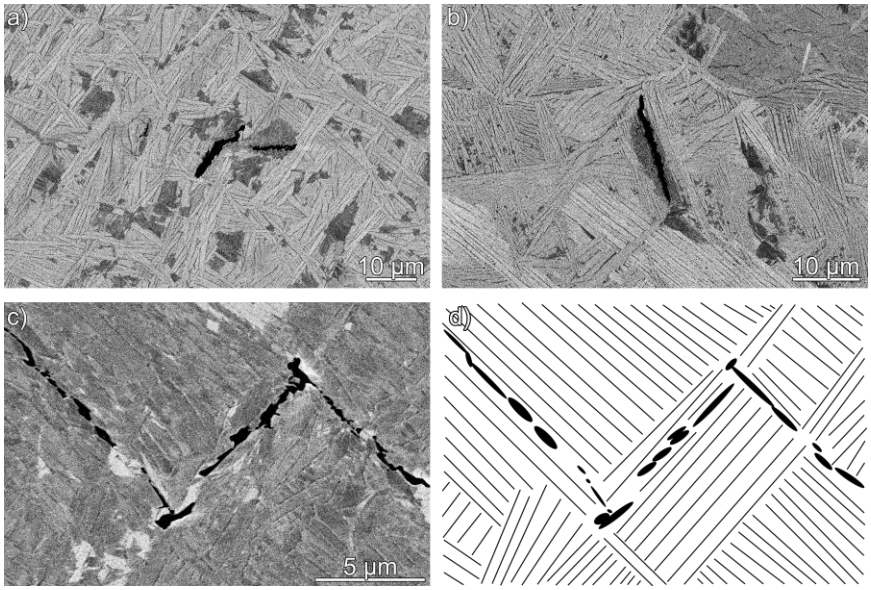

Figure 4.9. Voids away from prior β grain boundaries follow the orientations of surrounding lamellae. They often extend from or follow along boundaries between packets of lamellae with dissimilar orientations. This is found in all three samples, a) AC, b) DT-A, and c) DT-B. d) is a schematic illustration of c) where black lines represent β phase, white space is α, and black ellipses are voids. The impact direction is vertical in the image plane for all micrographs.

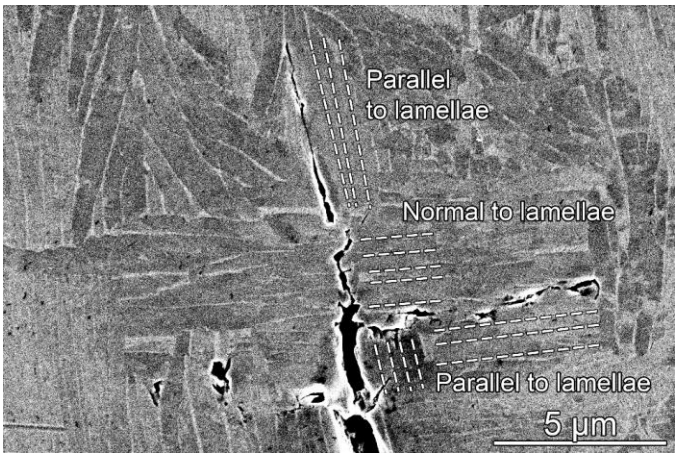

Figure 4.10. A void/crack that does not follow the orientations of the surrounding lamellae, here because it is apparently following the edges of lamellae that are not in the plane of the image.

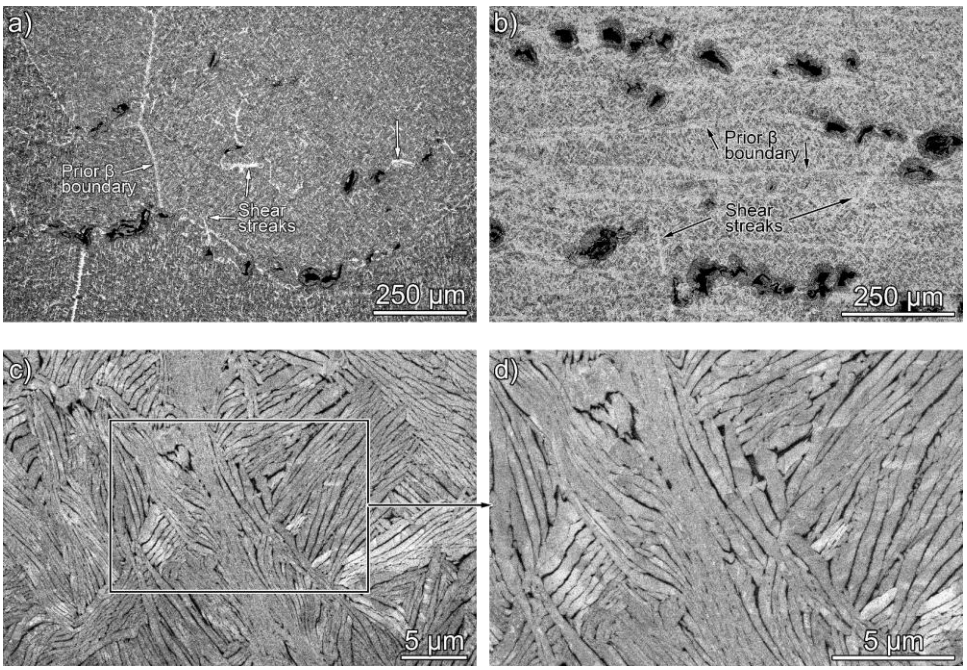

Figure 4.11. Paths of lighter material connecting large voids in a) AC and b) DT-B (backscatter SEM). At higher magnifications c and d) these paths appear to be regions of intense shear (TLD mode, secondary electrons). The impact direction is vertical in the image plane.

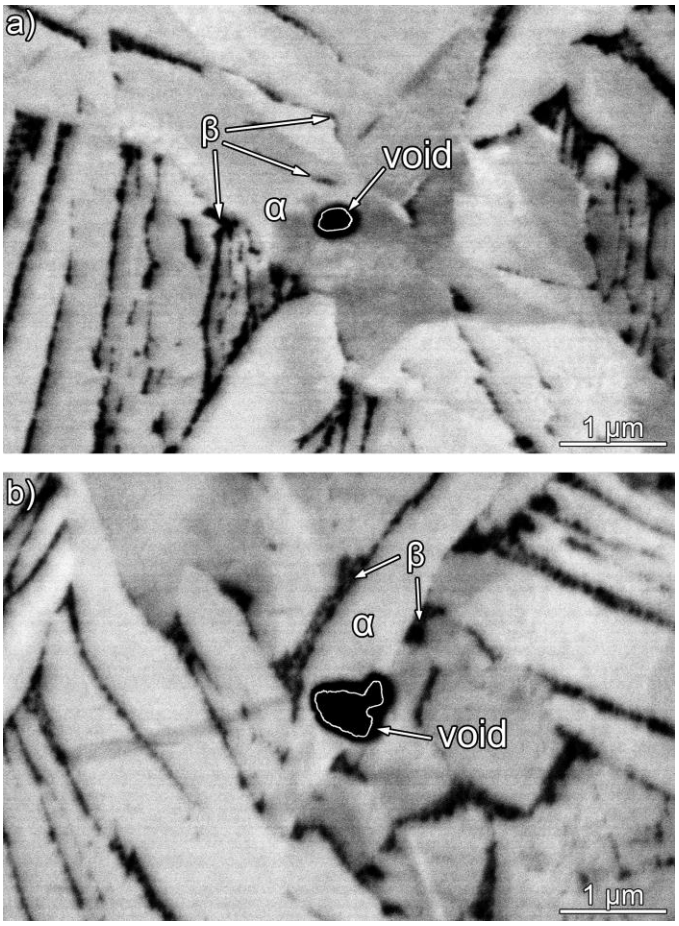

Figure 4.12. Backscatter SEM of small voids that appear to have nucleated a) within a single α lath and b) either within α or at an α/β interface. α phase is the thicker lighter laths; β is the thin dark layers separating α laths. The black regions of the voids are enlarged due to using backscatter mode, so the real edges are outlined based on secondary mode SEM images of the same locations.

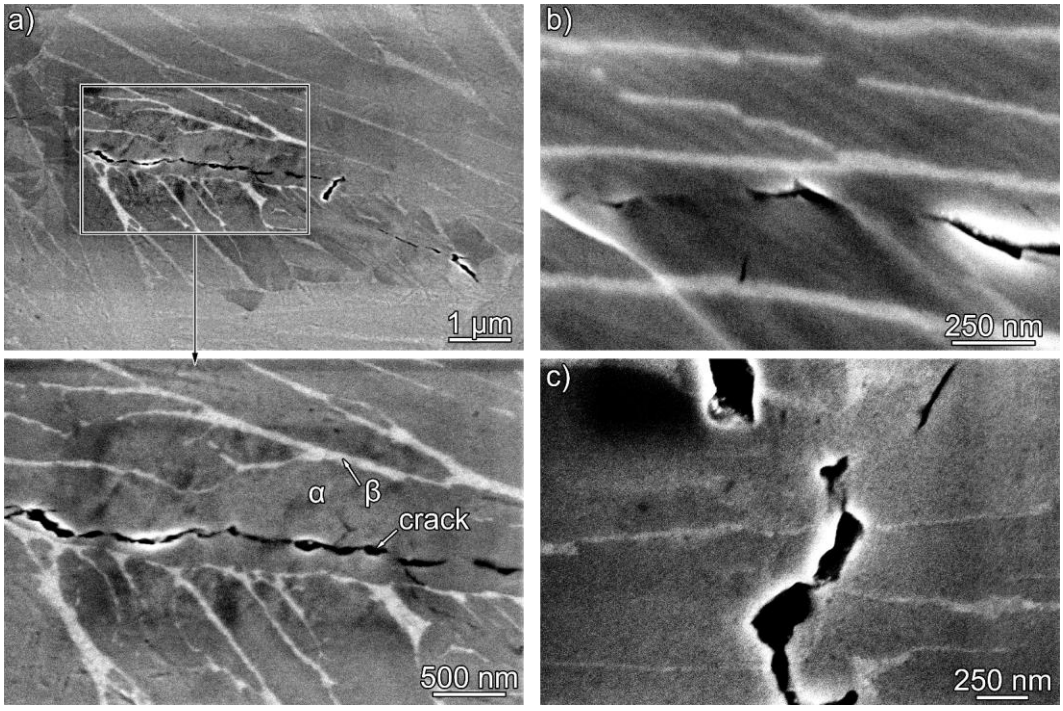

Figure 4.13. Secondary electron SEM images of small voids that may be shear-induced "tears" rather than voids nucleated due to imposed tensile stress. These cracks or tears can a), b) follow the phase boundary within a single α lath, or c) cut essentially perpendicular across the α/β interfaces and β phase. The impact direction is vertical in the image plane. These images were taken with a through-lens detector (TLD); phase contrast is due to differences in work functions.

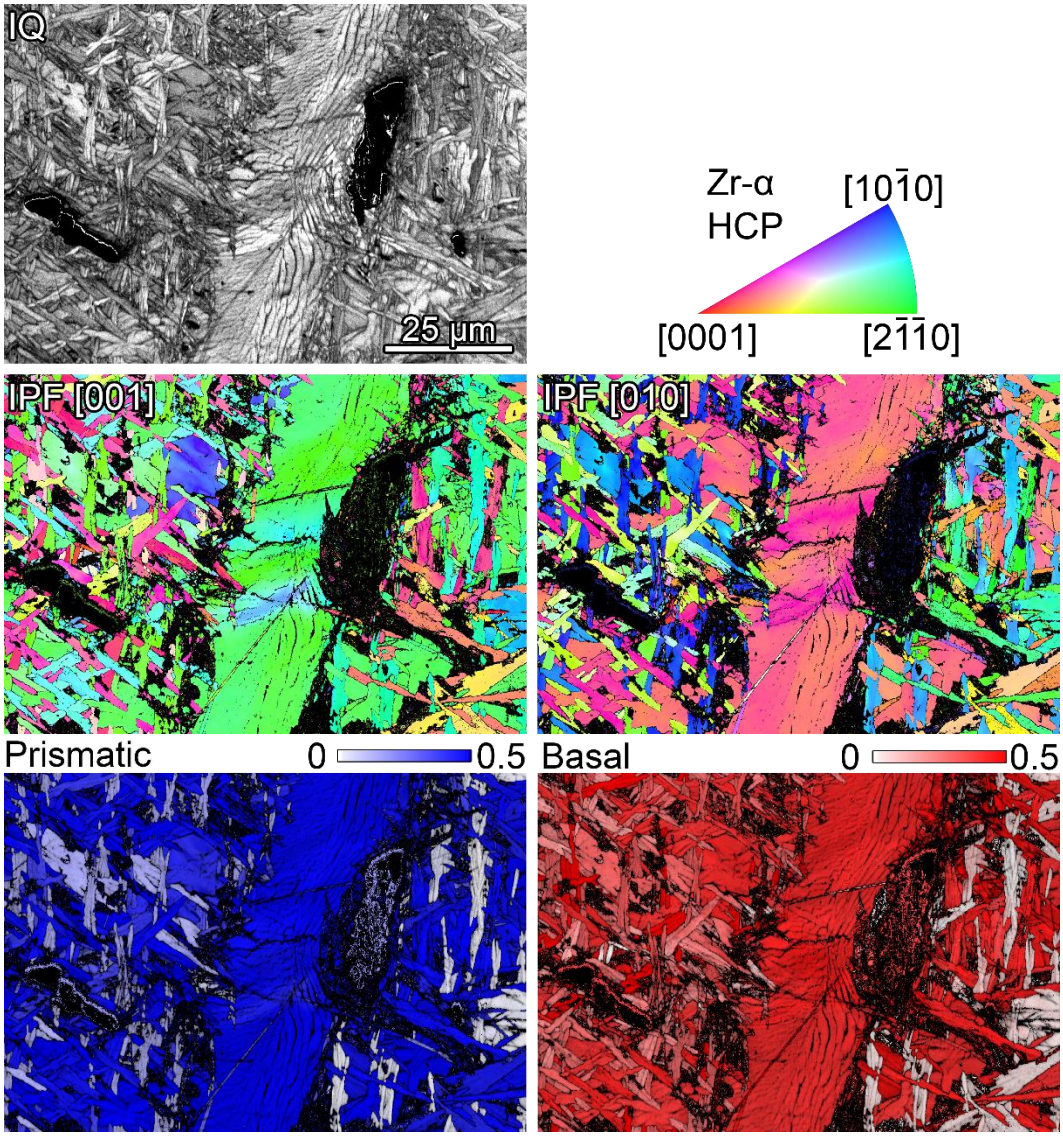

Figure 4.14. EBSD around 2 voids near a prior β boundary in the AC target. The boundary is vertical and central in the image; the impact direction was vertical. Top row: IQ map; second row: IPF maps for two directions, [001] (left) and [010] (right); bottom row: Schmid factor maps for Prismatic (left) and Basal (right) slip systems. The impact direction is vertical in the image plane.

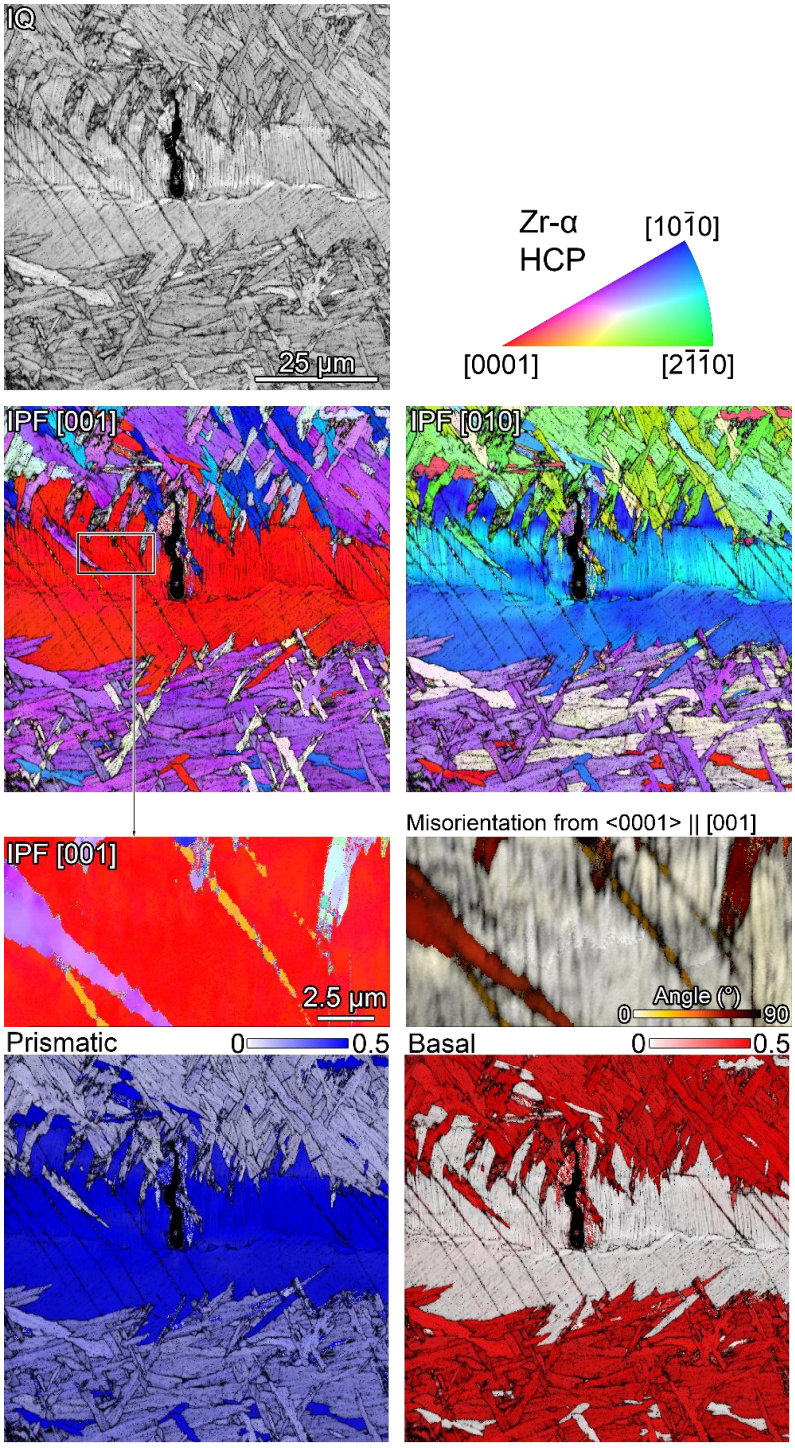

Figure 4.15. EBSD analysis around a void at a prior β boundary in the DT-B target. Top row to bottom: IQ, IPF maps for [001] and [010], higher mag [001] IPF and misorientation angle of apparent twins. The impact direction and DT processing direction are vertical in the image plane.

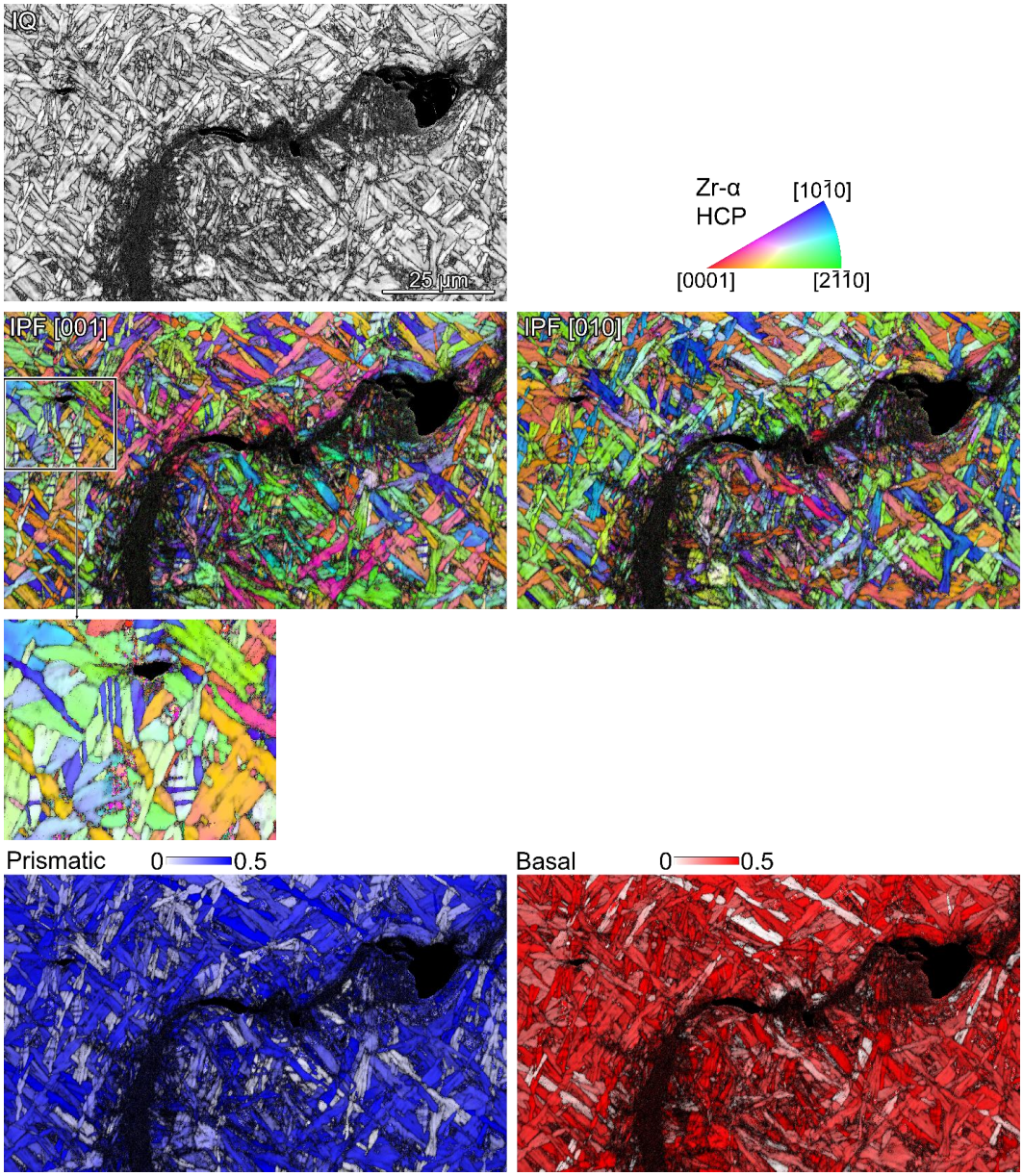

Figure 4.16. EBSD analysis of a shear feature in the AC target. The impact direction is vertical in the image plane. In the magnified region, twinning appears to have occurred in packets in center and slightly down and right of center. The impact direction is vertical in the image plane.

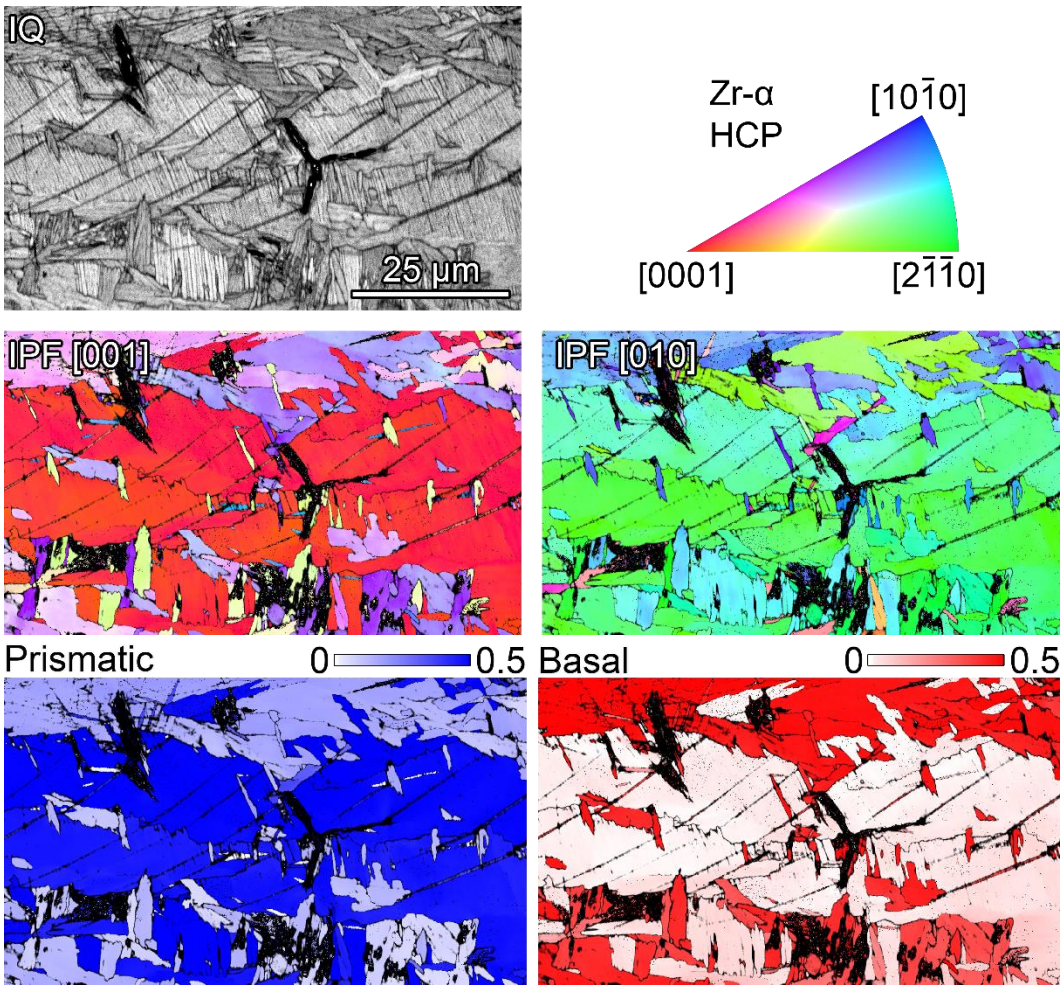

Figure 4.17. EBSD analysis around a void in the interior of a prior β in the DT-B target. From the top row to the bottom are: IQ (band contrast) map (and IPF reference), IPF maps for [001] and [010]; Schmid factor maps for Prismatic and Basal systems. The impact direction and DT processing direction are vertical in the image plane.

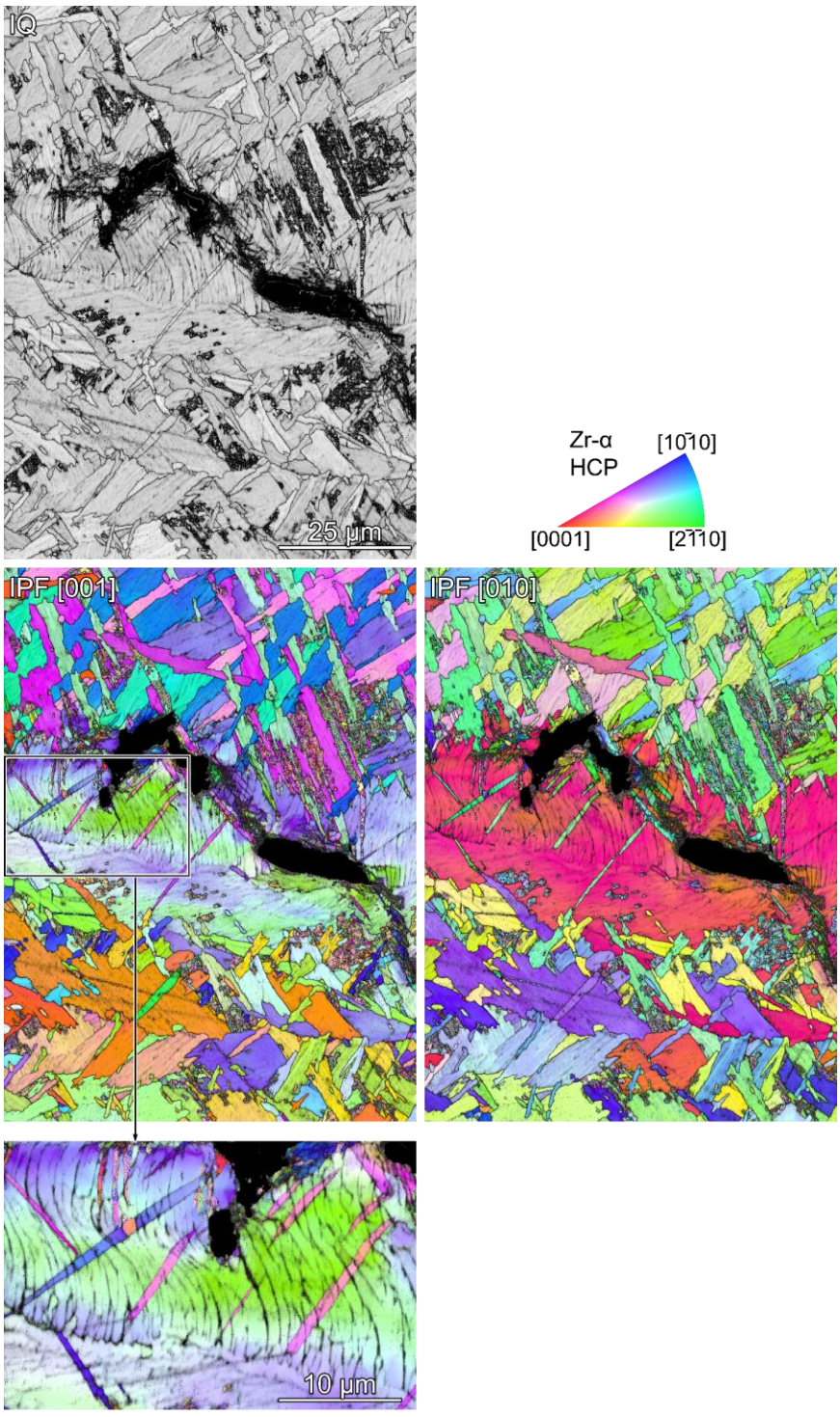

Figure 4.18. a) EBSD IQ (band contrast) and IPFs of a region in sample DT-B where the lamellae are distorted within the prior β grain boundary region. The impact direction and DT processing direction are vertical in the image plane.

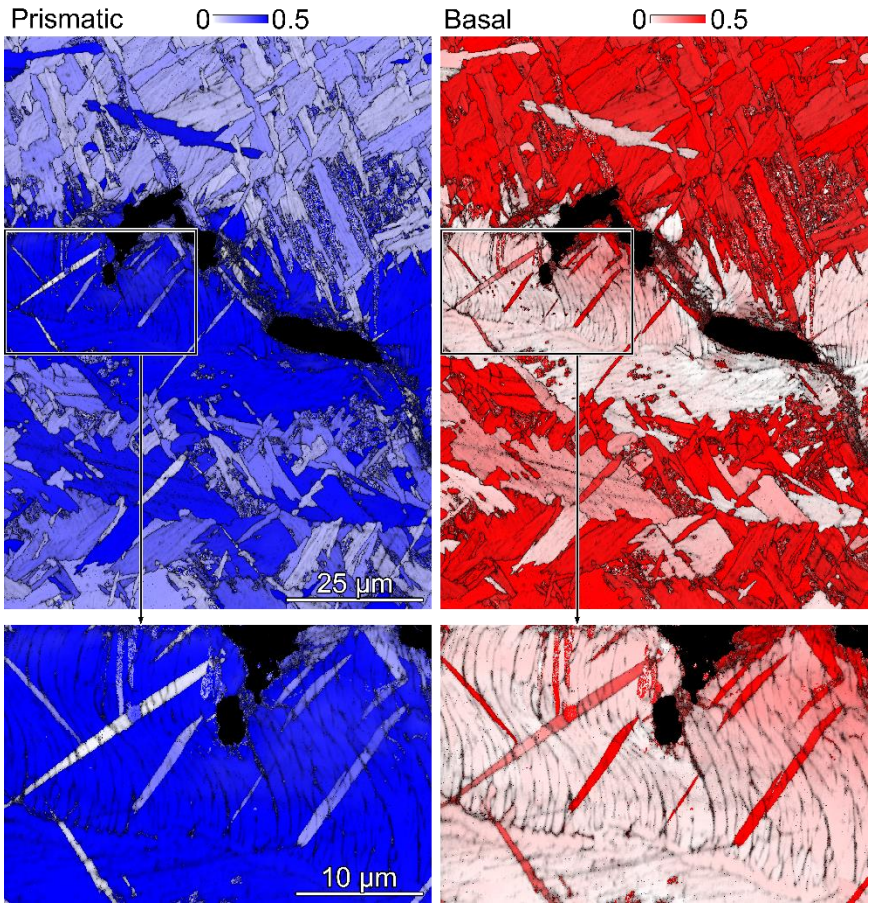

Figure 4.18. b) EBSD Schmid maps of a region in sample DT-B where the lamellae are distorted within the prior β grain boundary region. The impact direction and DT processing direction are vertical in the image plane.

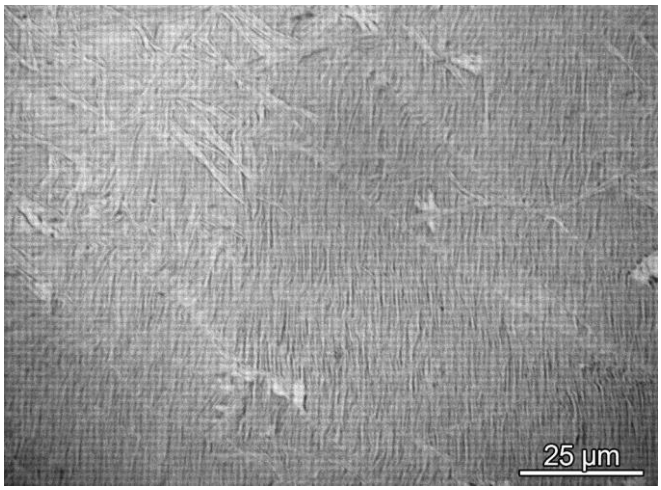

Figure 4.19. Optical micrograph of DT material compressed via SHPB normal to the processing direction (from other work on this same material) showing diagonal features qualitatively like those in flyer targets that were identified as twins.

Chapter 5

Effects of Constituent Properties on the Nature of Propagating Waves in Elastic Multiphase Composites

5.1 INTRODUCTION

When a load or deformation is applied to an object, the effects are often considered to be instantaneously spread to all parts such that the body immediately reaches a new equilibrium in response. In actuality, a finite time is required as the disturbance is transmitted throughout the body. Propagation of the disturbance occurs as material points force their neighbors to move from their initial position. In other words, the load is transmitted by mechanical waves[1–3]. The particular rate at which the waves propagate are dictated by the material properties of the medium[199,444,445], and the dynamic effects associated with wave motion are important when the times over which loading occurs is comparable to the time scale of the material response, generally on the order of 0.01 seconds and shorter. While changes to an applied load may be slow enough that equilibrium can be safely assumed, there are myriad other cases where travel times and response times are similar. For example, stress waves may need to be considered for evaluating effects of impacts which occur in systems as varied as projectiles and protection against them (both anthropological, e.g., bullets against armor, and natural, e.g., meteoroid impacts on orbiting satellites), planetary formation, and manufacturing/fabrication. They are also intentionally used non-destructively, such as for detection of damage in engineering components[199,446–448], measurement of material properties (e.g., elastic constants)[444,448,449], and during seismological study of planetary bodies[199,444,448,450,451].

The study of waves in solids extends, in some respects, back to the ancient Greeks with Pythagoras' interest in vibrations and music. Since roughly year 1700, work in this field has resulted in successful mathematical descriptions of wave motion in relatively simple systems, such as one-dimensional strings, infinite homogeneous bodies, and some semi-infinite arrangements[443–445,452]. Of greater practical interest is understanding wave motion in heterogeneous systems, such as finite bodies (requiring consideration of free surfaces) and multi-phase anisotropic media such as fiber-reinforced composites which have superior (quasi-static) mechanical performance over more conventional materials. Similarly, multilayers and laminates are finding use as structural components and their layers may have widely varying properties. Analysis of multilayers may also be generally applicable to models of the interior of the earth[199,446,450,451].

In all cases, wave motion is dictated by intrinsic material properties, specifically a stiffness, or resistance to deformation, and inertia, which opposes changes to motion[444,445]. Thus, when regions of disparate properties are in contact, wave character changes across the interface. The interaction of the wave with the interface itself also affects the waves in the body as various components are reflected, refracted, transmitted, and possibly experience mode conversion. Interactions with interfaces can lead to dispersion (change in pulse shape) and attenuation (decay in amplitude) that do not occur in simpler systems[445,447,448,451,452]. Surfaces and layers can also give rise to wave types other than the typical longitudinal and shear found in infinite bodies; the potential presence of Love, Lamb, and Stoneley waves[199,443,444,452] further complicates these problems.

The additional variables introduced when moving to inhomogeneous materials greatly complicate the subsequent analysis[445,447,448,453]. One approach is to replace the composite with

a homogeneous material having effective properties derived using the constituent properties and geometry of the problem[445,452,454–456]. These are primarily useful in the long-wavelength limit when wavelengths are very large relative to microstructural features[452,456]. However, not all composites of interest are adequately described by such approximations. In addition, homogenizing the medium precludes analysis of other aspects of wave propagation, such as dispersion due to internal interfaces and stress concentrations at internal interfaces which may be responsible for failure[445,454,456]. A considerable effort has been dedicated to solving problems where the individual constituents are kept separate. Full analytical solutions have been found for some, including propagation in various laminated spaces[446,451,454,456–460] and rods containing layers or various forms of anisotropy[461–463]. Two issues have been identified with respect to the existing work. One is that most prior studies have focused primarily on dispersion scattering and determining the phase velocity/frequency relationships; the stresses and displacements of interest for many structural applications have been relatively unexplored. In those instances where stress (or displacement or strain) is calculated, only a small number of points are examined[458,464–466]. Second, the exact solutions are typically so complicated as to preclude identifying the role of any individual material property or geometric parameter on calculated response. Parametric studies using numerical evaluation are necessary to draw any conclusions, and in some cases evaluation is preceded by making simplifying approximations such as infinitely long or short wavelengths or head of the pulse/far-field assumption[445,446,456–459,463,467].

The main goal of this work is to elucidate the effects of material properties, the associated dynamic properties of wave speed and impedance, and their mismatches on the nature of propagating (elastic) stress waves in multiphase composites. To this end, finite

element simulations are used to systematically explore density/modulus space in idealized systems of linear elastic phases. In section 2, a description of the FE model is presented. Simplified "single-fiber" cylindrical geometries are used to remove some of the confounding effects of the complex experimental microstructures. In sections 3 and 4, the stress states are evaluated with full-field distributions and stress/time plots for selected locations. Wave behavior is found to fall into 3 regimes depending on relative wave speeds of the two phases. Section 5 contains comparisons of results from FEA to simple mixture models to determine dynamic properties and a shear-lag type model to approximate shear stresses at interfaces.

5.2 METHODS

5.2.1 Physical model

The composite geometry comprises two coaxial cylinders with a single "fiber" phase embedded within an outer "matrix" phase. The fiber runs the entire length of the matrix. The length of the model, L = 10 m or 30 m, was chosen to prevent reflections from arriving at wavefronts during times of interest while maintaining a reasonable model size. The radii were varied to produce composites with a range of phase volume fractions. The fiber radius R_f is 0.5 or 1.5 m while the outer model radius R_m is 5, 2.5, or 2.1 m to achieve fiber fractions of v_f = 0.01, 0.09, 0.36, and 0.50. In the remainder of the article, dimensions are normalized by the model radius and indicated by an overtilde (~). Thus, normalized fiber radii are $\tilde{R}_f$ = 0.1, 0.3, 0.6, and 0.71, while normalized lengths $\tilde{L}$ are 2 and 6. In this manner, the fiber volume fraction v_f is calculated simply by $\tilde{R}_f^2$. Physical dimensions of the model combinations are given in Table 5.1.

5.2.2 Constituent properties

The primary goal of this work is to elucidate the effects of material properties, dynamic properties, and mismatches in properties between phases on stresses and stress wave propagation behavior. Among material properties, Young's modulus and density are most relevant for dynamic events as these dictate elastic wave speeds and acoustic impedances. The properties used for the matrix phase were fixed at E_m = 100 GPa and ρ_m = 10 g/cm^3. These values were chosen for their similarity to those of copper as this is a typical constituent in multiphase composites. The Young's modulus of the fiber phase is E_f = 50, 100, or 200 and the density is ρ_f = 5, 10, or 20 g/cm^3 (Figure 5.1). The Poisson's ratio, $\nu_f = \nu_m = 0.3$, is the same for both phases and constant across all composites. This value is similar to that of most metals. Subsequently, properties are normalized by the matrix values and are indicated by an overtilde. Thus, $\tilde{E}_f$ and $\tilde{\rho}_f$ take values of 0.5, 1, and 2, while fiber wave speeds ($\tilde{C}_f$) and impedances ($\tilde{Z}_f$) are calculated from these properties and equal 0.5, √2/2, 1, √2, and 2. These ratios of material properties and dynamic properties span much of the space which might be realistically attainable.

5.2.3 Finite element model

Simulations were conducted using the finite element (FE) software ABAQUS Explicit (version 6.14, Dassault Systemes, Velizy-Villacoublay, France) with an axisymmetric model having the half cross-section shown in Figure 5.2. The models are meshed with 4-node bilinear axisymmetric quadrilateral elements (CAX4R). The top surface is loaded by a compressive pressure which ramps linearly to σ_{app} = 500 MPa in compression over 0.1 ms (to reduce numerical artifacts) and then is held constant for an additional 3.5 or 10.5 ms for model lengths

10 m and 30 m, respectively. The hold durations are ~20% greater than the amount of time required for a wave traveling at the constrained wave speed of the matrix to traverse the entire length of the model. The loaded surface is free to move axially but is constrained to remain planar and perpendicular to the loading direction. The applied pressure is an average of across the entire surface. However, the constraint of uniform axial motion combined with dissimilar material properties leads to variation in the pressure applied to each element. The bottom of the model is constrained in the loading direction. The outer edge of the matrix is constrained to have no radial displacement. The model is therefore subject to uniaxial strain conditions. The fiber and matrix are strongly bonded at their interface; there are no constraints on motion at the interface except that both phases move together. All materials are linear elastic, homogeneous, and isotropic; strain, strain rate, and temperature effects are not considered.

5.2.4 Analysis methods

The FE results are evaluated qualitatively by the full-field spatial distributions of stress components, and quantitatively by extracting stresses along several lines of interest at select time steps. These lines are located (i) along the central axis; (ii) along the fiber/matrix interface; and (iii) either deep in the matrix to avoid influence by the fiber, interface, and outer boundary, or (if not possible) along the outer boundary. Data extraction points were identified by their initial (undeformed) coordinates. This ensured that the extraction line initially on the interface remains there even after deformation. When extracting data along the interface, averaging across the interface (i.e., combining data of both phases) was suppressed. The data output has minimum resolutions of 0.05 ms in time and 0.02 m in space. Wavefront positions were identified along an extraction line as that axial coordinate Y furthest from the loaded face at

which the axial stress is greater than a cutoff stress. The value of the cutoff stress is taken to be σ_{wf} = 100 MPa = σ_{app}/5. This is a compromise between various effects on the apparent wave speed in the composites. Instantaneous wave speeds were calculated by numerical differentiation of these axial positions with respect to time. Because these values can differ from the speeds calculated using the material properties, they are represented by S_i (for phase i) rather than C_i. The wavefront separation distance ΔY is the difference between wavefront positions at the same point in time.

5.2.5 Normalizations

The FE results are presented in non-dimensional terms, indicated again by overtildes. Stresses are normalized by the magnitude of the applied pressure (e.g., $\tilde{\sigma}_{yy} = \sigma_{yy} \,/\, |\sigma_{app}|$ and shear stress $\tilde{\tau}_{yy} = \tau_{ry} \,/\, |\sigma_{app}|$) and time by the time required for a longitudinal wave to traverse the radius of the model R_m ($\tilde{t} = t \times \frac{C_m}{R_m}$). Measured wave speeds are normalized by the constrained wave speed of the matrix phase determined by the material properties: $\tilde{S}_f = S_f/C_m$ and $\tilde{S}_m = S_m/C_m$. Wavefront positions are given in terms of model radius, Y / R_m. Wavefront separation, although also a distance, is normalized by *fiber* radius, $\Delta Y / R_f$.

5.3 RESULTS – Wave propagation

5.3.1 Full-field stress distributions

Stress distributions for all of the composite combinations and volume fractions are shown in Figures 5.3 – 5.6. These distributions are for "late" times; originally, these were thought to be representative of a steady state of sorts. However, it was found that there is an early "transient stage" which persists until and, in some instances, beyond the time increments

of these snapshots. The transient stage is an initial time during which the stress distributions change in a non-repetitive manner and ultimately end in favor of a true "steady state" wherein the stress distributions are comparatively regular although not completely static in time or space. The transient stage is of less interest since the expectation is for this to persist for an insignificant portion of the time a wave is propagating. An examination of the stress distributions reveals there are three domains in which behavior is similar (in both the transient and steady-state regimes). These domains are determined by the relative fiber wave speed with divisions of $\tilde{C}_f > 1$, $\tilde{C}_f = 1$, and $\tilde{C}_f < 1$. The transient stage persists for the entire simulated time for $\tilde{C}_f < 1$ and $v_f \leq 0.09$ and therefore the images here are for that period.

First consider the domain of $\tilde{C}_f > 1$. In both phases the axial stress rises over a distance that increases with phase modulus. There is a curved section of wavefront in the matrix extending radially outward from the interface starting at the wavefront of the fiber. The axial breadth increases with ΔC and E_f; at the higher fiber fractions it spans the matrix jacket and there appears flat but with an axial offset from the fiber wavefront. Thus, the axial stress wavefront has a non-planar shape despite a planar incident front and has "separated", with the portion in the fiber farther along the axis than the portion in the matrix. The ratio of their travel distances is less than the ratio of the wave speeds of the phases for all cases. The separation distances increase with $\tilde{C}_f$ and decrease with fiber fraction. The shear stress distributions show a large concentration that travels with the axial wavefront. The farthest forward point is on the interface and aligns with the axial stress rise in the fiber. At low fiber fractions the widest point is adjacent to the wavefront in the matrix while at higher v_f it is somewhat behind this. The width and length therefore depend on C_f, ΔC, and v_f. The radial stress distributions have relatively few features at the wavefront, but the front is noticeably non-planar despite the

imposed boundary conditions. Behind the wavefront, all stress components have an average value that depends on E_f in the axial and radial components (and is 0 MPa for shear stress). All also show fluctuating narrow bands of high or low stress that are inclined and propagate at constant angles relative to the incident wave direction. The angle depends on C_f and stress component; their magnitudes decrease with distance behind the wavefront. (Note that images are without deformation, so the angles do not exactly match the "real" orientations in the deformed material.) The shear stress also has periodic concentrations evident at the fiber/matrix interface, at the outer boundary, and near the fiber axis; their magnitude increases with E_f and ΔC and their frequency increases with v_f.

The second domain has $\tilde{C}_f = 1$. For all sets of fiber properties and volume fractions the axial stress wavefronts are essentially planar. The wavefront has finite width that is narrower than for the other $\tilde{C}_f$ domains and unaffected by fiber properties or volume fraction. For systems where the fiber is not identical to the matrix, there is separation of the wavefronts but the distance is essentially negligible compared to the separation for the other $\tilde{C}_f$ domains. There is no discernible shear stress concentration at the axial stress wavefront. Within the wake there are stress fluctuations that form and propagate as inclined streaks. Fluctuations occur for all stress components, including shear. Their spacing is regular and the angle depends on stress component but not fiber properties.

The final domain comprises composites with $\tilde{C}_f < 1$. For the late-time images included here, there is a transition in distribution: the domain of $v_f \leq 0.09$ being distinct from that of $v_f \geq 0.36$. However, at earlier times the higher fiber fractions show distributions like those pictured for the lower fractions; this is the change from "transient" to "steady-state". For $v_f \leq 0.09$, the wavefront is narrow in both phases regardless of fiber properties, nearly as narrow

as in the $\tilde{C}_f$ = 1 domain. The front in the matrix is largely planar and normal to the incident direction except a small, curved portion adjacent to the fiber/matrix interface. In contrast, the wavefront inside the fiber is straight but at a well-defined angle relative to the incident direction. In the full 3D geometry (recalling that the model is axisymmetric), this would form a cone within the fiber with the base parallel to the matrix wave front. The angle is constant with fiber fraction but varies with C_f. [At earlier times the angled front propagates inward and obscures the planar front that results from the imposed pressure. At these late times, no indications of that flat front in the fiber remains.] The "height" of the cone in the axial direction is similarly constant with v_f and increases with ΔC. In the shear distribution, there is a large zone of elevated stress but the shape is unlike that of the $\tilde{C}_f > 1$ domain. It begins at the interface but is most concentrated within the fiber. The portion in the fiber follows the inclined axial stress wavefront to the fiber axis and then falls to nothing along a line with the opposite angle that extends from the axis back out to the interface. Radial stresses are non-uniform near the wavefront and also have an angled wavefront in the fiber. The magnitude of the radial stresses near the front increase with ΔC and E_f. Throughout the wake there are large concentrations, especially in the shear stress, as well as fluctuations forming diagonal traces in all stress distributions.

The late-time behavior for the higher fiber fractions of $\tilde{C}_f < 1$ is more similar to the $\tilde{C}_f > 1$ domain. The axial stress wavefront in both phases has a substantial finite width that varies with phase modulus and ΔC, and there is an offset between the wavefronts with the matrix wave ahead of the fiber. The offset increases with ΔC and differs in the high-ρ and low-E systems, despite those systems having the same C_f. The wavefront is tilted in both phases but is less straight and at a smaller angle than the front in the fibers at low v_fs. The shear stress

distributions contain a large concentration which is centered on the interface, like the $\tilde{C}_f > 1$ domain rather than the low v_fs in the current domain. The concentration begins at the farthest forward point of the axial stress wavefront of the matrix and is widest next to the wavefront of the fiber, i.e., the same as in the $\tilde{C}_f > 1$ domain but with the phases reversed. The spatial extent of the concentration increases with ΔC and E_f. The radial stresses are roughly planar rather than the angled front found at lower fiber fractions. As with all of the other cases, all stress components show inclined traces of fluctuations throughout the wake.

5.3.2 Stress profiles

Line profiles of all stress components at several time increments are shown in Figures 5.7 – 10 for $v_f = 0.01$, 0.09, 0.36, and 0.50 respectively. For axial and radial stresses, the solid line is the stress of the matrix and the dashed line is the stress along the center axis of the fiber. Shear stress is taken from the fiber/matrix interface. The blue dashed lines mark the stress and position corresponding to the axial stress in the matrix attaining half of the average stress far in the wake behind the wave front. Each $\tilde{C}_f$ domain (> 1, = 1, < 1) exhibits a distinct set of profiles, with a transition occurring for $\tilde{C}_f < 1$ between $v_f = 0.09$ and $v_f = 0.36$.

Axial Stress

Both phases of all composites show a main wavefront with a wake containing fluctuations around an average stress, matching the observations from the full-field distributions. (“Composites” excludes the system where the fiber and matrix have identical

properties since this is effectively single-phase.) The magnitude of the fluctuations increases with fiber fraction. The average stress behind the wavefront in both phases is dictated primarily by the Young's modulus of the phase, increasing with E. There is also a dependence on fiber fraction in a manner that varies with fiber modulus; with increasing v_f the magnitude of the average stress in both phases decreases, does not change, or increases, for $\tilde{E}_f > 1$, $= 1$, and < 1, respectively. The ratio of average stresses in the two phases is constant, independent of vf, but is **not** equal to the ratio of the elastic moduli of the phases except in the limiting case in which $\tilde{E}_f = 1$ (Figure 5.11). Density, impedance, and their mismatches do not appear to affect the average stresses or the trend.

When $\tilde{C}_f > 1$, the wavefronts in both phases are wider than those obtained when $\tilde{C}_f = 1$. Most of the spreading occurs in the low-magnitude and high-magnitude stress components. The wavefront width within the fiber increases from ~1 R_m at $v_f = 0.01$ to ~7 R_m at $v_f = 0.50$. In the matrix it increases from nil when $v_f = 0.01$ to nearly as much as in the fiber when $v_f = 0.50$. For both phases the fronts are wider for higher ΔC and higher E. Separation between wavefronts is evident and increases with ΔC and E_f while decreasing by roughly half between $v_f = 0.01$ and 0.50. The separations become (on average) constant in time beyond an initial transition period (Figure 5.12). At the top of the wavefront, the stress overshoots the average stress behind the front (except when $v_f = 0.01$). The magnitude of the overshoot generally increases with v_f but can be obscured by simultaneous arrival of a fluctuation in the opposite direction.

When $\tilde{C}_f = 1$, the wavefronts are always steep with some widening over time due to dispersion (albeit miniscule in the plot scale). The fiber and matrix profiles are practically coincident until the stress in the matrix peaks. They are free of fluctuations at all v_fs to that

point as well. Simultaneous with the peak in matrix stress, the rate of stress rise in the fiber sharply falls before either continuing to increase or sharply decreasing. The former occurs when $\tilde{E}_f > 1$ and the latter when $\tilde{E}_f < 1$. Fluctuations occur throughout the wake in both phases and are similar in magnitude and frequency to those obtained when $\tilde{C}_f > 1$.

When $\tilde{C}_f < 1$, the shapes of the curves differ notably for low v_f (≤0.09) and high v_f (≥0.36). This matches the preceding comments regarding the transition and steady-state stages for the lower fiber fractions and indicates a fundamental difference in the nature of the wavefronts during those time periods. At low v_f, the wavefronts in both phases are steep and monotonic with widths similar to those for $\tilde{C}_f = 1$. Immediately after this peak, the stress in both phases drops to a local minimum before rising to a new (highest) peak. The distance associated with this second rise segment increases with ΔC and scales with R_f. Although not visible in the still images described above, this appears due to two circular waves that originate at the fiber/matrix interface: one from the matrix side which causes the decrease while the other from the fiber side causes the subsequent peak. At the higher fiber fractions, the stress profiles more closely resemble those for $\tilde{C}_f > 1$ in that the wavefronts are wide and have shallower slopes. The widths of the fronts are similar in both phases and those widths increase with $\tilde{C}_f$ and possibly density but decrease from $v_f = 0.36$ to 0.50. For all fiber fractions there is wavefront separation which increases with ΔE and ΔC. The separation for $v_f = 0.01$ and 0.09 is identical (when normalized by fiber radius) but then decreases as v_f is further increased. Likewise, separation only increases with E_f for the larger fiber fractions. The wake is comprised essentially only of the fluctuations common to all of the composite systems. As in the other systems, the stress at the top of the front overshoots the later average stress level.

Shear Stress

Shear stresses occur for all composites, even when the wavespeeds are matched. Magnitudes of the first peaks generally increase with the ratio of the faster wave speed to the slower (C_{fast}/C_{slow}) but not strictly with ΔC or C_f/C_m (Figure 5.13). Other factors also contribute such that composites with the same wave speed ratio can have different peak stresses. For example, at each v_f the stresses for $\tilde{C}_f$ = 1.41 consistently differ by ~10%. Meanwhile for composites with $\tilde{C}_f \neq 1$, the magnitude of the peak shear stress for each composite increases by ~5% from $v_f = 0.01$ to $v_f = 0.09$, but then decreases as v_f rises further; at $v_f = 0.50$, the greatest peak is roughly half the magnitude of that at $v_f = 0.09$.

The first domain, $\tilde{C}_f > 1$, exhibits a prominent leading peak that is sharp at low v_f and spreads with increasing v_f. Behind this, additional concentrations have magnitudes that decrease with distance behind the leading concentration. The largest of these trailing peaks increase from essentially nil at $v_f = 0.01$ to ~$0.1\sigma_{app}$ at $v_f = 0.50$, nearly as large as the leading peak. Noting again, though, that the leading peak decreases in magnitude with v_f so that largest trailing peaks are only half as large as at the smaller fiber volume fractions. In addition, for all cases the shear stress decreases to effectively nil at sufficiently large distances from the first concentration. The position of the first shear peak coincides with the location where the axial stress in the matrix phase reaches half of its wake average. For $v_f = 0.01$ and 0.09, the curvature leading up to the first peak appears exponential. At the higher fiber fractions, the overall shape appears broadly exponential but is disrupted by small-scale fluctuations.

In the second domain, $\tilde{C}_f$ = 1, the shear stress again exhibits a single leading concentration followed by fluctuations throughout the wake. The leading peaks are less than half the magnitude of the peaks in the other domains. Their magnitude does not change with

fiber fraction, but the trailing fluctuations increase with vf and ultimately exceed the first concentration by ~25-30%. The magnitudes are larger by a factor of 2 from low E_f + low ρ_f to high E_f + high ρ_f for $v_f \leq 0.09$ but are equal for $v_f \geq 0.36$; modulus, density, impedance, and their mismatches all change between those property combinations but are constant across fiber fractions. Unlike the case when $\tilde{C}_f > 1$, the midpoint of the axial stress lies just behind the start of the leading concentration rather than at the peak of the concentration. The peak instead appears simultaneous with the axial stress in the high-E phase, peaking during the initial rise. The leading edge of these concentration has a sharp rise, not an exponential shape.

In the domain of $\tilde{C}_f < 1$, the traces exhibit a distinct transition with v_f, as described in other sections. At $v_f \leq 0.09$, all traces show a large (negative) leading concentration followed by a series of fluctuations with large magnitudes but longer periods (lower frequencies) than fluctuations of other systems. Their magnitude increases by 50% as density increases from $\tilde{\rho}_f = 1$ to $\tilde{\rho}_f = 2$ and is constant between $v_f = 0.01$ to 0.09; their period is ~R_f+h regardless of fiber properties or fiber fraction. Like with $\tilde{C}_f = 1$, the start of the concentration, not the peak, corresponds to the matrix reaching half its average in the wake. The peak instead is near (but not coincident with) the wave in the fiber reaching half of its average stress. This is analogous to the peak location for $\tilde{C}_f > 1$ when the high-/low-C phases are reversed. The magnitude of the trailing fluctuations can be as large as the leading peak, $0.2\sigma_{app}$ or more. The leading portion of the profiles do not have an exponential shape. At the higher fiber fractions ($v_f \geq 0.36$), the line traces still show a leading concentration followed by large fluctuations, but also smaller, higher frequency fluctuations on top of this main trend. In some cases the shape of the leading concentration changes with time. For example, the curve corresponding to the earliest time (yellow line) has a non-exponential leading edge and rounded top, similar to the curves for

lower fiber fractions. However, at later times, the leading rise widens and becomes curved while the peak sharpens, ultimately appearing exponential. The relative location of the peak of the leading concentration evolves with the peak shape. While the concentration is rounded, the peak is near, but not concurrent with, the axial stress in the fiber reaching half its far-field average; when the peak is sharper and the decay exponential, the peak does align with the stress in the fiber reaching half its far-field average. In neither period is it aligned with the stress in the matrix reaching half its late average.

5.4 DISCUSSION OF STRESS DISTRIBUTIONS AND WAVE FEATURES FROM FEA

Connecting the observed stress distributions to wave propagation is most easily made by considering propagation according to Huygens' Principle: "Every point on a wavefront can be considered the source of a small secondary wavelet that travels outward in every forward direction with the velocity of the medium at that point. The wavefront at a later instant in time is found by drawing a tangent to the secondary wavelets"[468]. That is, for each time step, each point on the original front can be treated as a point source for a new wave. Thus, each new wave travels outward at the wave speed of the medium, forming many small spherical wavefronts when the medium is isotropic. Then the new wavefront at a specific time step is the tangent surface to the multitude of new, small wavefronts. As an example, every point on an initial spherical wavefront would produce a wavelet which would expand as a sphere from that point. All of these wavelet spheres would be the same size and overlap. The tangent surface to these forms the new wavefront which is also spherical but advanced forward from the original wavefront (Figure 5.14).

With the Huygens model in mind, the observations of the stress distributions described above are more easily explained. But rather than a single homogeneous material, the system of this work is a composite with different properties (especially wave speed) in the two phases. This gives rise to one of the most prominent features of the distributions: the wavefront separation for the case where $C_f \neq C_m$. Huygens wavelets originating from the planar portion of the wavefront far from the interface produce new planar wavefronts which travel at the wave speed of the phase in which it resides. And since the wave speeds differ and there has been no "communication" of the presence or constraint imposed by the other phase, the wavefronts advance through material as though in a single-phase material (at least, through material that is distant from the interface). Accordingly, the wavefronts grow progressively farther apart in the axial direction.

The portions of the wavefronts that are not parallel to the loaded face are also readily understood through the Huygens model as being due to waves induced in the low-*C* phase by the high-*C* phase. The neat, inclined fronts observed for $\widetilde{\boldsymbol{C}}_{\boldsymbol{f}} < 1$ at low fiber fractions are the clearest examples; nevertheless, the curved sections of wavefronts in other cases are also due to this effect (though with the addition of other waves and dispersive effects). Following the model, a point in the high-*C* phase produces a wavelet when the incident wave reaches it. If this point is away from the interface, the radial components of this wavelet are canceled by the radial components of wavelets from neighboring points, since all of those wavelets have the same wave speed. But a point near the interface has no neighbor in the low-*C* phase, so some components of the wavelet are not canceled and a wavelet propagates from the high-*C* phase into the low-*C* phase *ahead of* the incident wave in the low-*C* phase. Recall that the source of the wavelets is the incident wavefront in the high-*C* phase, and this is traveling axially. This

means that the leading point at which waves are being induced in the low-*C* phase by the high-*C* phase is moving axially. Combining this axial motion with the radial motion (the direction of the wavelets into the low-*C* phase) gives an angled wavefront in the low-*C* phase.

This type of "induced" wave formation and propagation is commonly used in geophysics to study the internal structure of the Earth through the measurement of so-called head waves[450,468,469]. A wave traveling along the interface between two seismic layers continually produces refracted waves in the top (slow) layer. This refracted wave is called the head wave (Figure 5.15). The head wave has a constant angle to the interface which is the critical refraction angle calculated with the relevant wave speeds of the phases used with Snell's Law[445,452,468]. The inclined wavefronts in the simulations here are thus simply head waves, and the inclination angle is therefore constant and specific to the wave speeds of the fiber and matrix. (The angle would also depend on the angle of the interface if it were not parallel to the incident wave's propagation direction.)

The wavelets induced in the slower phase are also responsible for the bands observed throughout the wake of many of the systems. The secondary wavefronts propagate across the model, reflecting and refracting at the fiber/matrix interface and the outer boundary. While not included in Figure 5.15, shear waves are also produced by an incident longitudinal wave as a requirement for continuity of local particle motion across the interface[445,468]. Thus, both normal and shear stresses occur in all of the composites. Although the direction of local motion at the tangent wavefronts is not aligned with the model axes, resolving the stresses into the coordinate system of the model leads to both axial and radial stress components. Only longitudinal wavelets are produced in the low-*C* phase due to the solutions to Snell's Law. The increase in amplitude of these streaks with $\widetilde{\boldsymbol{E}}_{\boldsymbol{f}}$ follows the general trend of increasing stress magnitudes

with modulus. The increase in magnitude with v_f may be due to decreasing volume in which the waves can disperse as well as increasing overlap with constructive interference.

The composites with $\widetilde{\boldsymbol{C}}_{\boldsymbol{f}} = 1$, with their essentially planar wavefront, do not appear to fit this picture of wave propagation. However, even though the wave speeds are equal, the moduli and impedances of the phases differ. As a result, the amplitudes of the wavelets differ and thus cancel incompletely, resulting in the diagonal streaks as the remainders propagate throughout the wake. Also, because the wave speeds are equal, longitudinal Huygens wavelets are produced in both phases; the angles are also equal even though the amplitudes differ. In contrast, the mismatched wave speeds for systems with $\widetilde{\boldsymbol{C}}_{\boldsymbol{f}} \neq 1$ always lead to no solution for the critical angle in one of the phases.

A final set of waves in these systems are release waves. These are analogous to those that arise at the outer surface of a free rod subject to longitudinal impact but unlike an isolated rod in vacuum or air, they are not generated at the outermost boundary, which is stationary here. Instead, they originate at the fiber/matrix interface which is free to displace in all directions. The non-zero properties of the matrix lead to deviations from release waves formed in isolated rods. For example, the magnitudes are reduced and shear release waves form in addition to longitudinal waves. For composites with $\tilde{C}_f > 1$, the release waves generated in the fiber also contribute to the transition segment upon transmitting across the interface. The release waves are difficult to distinguish in the later times but appear to contribute to the transition of the wavefront configuration, from ones like those when v_f is low and $\tilde{C}_f < 1$ to those obtained for all other composites in which $\tilde{C}_f \neq 1$.

Unlike the case of quasi-static iso-strain axial loading of a fiber composite, the axial stresses under dynamic loading are found to be dictated by more than the respective volume

fractions and elastic moduli of the constituents. In the former scenario, the stresses satisfy the relationships $\frac{\sigma_f}{\sigma_m} = \frac{E_f}{E_m}$ and $\sigma_c = \nu\sigma_f + \left(1 - \nu_f\right)\sigma_m$. In the current results for dynamic loading, composites with $E_f/E_m \neq 1$ do not follow these. In fact, the stress ratio is never equal to the modulus ratio and the stress magnitudes vary with fiber fraction. While the higher modulus phase (whether fiber or matrix) does bear a greater portion of the stress, the ratio of larger and smaller stresses $\sigma_{high}/\sigma_{low}$ is constant at 1.75 while the corresponding modulus ratio $E_{high}/E_{low} = 2$. The preceding relationships can be combined and rearranged to give the matrix stress expected in the quasi-static case $\frac{\sigma_m}{\sigma_c} = \left(\nu_f\left(\tilde{E}_f - 1\right) + 1\right)$, which further simplifies to $\frac{\sigma_m}{\sigma_c} = \frac{1}{1+\nu_f}$ and $\frac{\sigma_m}{\sigma_c} = \frac{1}{1-\nu_f/2}$ for $\tilde{E}_f$ = 2 and ½, respectively. Using the fiber fractions of the dynamic FEA models, the matrix stresses in quasi-static iso-strain loading are found to be lower (by 1% for $\nu_f = 0.01$ and rising to 11% for $\nu_f = 0.50$) than those found here for the dynamic FEA for $\tilde{E}_f$ = 2 (analogously, they are slightly higher for $\tilde{E}_f$ = ½). Thus, it appears that the phase with the higher modulus takes on a greater portion of the load than would occur at lower rate. One deviation from the assumptions of the quasi-static scenario is that during dynamic loading the stresses and strains are not uniform throughout the body even though the stress far from the wave front is relatively stable. The stress change with fiber fraction is in the same direction in both phases and the magnitudes are such that the volume weighted average stress always equals the applied stress, regardless of the combination of fiber fraction and moduli. At one limit the composite is almost entirely matrix (ν_f = 0.01) and the stress in the matrix is essentially the applied stress. The trend with increasing fiber fraction for both $\tilde{E}_f$ regimes is toward the opposite end such that once the entire composite is fiber the stress in the fiber will be the applied stress.

The small dispersion noted for the "single-phase" systems is attributed to the loading being ramped rather than sharply stepped and therefore occurs for all systems. Dispersion related to wave speed mismatch is an order of magnitude greater though. These plots also show that the separation distance depends on the stress magnitude used for identifying the wavefront. For example, at $\tilde{C}_f = 2$, a cutoff of $\sigma_{WF} = |\sigma_{app}/1000|$ would give much more separation than a cutoff of $\sigma_{WF} = |\sigma_{app}/5|$ (which was used here). However, due to dispersion at the wavefront, measuring with a low stress does not give a good indication of the locations at which stresses become significant. Modulus magnitude affects separation distance because it determines the peak magnitude of stress in the phase. Therefore, a phase with a higher E will have a steeper stress rise and therefore a wavefront which is slightly farther forward than one with a lower E. This is the cause of the small wavefront separation in composites with $C_f = C_m$. Either larger modulus ratio or smaller density ratio is also associated with greater separation distance – high E_f has greater separation than low ρ_f and low E_f has greater separation than high ρ_f while impedance is constant among high E_f and high ρ_f systems and low ρ_f and low E_f systems, respectively.

The small-scale fluctuations that occur for all stress components of all composites are almost certainly due to "secondary" waves traveling non-axially through the systems. Their magnitudes are smaller and diminish with time (or equivalently, with distance behind the front) because each reflection and refraction at the fiber/matrix interface decreases their stress amplitude. The fluctuations become more frequent for higher fiber fractions because the thinner matrix jacket allows more waves to interact with the fiber/matrix interface during the simulation time. Although these simulations used axisymmetric models with a fixed boundary,

waves reflected from the outer edge could be interpreted as waves emitted from other fibers in a full 3D array.

The stress overshoot that occurs near the top of the wavefronts initially appears like the typical Pochhammer-Chree dispersion effect. But upon further inspection it becomes apparent that this cannot be the case, since it is absent when the fiber and matrix properties are equivalent. In free rods, this effect is due to release waves from the outer – i.e., free – edge of the cylinder[199]. In the present simulations, that boundary is fixed and hence no release wave is initiated there. However, the fiber/matrix interface is mobile and generates waves analogous to release waves.

Large fluctuations are present in only one behavioral domain, characterized by $C_f < C_m$. They exist for all (observed) times for low fiber fractions and early times for higher fiber fractions. Because the leading wavefront occurs in the matrix, large waves are induced in the fiber ahead of the fiber wavefront and produce relatively large concentrations. This occurs at early times for all fiber fractions as the matrix wavefront jumps ahead of the fiber wavefront. If the fiber fraction is small, the wave in the matrix is never slowed by the fiber over the duration of the simulations; these waves are always generated and dominant, producing a "pseudo steady state". When the fiber fraction is sufficiently large, the wave in the matrix is sufficiently slowed that other waves dominate the behavior and a true steady state sets in.

Shear stresses arise whenever there is a mismatch in any of the material properties of the phases, even if the wave speeds of the phases are equal. The shapes of the stress profiles and their relation to the axial stress components indicate dissimilar sources of shearing. In cases where the peak of the shear concentration corresponds to attaining a stress in the lower-wave speed phase, the shear stresses arise primarily from the differences in axial stress (and

hence strain) between phases. In particular, the phase with the higher wave speed has deformed significantly while the adjacent material has not. Thus, the maximum shear stress increases with the ratio between the higher and lower wave speeds (*not* strictly fiber to matrix wave speed ratio, C_f/C_m), as shown in Figure 5.13. The fiber fraction affects the shear stress through its influence on axial stresses and wavefront positions, thereby contributing to the decrease in shear stresses with increasing fiber fraction. The shear strains near the wavefront for cases where $C_f = C_m$ are due to small differences in the axial wavefront locations and therefore small differences in the axial strains near the front. The shear stresses in the wake are due to secondary waves induced by reflection and refraction at the fiber/matrix interface and outer boundary, similar to the axial stress fluctuations. In all cases, a shear stress contribution could also be related to radial expansion and the gradient in displacement produced as the high-E phase expands into the low-E phase to balance radial stresses.

The exponential shape of the shear stresses for composites with $\tilde{C}_f \neq 1$ is explored further in Section 5.2. The flatter, non-exponential profile for composites with $\tilde{C}_f = 1$ may be due to the concentrations there being due to emitted secondary waves rather than an axial deformation mismatch. As evident in the full-field stress distributions, the greatest concentrations in this composite class occur within the fiber rather than at the interface. Since the measurement line for the plots in this section follows the fiber/matrix interface, it does not traverse the peak of the concentration.

In all systems with $\tilde{C}_f \neq 1$, the distance required for axial and shear stress to reach significant fractions of their peak magnitudes is greater when the axial motion is mediated by shear. The distance increases with fiber volume fraction from $v_f = 0.01$ to 0.09, then decreases as v_f continues to rise. In the cases where the shear profile is generally exponential (i.e., $\tilde{C}_f > 1$

and $\nu_f \geq 0.36$ for $\tilde{C}_f < 1$), the distance to reach half the peak shear stress increases from ~0.4 R_m to 1.2 R_m and then decreases to ~1.5 R_m (roughly 2 m to 6 m to ~4.4 m in unnormalized units). An implication is that disrupting the interface may prevent shear or axial stress from reaching unacceptable levels, though the geometric change to do so will also induce a stress concentration. Alternatively, reducing the fraction of one (or perhaps both) of the phases appears it could also reduce the maximum shear stress.

5.5 COMPOSITE MODELS

5.5.1 Dynamic composite properties

In the preceding discussion it was noted that the steady-state wavefront locations when $C_f \neq C_m$ do not match the ratio of the constituent wave speeds. In other words, the effective wave speed in at least one phase is different from the wave speed expected from the material properties of that phase. This is confirmed by determining the instantaneous propagation rates in the center of the fiber and the outside of the matrix (Figure 5.16). The substantial periodic oscillations in the instantaneous rate due to arrival of various reflected and refracted waves whose local material motion briefly modifies the incident wave and causes the wavefront at the measurement point to jump backward or forward (Figure 5.17). But even the "typical" rates often differ from the rate expected by the modulus and density of the phases. For example, when $\tilde{E}_f = 2$, $\rho_f = 1$ and $\nu_f = 0.36$, the rate of the initial transient is ~1.35C_m rather than the expected value of 1.41C_m. Accounting for the temporary drops brings the average rate down to 1.17C_m. Also note that the rate in both phases ultimately reaches the same value, essentially an "effective" wave speed for the composite which is not equal to the material wave speed of either constituent except when the constituent wave speeds are identical.

A practical interest is to predict effective dynamic properties of a composite during steady state, namely the composite wave speed and the composite acoustic impedance. This was done in the following way. For the FEA models, the impedance of each composite (Z_{cFEA}) was determined using

$$Z_{cFEA} = C_{ss} \cdot \rho_c \tag{5.1}$$

$$\rho_c = v_f \rho_f + (1 - v_f)\rho_m \tag{5.2}$$

where C_{ss} is the average measured wavefront speed in the steady state regime and ρ_c is the average density of the composite (calculated with a standard rule of mixtures). C_{ss} was determined by averaging the instantaneous wave speeds in the steady-state regime. For simulations lacking this regime, the transient stage was used instead. An additional set of simulations with a fiber fraction of $v_f = 0.25$ was also included. For comparison, the composite impedance is estimated using the volume fraction rule of mixtures (ROM) of each of the constituent properties via the equation

$$Z_{cROM} = (E_c \rho_c)^{0.5} = \left(\left(v_f E_f + \left(1 - v_f\right)E_m\right) \cdot \left(v_f \rho_f + (1 - vf)\rho_m\right)\right)^{0.5} \tag{5.3}$$

where E is Young's modulus, ρ is density, and the subscript indicates the phase. For uniaxial strain conditions E_i would typically be modified with a correction factor. However, that correction depends solely on the Poisson's ratio; here the Poisson's ratios of the fiber and the matrix are equal, so there is no need for correction factor. The steady-state composite wave speed was then calculated using

$$C_{ssROM} = Z_{cROM}/\rho_c \tag{5.4}$$

The predictions are subsequently normalized by the respective matrix values.

The predicted values are compared with those derived from the FEA simulations in Figure 5.18. The calculated impedances are within ~10% of the FEA values at all fiber volume

fractions. The largest deviations are for intermediate fiber fractions. The measured wave speeds appear unaffected by phase fraction at the lowest fiber fractions. This leads to large discrepancies between the measured and calculated values at the lowest fiber fractions. As the fiber fraction increases, the discrepancies between the measured and estimated values decrease. The large discrepancies at the lower fiber fractions are likely due to the fact that the wave speeds here never reach steady-state and thus results in the transient domain have been employed. Discrepancies at higher volume fractions are likely related to the bounds of the steady-state intervals over which data were collected. The inclusion or omission of sharp, large-magnitude changes in speed affects the average.

So, the dynamic properties of these multiphase composites are governed by an average of the material properties and phase fractions of the constituents. The steady-state wave speed can be predicted reasonably well from the composite impedance. In turn, the composite impedance can be found by using a volume-weighted average of the constituent properties. Note that in the models developed here the relationship between dynamic properties and fiber fraction is nonlinear, whereas a simple rule of mixtures of the dynamic properties of the constituent phases produces a linear dependence on fiber fraction.

5.5.2 On the Use of Shear Lag-Based Models

For all volume fractions and fiber properties there exists a regime in which the decay of shear stress ahead of its first peak occurs at an apparently exponential rate. These regimes correspond to the true steady state (described above in Section 5.4) and the exponential shape of the decay can be seen in the stress line traces Figures 5.7 – 5.10. An exponential decay shape matches that expected from an analytical model based on shear lag theory[470]. In this model, an axial load is applied to a central fiber that is surrounded by a coating and matrix with no

external load (Figure 5.19). The axial strains in the fiber are assumed to be uniform in-plane and vary only with depth. All phases are assumed to be purely elastic (though the analysis is valid for cases of plasticity or rupture and sliding in the coating) and in fact for comparison to the present FE results the coating is absent, i.e. thickness = 0. Shear stress arises due to the difference in axial strain between the fiber and the surrounding matrix.

The current dynamic FEA simulations appear to produce an analogous situation, with a difference in axial strain between the two phases. Unlike the problem setup of the analytical model, the difference in axial strain in the dynamic FEA is due not (solely) to the difference in moduli and location of loading, but rather to the difference in wave speeds between the phases. Because stress waves travel through the phases at different rates, the phase with higher wave speed undergoes axial straining at a time when the other phase is still unstressed/unstrained. As discussed in Section 4, the composite systems loaded dynamically reach a "steady state" in which the distance between the wavefronts in the two phases is relatively constant. As the wavefront moves through space, this situation might be thought of as a quasi-static state in a moving reference frame. Thus, the analytical model based on shear lag may be applicable. To determine if this is the case, shear stresses from the dynamic loading FEA are compared to those calculated with the aforementioned analytical model[470] and to those from FEA of quasi-static (QS) loading.

The model geometries used for the QS FEA are identical to those of the dynamic simulations. The differences are in the boundary conditions: pressure is applied only to the fiber surface (ramping to the same applied pressure σ_{app} = 500 MPa), the outer edge is free to move radially, and there is no constraint on the vertical motion of nodes of the top surface. (Note that the free outer boundary more closely matches the assumptions of the analytical

model than the conditions of the FEA.) The meshes and material descriptions are identical to those of the dynamic FEA. The analytical model requires a cutoff radius at which to end the integration. Here the radius of the FEA model is used, varying from 5 (meters) to 2.125 (meters) as fiber volume fraction increases from 0.01 to 0.50

For displaying the results, the same time increment of the dynamic FEA could not be used for all sets of fiber properties because the high Cf composites have reflections from the bottom of the model arriving (and hence altering the stress state) at "late" times, while the low Cf composites have not reached steady state at "early" times. The curves from the dynamic FEA are taken from the "true steady-state" regime for $v_f = 0.36$ and 0.50 but from the initial (and only) plateau for $v_f = 0.01$ and $v_f = 0.09$. Therefore, the times used are $t = 1.0$ ms for $v_f = 0.01$, 3.0 ms for $v_f = 0.09$, 3.0 ms for $v_f > 0.09$ and $C_f \geq C_m$ and 6.0 ms for $v_f > 0.09$ and $C_f < C_m$. The QS FEA predicts a peak in shear stress near the top of the fiber and the analytical model has a vertical asymptote at the same location, corresponding to a distance of 0 m in both cases. For comparison to the dynamic FEA, the vertical axes of these results are placed where the shear stress of the dynamic FEA result has fallen to 80% of the peak magnitude behind the peak. All fiber fractions for a given E_f/ρ_f combination are plotted together and offset along the stress axis. Because the load is applied to the fiber in the QS and analytical calculations, the sign of the predicted stress is always positive; the curves are inverted in cases where the dynamic FEA produces negative shear stress at the front (i.e., where the matrix has the higher wave speed and the load appears to be applied to the matrix).

In the domain in which $C_f > C_m$, the shapes of the wavefront profiles from the dynamic simulations generally resemble the stress distributions of the analytical and QS FEA (Figure 5.20). At the low fiber fractions ($v_f = 0.01$ and 0.09), the composites with high E_f and

high E_f + low ρ_f fibers have peak magnitudes, locations, and decay distances within a few percent across all calculation types. For the composite with low ρ_f the peaks of the dynamic FEA are half those of the non-dynamic despite this system having the same C_f (and hence same ΔC and C_f/C_m ratio) as the high E_f composite. At the higher fiber fractions (v_f = 0.36 and 0.50), disparities between dynamic and non-dynamic results as well as between the two non-dynamic models are greater. In particular, the shapes begin to differ as the dynamic results the curves gain small fluctuations ahead of and during the main peak. As a result, the peaks are flattened and broadened, and the portion ahead of the peak can be steepened and/or non-monotonic. At these fiber fractions, the dynamic FEA peak magnitudes of the two composites with stiff fibers are ~70% those of the QS FEA and less than 25% those of the analytical model while for the low ρ_f composite they are 50% and less than 20%. The decay distances remain similar across the models and fiber types though, including now for the low ρ_f fiber. Since the peak magnitudes vary, the decay rates are dissimilar between calculations though. At both low and high fiber fractions, the similarity between models qualitatively increases with wave speed mismatch.

In the domain of $C_f < C_m$ the comparisons are more varied. At the low fiber fractions the dynamic stress profiles are rounder and broader than the non-dynamic, with the decay ahead of the peak never being exponential. The peak magnitudes of the dynamic FEA are less than the QS and analytical values, by ~10% for high ρ_f alone, ~20% for high ρ_f + low E_f, and 50% for compliant alone. The decay from the peak for the dynamic FEA changes concavity but is faster on average and decreases to ~0 MPa in less than half the distance as the non-dynamic calculations. The shape difference also means the peak locations are offset, with the high ρ_f + low E_f composite having the greatest disparity at roughly half the decay distance of

the analytical model. At higher fiber fractions, the magnitudes in the dynamic FEA decrease and the differences in peak heights increase to a factor of 2 or more for all composites. However, the shape of the wavefront decay in the dynamic FEA more closely matches the exponential form, apart from occasional small local peaks like those in the $C_f > C_m$ domain. Decay distances for these fiber fractions are within 10% of those from the non-dynamic calculations.

When $C_f = C_m$, the dynamic FEA is not well-predicted by the analytical model or the QS FEA for any fiber fraction. The peak magnitudes from the dynamic FEA are ~20% of the other calculations, the decay distance is similarly shorter, and the decay shape is closer to linear than exponential.

5.5.3 Discussion of Composite Models

Similarity between the dynamic and non-dynamic models generally increases with ΔC, presumably because the stress gradients increase. Wave speed mismatch is not the sole determiner though; fiber fraction has a significant impact, with disparities increasing with v_f. This is likely due to the geometries at the higher fractions being inconsistent with assumptions of the non-dynamic models. For example, with a large fiber (thin matrix) the assumption that shear stress at the interface is only due to axial stress on the fiber may be invalid; numerous reflected waves overlap and contribute to the stress state. The extra "bumps" in the dynamic FEA stress profiles are evidence of this – for $\tilde{C}_f \neq 1$, the disruptions in the exponential shape ahead of the peak are due to superposed waves on top of the main incident wave. In addition, both $\tilde{C}_f \neq 1$ regimes have a pair of composite systems which differ in their deviation from the

dynamic FEA despite the fibers of each pair having the same C_f and hence same ΔC and C_f/C_m ratio. In the $\tilde{C}_f > 1$ regime, the disparity is greater for the low ρ_f than the high E_f system. In the $C_f < C_m$ regime, the disparity is greater for the low E_f than for the high ρ_f system. In both domains, the composite with the greater deviation is the one with lower density, modulus, and impedance of the pair. They also have the same Z_f and $Z_f < Z_m$. Considering the other trends, it is expected that E_f drives this, with higher E_f leading to higher stresses and axial stress gradients, and the primary discrepancy is the peak height rather than decay distance. There may be a confounding effect with Z_f, ρ_f, or their mismatches though.

The poor agreement between the analytical model and the dynamic FEA for $\tilde{C}_f < 1$ and low fiber fractions is likely because the stress state is inconsistent with that assumed by the shear lag model. For example, as can be seen in the full-field stress distributions, the axial stress in the fiber is not uniform within each transverse plane. Drawing on observations throughout the current work, the stress state in those systems has not reached the true steady-state condition which most closely matches the stress distribution expected for shear lag theory. Simulations conducted to later times should be able to reach that state (also requiring greater model lengths to prevent the waves from reflecting off the bottom surface).

The lack of similarity for cases in which $C_f = C_m$ is unsurprising as the wavefronts are offset only over a short distance and by a small amount due to the modulus mismatch; the material on both sides of the interface is highly stressed whereas the shear lag model assumes one side is stress-free for a large distance away from the interface.

5.6 CONCLUSIONS

The current study has simulated elastic wave propagation in two-phase coaxial cylindrical composites. The Young's modulus and density of the inner phase were varied and the effects on the evolving waves were assessed in terms of the full-field stress distributions and line traces at selected locations. The primary goals were to: (1) Describe how elastic stress waves propagate through multi-phase materials and (2) describe how those waves and the resulting stress distributions are affected by phase properties and mismatches. Relevant conclusions are:

- There are three domains of wave propagation behavior governed by the wave speed mismatch and characterized by: $\tilde{C}_f > 1$, $\tilde{C}_f = 1$, and $\tilde{C}_f < 1$. The first proceeds quickly into a high-shear stress mode related to differences in axial displacements, the second has little shear activity but can have significant axial stress concentrations, and the last has a significant early transient stage where the wavefront stress is dominated by the matrix phase.
- Shear stresses arise for any mismatch in phase properties, even when longitudinal wave speeds are equal. When wave speeds differ, shear is due to a disparity in axial straining. When wave speeds are matched, shear is due to secondary waves related to the mismatched axial stresses.
- Ratios of material properties, rather than absolute differences, dictate the nature of propagating stress waves.
- The effective dynamic properties of multiphase composites can be estimated from the material properties and phase fractions of the constituents using analytical composite models.

- The shear stress at the interface near the wavefront during the late-time, steady-state regime can be reasonably approximated using a shear lag-type model for composites with $C_f \neq C_m$ and low fiber volume fraction.
- Axial stress gradients in composites with constituents aligned with the propagation direction are reduced magnitude compared to monolithic materials. The gradients are reduced with increasing fiber fraction at least up to $v_f = 0.50$ and wave speed mismatch. Shear stresses are concomitantly increased.
- There is a shear transfer distance and width over which stresses accumulate.
- The shear stress concentration decreases in magnitude but increases in width with increasing fiber volume fraction.
- Release waves initiate in both phases at the fiber/matrix interface. These appear to be important for transitioning between the transient and steady states.

Acknowledgements

This work was supported by the Department of Energy, National Nuclear Security Administration under Award no. DE-NA0003857.

Table 1. Physical and normalized dimensions of the FEA models.

Fiber radius R_f	Model length L	Model radius R_m	Normalized fiber radius $\tilde{R}_f$	Normalized length $\tilde{L}$	Fiber volume fraction v_f
0.5	10	5	0.1	2	0.01
		5	0.3		0.09
1.5	30	2.5	0.6	6	0.36
		2.1	0.71		0.50

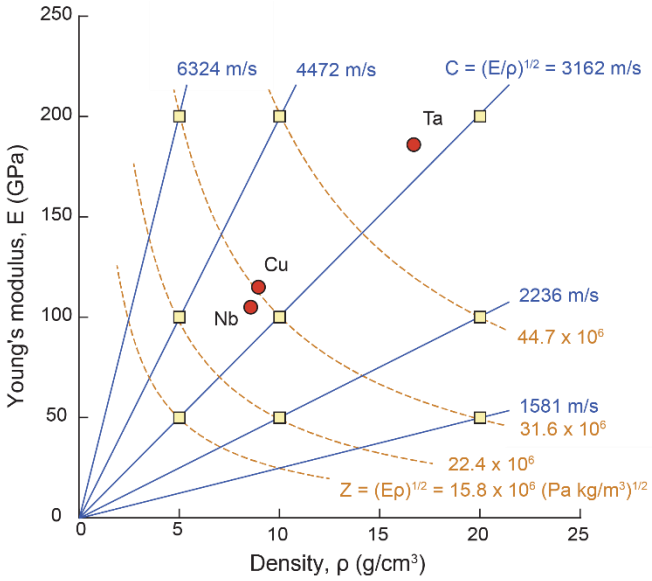

Figure 5.1. Material property space probed in this work. In all cases the matrix properties were taken as $E_m = 100$ GPa and $\rho_m = 10$ g/cm^3 while the fiber properties were assigned the combinations indicated by yellow squares. Poisson's ratio for both phases was fixed at 0.3.

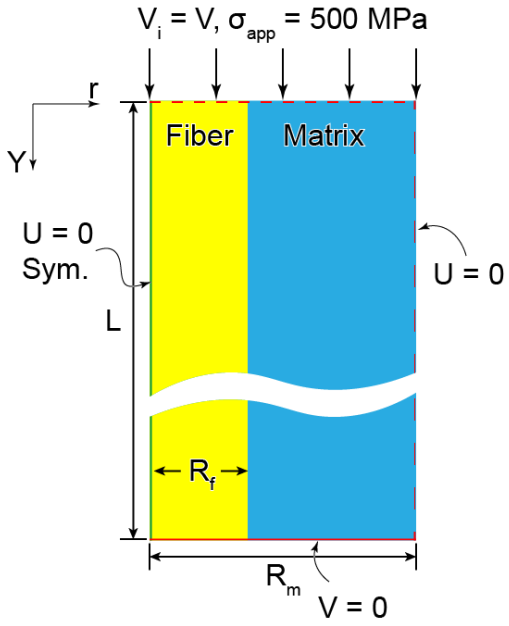

Figure 5.2. Schematic of the geometry simulated for this work. Unlabeled dimensions are given in Table 5.1.

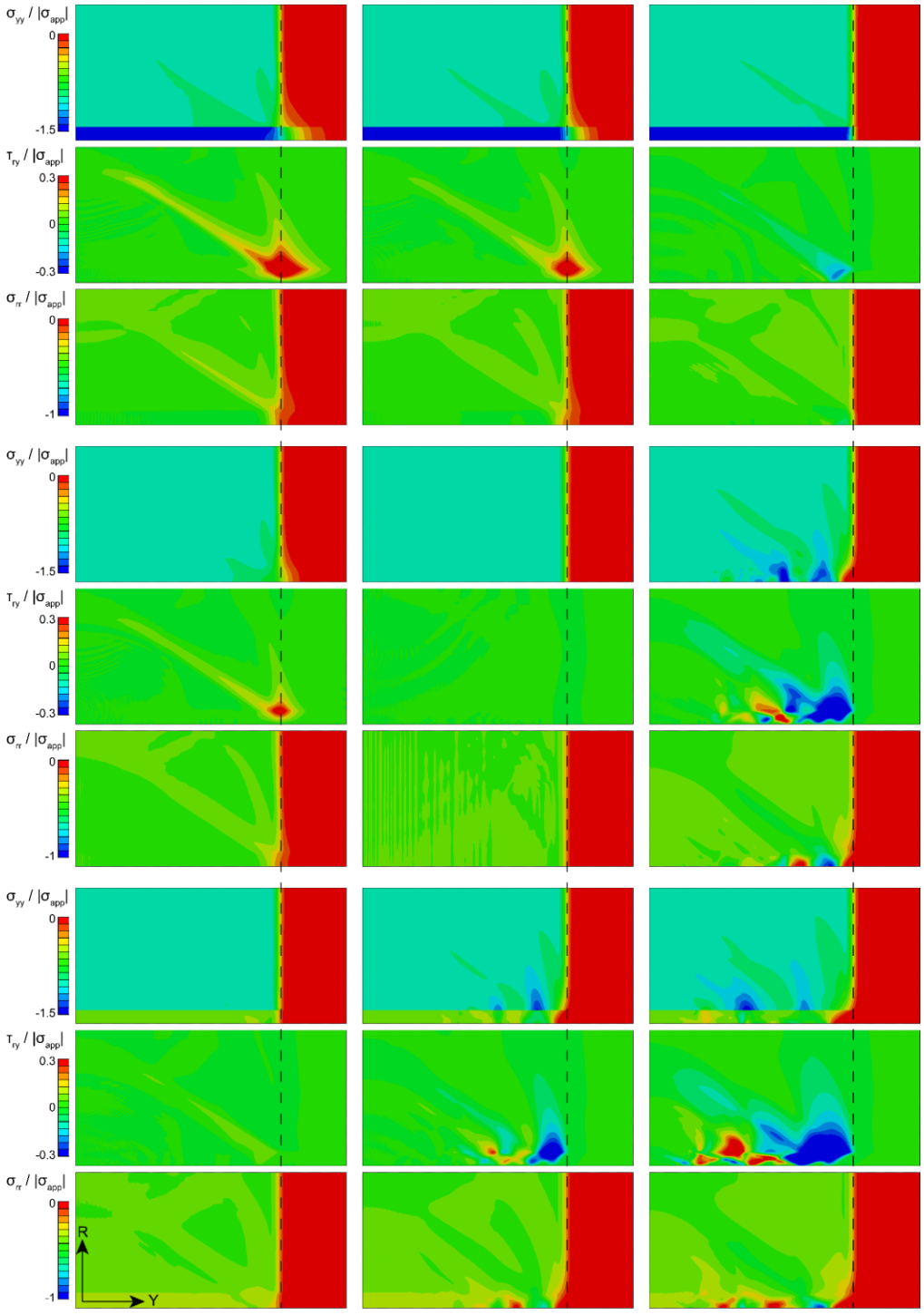

Figure 5.3. Full-field axial, shear, and radial stress distributions at a late time for composites with fiber fraction $v_f = 0.01$. The dashed line marks the approximate location of the incident wavefront in the matrix. For this volume fraction, only the systems with $\tilde{C}_f \geq 1$ are believed to have reached steady state at this time step.

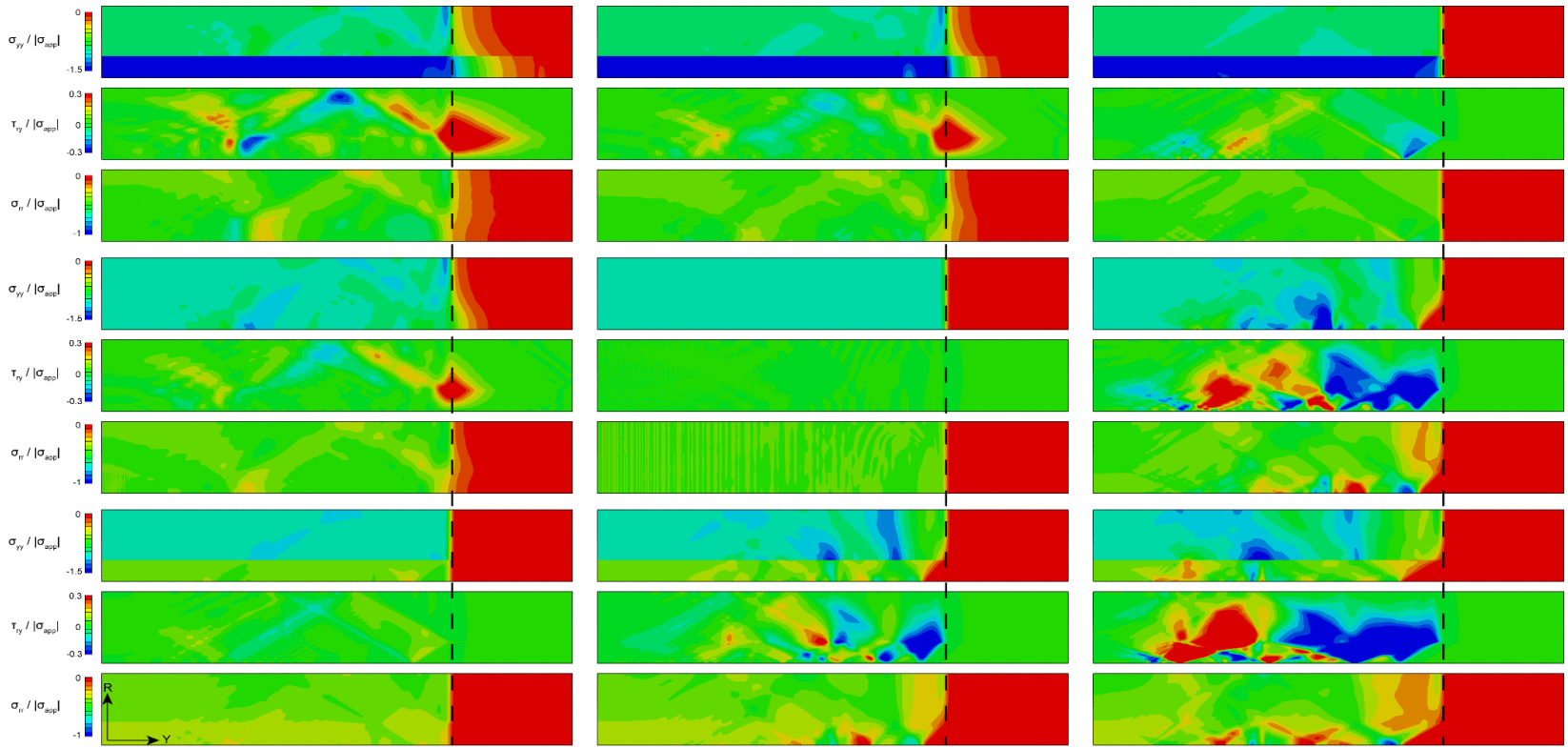

Figure 5.4. Full-field stress distributions at a late time for composites with fiber fraction $v_f = 0.09$. The wavefront in the matrix is again marked with a dashed line and only composites with $\tilde{C}_f \geq 1$ have reached their steady state.

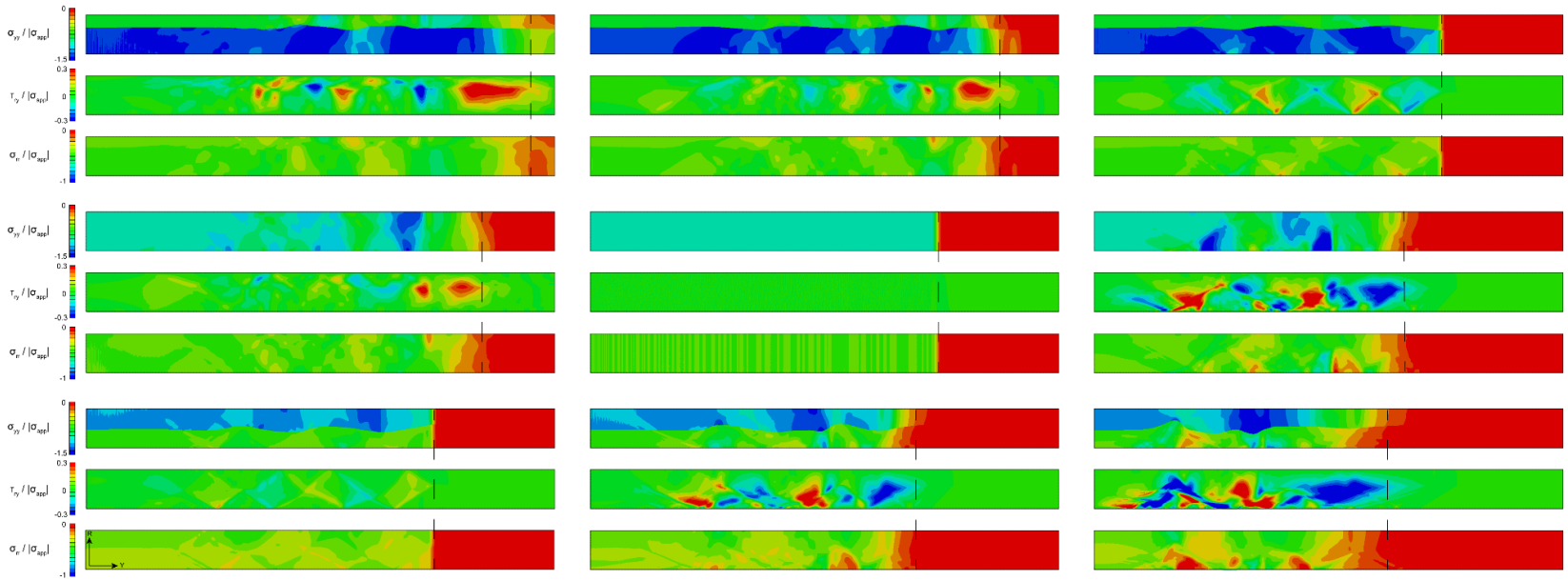

Figure 5.5. Full-field stress distributions at a late time for composites with fiber fraction $v_f = 0.36$. At this time for fiber fraction, all systems have progressed into their steady state.

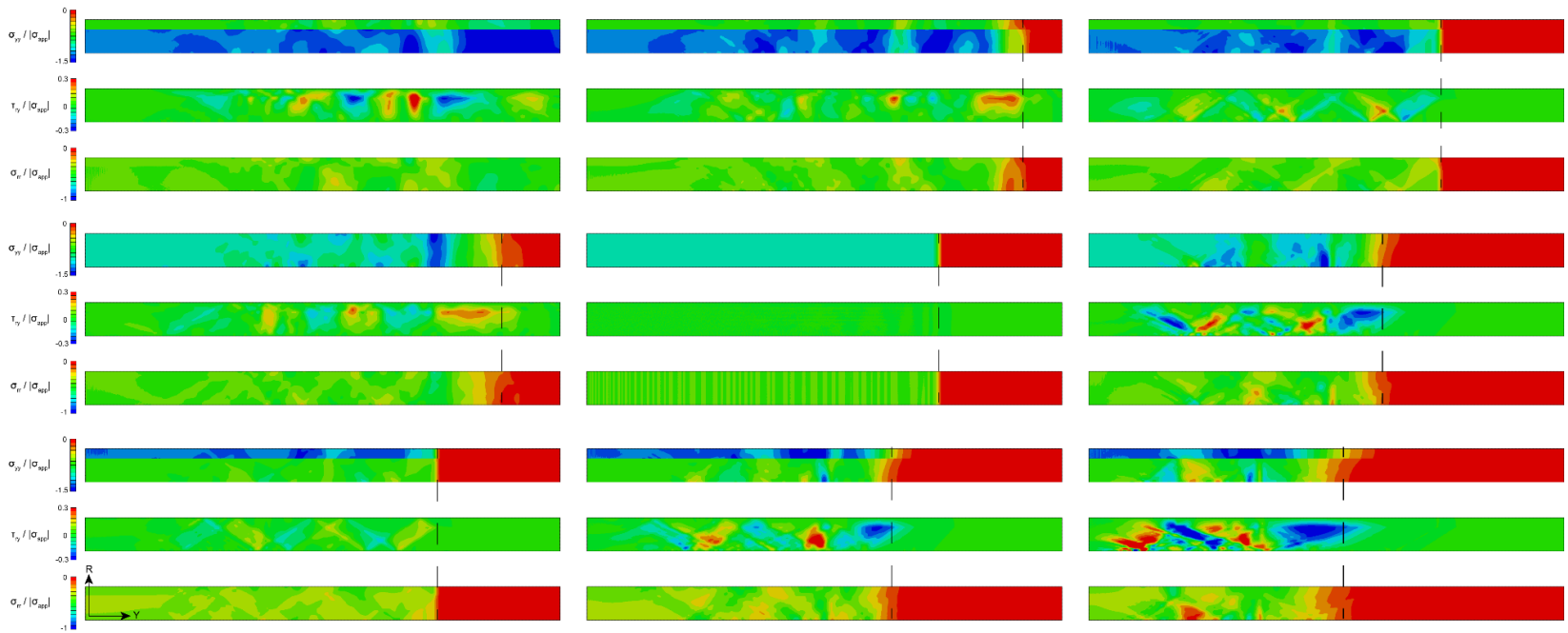

Figure 5.6. Full-field stress distributions for composites with fiber fraction v_f = 0.50. At this time for fiber fraction, all systems have progressed into their steady state.

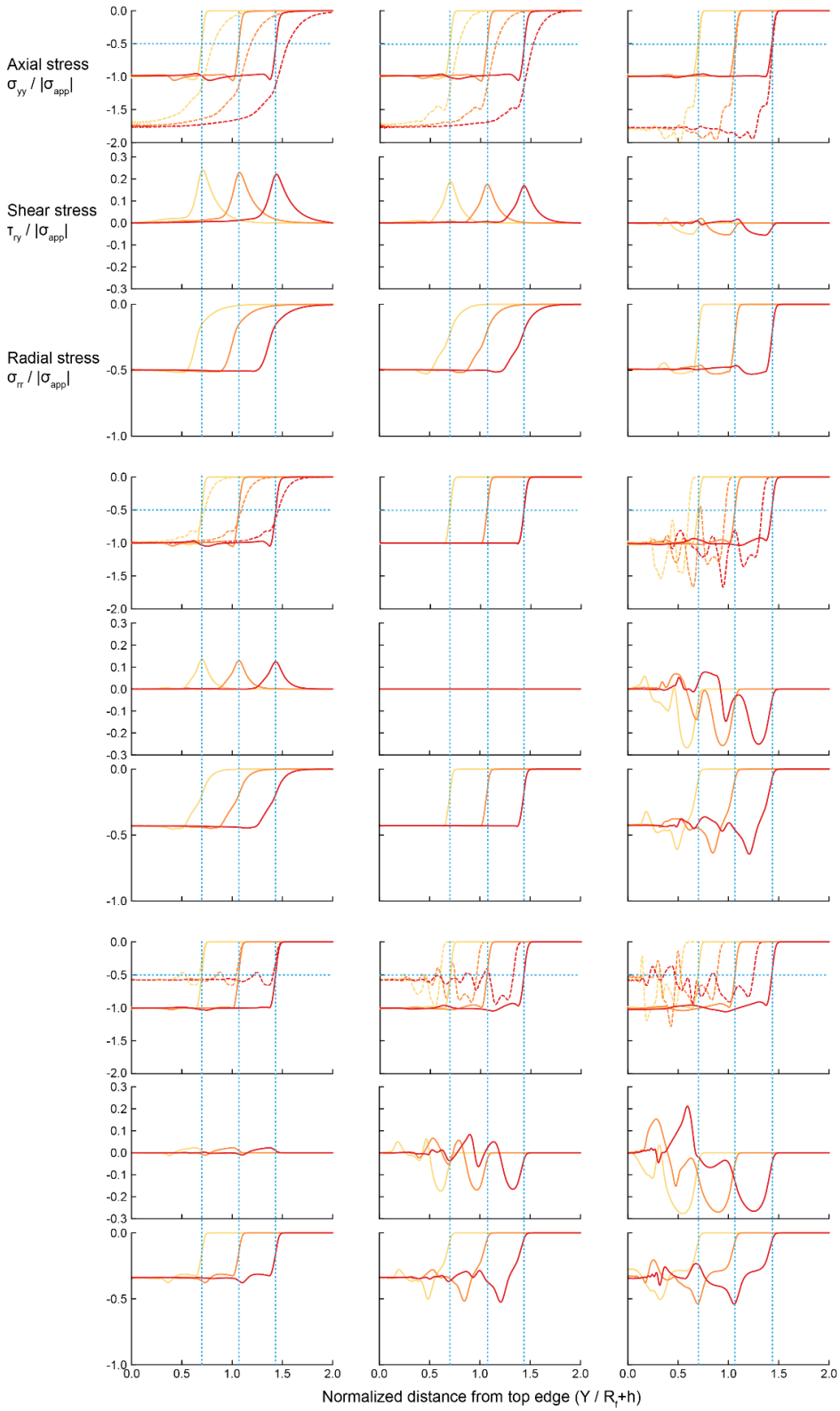

Figure 5.7. Stress profiles over time for all composite systems with $v_f = 0.01$.

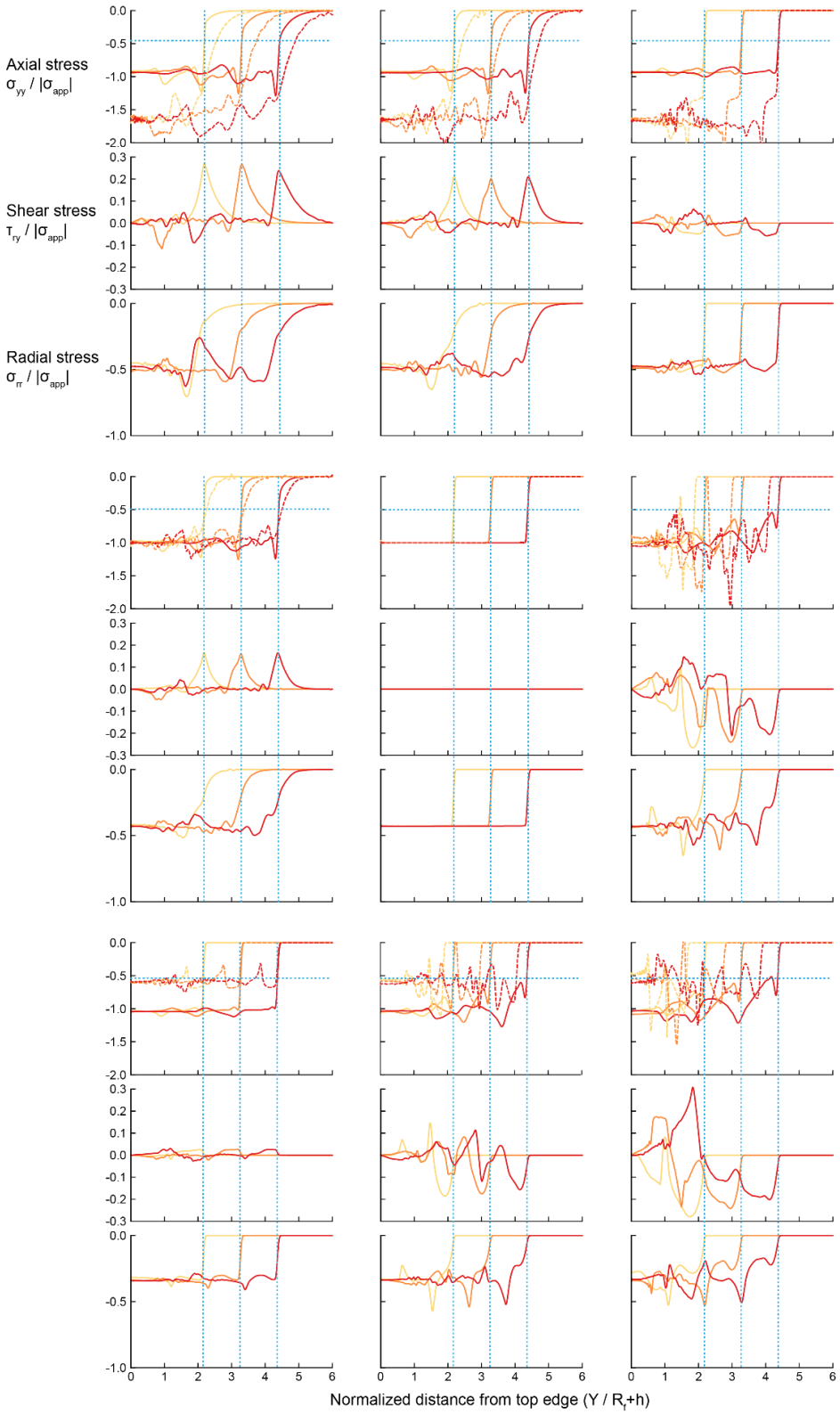

Figure 5.8. Stress profiles over time for all composite systems with $v_f = 0.09$.

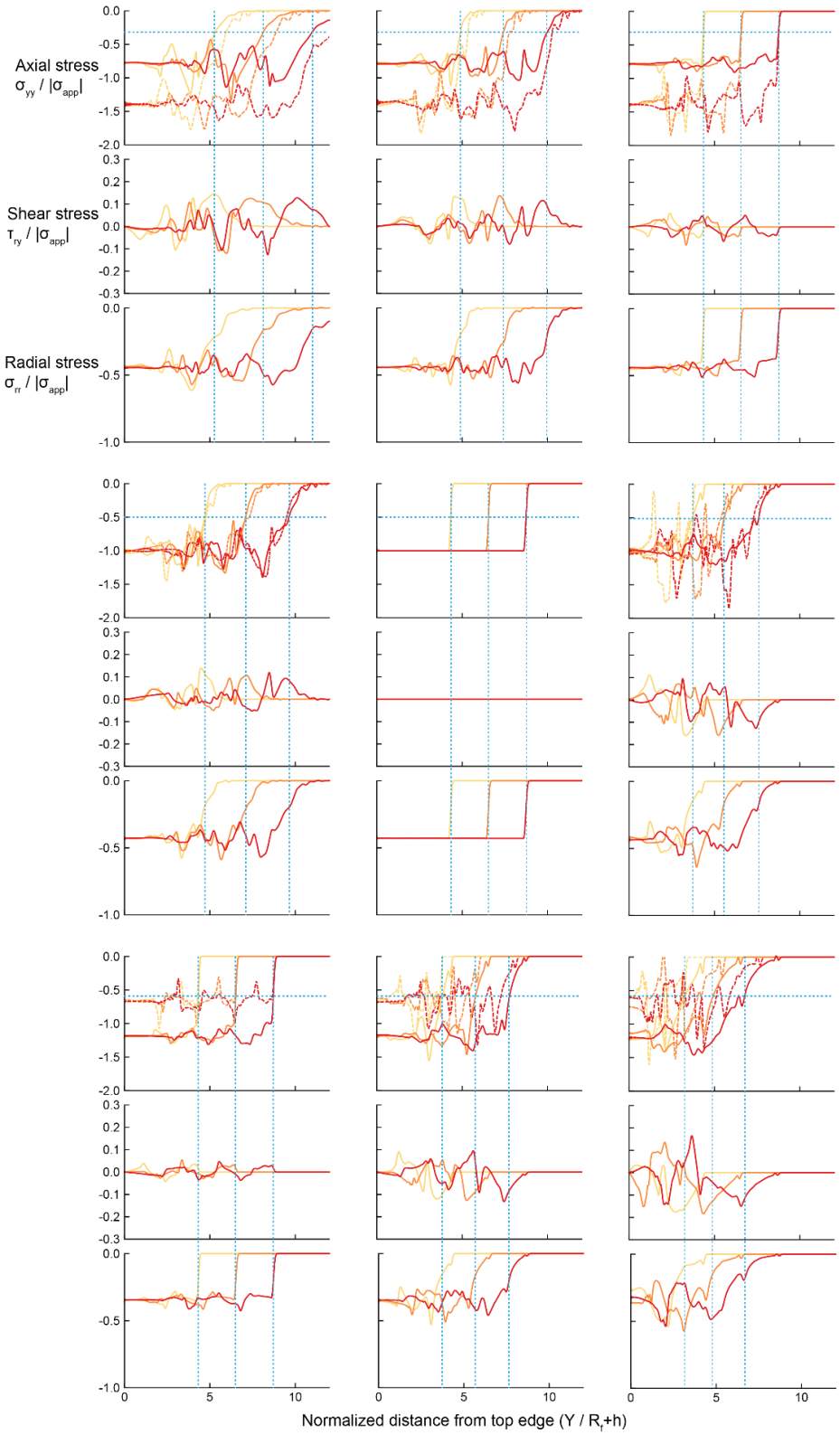

Figure 5.9. Stress profiles over time for all composite systems with $v_f = 0.36$.

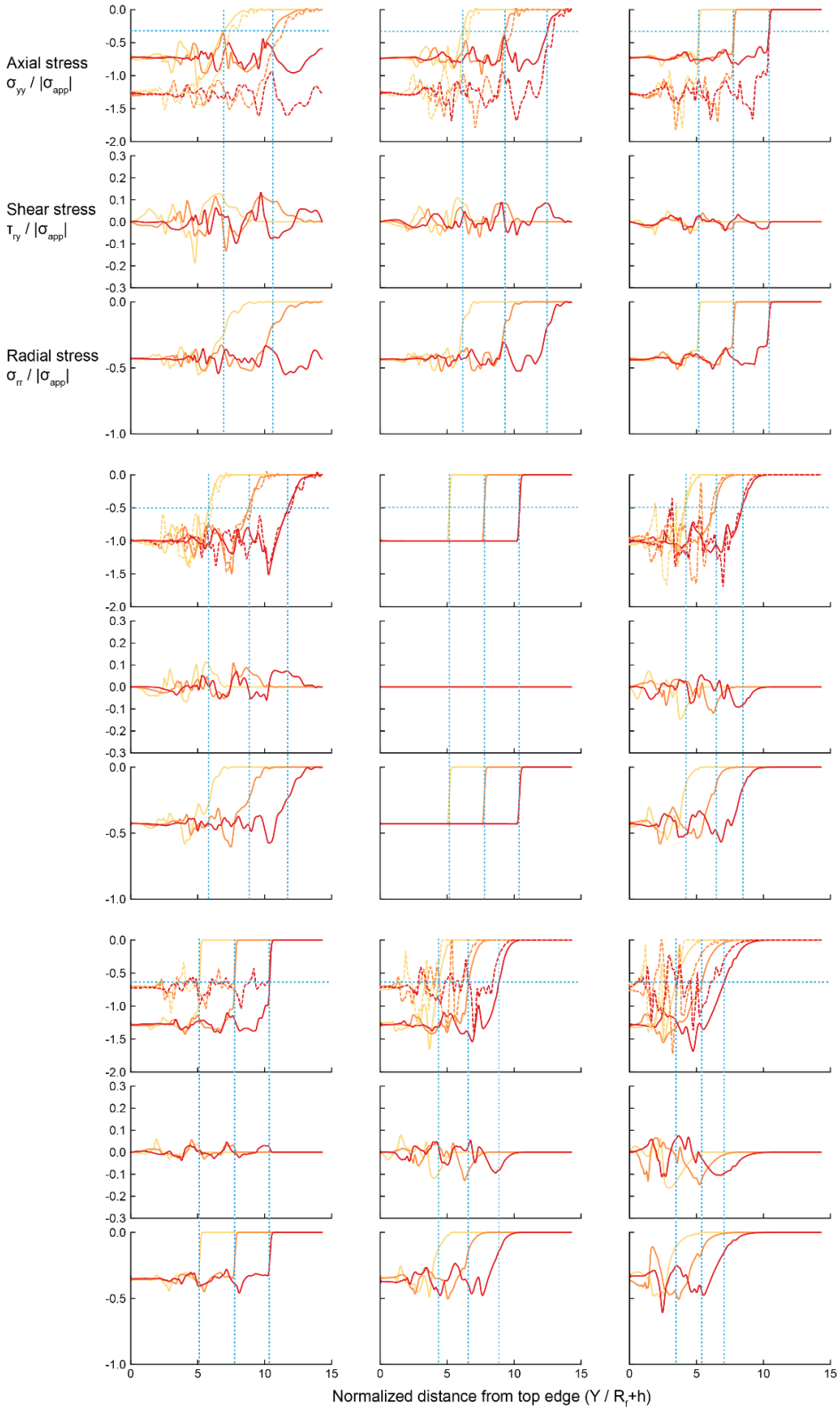

Figure 5.10. Stress profiles over time for all composite systems with $v_f = 0.50$.

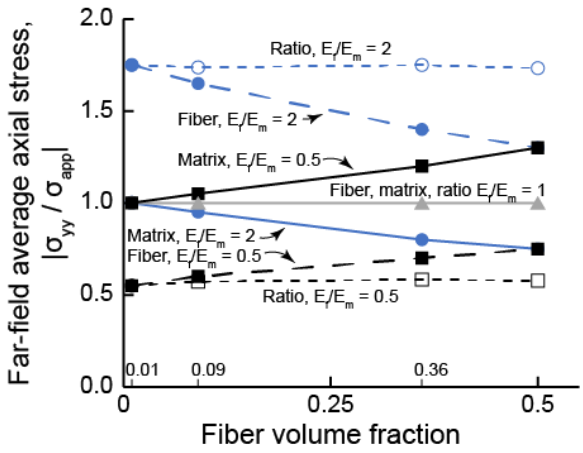

Figure 5.11. Variation in axial stress in fiber and matrix far behind the wave front with change in fiber volume fraction.

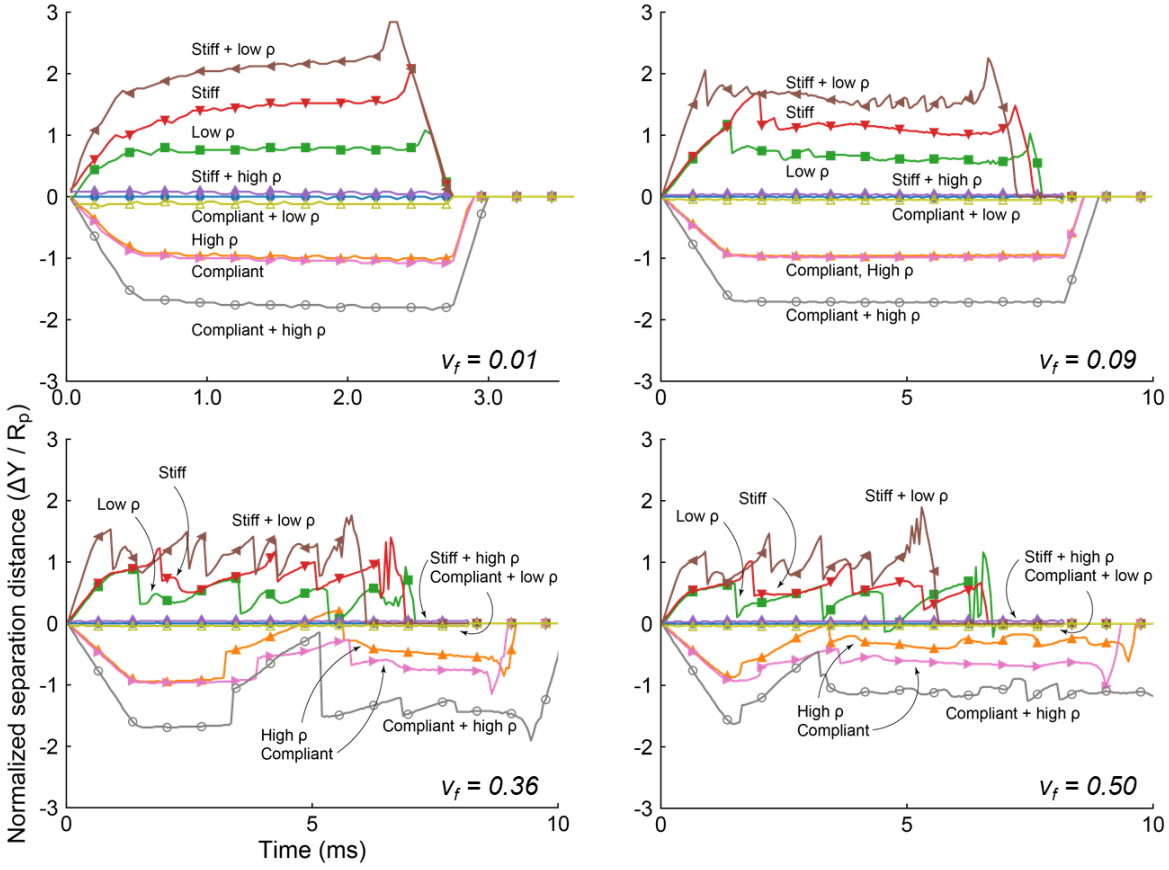

Figure 5.12. Separation distance between axial stress wavefronts at the fiber axis and in the matrix using a magnitude of $|\sigma_{app}/5|$ as the criterion for the location of the front.

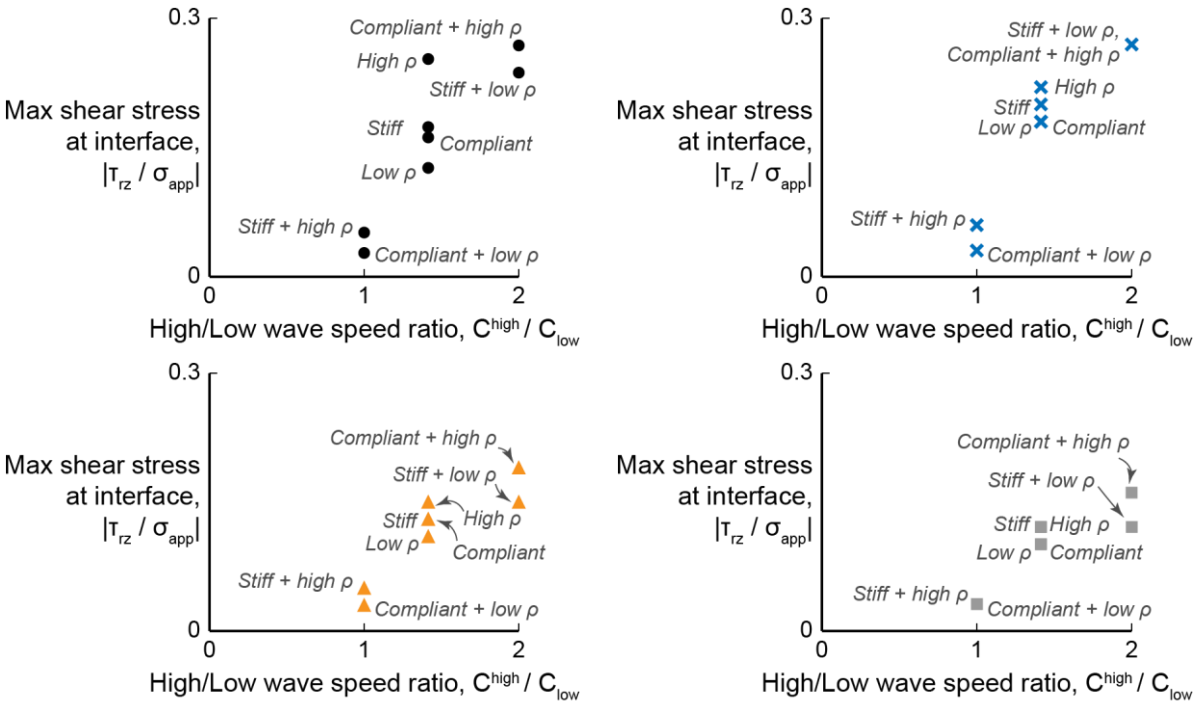

Figure 5.13. Maximum shear stress increases with ratio between the higher and lower wave speeds, regardless of which phase has the higher speed, and decreases as fiber volume fraction rises. Top row: $v_f = 0.01$ (left), $v_f = 0.09$ (right); bottom row: $v_f = 0.36$ (left), $v_f = 0.50$ (right).

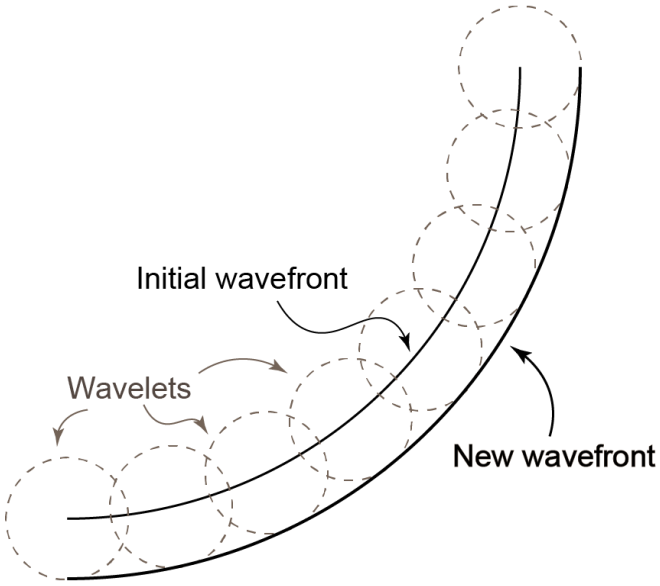

Figure 5.14. Schematic of wave propagation by generation of wavelets according to Huygens' Principle.

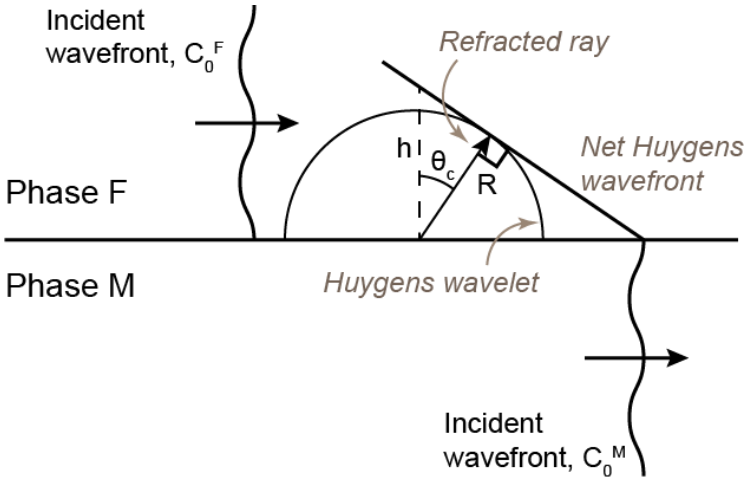

Figure 5.15. Head waves form in a slow-wave speed phase adjacent to a higher wave speed phase as a new wave is injected across the interface ahead of the incident wave in the phase with the lower wave speed[469].

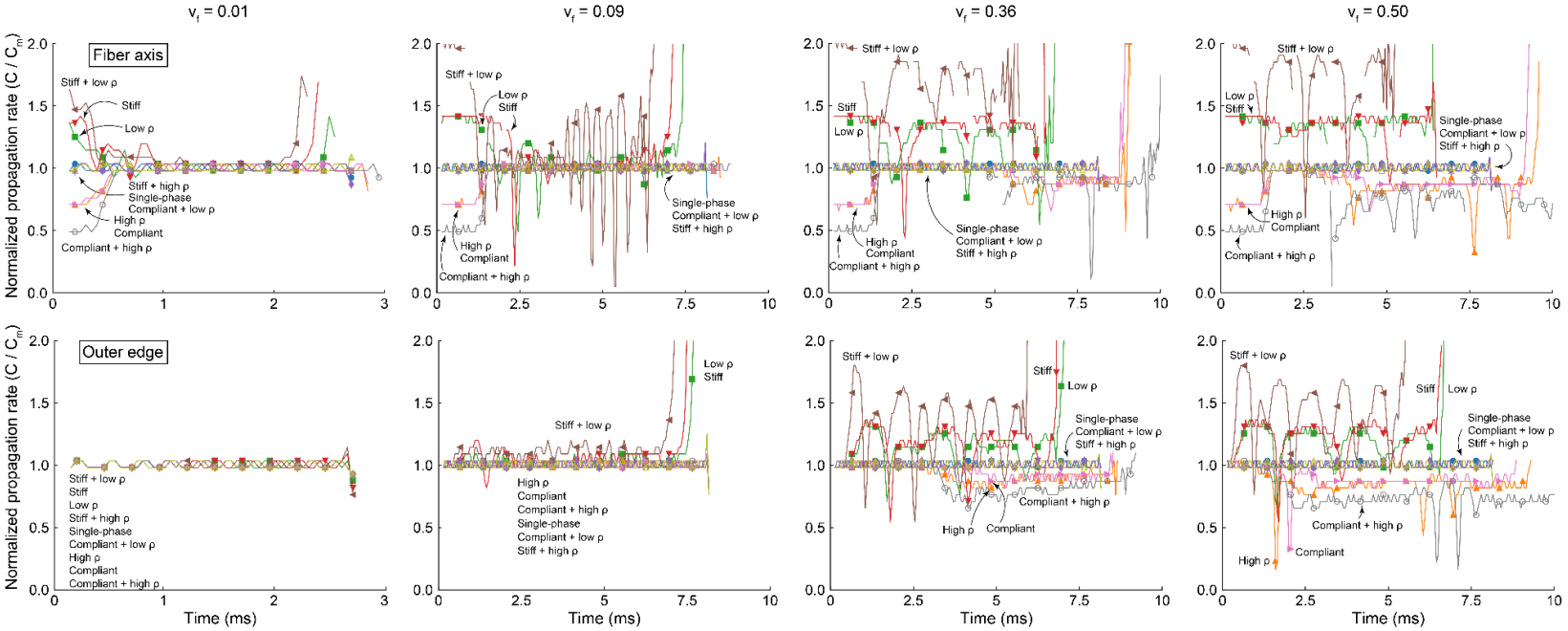

Figure 5.16. Instantaneous propagation rates over time for the wavefronts at the centerline of the fiber (top row) and outer edge of the matrix (bottom row) for composites of each of the fiber fractions used in these simulations.

.

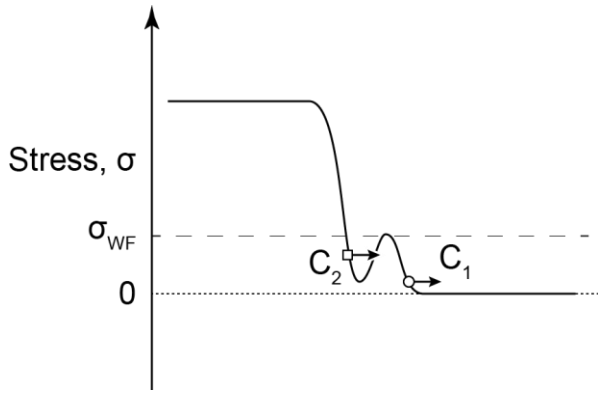

Figure 5.17. Schematic illustrating how local modifications to the stress at the wavefront (due to secondary/induced waves) temporarily alter the position and thereby affect the apparent instantaneous wave speed calculation.

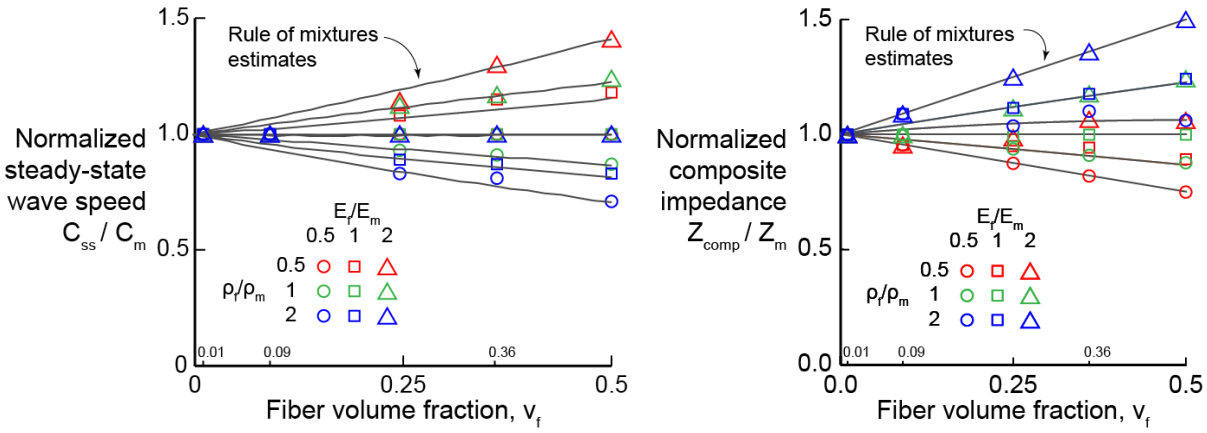

Figure 5.18. Comparison of predicted to measured dynamic properties of the composite with change to volume fraction of fiber.

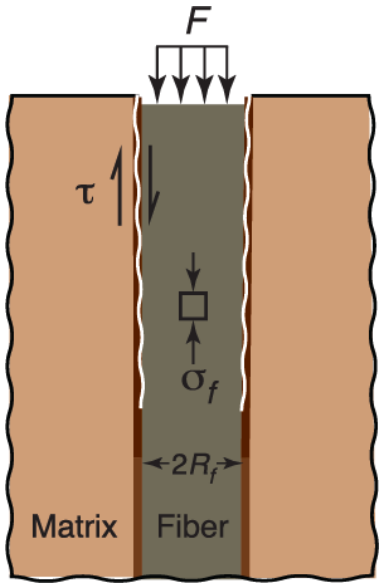

Figure 5.19. The analytical model based on shear-lag considers a geometry of an axially-loaded fiber surrounded by a thin matrix and a larger matrix jacket. Shear stresses develop at the interface as a result of a disparity in axial strain between the fiber and surrounding matrix[470].

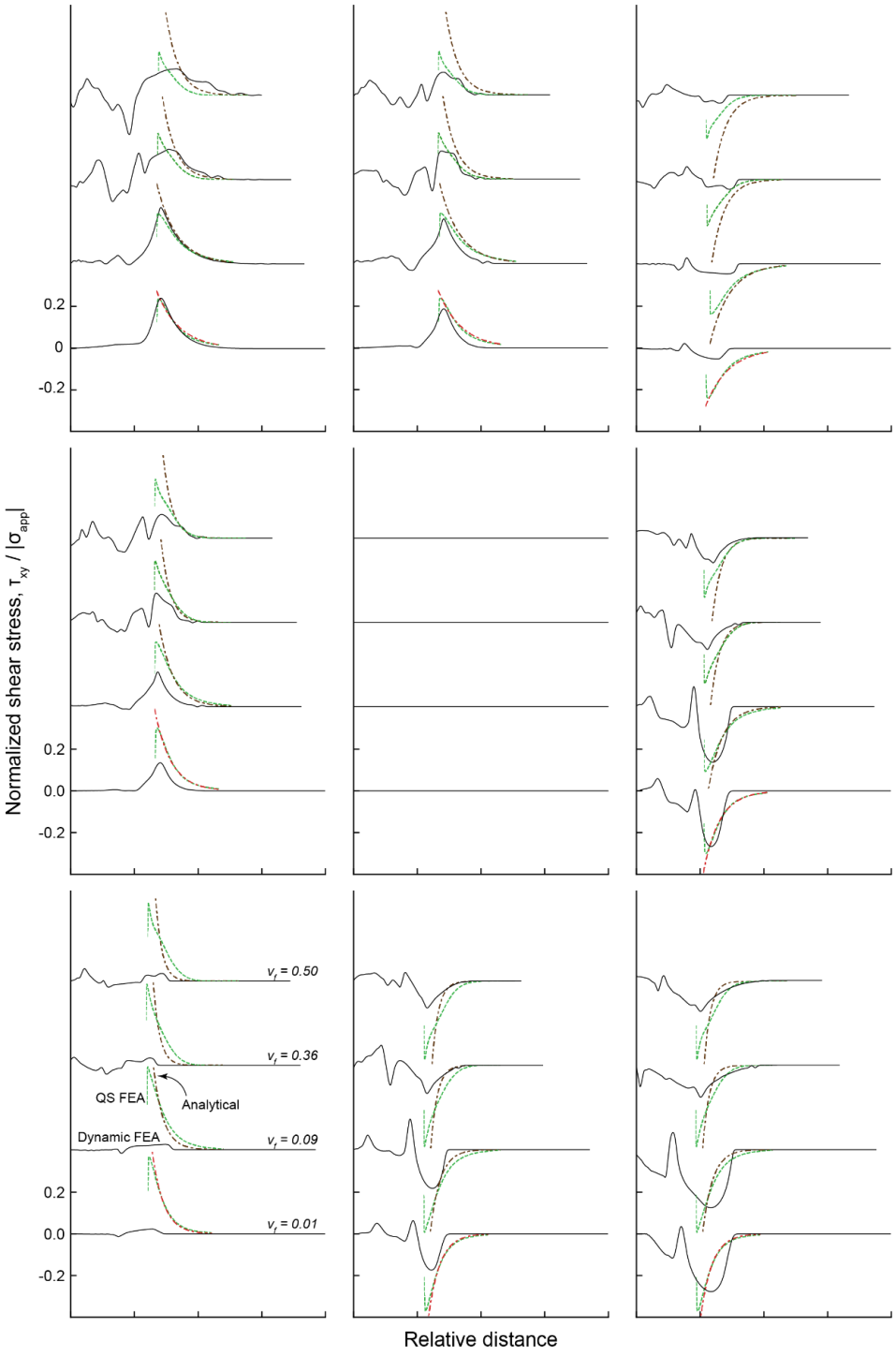

Figure 5.20. Comparison of shear stresses from the dynamic FEA to the analytical shear lag-type model[470] and quasi-static FEA. The horizontal positions are aligned for each set of curves to better compare relative widths. The analytical model produces similar shear stress distributions to the dynamic FEA for cases where the traveling wavefronts are widely separated.

Chapter 6

Summary, Conclusions, and Future Work

The work presented in preceding chapters furthers the understanding of the behavior of metal composite materials at high strain rates. Of particular interest to this area are the roles of microstructural heterogeneities (e.g., second phases and phase interfaces) and constituent properties on damage and the localization of deformation during dynamic loading. The three sets of experimental investigations provide information on the role of microstructure in strain localization as well as to general mechanical performance. The simulations help to elucidate the effects of property mismatches on wave propagation in these types of materials.

6.1 MECHANICAL BEHAVIOR OF SPD Cu/Nb COMPOSITES

Chapter 2 was primarily concerned with an experimental investigation of a multiphase Cu/Nb composite processed through equal-channel angular extrusion (ECAE). This is the first time (to the author's knowledge) that the behavior of the ECAE Cu/18wt% Nb composite has been evaluated under dynamic loading. This material had previously been briefly assessed in quasi-static tension[3]. Other Cu/Nb composites of similar composition, fabricated using accumulative drawing and bundling, have also been evaluated at low rates in tension or via indentation[10,12,18,286,290,296]. ARB Cu/50vol% Nb composites have also been the subject of considerable investigation in both compression and tension[59,74,78,85], but only at quasi-static rates.

The mechanical response of the ECAE composite is comparable to that of a Cu/50 vol% Nb ARB laminate; the strengthening mechanisms differ though. The strength of the ECAE composite is derived primarily from Hall-Petch grain size strengthening and dislocation storage, both effected by the ECAE processing. The strength is roughly as predicted from a weighted combination of the constituents. In contrast, other Cu/Nb composites reported in literature have achieved strengths exceeding the rule of mixtures estimates. In those cases, the excess strengthening is attributed to extensive refinement of the Nb phase and of the spacing between bi-phase interfaces in combination with the stability of those interfaces. Two implications arise: (i) realizing the benefit of the bi-phase interfaces requires reducing their spacing to less than 200 nm (the value of the ARB laminate used here), and (ii) that the strength of the ECAE composite should be increased by reducing spacing between the Nb particles. Segal et al. showed that repeating ECAE path A up to 24 passes continues to reduce the thickness and spacing of the Nb with attendant increases in yield stress and ultimate tensile strength[3]. Combining ECAE processing with other approaches could achieve the same, for example, rolling or drawing of the billet after several passes of ECAE.

Composites with anomalously high strengths have elongated continuous phases, either filamentary (after ~24 passes of ECAE[3] or extensive drawing[12]) or planar (ARB and PVD nanolaminates[59,78]. ECAE extrusion sequences besides path A would alter the phase morphology and texture, helping to elucidate the role of phase morphology on the performance. For ECAE composites where the bi-phase interfaces meaningfully contribute to the response, the structure of the Cu/Nb interface should be examined via TEM. The difference in interface structure between PVD and ARB Cu/Nb nanolayers produces a pronounced disparity in shear

strength of their interfaces which carries into response along other directions; analogous details for ECAE composites are currently unknown.

The kink band formation after compression along TD and ED of the ECAE material is a deformation mode not previously reported for particle-type composites or generally for pure metals except single crystals. The composite is therefore more prone to localized deformation than is usual for copper. Previous reports of localized deformation were based on forced-localization test geometries,[203,385,471] intentionally alloying to increase the propensity for shear banding[204], or using substantially greater strain rates (~6800 /s, roughly double the rates used here)[472]. However, kink banding is distinct from the (adiabatic) shear banding mechanism that is often observed in these cases and for other metals subjected to high strain rate loading. Of the two modes, kink bands are likely to be preferred for most applications since they can grow stably to high global strains with nearly constant or even rising global load whereas adiabatic shear bands often lead to precipitous loss of load-bearing capacity.

The features of the ECAE composite that cause kinking and promote kinking over ASBs have not been elucidated yet. Texture (from processing) likely plays a significant role since kinking is believed to require anisotropy in plastic response. A highly textured single-phase polycrystal may have sufficiently aligned planes (a la single crystals) to kink. (The lack of particle fiducial markers would hinder identification of kink bands, but paint speckles applied to the surface should suffice.) However, it is unclear whether the Nb particles are critical; the particle strings may also promote shearing along planes parallel to the loading direction. One potential instance of kink bands in a textured, single phase polycrystal has been reported: pure Ta, processed by 4 passes of ECAE path C and compressed at ~6000 /s, exhibits an “X” shape on exterior faces[169]. The same pattern formed on the surface of the ARB

composites during high strain rate compression (Figure 6.1). No microstructural analysis of the localization in the Ta was reported whereas the ARB composite, as shown in Chapter 2, definitely formed kink bands. If kinking did occur in the Ta, it would show that the second phase is unnecessary. If the second phase either is necessary or contributes to kink formation, the effects of material properties of the second phase and phase morphology are unknown.

Annealing and processing by ECAE path E (which incorporates rotations about the extrusion axis between passes of 180°, 90°, 180°, 90°, …) could be used to investigate the importance of texture. Annealing the current material would eliminate the texture without affecting the particle arrangement but would also remove the strain hardening; processing the same starting billet via path E instead of path A would yield a more random texture and equiaxed microstructure while still providing work hardening and grain refinement. Strain hardening is not known to be necessary for kink banding, but the higher flow stresses and reduced capacity for further hardening increase the propensity for shear banding. Therefore, the path E approach should elucidate the competition between shear banding and kink banding.

FE simulations and experiments with various elements for the second phase could be used to probe effects on kinking of particle strength and hardness, interface shear properties, second-phase morphology (e.g., spherical vs. ribbon-like vs. rod-like), and thermal properties (heat capacity, thermal conductivity). The simulations could also reveal whether the onset of kink band formation is related to properties of the particles or is dominated by the matrix and specimen/loading geometry. Realizable material systems that might be of interest for studying the effect of material property combinations include Cu-Pb (compared to Cu, Pb has lower thermal conductivity, lower strength, and lower heat capacity); Cu-Ag (higher conductivity,

lower strength, comparable heat capacity); Cu-Ta (lower conductivity, higher strength, lower heat capacity); Cu-Fe (lower conductivity, higher strength, higher heat capacity).

A tangential intriguing question is whether kinking is reversible and repeatable. Kinking was found to be reversible in single crystal zinc[473] and is claimed to occur in MAX phases[474,475] (although this claim has been disputed[476]). If it occurs in the ECAE or ARB composites, this could potentially give rise to a large non-linear pseudo-plastic behavior. Experimental verification should be straightforward: A sample known to kink could be loaded in compression to form kink bands, the loading reversed to tension until at the initial length, then the sample sectioned for metallographic inspection. Although deformation is typically expected to harden metals, the ECAE composites are expected to be saturated with dislocations and show little strain hardening. The recrystallization observed within the kink bands may even soften the bands. The relative hardness could be verified with indentation inside regions identified as recrystallized (either through EBSD or an acid etch of the copper to locate large grains).

6.2 LOCALIZATION AND FAILURE IN Zr-2.5wt% Nb ALLOYS

Chapters 3 and 4 cover a set of experiments directed at assessing and comparing the performance of two types of Zr-2.5 wt% Nb materials. Both possess a hierarchical bi-phase lamellar microstructure but the compression processing of the DT version reoriented prior β grain boundaries. Those prior β grain boundaries were found to dictate failure behavior in both materials. In dynamic compression, loading normal to prior β boundaries is associated with increased propensity for adiabatic shear band formation. During the tension phase of flyer

impact/spallation tests, voids tend to form near prior boundaries that are oriented nearly normal to the impact direction.

The detrimental effect of these boundaries is attributed to the large colonies which decorate them. Although the colonies comprise alternating phases with different crystal structures, shared slip directions cause them to act like single larger grains. The small number of slip systems in the HCP α phase limits the ability of the colonies to accommodate deformation; incompatibility with neighboring colonies or adjacent basketweave microstructure leads to local stress elevation which in turn promotes void nucleation. The surrounding microstructure, consisting of much smaller "grains" (i.e., packets of only a few laths) with multiple unaligned slip directions, is comparatively better able to accommodate general deformation. The limited number of slip systems and high strain rates can also lead to activation of alternative deformation modes in large colonies, notably twinning.

Future work with these materials could help to elucidate the microstructural origins of adiabatic shear bands which, in these alloys and in general, are not well understood. Analytical models largely have focused on global measures (e.g., macroscale stresses and strains) and average material properties (heat capacity, thermal softening rates) to generate criteria based on critical strains and strain rates for shear band formation. However, these efforts do not provide information on the microstructural heterogeneities which contribute to formation of ASBs. Numerical simulations could be used to probe the connections implicated by the experimental portion of this work. For example, investigating strain accumulation in the boundary colonies and the role of texture in those colonies. This could be supplemented by additional orientation measurements. EBSD would be overly time consuming for large-scale texture measurements in these materials but XRD could be used to generate pole figures for

millimeter-scale areas. EBSD could then be used for targeting regions at and near the prior boundaries. Additionally, using high-magnification (possibly SEM) DIC to study strain apportionment throughout loading would be desirable to determine if prior grain boundaries accumulate strain in the manner expected.

Similarly, crystal plasticity FEA could help to elucidate void formation and growth during spallation. Possible problems of interest include (i) the observed preference for void formation at colony/packet edges and near non-lamellar α as opposed to colony centers, (ii) effects of orientation of microstructure, and (iii) the role of the layered microstructure. Incompatible deformation of neighboring colonies is believed to elevate stresses near colony edges and induce void nucleation; these simulations could be used to determine the relative importance of elastic and plastic anisotropy to those stresses. Boundary orientation with respect to loading direction correlates strongly with void formation, with perpendicular boundaries being strongly preferred for damage due to greater normal stresses at the boundaries. However, in the current experiments, voids also seem to prefer boundaries oriented parallel to the loading direction over non-boundary regions. This suggests an additional influence on the local stress state. After voids nucleate, their growth is seemingly correlated with directionality in the local microstructure: the spatial orientation of adjacent laths and colony/packet boundaries can seemingly dictate growth. Voids may grow parallel to lath direction, even perpendicular to the impact, or be halted by colony boundaries perpendicular to the growth axis even seemingly favorable based on the loading direction. These result in void damage which is elongated rather than spherical as is typical in single-phase materials. Finally, the effect of the second phase should be further investigated. Other composites more commonly considered layered (e.g., Cu/Nb nanolaminates) have stable microstructures as a result of the bi-metal interfaces

accommodating dislocations and other defects[9,332]. It is not yet known whether the Zr-Nb alloy system will behave similarly or by the same mechanisms.

6.3 WAVE PROPAGATION VIA FEA

Chapter 5 concerns wave propagation in multi-phase systems. The relative wave speeds of the two phases determine which of three behavioral domains is followed by the stress waves. Simple relationships were found to relate the constituent properties to the effective dynamic properties of the composite. Finally, the shear stress associated with wavefronts that are traveling at a steady separation distance was found to be reasonably approximated by a shear-lag type model for certain fiber fraction ranges.

The material response used here, linear elastic, is highly simplified compared to real material behavior of most interest. The use of constitutive models that incorporate plasticity, rate dependence, and temperature should give stress distributions which more closely resemble those in real dynamic tests. These will be accompanied by increased difficulty in correlated observations with their source as the various waves overlap with one another. For example, a bilinear constitutive law with a lower slope after yielding will give 2 longitudinal waves, each propagating at a particular and unchanging wave speed – each given by $C = \left(\frac{d\sigma/d\epsilon}{\rho}\right)^{1/2}$ but one in the elastic regime and the other in the plastic so that the numerator is distinct. The plastic portion will trail the elastic, falling farther behind with time, thereby continually altering the stress distribution from that in a linear elastic case. Variations on only bilinear elastic are myriad and appear to offer an extensive study. Some possible combinations are: One phase with plasticity; both phases with plasticity; the phase that goes plastic could have the higher elastic wave speed or the lower elastic wave speed; the plastic wave speed could be less than

or greater than (or equal to) the elastic wave speed of the other phase; the yield points could be different. A combination of practical interest to ductile metal composites is both phases having plasticity but dissimilar yield points and dissimilar tangent moduli. In any of these, individual interaction of a wave "component" (an elastic wave or a plastic wave) with boundaries and interfaces between phases should follow the same relationships as elastic waves. The differences will arise from the ways in which the stresses affect the medium and combine with each other.

An alternative route would be to study the effects of microstructure on the waves. Interfaces that are curved or inclined relative to the incident wavefront will produce secondary reflected, refracted, and transmitted waves that are unlike those in the current simulations with only parallel boundaries. Preliminary results show a "focusing" type effect of curved surfaces which could potentially be relevant to real materials if it causes or prevents localized yielding. Lingering questions remain regarding the transitions between stages of wave propagation in the purely elastic model. For instance, it is not clear which events in the low C_f regime mark or cause the change from the initial transient to the steady state regime. There is also no proof that the end states here are the "real" final or steady states of propagation. Increasing the time and distance in simulations would clarify whether there are additional transitions in propagation behavior.

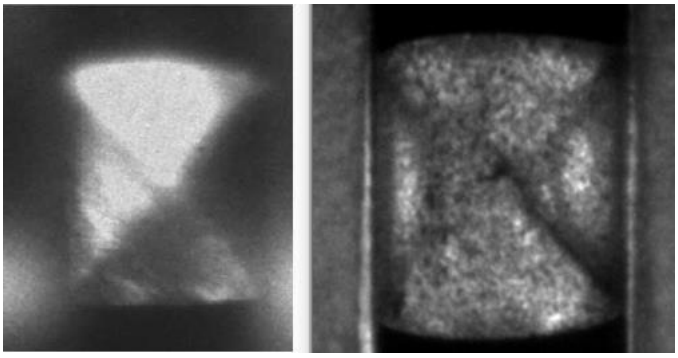

Figure 6.1. Similar "X"-shaped patterns formed during high strain rate compression of (left) pure Ta processed by ECAE path C^{169} and (right) Cu/50% Nb processed by ARB tested for the work in Chapter 2. Both images taken in-situ, left using a DRS Hadland Super 8 and right using a DRS Hadland Imacon 200.

REFERENCES

1. Russell, A. M., Chumbley, L. S. & Tian, Y. Deformation processed metal-metal composites. *Adv. Eng. Mater.* **2**, 11–22 (2000).
2. Misra, A., Göken, M., Mara, N. A. & Beyerlein, I. J. Hierarchical and heterogeneous multiphase metallic nanomaterials and laminates. *MRS Bull.* **46**, 236–243 (2021).
3. Segal, V. M., Hartwig, K. T. & Goforth, R. E. In situ composites processed by simple shear. *Mater. Sci. Eng. A* **224**, 107–115 (1997).
4. Trybus, C. L. & Spitzig, W. A. Characterization of the strength and microstructural evolution of a heavily cold rolled Cu-20% Nb composite. *Acta Metall.* **37**, 1971–1981 (1989).
5. Raabe, D. *et al.* Metallic composites processed via extreme deformation: Toward the limits of strength in bulk materials. *MRS Bull.* **35**, 982–991 (2010).
6. Rajagopalan, M. *et al.* Nanotechnology enabled design of a structural material with extreme strength as well as thermal and electrical properties. *Mater. Today* **31**, 10–20 (2019).
7. Turnage, S. A. *et al.* Anomalous mechanical behavior of nanocrystalline binary alloys under extreme conditions. *Nat. Commun.* **9**, 1–10 (2018).
8. Beyerlein, I. J. *et al.* Structure-property-functionality of bimetal interfaces. *J. Mater.* **64**, 1192–1207 (2012).
9. Carpenter, J. S. *et al.* Thermal stability of Cu-Nb nanolamellar composites fabricated via accumulative roll bonding. *Philos. Mag.* **93**, 718–735 (2013).
10. Raabe, D., Miyake, K. & Takahara, H. Processing, microstructure, and properties of ternary high-strength Cu-Cr-Ag in situ composites. *Mater. Sci. Eng. A* **291**, 186–197 (2000).
11. Frommeyer, G. & Wassermann, G. Microstructure and anomalous mechanical properties of in situ-produced silver-copper composite wires. *Acta Metall.* **23**, 1353–1360 (1975).
12. Bevk, J., Harbison, J. P. & Bell, J. L. Anomalous increase in strength of in situ formed Cu-Nb multifilamentary composites. *J. Appl. Phys.* **49**, 6031–6038 (1978).
13. Verhoeven, J. D., Spitzig, W. A., Schmidt, F. A., Krotz, P. D. & Gibson, E. D. Processing

to optimize the strength of heavily drawn Cu-Nb alloys. *J. Mater. Sci.* **24**, 1015–1020 (1989).

14. Thilly, L. *et al.* High-strength materials: in-situ investigations of dislocation behaviour in Cu-Nb multifilamentary nanostructured composites. *Philos. Mag. A* **82**, 925–942 (2002).
15. Spitzig, W. A., Downing, H. L. & Renaud, C. V. Influence of axisymmetric deformation processing methods on the mechanical properties of cu-nb composites. *Mater. Manuf. Process.* **7**, 1–13 (1992).
16. Thilly, L., Véron, M., Ludwig, O. & Lecouturier, F. Deformation mechanism in high strength Cu/Nb nanocomposites. *Mater. Sci. Eng. A* **309**–**310**, 510–513 (2001).
17. Vidal, V., Thilly, L., Lecouturier, F. & Renault, P. O. Effects of size and geometry on the plasticity of high-strength copper/tantalum nanofilamentary conductors obtained by severe plastic deformation. *Acta Mater.* **54**, 1063–1075 (2006).
18. Dubois, J. B., Thilly, L., Renault, P. O. & Lecouturier, F. Cu-Nb nanocomposite wires processed by severe plastic deformation: Effects of the multi-scale microstructure and internal stresses on elastic-plastic properties. *Adv. Eng. Mater.* **14**, 998–1003 (2012).
19. Popova, E. N., Deryagina, I. L., Valova-Zaharevskaya, E. G., Ruello, M. L. & Popov, V. V. Microstructural features in multicore Cu–Nb composites. *Materials (Basel).* **14**, 1–13 (2021).
20. Hong, S. I. & Hill, M. A. Microstructure and conductivity of Cu-Nb microcomposites fabricated by the bundling and drawing process. *Scr. Mater.* **44**, 2509–2515 (2001).
21. Pantsyrny, V. I. *et al.* High strength, high conductivity microcomposite Cu-Nb wires with cross sections in the range of 0.01-100 mm2. *IEEE Trans. Appl. Supercond.* **18**, 616–619 (2008).
22. Spitzig, W. A., Pelton, A. R. & Laabs, F. C. Characterization of the strength and microstructure of heavily cold worked CuNb composites. *Acta Metall.* **35**, 2427–2442 (1987).
23. Raabe, D., Heringhaus, F., Hangen, U. & Gottstein, G. Investigation of a Cu-20 mass% Nb in situ Composite Part I: Fabrication, Microstructure and Mechanical Properties. *Zeitschrift für Met.* **86**, 405–415 (1995).
24. Funkenbusch, P. D. & Courtney, T. H. On the strength of heavily cold worked in situ

composites. *Acta Metall.* **33**, 913–922 (1985).

25. Biselli, C. & Morris, D. G. Microstructure and strength of Cu-Fe in situ composites after very high drawing strains. *Acta Mater.* **44**, 493–504 (1996).
26. Raabe, D. & Mattissen, D. MICROSTRUCTURE AND MECHANICAL PROPERTIES OF A CAST AND WIRE-DRAWN TERNARY Cu-Ag-Nb IN SITU COMPOSITE. *Acta Mater* **46**, 5973–5984 (1998).
27. Verhoeven, J. D., Downing, H. L., Chumbley, L. S. & Gibson, E. D. The resistivity and microstructure of heavily drawn Cu-Nb alloys. *J. Appl. Phys.* **65**, 1293–1301 (1989).
28. Go, Y. S. & Spitzig, W. A. Strengthening in deformation-processed Cu-20% Fe composites. *J. Mater. Sci.* **26**, 163–171 (1991).
29. Spitzig, W. A. & Krotz, P. D. A COMPARISON OF THE STRENGTH AND MICROSTRUCTURE OF HEAVILY COLD WORKED Cu-20% Nb COMPOSITES FORMED BY DIFFERENT MELTING PROCEDURES. *Scr. Metall.* **21**, 1143–1146 (1987).
30. Lee, K. H. & Hong, S. I. Interfacial and twin boundary structures of nanostructured Cu-Ag filamentary composites. *J. Mater. Res.* **18**, 2194–2202 (2003).
31. Takeuchi, T., Togano, K., Inoue, K. & Maeda, H. Fibrous chromium and molybdenum fabricated by cold working Cu-Cr and Cu-Mo binary alloys. *J. Less-Common Met.* **157**, 25–35 (1990).
32. Xu, K. *et al.* Characterization of strength and microstructure in deformation processed Al-Mg composites. *J. Mater. Sci.* **34**, 5955–5959 (1999).
33. Russell, A. M. *et al.* A high-strength, high-conductivity Al-Ti deformation processed metal metal matrix composite. *Compos. Part A Appl. Sci. Manuf.* **30**, 239–247 (1999).
34. Russell, A. M. *et al.* In situ strengthening of titanium with yttrium: texture analysis. *J. Mater. Sci.* **30**, 4249–4262 (1995).
35. Dupouy, F. *et al.* Microstructural characterization of high strength and high conductivity nanocomposite wires. *Scr. Mater.* **34**, 1067–1073 (1996).
36. Hong, S. I., Hill, M. A., Sakai, Y., Wood, J. T. & Embury, J. D. On the stability of cold drawn, two-phase wires. *Acta Metall. Mater.* **43**, 3313–3323 (1995).
37. Hong, S. I. & Hill, M. A. Mechanical stability and electrical conductivity of Cu-Ag filamentary microcomposites. *Mater. Sci. Eng. A* **264**, 151–158 (1999).

38. Misra, A. & Thilly, L. Structural metals at extremes. *MRS Bull.* **35**, 965–977 (2010).
39. Embury, J. D. & Hirth, J. P. On dislocation storage and the mechanical response of fine scale microstructures. *Acta Metall. Mater.* **42**, 2051–2056 (1994).
40. Embury, J. D. & Sinclair, C. W. The mechanical properties of fine-scale two-phase materials. *Mater. Sci. Eng. A* **319**–**321**, 37–45 (2001).
41. Thilly, L. *et al.* A new criterion for elasto-plastic transition in nanomaterials: Application to size and composite effects on Cu-Nb nanocomposite wires. *Acta Mater.* **57**, 3157–3169 (2009).
42. Thilly, L. *et al.* Evidence of internal Bauschinger test in nanocomposite wires during in situ macroscopic tensile cycling under synchrotron beam. *Appl. Phys. Lett.* **90**, 1–4 (2007).
43. Krotz, P. D., Spitzig, W. A. & Laabs, F. C. High temperature properties of heavily deformed Cu20%Nb and Cu20%Ta composites. *Mater. Sci. Eng. A* **110**, 37–47 (1989).
44. Deng, L., Han, K., Wang, B., Yang, X. & Liu, Q. Thermal stability of Cu-Nb microcomposite wires. *Acta Mater.* **101**, 181–188 (2015).
45. Sandim, H. R. Z., Sandim, M. J. R., Bernardi, H. H., Lins, J. F. C. & Raabe, D. Annealing effects on the microstructure and texture of a multifilamentary Cu-Nb composite wire. *Scr. Mater.* **51**, 1099–1104 (2004).
46. Deng, L. *et al.* Response of microstructure to annealing in in situ Cu–Nb microcomposite. *J. Mater. Sci.* **54**, 840–850 (2019).
47. Sandim, M. J. R. *et al.* Annealing effects on the microstructure, electrical, and magnetic properties of jelly-rolled Cu-Nb composite wires. *Supercond. Sci. Technol.* **18**, 35–40 (2005).
48. Deng, L. *et al.* Hardness, electrical resistivity, and modeling of in situ Cu-Nb microcomposites. *J. Alloys Compd.* **602**, 331–338 (2014).
49. Jin, Y., Adachi, K., Takeuchi, T. & Suzuki, H. G. Ageing characteristics of Cu-Cr in-situ composite. *J. Mater. Sci.* **33**, 1333–1341 (1998).
50. Song, J. S., Hong, S. I. & Park, Y. G. Deformation processing and strength/conductivity properties of Cu-Fe-Ag microcomposites. *J. Alloys Compd.* **388**, 69–74 (2005).
51. Hong, S. I. & Song, J. S. Strength and conductivity of Cu-9Fe-1.2X (X = Ag or Cr) filamentary microcomposite wires. *Metall. Mater. Trans. A* **32**, 985–991 (2001).

52. Knezevic, M. *et al.* Texture evolution in two-phase Zr/Nb lamellar composites during accumulative roll bonding. *Int. J. Plast.* **57**, 16–28 (2014).
53. Sáenz-Trevizo, A. & Hodge, A. M. Nanomaterials by design: A review of nanoscale metallic multilayers. *Nanotechnology* **31**, (2020).
54. Ardeljan, M. *et al.* Room temperature deformation mechanisms of Mg/Nb nanolayered composites. *J. Mater. Res.* **33**, 1311–1332 (2018).
55. Mara, N. A., Bhattacharyya, D., Dickerson, P., Hoagland, R. G. & Misra, A. Deformability of ultrahigh strength 5 nm Cu/Nb nanolayered composites. *Appl. Phys. Lett.* **92**, (2008).
56. Hoagland, R. G., Kurtz, R. J. & Henager, C. H. Slip resistance of interfaces and the strength of metallic multilayer composites. *Scr. Mater.* **50**, 775–779 (2004).
57. Han, W. Z. *et al.* Role of interfaces in shock-induced plasticity in Cu/Nb nanolaminates. *Philos. Mag.* **91**, 4172–4185 (2011).
58. Nasim, M., Li, Y., Wen, M. & Wen, C. A review of high-strength nanolaminates and evaluation of their properties. *J. Mater. Sci. Technol.* **50**, 215–244 (2020).
59. Nizolek, T., Beyerlein, I. J., Mara, N. A., Avallone, J. T. & Pollock, T. M. Tensile behavior and flow stress anisotropy of accumulative roll bonded Cu-Nb nanolaminates. *Appl. Phys. Lett.* **108**, (2016).
60. Cui, Y., Derby, B., Li, N. & Misra, A. Design of bicontinuous metallic nanocomposites for high-strength and plasticity. *Mater. Des.* **166**, 107602 (2019).
61. Nizolek, T. *et al.* Processing and Deformation Behavior of Bulk Cu–Nb Nanolaminates. *Metallogr. Microstruct. Anal.* **3**, 470–476 (2014).
62. Valiev, R. Z. *et al.* Producing Bulk Ultrafine-Grained Materials by Severe Plastic Deformation: Ten Years Later. *J. Mater.* **68**, 1216–1226 (2006).
63. Valiev, R. Z., Islamgaliev, R. K. & Alexandrov, I. V. *Bulk nanostructured materials from severe plastic deformation*. *Progress in Materials Science* vol. 45 (2000).
64. Zheng, S., Carpenter, J. S., McCabe, R. J., Beyerlein, I. J. & Mara, N. A. Engineering interface structures and thermal stabilities via SPD processing in bulk nanostructured metals. *Sci. Rep.* **4**, 1–6 (2014).
65. Wen, S. P., Zeng, F., Pan, F. & Nie, Z. R. The influence of grain morphology on indentation deformation characteristic of metallic nano-multilayers. *Mater. Sci. Eng. A*

526, 166–170 (2009).

66. Misra, A. *et al.* Structure and mechanical properties of Cu-X (X = Nb,Cr,Ni) nanolayered composites. *Scr. Mater.* **39**, 555–560 (1998).
67. Misra, A. & Hoagland, R. G. Plastic flow stability of metallic nanolaminate composites. *J. Mater. Sci.* **42**, 1765–1771 (2007).
68. Kang, B. C., Kim, H. Y., Kwon, O. Y. & Hong, S. H. Bilayer thickness effects on nanoindentation behavior of Ag/Ni multilayers. *Scr. Mater.* **57**, 703–706 (2007).
69. Carpenter, J. S., Misra, A., Uchic, M. D. & Anderson, P. M. Strain rate sensitivity and activation volume of Cu/Ni metallic multilayer thin films measured via micropillar compression. *Appl. Phys. Lett.* **101**, (2012).
70. Ma, Y. J., Wei, M. Z., Sun, C., Cao, Z. H. & Meng, X. K. Length scale effect on the thermal stability of nanoscale Cu/Ag multilayers. *Mater. Sci. Eng. A* **686**, 142–149 (2017).
71. Misra, A., Kung, H. & Hoagland, R. G. Thermal Stability of Self-Supported Metallic Multilayered Thin Films. *Mater. Res. Soc. Symp. Proc.* **695**, 1–6 (2002).
72. Nasim, M., Li, Y., Dargusch, M. & Wen, C. Ultra-strong and ductile Ta/Co nanolaminates strengthened via grain-boundary expanding and interfacial sliding. *Appl. Mater. Today* **23**, 100983 (2021).
73. Mara, N. A. & Beyerlein, I. J. Review: Effect of bimetal interface structure on the mechanical behavior of Cu-Nb fcc-bcc nanolayered composites. in *Journal of Materials Science* vol. 49 6497–6516 (Kluwer Academic Publishers, 2014).
74. Misra, A., Hirth, J. P. & Hoagland, R. G. Length-scale-dependent deformation mechanisms in incoherent metallic multilayered composites. *Acta Mater.* **53**, 4817–4824 (2005).
75. Mitchell, T. E., Lu, Y. C., Jr, A. J. G., Nastasi, M. & Kung, H. Structure and mechanical properties of Copper/Niobium Multilayers. *J. Am. Ceram. Soc.* **80**, 1673–1676 (1997).
76. Mara, N. A., Bhattacharyya, D., Hirth, J. P., Dickerson, P. & Misra, A. Mechanism for shear banding in nanolayered composites. *Appl. Phys. Lett.* **97**, (2010).
77. Nizolek, T. Plastic Anisotropy and Kink Band Formation in Fine Grained Copper-Niobium Multilayers Produced by Accumulative Roll Bonding. (2016).
78. Mara, N. A., Bhattacharyya, D., Hoagland, R. G. & Misra, A. Tensile behavior of 40 nm

Cu/Nb nanoscale multilayers. *Scr. Mater.* **58**, 874–877 (2008).

79. Cui, Y., Li, N. & Misra, A. An overview of interface-dominated deformation mechanisms in metallic nanocomposites elucidated using in situ straining in a TEM. *J. Mater. Res.* **34**, 1469–1478 (2019).
80. Carpenter, J. S., Misra, A. & Anderson, P. M. Achieving maximum hardness in semi-coherent multilayer thin films with unequal layer thickness. *Acta Mater.* **60**, 2625–2636 (2012).
81. Tabor, D. A simple theory of static and dynamic hardness. *Proc. R. Soc. London. Ser. A. Math. Phys. Sci.* **192**, 247–274 (1948).
82. Jankowski, A. F., Sedillo, E. M. & Hayes, J. P. Elastic property dependence on layer periodicity in cu/ni superlattices. *Jpn. J. Appl. Phys.* **33**, 5019–5025 (1994).
83. Mara, N. A. *et al.* High-temperature mechanical behavior/microstructure correlation of Cu/Nb nanoscale multilayers. *Mater. Sci. Eng. A* **493**, 274–282 (2008).
84. Beyerlein, I. J. *et al.* Emergence of stable interfaces under extreme plastic deformation. *Proc. Natl. Acad. Sci. U. S. A.* **111**, 4386–4390 (2014).
85. Nizolek, T., Mara, N. A., Beyerlein, I. J., Avallone, J. T. & Pollock, T. M. Enhanced plasticity via kinking in cubic metallic nanolaminates. *Adv. Eng. Mater.* **17**, 781–785 (2015).
86. An, Q., Yang, W., Liu, B. & Zheng, S. Interface effects on the properties of Cu-Nb nanolayered composites. *J. Mater. Res.* **35**, 2684–2700 (2020).
87. Carpenter, J. S. *et al.* Processing parameter influence on texture and microstructural evolution in cu-nb multilayer composites fabricated via accumulative roll bonding. *Metall. Mater. Trans. A Phys. Metall. Mater. Sci.* **45**, 2192–2208 (2014).
88. Zeng, L. F. *et al.* High strength and thermal stability of bulk Cu/Ta nanolamellar multilayers fabricated by cross accumulative roll bonding. *Acta Mater.* **110**, 341–351 (2016).
89. McCabe, R. J., Carpenter, J. S., Vogel, S., Mara, N. A. & Beyerlein, I. J. Recrystallization and Grain Growth in Accumulative Roll-Bonded Metal Composites. *Jom* **67**, 2810–2819 (2015).
90. Carpenter, J. S. *et al.* Bulk texture evolution of Cu-Nb nanolamellar composites during accumulative roll bonding. *Acta Mater.* **60**, 1576–1586 (2012).

91. Yang, W. *et al.* Strength and ductility of bulk Cu/Nb nanolaminates exposed to extremely high temperatures. *Scr. Mater.* **166**, 73–77 (2019).
92. Wang, J. *et al.* Structure and property of interfaces in ARB Cu/Nb laminated composites. *JOM* **64**, 1208–1217 (2012).
93. Carpenter, J. S. *et al.* A comparison of texture results obtained using precession electron diffraction and neutron diffraction methods at diminishing length scales in ordered bimetallic nanolamellar composites. *Scr. Mater.* **67**, 336–339 (2012).
94. Wang, J., Zhou, Q., Shao, S. & Misra, A. Strength and plasticity of nanolaminated materials. *Mater. Res. Lett.* **5**, 1–19 (2017).
95. Sahay, R. *et al.* Crystallographic Anisotropy Dependence of Interfacial Sliding Phenomenon in a Cu(16)/Nb(16) ARB (Accumulated Rolling Bonding) Nanolaminate. *Nanomaterials* **12**, (2022).
96. Lim, S. C. V. & Rollett, A. D. Length scale effects on recrystallization and texture evolution in Cu layers of a roll-bonded Cu-Nb composite. *Mater. Sci. Eng. A* **520**, 189–196 (2009).
97. Zeng, L. F. *et al.* Development of interface-dominant bulk Cu/V nanolamellar composites by cross accumulative roll bonding. *Sci. Rep.* **7**, 1–9 (2017).
98. Beyerlein, I. J. *et al.* Interface-driven microstructure development and ultra high strength of bulk nanostructured Cu-Nb multilayers fabricated by severe plastic deformation. *J. Mater. Res.* **28**, 1799–1812 (2013).
99. Wang, F., Huang, P., Xu, M., Lu, T. J. & Xu, K. W. Shear banding deformation in Cu/Ta nano-multilayers. *Mater. Sci. Eng. A* **528**, 7290–7294 (2011).
100. Demkowicz, M. J. & Thilly, L. Structure, shear resistance and interaction with point defects of interfaces in Cu-Nb nanocomposites synthesized by severe plastic deformation. *Acta Mater.* **59**, 7744–7756 (2011).
101. Radchenko, I., Anwarali, H. P., Tippabhotla, S. K. & Budiman, A. S. Effects of interface shear strength during failure of semicoherent Metal–Metal nanolaminates: An example of accumulative roll-bonded Cu/Nb. *Acta Mater.* **156**, 125–135 (2018).
102. Misra, A. & Kung, H. Deformation behavior of nanostructured metallic multilayers. *Adv. Eng. Mater.* **3**, 217–222 (2001).
103. Was, G. S. & Foecke, T. Deformation and fracture in microlaminates. *Thin Solid Films*

286, 1–31 (1996).

104. Nan, L., Wang, J., Misra, A. & Huang, J. Y. Direct observations of confined layer slip in Cu/Nb multilayers. *Microsc. Microanal.* **18**, 1155–1162 (2012).
105. Subedi, S., Beyerlein, I. J., LeSar, R. & Rollett, A. D. Strength of nanoscale metallic multilayers. *Scr. Mater.* **145**, 132–136 (2018).
106. Zhang, J. Y. *et al.* Length scale-dependent deformation behavior of nanolayered Cu/Zr micropillars. *Acta Mater.* **60**, 1610–1622 (2012).
107. Hoagland, R. G., Hirth, J. P. & Misra, A. On the role of weak interfaces in blocking slip in nanoscale layered composites. *Philos. Mag.* **86**, 3537–3558 (2006).
108. Fu, E. G. *et al.* Mechanical properties of sputtered Cu/V and Al/Nb multilayer films. *Mater. Sci. Eng. A* **493**, 283–287 (2008).
109. Yu, K. Y., Liu, Y., Rios, S., Wang, H. & Zhang, X. Strengthening mechanisms of Ag/Ni immiscible multilayers with fcc/fcc interface. *Surf. Coatings Technol.* **237**, 269–275 (2013).
110. Wang, J., Hoagland, R. G., Hirth, J. P. & Misra, A. Atomistic modeling of the interaction of glide dislocations with 'weak' interfaces. *Acta Mater.* **56**, 5685–5693 (2008).
111. Misra, A., Hoagland, R. G. & Kung, H. Thermal stability of self-supported nanolayered Cu/Nb films. *Philos. Mag.* **84**, 1021–1028 (2004).
112. Lewis, A. C., Josell, D. & Weihs, T. P. Stability in thin film multilayers and microlaminates: The role of free energy, structure, and orientation at interfaces and grain boundaries. *Scr. Mater.* **48**, 1079–1085 (2003).
113. Wan, H., Shen, Y., Wang, J., Shen, Z. & Jin, X. A predictive model for microstructure evolution in metallic multilayers with immiscible constituents. *Acta Mater.* **60**, 6869–6881 (2012).
114. Appleget, C. D., Riano, J. S. & Hodge, A. M. An Overview of Nano Multilayers as Model Systems for Developing Nanoscale Microstructures. *Materials (Basel).* **15**, 1–14 (2022).
115. Misra, A. & Hoagland, R. G. Effects of elevated temperature annealing on the structure and hardness of copper/niobium nanolayered films. *J. Mater. Res.* **20**, 2046–2054 (2005).
116. Troche, P. *et al.* Thermally driven shape instability of multilayer structures. *Mater. Res.*

Soc. Symp. - Proc. **581**, 635–640 (2000).

117. Sharma, G., Ramanujan, R. V. & Tiwari, G. P. Instability mechanisms in lamellar microstructures. *Acta Mater.* **48**, 875–889 (2000).
118. Knoedler, H. L., Lucas, G. E. & Levi, C. G. Morphological stability of copper-silver multilayer thin films at elevated temperatures. *Metall. Mater. Trans. A Phys. Metall. Mater. Sci.* **34 A**, 1043–1054 (2003).
119. Zheng, S., Carpenter, J. S., Wang, J., Mara, N. A. & Beyerlein, I. J. An interface facet driven Rayleigh instability in high-aspect-ratio bimetallic nanolayered composites. *Appl. Phys. Lett.* **105**, (2014).
120. Ramos, A. S., Cavaleiro, A. J., Vieira, M. T., Morgiel, J. & Safran, G. Thermal stability of nanoscale metallic multilayers. *Thin Solid Films* **571**, 268–274 (2014).
121. Moszner, F. *et al.* Thermal stability of Cu/W nano-multilayers. *Acta Mater.* **107**, 345–353 (2016).
122. Zhai, Q., Kong, D., Morrone, A. & Ebrahimi, F. Characterization of High Strength Cu/Ag Multilayered Composites. in *Materials Research Society Symposium Proceedings* vol. 451 489–494 (1997).
123. Lee, H. J., Kwon, K. W., Ryu, C. & Sinclair, R. Thermal stability of a Cu/Ta multilayer: An intriguing interfacial reaction. *Acta Mater.* **47**, 3965–3975 (1999).
124. Ebrahimi, F., Zhai, Q. & Kong, D. Mechanical properties of Cu/Ag multilayered composites. *Mater. Sci. Eng. A* **255**, 20–32 (1998).
125. Zhang, W., Kennedy, G. B., Muly, K., Li, P. & Thadhani, N. N. Effect of aging state on shock induced spall behavior of ultrahigh strength Al–Zn–Mg–Cu alloy. *Int. J. Impact Eng.* **146**, 103725 (2020).
126. Zhang, L. F. *et al.* Study on thermal stability and irradiation response of copper/iron nano-multilayer composite fabricated by cross accumulative roll bonding. *J. Nucl. Mater.* **543**, (2021).
127. You, C. *et al.* High strength, high electrical conductivity and thermally stable bulk Cu/Ag nanolayered composites prepared by cross accumulative roll bonding. *Mater. Des.* **200**, 109455 (2021).
128. Zhang, X., Schulze, R. K., Wang, H. & Misra, A. Thermal stability of sputtered Cu/304 stainless steel multilayer films. *J. Appl. Phys.* **101**, (2007).

129. Edelstein, A. S. *et al.* Intermetallic phase formation during annealing of Al/Ni multilayers. *J. Appl. Phys.* **76**, 7850–7859 (1994).
130. Schoeppner, R. L. *et al.* Precipitate strengthening and thermal stability in three component metallic nanolaminate thin films. *Mater. Sci. Eng. A* **712**, 485–492 (2018).
131. Zheng, S. J. *et al.* Plastic instability mechanisms in bimetallic nanolayered composites. *Acta Mater.* **79**, 282–291 (2014).
132. Han, S. M., Phillips, M. A. & Nix, W. D. Study of strain softening behavior of Al-Al3Sc multilayers using microcompression testing. *Acta Mater.* **57**, 4473–4490 (2009).
133. Dayal, P., Quadir, M. Z., Kong, C., Savvides, N. & Hoffman, M. Transition from dislocation controlled plasticity to grain boundary mediated shear in nanolayered aluminum/palladium thin films. *Thin Solid Films* **519**, 3213–3220 (2011).
134. Cui, Y., Derby, B., Li, N., Mara, N. A. & Misra, A. Suppression of shear banding in high-strength Cu/Mo nanocomposites with hierarchical bicontinuous intertwined structures. *Mater. Res. Lett.* **6**, 184–190 (2018).
135. Buehler, M. J. & Misra, A. Mechanical behavior of nanocomposites. *MRS Bull.* **44**, 19–24 (2019).
136. Powers, M., Stewart, J. A., Dingreville, R., Derby, B. K. & Misra, A. Compositionally-driven formation mechanism of hierarchical morphologies in co-deposited immiscible alloy thin films. *Nanomaterials* **11**, 1–13 (2021).
137. Derby, B., Cui, Y., Baldwin, J. K. & Misra, A. Effects of substrate temperature and deposition rate on the phase separated morphology of co-sputtered, Cu-Mo thin films. *Thin Solid Films* **647**, 50–56 (2018).
138. Powers, M., Derby, B., Nerlige Manjunath, S. & Misra, A. Hierarchical morphologies in co-sputter deposited thin films. *Phys. Rev. Mater.* **4**, 1–13 (2020).
139. Raeker, E., Powers, M. & Misra, A. Mechanical performance of co-deposited immiscible Cu–Ta thin films. *Sci. Rep.* **10**, 1–10 (2020).
140. Darling, K. A., Roberts, A. J., Mishin, Y., Mathaudhu, S. N. & Kecskes, L. J. Grain size stabilization of nanocrystalline copper at high temperatures by alloying with tantalum. *J. Alloys Compd.* **573**, 142–150 (2013).
141. Darling, K. A. *et al.* Microstructure and mechanical properties of bulk nanostructured Cu-Ta alloys consolidated by equal channel angular extrusion. *Acta Mater.* **76**, 168–185

(2014).

142. Rajagopalan, M. *et al.* Microstructural evolution in a nanocrystalline Cu-Ta alloy: A combined in-situ TEM and atomistic study. *Mater. Des.* **113**, 178–185 (2017).
143. Koju, R. K., Darling, K. A., Kecskes, L. J. & Mishin, Y. Zener Pinning of Grain Boundaries and Structural Stability of Immiscible Alloys. *Jom* **68**, 1596–1604 (2016).
144. Atwater, M. A. *et al.* The thermal stability of nanocrystalline copper cryogenically milled with tungsten. *Mater. Sci. Eng. A* **558**, 226–233 (2012).
145. Botcharova, E., Freudenberger, J. & Schultz, L. Mechanical alloying of copper with niobium and molybdenum. *J. Mater. Sci.* **9**, 5287–5290 (2004).
146. Botcharova, E., Freudenberger, J. & Schultz, L. Mechanical and electrical properties of mechanically alloyed nanocrystalline Cu-Nb alloys. *Acta Mater.* **54**, 3333–3341 (2006).
147. Casem, D., Ligda, J., Walter, T., Darling, K. & Hornbuckle, B. Strain-Rate Sensitivity of Nanocrystalline Cu–10Ta to 700,000/s. *J. Dyn. Behav. Mater.* **6**, 24–33 (2020).
148. Kingstedt, O. T., Eftink, B., Lambros, J. & Robertson, I. M. Quasi-static and dynamic compressive deformation of a bulk nanolayered Ag-Cu eutectic alloy: Macroscopic response and dominant deformation mechanisms. *Mater. Sci. Eng. A* **595**, 54–63 (2014).
149. Eftink, B. P. *et al.* Anomalous deformation twinning in coarse-grained Cu in Ag60Cu40 composites under high strain-rate compressive loading. *Mater. Sci. Eng. A* **618**, 254–261 (2014).
150. Nizolek, T. J., Pollock, T. M. & McMeeking, R. M. Kink band and shear band localization in anisotropic perfectly plastic solids. *J. Mech. Phys. Solids* **146**, 104183 (2021).
151. Li, S., Beyerlein, I. J. & Bourke, M. A. M. Texture formation during equal channel angular extrusion of fcc and bcc materials: Comparison with simple shear. *Mater. Sci. Eng. A* **394**, 66–77 (2005).
152. Segal, V. M. Materials processing by simple shear. *Mater. Sci. Eng. A* **197**, 157–164 (1995).
153. Segal, V. Equal-channel angular extrusion (ECAE): From a laboratory curiosity to an industrial technology. *Metals (Basel).* **10**, (2020).
154. Valiev, R. Z. & Langdon, T. G. Principles of equal-channel angular pressing as a processing tool for grain refinement. *Prog. Mater. Sci.* **51**, 881–981 (2006).

155. Li, S., Gazder, A. A., Beyerlein, I. J., Davies, C. H. J. & Pereloma, E. V. Microstructure and texture evolution during equal channel angular extrusion of interstitial-free steel: Effects of die angle and processing route. *Acta Mater.* **55**, 1017–1032 (2007).
156. Beyerlein, I. J., Lebensohn, R. A. & Tomé, C. N. Modeling texture and microstructural evolution in the equal channel angular extrusion process. *Mater. Sci. Eng. A* **345**, 122–138 (2003).
157. Levin, Z. S., Demkowicz, M. J. & Hartwig, K. T. Copper-tantalum metal matrix composites consolidated from powder blends by severe plastic deformation. *Metals (Basel).* **11**, (2021).
158. Levin, Z. S. & Ted Hartwig, K. Hardness and microstructure of tungsten heavy alloy subjected to severe plastic deformation and post-processing heat treatment. *Mater. Sci. Eng. A* **635**, 94–101 (2015).
159. Dupuy, L. & Rauch, E. F. Deformation paths related to equal channel angular extrusion. *Mater. Sci. Eng. A* **337**, 241–247 (2002).
160. Skrotzki, W. *et al.* Microstructure and texture gradient in copper deformed by equal channel angular pressing. *Acta Mater.* **55**, 2013–2024 (2007).
161. Li, S., Beyerlein, I. J. & Necker, C. T. On the development of microstructure and texture heterogeneity in ECAE via route C. *Acta Mater.* **54**, 1397–1408 (2006).
162. Beyerlein, I. J. & Tóth, L. S. Texture evolution in equal-channel angular extrusion. *Prog. Mater. Sci.* **54**, 427–510 (2009).
163. Mishra, A., Kad, B. K., Gregori, F. & Meyers, M. A. Microstructural evolution in copper subjected to severe plastic deformation: Experiments and analysis. *Acta Mater.* **55**, 13–28 (2007).
164. Dalla Torre, F. *et al.* Microstructures and properties of copper processed by equal channel angular extrusion for 1-16 passes. *Acta Mater.* **52**, 4819–4832 (2004).
165. Dalla Torre, F. H., Gazder, A. A., Gu, C. F., Davies, C. H. J. & Pereloma, E. V. Grain size, misorientation, and texture evolution of copper processed by equal channel angular extrusion and the validity of the Hall-Petch relationship. *Metall. Mater. Trans. A Phys. Metall. Mater. Sci.* **38**, 1080–1095 (2007).
166. Ferrasse, S., Segal, V. M., Ted Hartwig, K. & Goforth, R. E. Microstructure and properties of copper and aluminum alloy 3003 heavily worked by equal channel angular

extrusion. *Metall. Mater. Trans. A Phys. Metall. Mater. Sci.* **28**, 1047–1057 (1997).

167. Li, S., Gazder, A. A., Beyerlein, I. J., Pereloma, E. V. & Davies, C. H. J. Effect of processing route on microstructure and texture development in equal channel angular extrusion of interstitial-free steel. *Acta Mater.* **54**, 1087–1100 (2006).
168. Lugo, N., Llorca, N., Suñol, J. J. & Cabrera, J. M. Thermal stability of ultrafine grains size of pure copper obtained by equal-channel angular pressing. *J. Mater. Sci.* **45**, 2264–2273 (2010).
169. Wei, Q. *et al.* Microstructure and mechanical properties of tantalum after equal channel angular extrusion (ECAE). *Mater. Sci. Eng. A* **358**, 266–272 (2003).
170. Pan, Z. *et al.* Microstructural evolution and mechanical properties of niobium processed by equal channel angular extrusion up to 24 passes. *Acta Mater.* **60**, 2310–2323 (2012).
171. Meyers, M. A., Mishra, A. & Benson, D. J. Mechanical properties of nanocrystalline materials. *Prog. Mater. Sci.* **51**, 427–556 (2006).
172. Al-Maharbi, M., Karaman, I. & Purcek, G. Flow response of a severe plastically deformed two-phase zinc-aluminum alloy. *Mater. Sci. Eng. A* **527**, 518–525 (2010).
173. Tolaminejad, B., Hoseini Athar, M. M., Arabi, H. & Karimi Taheri, A. Enhanced grain refinement of commercial pure copper using the ECAE of Al–Cu–Al tri-layer composite. *Eng. Sci. Technol. an Int. J.* **19**, 254–259 (2016).
174. Sun, P. L. & Huang, S. J. Effect of strain-path change on the anisotropic mechanical properties of a commercially pure aluminum. *IOP Conf. Ser. Mater. Sci. Eng.* **219**, (2017).
175. Beyerlein, I. J., Alexander, D. J. & Tome, C. N. Plastic anisotropy in aluminum and copper pre-strained by equal channel angular extrusion. *J. Mater. Sci.* **42**, 1733–1750 (2007).
176. Alexander, D. J. & Beyerlein, I. J. Anisotropy in mechanical properties of high-purity copper processed by equal channel angular extrusion. *Mater. Sci. Eng. A* **410**–**411**, 480–484 (2005).
177. Beyerlein, I. J. & Tomé, C. N. Modeling transients in the mechanical response of copper due to strain path changes. *Int. J. Plast.* **23**, 640–664 (2007).
178. Purcek, G. *et al.* Optimization of strength, ductility and electrical conductivity of Cu-Cr-Zr alloy by combining multi-route ECAP and aging. *Mater. Sci. Eng. A* **649**, 114–

122 (2016).

179. Purcek, G., Saray, O., Karaman, I. & Maier, H. J. High strength and high ductility of ultrafine-grained, interstitial-free steel produced by ecae and annealing. *Metall. Mater. Trans. A Phys. Metall. Mater. Sci.* **43**, 1884–1894 (2012).
180. Purcek, G., Saray, O., Karaman, I. & Haouaoui, M. Microstructural evolution and mechanical response of equal-channel angular extrusion-processed Al-40Zn-2Cu alloy. *Metall. Mater. Trans. A Phys. Metall. Mater. Sci.* **40**, 2772–2783 (2009).
181. Susan, D. F., Jozaghi, T., Karaman, I. & Rodelas, J. M. Equal channel angular extrusion for bulk processing of Fe-Co-2V soft magnetic alloys, part I: Processing and mechanical properties. *J. Mater. Res.* **33**, 2168–2175 (2018).
182. Semenova, I. P., Raab, G. I., Saitova, L. R. & Valiev, R. Z. The effect of equal-channel angular pressing on the structure and mechanical behavior of Ti-6Al-4V alloy. *Mater. Sci. Eng. A* **387**–**389**, 805–808 (2004).
183. Xu, C., Furukawa, M., Horita, Z. & Langdon, T. G. Using ECAP to achieve grain refinement, precipitate fragmentation and high strain rate superplasticity in a spray-cast aluminum alloy. *Acta Mater.* **51**, 6139–6149 (2003).
184. Murayama, M., Horita, Z. & Hono, K. Microstructure of two-phase Al-1.7 at% Cu alloy deformed by equal-channel angular pressing. *Acta Mater.* **49**, 21–29 (2001).
185. Huang, Y., Robson, J. D. & Prangnell, P. B. The formation of nanograin structures and accelerated room-temperature theta precipitation in a severely deformed Al-4 wt.% Cu alloy. *Acta Mater.* **58**, 1643–1657 (2010).
186. Tsai, M. S., Sun, P. L., Kao, P. W. & Chang, C. P. Influence of severe plastic deformation on precipitation hardening in an Al-Mg-Si Alloy: Microstructure and mechanical properties. *Mater. Trans.* **50**, 771–775 (2009).
187. Ma, X. L. *et al.* Dynamic precipitation and recrystallization in Mg-9wt.%Al during equal-channel angular extrusion: A comparative study to conventional aging. *Acta Mater.* **172**, 185–199 (2019).
188. Deschamps, A. *et al.* Low-temperature dynamic precipitation in a supersaturated Al-Zn-Mg alloy and related strain hardening. *Philos. Mag. A Phys. Condens. Matter, Struct. Defects Mech. Prop.* **79**, 2485–2504 (1999).
189. Arab, M. S., El Mahallawy, N., Shehata, F. & Agwa, M. A. Refining SiCp in reinforced

Al-SiC composites using equal-channel angular pressing. *Mater. Des.* **64**, 280–286 (2014).

190. Huang, S. J., Lin, P. C. & Aoh, J. N. Mechanical behavior enhancement of AM60/Al2O3p magnesium metal-matrix nanocomposites by ECAE. *Mater. Manuf. Process.* **30**, 1272–1277 (2015).
191. Mathaudhu, S. N., Ted Hartwig, K. & Karaman, I. Consolidation of blended powders by severe plastic deformation to form amorphous metal matrix composites. *J. Non. Cryst. Solids* **353**, 185–193 (2007).
192. Cho, K. J., Lee, J. H., Oh, K. W., Nathanael, A. J. & Hong, S. I. Microstructural evolution of Cu-Ag in-situ composites processed by equal channel angular pressing (ECAP). *ICCM Int. Conf. Compos. Mater.* 1–6 (2011).
193. Darling, K. A., Huskins, E. L., Schuster, B. E., Wei, Q. & Kecskes, L. J. Mechanical properties of a high strength Cu-Ta composite at elevated temperature. *Mater. Sci. Eng. A* **638**, 322–328 (2015).
194. Wei, Q. *et al.* Adiabatic shear banding in ultrafine-grained Fe processed by severe plastic deformation. *Acta Mater.* **52**, 1859–1869 (2004).
195. Wei, Q. *et al.* Dynamic behaviors of body-centered cubic metals with ultrafine grained and nanocrystalline microstructures. *Mater. Sci. Eng. A* **493**, 58–64 (2008).
196. Kannan, V. *et al.* The effect of strain rate on the mechanisms of plastic flow and failure of an ECAE AZ31B magnesium alloy. *J. Mater. Sci.* **54**, 13394–13419 (2019).
197. Li, J., Suo, T., Li, Y., Kecskes, L. J. & Wei, Q. Mechanical properties and failure of ECAE processed Mg97Y2Zn1 at different strain rates. *Mater. Sci. Eng. A* **762**, 138094 (2019).
198. Dodd, B. & Bai, Y. *Adiabatic Shear Localization*. *Adiabatic Shear Localization* (Elsevier, 2012). doi:10.1016/C2011-0-06979-X.
199. Meyers, M. A. *Dynamic Behavior of Materials*. *Dynamic Behavior of Materials* (John Wiley & Sons, 1994).
200. Zhao, Y. H., Liao, X. Z., Cheng, S., Ma, E. & Zhu, Y. T. Simultaneously increasing the ductility and strength of nanostructured alloys. *Adv. Mater.* **18**, 2280–2283 (2006).
201. Dalla Torre, F. H., Gazder, A. A., Pereloma, E. V. & Davies, C. H. J. Recent progress on the study of the microstructure and mechanical properties of ECAE copper. *J. Mater.*

Sci. **42**, 9097–9111 (2007).

202. Semiatin, S. L. & DeLo, D. P. Equal channel angular extrusion of difficult-to-work alloys. *Mater. Des.* **21**, 311–322 (2000).
203. Mishra, A. *et al.* High-strain-rate response of ultra-fine-grained copper. *Acta Mater.* **56**, 2770–2783 (2008).
204. Li, J., Li, Y., Huang, C., Suo, T. & Wei, Q. On adiabatic shear localization in nanostructured face-centered cubic alloys with different stacking fault energies. *Acta Mater.* **141**, 163–182 (2017).
205. Kim, Y. G., Hwang, B., Lee, S., Lee, C. W. & Shin, D. H. Dynamic deformation and fracture behavior of ultra-fine-grained pure copper fabricated by equal channel angular pressing. *Mater. Sci. Eng. A* **504**, 163–168 (2009).
206. Dong, Y. C., Alexandrov, I. V. & Wang, J. T. The dynamic behavior of ultra-fine-grained copper fabricated by equal channel angular pressing. *Mater. Sci. Forum* **667**–**669**, 891–896 (2011).
207. Lutjering, G. & Williams, J. C. *Titanium*. (Springer-Verlag, 2007). doi:10.1108/eb007316.
208. Garzarolli, F., Adamson, R. & Coleman, K. Microstructure of Zirconium Alloys and Effects on Performance. *Adv. Nucl. Technol. Int. Eur. AB, ANT Int.* 41 (2015).
209. Tiwary, C. S. *et al.* Five decades of research on the development of eutectic as engineering materials. *Prog. Mater. Sci.* **123**, 100793 (2022).
210. Chanda, B., Potnis, G., Jana, P. P. & Das, J. A review on nano-/ultrafine advanced eutectic alloys. *J. Alloys Compd.* **827**, 154226 (2020).
211. Wang, L. *et al.* Simultaneously enhancing strength and ductility of Ti-6Al-4V alloy with the hierarchical structure via a novel thermal annealing treatment. *Mater. Charact.* **176**, 111112 (2021).
212. Chadwick, G. A. Structure and Properties of Eutectic Alloys. *Met. Sci.* **9**, 300–304 (1975).
213. Chadwick, G. A. Yield Point Analyses in Eutectic. *Acta Metall.* **24**, 1137–1146 (1976).
214. Cooksey, D. J. S., Munson, D., Wilkinson, M. P. & Hellawell, A. The freezing of some continuous binary eutectic mixtures. *Philos. Mag.* **10**, 745–769 (1964).
215. Kingstedt, O. T., Eftink, B. P., Robertson, I. M. & Lambros, J. Anisotropic dynamic

compression response of a directionally-cast silver-copper eutectic alloy. *Acta Mater.* **105**, 273–283 (2016).

216. Sun, B. B. *et al.* Ultrafine composite microstructure in a bulk Ti alloy for high strength, strain hardening and tensile ductility. *Acta Mater.* **54**, 1349–1357 (2006).
217. Ma, E. & Zhu, T. Towards strength–ductility synergy through the design of heterogeneous nanostructures in metals. *Mater. Today* **20**, 323–331 (2017).
218. Shukla, S. *et al.* Hierarchical features infused heterogeneous grain structure for extraordinary strength-ductility synergy. *Mater. Res. Lett.* **6**, 676–682 (2018).
219. Kang, L. M. & Yang, C. A Review on High-Strength Titanium Alloys: Microstructure, Strengthening, and Properties. *Adv. Eng. Mater.* **21**, (2019).
220. He, G., Eckert, J., Löser, W. & Schultz, L. Novel Ti-base nanostructure-dendrite composite with enhanced plasticity. *Nat. Mater.* **2**, 33–37 (2003).
221. Conrad, H. Thermally activated deformation of metals. *Jom* **16**, 582–588 (1964).
222. Rusty Gray, G. T. High-strain-rate deformation: Mechanical behavior and deformation substructures induced. *Annu. Rev. Mater. Res.* **42**, 285–303 (2012).
223. Sheinerman, A. G. & Bobylev, S. V. A model of enhanced strain rate sensitivity in nanocrystalline and ultrafine-grained metals. *Rev. Adv. Mater. Sci.* **57**, 1–10 (2018).
224. Wang, Y. M. & Ma, E. Strain hardening, strain rate sensitivity, and ductility of nanostructured metals. *Mater. Sci. Eng. A* **375**–**377**, 46–52 (2004).
225. Borodin, E. N., Gruzdkov, A. A., Mayer, A. E. & Selyutina, N. S. Physical nature of strain rate sensitivity of metals and alloys at high strain rates. *J. Phys. Conf. Ser.* **991**, (2018).
226. Chen, J., Lu, L. & Lu, K. Hardness and strain rate sensitivity of nanocrystalline Cu. *Scr. Mater.* **54**, 1913–1918 (2006).
227. Armstrong, R. W. & Walley, S. M. High strain rate properties of metals and alloys. *Int. Mater. Rev.* **53**, 105–128 (2008).
228. Zhou, Q. *et al.* Strain rate sensitivity of Cu/Ta multilayered films: Comparison between grain boundary and heterophase interface. *Scr. Mater.* **111**, 123–126 (2016).
229. Dao, M., Lu, L., Asaro, R. J., De Hosson, J. T. M. & Ma, E. Toward a quantitative understanding of mechanical behavior of nanocrystalline metals. *Acta Mater.* **55**, 4041–4065 (2007).

230. Wei, Q., Cheng, S., Ramesh, K. T. & Ma, E. Effect of nanocrystalline and ultrafine grain sizes on the strain rate sensitivity and activation volume: Fcc versus bcc metals. *Mater. Sci. Eng. A* **381**, 71–79 (2004).
231. Lu, Y. Y. *et al.* The microstructure and mechanical behavior of Mg/Ti multilayers as a function of individual layer thickness. *Acta Mater.* **63**, 216–231 (2014).
232. Liu, Y., Yang, K. M., Hay, J., Fu, E. G. & Zhang, X. The effect of coherent interface on strain-rate sensitivity of highly textured Cu/Ni and Cu/V multilayers. *Scr. Mater.* **162**, 33–37 (2019).
233. Zhou, Q., Wang, F., Huang, P. & Xu, K. W. Strain rate sensitivity and related plastic deformation mechanism transition in nanoscale Ag/W multilayers. *Thin Solid Films* **571**, 253–259 (2014).
234. Huang, P., Wang, F., Xu, M., Lu, T. J. & Xu, K. W. Strain rate sensitivity of unequal grained nano-multilayers. *Mater. Sci. Eng. A* **528**, 5908–5913 (2011).
235. Cao, Z. H. *et al.* Cyclic deformation induced strengthening and unusual rate sensitivity in Cu/Ru nanolayered films. *Int. J. Plast.* **99**, 43–57 (2017).
236. Snel, J. *et al.* Deformation Mechanism Map of Cu/Nb Nanoscale Metallic Multilayers as a Function of Temperature and Layer Thickness. *Jom* **69**, 2214–2226 (2017).
237. Zhang, Z., Jun, T. S., Britton, T. B. & Dunne, F. P. E. Determination of Ti-6242 α and β slip properties using micro-pillar test and computational crystal plasticity.pdf. *J. Mech. Phys. Solids* **95**, 393–410 (2016).
238. Zhang, Z., Jun, T. S., Britton, T. B. & Dunne, F. P. E. Intrinsic anisotropy of strain rate sensitivity in single crystal alpha titanium. *Acta Mater.* **118**, 317–330 (2016).
239. Jun, T. S., Armstrong, D. E. J. & Britton, T. B. A nanoindentation investigation of local strain rate sensitivity in dual-phase Ti alloys. *J. Alloys Compd.* **672**, 282–291 (2016).
240. Savage, M. F., Tatalovich, J. & Mills, M. J. Anisotropy in the room-temperature deformation of α-β colonies in titanium alloys: Role of the α-β interface. *Philos. Mag.* **84**, 1127–1154 (2004).
241. Zheng, Z., Waheed, S., Balint, D. S. & Dunne, F. P. E. Slip transfer across phase boundaries in dual phase titanium alloys and the effect on strain rate sensitivity. *Int. J. Plast.* **104**, 23–38 (2018).
242. Zhang, J. Y. *et al.* Strain rate sensitivity of nanolayered Cu/X (X=Cr, Zr) micropillars:

Effects of heterophase interface/twin boundary. *Mater. Sci. Eng. A* **612**, 28–40 (2014).

243. Molinari, A. & Clifton, R. J. Analytical Characterization of Shear Localization in Thermoviscoplastic Materials. *Am. Soc. Mech. Eng.* **54**, 806–812 (1987).
244. Antolovich, S. D. & Armstrong, R. W. Plastic strain localization in metals: Origins and consequences. *Prog. Mater. Sci.* **59**, 1–160 (2014).
245. Bordignon, N., Piccolroaz, A., Dal Corso, F. & Bigoni, D. Strain localization and shear band propagation in ductile materials. *Front. Mater.* **2**, 1–13 (2015).
246. Walley, S. M. Shear localization: A historical overview. *Metall. Mater. Trans. A Phys. Metall. Mater. Sci.* **38 A**, 2629–2654 (2007).
247. Tresca, M. H. *On Further Applications of the Flow of Solids*. (1878).
248. Marchand, A. & Duffy, J. An experimental study of the formation process of adiabatic shear bands in a structural steel. *J. Mech. Phys. Solids* **36**, 251–283 (1988).
249. Duffy, J. & Chi, Y. C. On the measurement of local strain and temperature during the formation of adiabatic shear bands. *Mater. Sci. Eng. A* **157**, 195–210 (1992).
250. Staker, M. R. The relation between adiabatic shear instability strain and material properties. *Acta Metall.* **29**, 683–689 (1981).
251. Wright, T. W. & Walter, J. W. *On Stress Collapse in Adiabatic Shear Bands*. (1987).
252. Guo, Y. Z., Li, Y. L., Pan, Z., Zhou, F. H. & Wei, Q. A numerical study of microstructure effect on adiabatic shear instability: Application to nanostructured ultrafine grained materials.pdf. *Mech. Mater.* **42**, 1020–1029 (2010).
253. Duffy, J. *The Dynamic Plastic Deformation of Metals: A Review*. (1982).
254. Kuroda, M. & Tvergaard, V. Effects of texture on shear band formation in plane strain tension/compression and bending. *Int. J. Plast.* **23**, 244–272 (2007).
255. Joshi, S. P. & Ramesh, K. T. Grain size dependent shear instabilities in body-centered and face-centered cubic materials. *Mater. Sci. Eng. A* **493**, 65–70 (2008).
256. Lee, C. S. & Duggan, B. J. A dislocation avalanche theory of shear banding. *Acta Metall. Mater.* **42**, 857–860 (1994).
257. Dillamore, I. L., Roberts, J. G. & Bush, A. C. Occurrence of shear bands in heavily rolled cubic metals. *Met. Sci.* **13**, 73–77 (1979).
258. Wei, Q., Jia, D., Ramesh, K. T. & Ma, E. Evolution and microstructure of shear bands in nanostructured Fe. *Appl. Phys. Lett.* **81**, 1240–1242 (2002).

259. Rittel, D., Landau, P. & Venkert, A. Dynamic recrystallization as a potential cause for adiabatic shear failure. *Phys. Rev. Lett.* **101**, 2–5 (2008).
260. Rittel, D., Wang, Z. G. & Merzer, M. Adiabatic shear failure and dynamic stored energy of cold work. *Phys. Rev. Lett.* **96**, 1–4 (2006).
261. Landau, P., Osovski, S., Venkert, A., Gärtnerová, V. & Rittel, D. The genesis of adiabatic shear bands. *Sci. Rep.* **6**, 4–9 (2016).
262. Longere, P. Respective/combined roles of thermal softening and dynamic recrystallization in adiabatic shear banding initiation. *Mech. Mater.* **117**, 81–90 (2018).
263. Osovski, S., Rittel, D., Landau, P. & Venkert, A. Microstructural effects on adiabatic shear band formation. *Scr. Mater.* **66**, 9–12 (2012).
264. Dai, L. H., Liu, L. F. & Bai, Y. L. Formation of adiabatic shear band in metal matrix composites. *Int. J. Solids Struct.* **41**, 5979–5993 (2004).
265. Liu, X. *et al.* Influence of microstructure and strain rate on adiabatic shearing behavior in Ti-6Al-4V alloys. *Mater. Sci. Eng. A* **501**, 30–36 (2009).
266. Zheng, C. *et al.* Capturing of the propagating processes of adiabatic shear band in Ti-6Al-4V alloys under dynamic compression. *Mater. Sci. Eng. A* **658**, 60–67 (2016).
267. Han, W. Z. *et al.* Deformation and failure of shocked bulk Cu-Nb nanolaminates. *Acta Mater.* **63**, 150–161 (2014).
268. Chen, J., Mathaudhu, S. N., Thadhani, N. & Dongare, A. M. Unraveling the Role of Interfaces on the Spall Failure of Cu/Ta Multilayered Systems. *Sci. Rep.* **10**, 1–15 (2020).
269. Zhang, R. F., Germann, T. C., Wang, J., Liu, X. Y. & Beyerlein, I. J. Role of interface structure on the plastic response of Cu/Nb nanolaminates under shock compression: Non-equilibrium molecular dynamics simulations. *Scr. Mater.* **68**, 114–117 (2013).
270. Fensin, S. J. *et al.* Dynamic failure in two-phase materials. *J. Appl. Phys.* **118**, (2015).
271. Me-Bar, Y., Boas, M. & Rosenberg, Z. *Spall Studies on Ti-6AI-4V*. *Materials Science and Engineering* vol. 85 (1987).
272. Boidin, X., Chevrier, P., Klepaczko, J. R. & Sabar, H. Identification of damage mechanism and validation of a fracture model based on mesoscale approach in spalling of titanium alloy. *Int. J. Solids Struct.* **43**, 4595–4615 (2006).
273. Ren, Y. *et al.* Shock-induced mechanical response and spall fracture behavior of an

extra-low interstitial grade Ti-6Al-4V alloy. *Mater. Sci. Eng. A* **578**, 247–255 (2013).

274. Yang, Y. *et al.* Effects of the phase interface on spallation damage nucleation and evolution in multiphase alloy. *J. Alloys Compd.* **740**, 321–329 (2018).
275. Chen, J., Mathaudhu, S. N., Thadhani, N. & Dongare, A. M. Correlations between dislocation density evolution and spall strengths of Cu/Ta multilayered systems at the atomic scales: The role of spacing of KS interfaces. *Materialia* **5**, 100192 (2019).
276. Wielewski, E., Appleby-Thomas, G. J., Hazell, P. J. & Hameed, A. An experimental investigation into the micro-mechanics of spall initiation and propagation in Ti-6Al-4V during shock loading. *Mater. Sci. Eng. A* **578**, 331–339 (2013).
277. Hazell, P. J., Appleby-Thomas, G. J., Wielewski, E. & Escobedo, J. P. The shock and spall response of three industrially important hexagonal close-packed metals: Magnesium, titanium and zirconium. *Philos. Trans. R. Soc. A Math. Phys. Eng. Sci.* **372**, (2014).
278. Gray, G. T., Bourne, N. K., Vecchio, K. S. & Millett, J. C. F. Influence of anisotropy (crystallographic and microstructural) on spallation in Zr, Ta, HY-100 steel, and 1080 eutectoid steel. *Int. J. Fract.* **163**, 243–258 (2010).
279. Hazell, P. J., Appleby-Thomas, G. J., Wielewski, E., Stennett, C. & Siviour, C. The influence of microstructure on the shock and spall behaviour of the magnesium alloy, Elektron 675. *Acta Mater.* **60**, 6042–6050 (2012).
280. Meyers, M. A. & Taylor Aimone, C. Dynamic fracture (spalling) of metals. *Prog. Mater. Sci.* **28**, 1–96 (1983).
281. Gray, G. T. Material response to shock/dynamic loading: Windows into kinetic and stress-state effects on defect generation and damage evolution. *AIP Conf. Proc.* **1426**, 19–26 (2012).
282. Clifton, R. J. Dynamic plasticity. *J. Appl. Mech.* **50**, 941–952 (1983).
283. Ardeljan, M. *et al.* A study of microstructure-driven strain localizations in two-phase polycrystalline HCP/BCC composites using a multi-scale model. *Int. J. Plast.* **74**, 35–57 (2015).
284. Rusty, G. T. & Iii, G. Classic Split-Hopkinson Pressure Bar Testing. *Mech. Test. Eval.* 462–476 (2018) doi:10.31399/asm.hb.v08.a0003296.
285. Ramesh, K. T. High Strain Rate and Impact Experiments. in *Handbook of Experimental*

Solid Mechanics (ed. Sharpe Jr., W. N.) (Springer, 2008).

286. Otooni, M. A., Brown, I., You, X. & Foner, S. Tantalum ion implantation into Cu-12Nb for electromagnetic railgun technology. *Mater. Res. Soc. Symp. Proc.* **316**, 569–575 (1994).
287. Ferrasse, S., Segal, V. M., Alford, F., Kardokus, J. & Strothers, S. Scale up and application of equal-channel angular extrusion for the electronics and aerospace industries. *Mater. Sci. Eng. A* **493**, 130–140 (2008).
288. Tschopp, M. A., Murdoch, H. A., Kecskes, L. J. & Darling, K. A. Bulk nanocrystalline metals: Review of the current state of the art and future opportunities for copper and copper alloys. *J. Mater.* **66**, 1000–1019 (2014).
289. Ding, C., Xu, J., Shan, D., Guo, B. & Langdon, T. G. Sustainable fabrication of Cu/Nb composites with continuous laminated structure to achieve ultrahigh strength and excellent electrical conductivity. *Compos. Part B Eng.* **211**, 108662 (2021).
290. Edgecumbe Summers, T. S. *et al.* ECAE-PROCESSED Cu-Nb AND Cu-Ag NANOCOMPOSITE WIRES FOR PULSE MAGNET APPLICATIONS. *Adv. Cryog. Eng.* **42**, 499–505 (1996).
291. Chookajorn, T., Murdoch, H. A. & Schuh, C. A. Design of Stable Nanocrystalline Alloys. *Science (80-.).* **337**, 951–955 (2012).
292. Valiev, R. Z. *et al.* Fundamentals of superior properties in bulk NanoSPD materials. *Mater. Res. Lett.* **4**, 1–21 (2016).
293. Valiev, R. Z., Alexandrov, I. V., Zhu, Y. T. & Lowe, T. C. Paradox of strength and ductility in metals processed by severe plastic deformation. *J. Mater. Res.* **17**, 5–8 (2002).
294. Raabe, D., Ohsaki, S. & Hono, K. Mechanical alloying and amorphization in Cu-Nb-Ag in situ composite wires studied by transmission electron microscopy and atom probe tomography. *Acta Mater.* **57**, 5254–5263 (2009).
295. Langdon, T. G. Twenty-five years of ultrafine-grained materials: Achieving exceptional properties through grain refinement. *Acta Mater.* **61**, 7035–7059 (2013).
296. Buet, E. *et al.* Microstructure and texture of copper/niobium composites processed by ECAE. *Int. J. Mater. Form.* **5**, 121–127 (2012).
297. Gray, G. T., Lowe, T. C., Cady, C. M., Valiev, R. Z. & Aleksandrov, I. V. Influence of

strain rate & temperature on the mechanical response of ultrafine-grained Cu, Ni, and Al-4Cu-0.5Zr. *Nanostructured Mater.* **9**, 477–480 (1997).

298. Aimone, P. H. C. Starck, Inc. (2019).
299. Albert, C. & Albert, L. ACI Alloys. (2019).
300. Nizolek, T. J. *et al.* Strain fields induced by kink band propagation in Cu-Nb nanolaminate composites. *Acta Mater.* **133**, 303–315 (2017).
301. Lenthe, W. C., Singh, S. & Graef, M. De. A spherical harmonic transform approach to the indexing of electron back-scattered diffraction patterns. *Ultramicroscopy* **207**, 112841 (2019).
302. Bachmann, F., Hielscher, R. & Schaeben, H. Texture analysis with MTEX- Free and open source software toolbox. *Solid State Phenom.* **160**, 63–68 (2010).
303. Li, S., Beyerlein, I. J. & Alexander, D. J. Characterization of deformation textures in pure copper processed by equal channel angular extrusion via route A. *Mater. Sci. Eng. A* **431**, 339–345 (2006).
304. Estrin, Y. *et al.* Effect of microstructure on plastic deformation of Cu at low homologous temperatures. *Acta Mater.* **54**, 5581–5590 (2006).
305. Field, D. P., Bradford, L. T., Nowell, M. M. & Lillo, T. M. The role of annealing twins during recrystallization of Cu. *Acta Mater.* **55**, 4233–4241 (2007).
306. Beyerlein, I. J., Li, S. & Alexander, D. J. Modeling the plastic anisotropy in pure copper after one pass of ECAE. *Mater. Sci. Eng. A* **410**–**411**, 201–206 (2005).
307. Hsu, S. Y., Vogler, T. J. & Kyriakides, S. On the axial propagation of kink bands in fiber composites : Part ii analysis. *Int. J. Solids Struct.* **36**, 575–595 (1999).
308. Piela, K. & Korbel, A. Mechanism of kink band formation in zinc single crystals. *Int. J. Mater. Res.* **112**, 63–67 (2021).
309. Bernard Anderson, T. The relationship between kink-bands and shear fractures in the experimental deformation of slate. *J. Geol. Soc. London.* **130**, 367–382 (1974).
310. Hunt, G. W., Dodwell, T. J. & Hammond, J. On the nucleation and growth of kink and shear bands. *Philos. Trans. R. Soc. A Math. Phys. Eng. Sci.* **371**, (2013).
311. Tenckhoff, E. *Deformation Mechanisms, Texture, and Anisotropy in Zirconium and Zircaloy*. (1988).
312. Whitmarsh, C. L. *Review of Zircaloy-2 and Zircaloy-4 Properties Relevant to N.S.*

Savannah Reactor Design. vol. 17 (1962).

313. Allegheny Technologies Incorporated. Zirconium Alloys Technical Data Sheet. vol. 1 1–3 (2015).
314. Lemaignan, C. & Motta, A. Zirconium Alloys in Nuclear Applications. in *Nuclear Materials, Part 2* (eds. Frost, B. R. T., Cahn, R. W., Haasen, P. & Kramer, E. J.) vol. 10B 1–47 (VCH Verlagsgesellschaft mbH, 1994).
315. Himbeault, D. D., Chow, C. K. & Puls, M. P. Deformation behavior of irradiated Zr-2.5Nb pressure tube material. *Metall. Mater. Trans. A* **25**, 135–145 (1994).
316. Holt, R. A. & Zhao, P. Micro-texture of extruded Zr-2.5Nb tubes. *J. Nucl. Mater.* **335**, 520–528 (2004).
317. Zhang, M. *et al.* Effect of annealing treatment on the microstructure and mechanical properties of a duplex Zr-2.5Nb alloy. *Mater. Sci. Eng. A* **706**, 236–241 (2017).
318. Fuloria, D., Kumar, N., Jayaganthan, R., Jha, S. K. & Srivastava, D. An investigation of effect of annealing at different temperatures on microstructures and bulk textures development in deformed Zircaloy-4. *Mater. Charact.* **129**, 217–233 (2017).
319. Lutjering, G. Influence of processing on microstructure and mechanical properties of (a+b) titanium alloys. *Mater. Sci. Eng.* **243**, 32–45 (1998).
320. Straumal, B. B. *et al.* Phase transformations in the severely plastically deformed Zr-Nb alloys. *Mater. Lett.* **81**, 225–228 (2012).
321. Dai, C., Saidi, P., Béland, L. K., Yao, Z. & Daymond, M. R. Asymmetrical response of edge pyramidal dislocations in HCP zirconium under tension and compression: A molecular dynamics study. *Comput. Mater. Sci.* **170**, 109183 (2019).
322. Tewari, R., Srivastava, D., Dey, G. K., Chakravarty, J. K. & Banerjee, S. Microstructural evolution in zirconium based alloys. *J. Nucl. Mater.* **383**, 153–171 (2008).
323. Dai, J. *et al.* Comparative study of microstructural characteristics and hardness of β-Quenched Zr702 and Zr-2.5Nb alloys. *Materials (Basel).* **12**, 1–11 (2019).
324. Yang, Z. N. *et al.* Formation of duplex microstructure in Zr-2.3Nb alloy and its plastic behaviour at various strain rates. *Int. J. Plast.* **54**, 163–177 (2014).
325. Wang, Y., Chen, M., Zhou, F. & Ma, E. High tensile ductility in a nanostructured metal. *Nature* **419**, 912 (2002).
326. Zhu, Y. *et al.* Heterostructured materials: superior properties from hetero-zone

interaction. *Mater. Res. Lett.* **9**, 1–31 (2021).

327. Wu, X. *et al.* Heterogeneous lamella structure unites ultrafine-grain strength with coarse-grain ductility. *Proc. Natl. Acad. Sci. U. S. A.* **112**, 14501–14505 (2015).
328. Bao, X., Chen, W., Zhang, J., Yue, Y. & Sun, J. Achieving high strength-ductility synergy in a hierarchical structured metastable β-titanium alloy using through-transus forging. *J. Mater. Res. Technol.* **11**, 1622–1636 (2021).
329. Zhang, J. W., Beyerlein, I. J. & Han, W. Z. Hierarchical 3D Nanolayered Duplex-Phase Zr with High Strength, Strain Hardening, and Ductility. *Phys. Rev. Lett.* **122**, (2019).
330. Zou, X. W., Zhang, J. W. & Han, W. Z. Thermal stable hierarchical 3D nanolayered Zr-2.5Nb. *J. Mater. Res.* **36**, 2630–2638 (2021).
331. Beyerlein, I. J. & Wang, J. Interface-driven mechanisms in cubic/noncubic nanolaminates at different scales. *MRS Bull.* **44**, 31–39 (2019).
332. Beyerlein, I. J., Demkowicz, M. J., Misra, A. & Uberuaga, B. P. Defect-interface interactions. *Prog. Mater. Sci.* **74**, 125–210 (2015).
333. Misra, A., Demkowicz, M. J., Zhang, X. & Hoagland, R. G. The Radiation Damage Tolerance of Ultra-High Strength Nanolayered Composites. *J. Mater.* 62–65 (2007).
334. Abriata, J. P. & Bolcich, J. C. The Nb-Zr (Niobium-Zirconium) system. *Bull. Alloy Phase Diagrams* **3**, 34–44 (1982).
335. Zhan, H., Kent, D., Wang, G. & Dargusch, M. S. The dynamic response of a β titanium alloy to high strain rates and elevated temperatures. *Mater. Sci. Eng. A* **607**, 417–426 (2014).
336. Meyers, M. A., Subhash, G., Kad, B. K. & Prasad, L. Evolution of microstructure and shear-band formation in α-hcp titanium. *Mech. Mater.* **17**, 175–193 (1994).
337. Zhang, Z., Eakins, D. E. & Dunne, F. P. E. On the formation of adiabatic shear bands in textured HCP polycrystals. *Int. J. Plast.* **79**, 196–216 (2016).
338. Zou, D. L., Luan, B. F., Liu, Q., Chai, L. J. & Chen, J. W. Formation and evolution of adiabatic shear bands in zirconium alloy impacted by split Hopkinson pressure bar. *J. Nucl. Mater.* **437**, 380–388 (2013).
339. Xu, Y., Zhang, J., Bai, Y. & Meyers, M. A. Shear localization in dynamic deformation: Microstructural evolution. *Metall. Mater. Trans. A Phys. Metall. Mater. Sci.* **39 A**, 811–843 (2008).

340. Liu, X. *et al.* Dynamic Mechanical Behavior and Adiabatic Shear Bands of Ultrafine Grained Pure Zirconium. *J. Wuhan Univ. Technol. Mater. Sci. Ed.* **35**, 200–207 (2020).
341. Zheng, C. *et al.* Failure mechanisms in ballistic performance of Ti-6Al-4V targets having equiaxed and lamellar microstructures. *Int. J. Impact Eng.* **85**, 161–169 (2015).
342. Lee, D. G., Kim, S., Lee, S. & Lee, C. S. Effects of Microstructural Morphology on Quasi-Static and Dynamic Deformation Behavior of Ti-6Al-4V Alloy. *Metall. Mater. Trans. A* **32A**, 315–324 (2001).
343. Lee, D.-G., Lee, S., Lee, C. S. & Hur, S. Effects of Microstructural Parameters on the Quasi-static and Dynamic Deformation Behaviors of Ti-6Al-4V Alloys with Widmanstatten Structures. *Metall. Mater. Trans. A* **34A**, 2541–2548 (2003).
344. Xu, Y., Bai, Y. & Meyers, M. A. Deformation, Phase Transformation and Recrystallization in the Shear Bands Induced by High-Strain Rate Loading in Titanium and Its Alloys. *J. Mater. Sci. Technol.* **22**, 737–746 (2006).
345. Han, W. Z. private communication. (2022).
346. Okamoto, H. Nb-Zr (Niobium-Zirconium). *J. Phase Equilibria* **13**, 1992 (1992).
347. Zhang, J. W., Beyerlein, I. J. & Han, W. Z. *Supplementary Info - Hierarchical 3D Nanolayered Duplex-Phase Zr with High Strength, Strain Hardening, and Ductility Methods*. (2019).
348. Rajan, V. P. & Zok, F. W. Effects of non-uniform strains on tensile fracture of fiber-reinforced ceramic composites. *J. Mech. Phys. Solids* **60**, 2003–2018 (2012).
349. Wright, S. I. *et al.* Introduction and comparison of new EBSD post-processing methodologies. *Ultramicroscopy* **159**, 81–94 (2015).
350. Lütjering, G. Property optimization through microstructural control in titanium and aluminum alloys. *Mater. Sci. Eng.* **263**, 117–126 (1999).
351. Wu, S. Y. *et al.* Dynamic shear localization of a titanium alloy under high-rate tension characterized by x-ray digital image correlation. *Mater. Charact.* **137**, 58–66 (2018).
352. Lunt, D. *et al.* The effect of loading direction on strain localisation in wire arc additively manufactured Ti–6Al–4V. *Mater. Sci. Eng. A* **788**, (2020).
353. Al-Bermani, S. S., Blackmore, M. L., Zhang, W. & Todd, I. The origin of microstructural diversity, texture, and mechanical properties in electron beam melted Ti-6Al-4V. *Metall. Mater. Trans. A Phys. Metall. Mater. Sci.* **41**, 3422–3434 (2010).

354. Garlea, E. *et al.* Intergranular strain evolution in a zircaloy-4 alloy with basketweave morphology. *Metall. Mater. Trans. A Phys. Metall. Mater. Sci.* **41**, 1255–1260 (2010).
355. Lee, E., Banerjee, R., Kar, S., Bhattacharyya, D. & Fraser, H. L. Selection of α variants during microstructural evolution in α/β titanium alloys. *Philos. Mag.* **87**, 3615–3627 (2007).
356. Romero, J., Preuss, M. & Quinta da Fonseca, J. Texture memory and variant selection during phase transformation of a zirconium alloy. *Acta Mater.* **57**, 5501–5511 (2009).
357. Jha, J. S., Toppo, S. P., Singh, R., Tewari, A. & Mishra, S. K. Deformation behavior of Ti-6Al-4V microstructures under uniaxial loading Equiaxed Vs. transformed-β microstructures.pdf. *Mater. Charact.* **171**, (2021).
358. Chai, L., Luan, B., Zhang, M., Murty, K. L. & Liu, Q. Experimental observation of 12 α variants inherited from one β grain in a Zr alloy. *J. Nucl. Mater.* **440**, 377–381 (2013).
359. Zhang, J. W., Leu, B., Kumar, M. A., Beyerlein, I. J. & Han, W. Z. Twin hopping in nanolayered Zr-2.5Nb. *Mater. Res. Lett.* **8**, 307–313 (2020).
360. Zhu, Y. T., Liao, X. Z. & Wu, X. L. Deformation twinning in nanocrystalline materials. *Prog. Mater. Sci.* **57**, 1–62 (2012).
361. Gray, G. T. Deformation Twinning: Influence of Strain Rate. in *TMS Meeting Symposium on Twinning in Advanced Materials* (1993).
362. Chen, S. R. & Gray, G. T. Influence of twinning on the constitutive reponses of Zr: Experiments and modeling. in *Journal De Physique. IV : JP* vol. 7 (1997).
363. Book, T. A. & Sangid, M. D. Strain localization in Ti-6Al-4V Widmanstätten microstructures produced by additive manufacturing. *Mater. Charact.* **122**, 104–112 (2016).
364. Filip, R., Kubiak, K., Ziaja, W. & Sieniawski, J. The effect of microstructure on the mechanical properties of two-phase titanium alloys. *J. Mater. Process. Technol.* **133**, 84–89 (2003).
365. Britton, T. B., Dunne, F. P. E. & Wilkinson, A. J. On the mechanistic basis of deformation at the microscale in hexagonal close-packed metals. *Proc. R. Soc. A Math. Phys. Eng. Sci.* **471**, (2015).
366. Lin, F. S., Starke, E. A. & Gysler, A. The effect of microstructure on the deformation modes and mechanical properties of Ti-6Al-2Nb-1Ta-0.8Mo: Part II. Equiaxed

structures. *Metall. Trans. A* **15**, 1873–1881 (1984).

367. Wenk, H. R., Lonardelli, I. & Williams, D. Texture changes in the hcp → bcc → hcp transformation of zirconium studied in situ by neutron diffraction. *Acta Mater.* **52**, 1899–1907 (2004).

368. Gey, N. *et al.* Study of the α/β phase transformation of Zy-4 in presence of applied stresses at heating: Analysis of the inherited microstructures and textures. *J. Nucl. Mater.* **302**, 175–184 (2002).

369. Bate, P. S. & Hutchinson, W. B. Imposed stress and variant selection: The role of symmetry and initial texture. *J. Appl. Crystallogr.* **41**, 210–213 (2008).

370. Daymond, M. R., Holt, R. A., Cai, S., Mosbrucker, P. & Vogel, S. C. Texture inheritance and variant selection through an hcp-bcc-hcp phase transformation. *Acta Mater.* **58**, 4053–4066 (2010).

371. Calnan, E. A. & Clews, C. J. B. LXV. The development of deformation textures in metals.— Part II . Body-centred cubic metals . *London, Edinburgh, Dublin Philos. Mag. J. Sci.* **42**, 616–635 (1951).

372. Gong, J., Benjamin Britton, T., Cuddihy, M. A., Dunne, F. P. E. & Wilkinson, A. J. (a) Prismatic, (a) basal, and (c+a) slip strengths of commercially pure Zr by micro-cantilever tests. *Acta Mater.* **96**, 249–257 (2015).

373. Zhang, Z. & Dunne, F. P. E. Microstructural heterogeneity in rate-dependent plasticity of multiphase titanium alloys. *J. Mech. Phys. Solids* **103**, 199–220 (2017).

374. Li, J., Li, Y., Suo, T. & Wei, Q. Numerical simulations of adiabatic shear localization in textured FCC metal based on crystal plasticity finite element method. *Mater. Sci. Eng. A* **737**, 348–363 (2018).

375. Batra, R. C. EFFECT OF MATERIAL PARAMETERS ON THE INITIATION AND GROWTH OF ADIABATIC SHEAR BANDS. *Int. J. Eng. Sci.* **23**, 1435–1446 (1987).

376. Rodriguez, O. L. *et al.* Dynamic tensile behavior of electron beam additive manufactured Ti6Al4V. *Mater. Sci. Eng. A* **641**, 323–327 (2015).

377. Chesnutt, J. C. & Froes, F. H. Effect of α-phase morphology and distribution on the tensile ductility of a metastable beta titanium alloy. *Metall. Trans. A* **8**, 1013–1017 (1977).

378. Peters, J. O., Lütjering, G., Koren, M., Puschnik, H. & Boyer, R. R. Processing,

microstructure, and properties of β-CEZ. *Mater. Sci. Eng. A* **213**, 71–80 (1996).

379. Luan, J. H. *et al.* Compositional and microstructural optimization and mechanical-property enhancement of cast Ti alloys based on Ti-6Al-4V alloy. *Mater. Sci. Eng. A* **704**, 91–101 (2017).
380. Jones, I. P. & Hutchinson, W. B. Stress-state dependence of slip in Titanium-6Al-4V and other H.C.P. metals. *Acta Metall.* **29**, 951–968 (1981).
381. Lowden, M. A. W. & Hutchinson, W. B. Texture strengthening and strength differential in titanium-6Al-4V. *Metall. Trans. A* **6**, 441–448 (1975).
382. Padilla, H. A., Smith, C. D., Lambros, J., Beaudoin, A. J. & Robertson, I. M. Effects of deformation twinning on energy dissipation in high rate deformed zirconium. *Metall. Mater. Trans. A Phys. Metall. Mater. Sci.* **38 A**, 2916–2927 (2007).
383. Tong, V., Wielewski, E. & Britton, B. Characterisation of slip and twinning in high rate deformed zirconium with electron backscatter diffraction. 1–45 (2018).
384. Long, F., Balogh, L. & Daymond, M. R. Evolution of dislocation density in a hot rolled Zr–2.5Nb alloy with plastic deformation studied by neutron diffraction and transmission electron microscopy. *Philos. Mag.* **97**, 2888–2914 (2017).
385. Andrade, U., Meyers, M. A., Vecchio, K. S. & Chokshi, A. H. Dynamic recrystallization in high-strain, high-strain-rate plastic deformation of copper. *Acta Metall. Mater.* **42**, 3183–3195 (1994).
386. Kad, B. K., Gebert, J. M., Perez-Prado, M. T., Kassner, M. E. & Meyers, M. A. Ultrafine-grain-sized zirconium by dynamic deformation. *Acta Mater.* **54**, 4111–4127 (2006).
387. Grebe, H. A., Pak, H. R. & Meyers, M. A. Adiabatic shear localization in titanium and Ti-6 pct Al-4 pct V alloy. *Metall. Trans. A* **16**, 761–775 (1985).
388. Gey, N., Humbert, M., Gautier, E. & Béchade, J. L. Study of the β→α variant selection for a zircaloy-4 rod heated to the β transus in presence or not of an axial tensile stress. *J. Nucl. Mater.* **328**, 137–145 (2004).
389. Kerr, D., Cochrane, C. & Daymond, M. R. Phase Transformation and Atypical Variants in an Extruded Two Phase Zirconium Tube. *Metall. Mater. Trans. A Phys. Metall. Mater. Sci.* **51**, 2724–2737 (2020).
390. Beyerlein, I. J. *et al.* Radiation damage tolerant nanomaterials. *Mater. Today* **16**, 443–449 (2013).

391. Lien, H. H., Mazumder, J., Wang, J. & Misra, A. Ultrahigh strength and plasticity in laser rapid solidified Al–Si nanoscale eutectics. *Mater. Res. Lett.* **8**, 291–298 (2020).
392. Gray, G. T., Bourne, N. K., Zocher, M. A., Maudlin, P. J. & Millett, J. C. F. Influence of crystallographic anisotropy on the Hopkinson fracture "spallation" of zirconium. **836**, 509–512 (1999).
393. Cerreta, E., Gray, G. T., Hixson, R. S., Rigg, P. A. & Brown, D. W. The influence of interstitial oxygen and peak pressure on the shock loading behavior of zirconium. *Acta Mater.* **53**, 1751–1758 (2005).
394. Cerreta, E. K. *et al.* The influence of peak shock stress on the high pressure phase transformation in Zr. *J. Phys. Conf. Ser.* **500**, 1–7 (2014).
395. Ren, Y. *et al.* Spall strength and fracture behavior of Ti–10V–2Fe–3Al alloy during one-dimensional shock loading. *Int. J. Impact Eng.* **111**, 77–84 (2018).
396. Escobedo, J. P., Dennis-Koller, D., Cerreta, E. K. & Bronkhorst, C. A. Effects of grain boundary structure and distribution on the spall response of copper. *AIP Conf. Proc.* **1426**, 1321–1324 (2012).
397. Perez-Bergquist, A. G. *et al.* The role of the structure of grain boundary interfaces during shock loading. *AIP Conf. Proc.* **1426**, 1359–1362 (2012).
398. Fensin, S. J. *et al.* Effect of loading direction on grain boundary failure under shock loading. *Acta Mater.* **64**, 113–122 (2014).
399. Minich, R. W., Cazamias, J. U., Kumar, M. & Schwartz, A. J. Effect of microstructural length scales on spall behavior of copper. *Metall. Mater. Trans. A Phys. Metall. Mater. Sci.* **35 A**, 2663–2673 (2004).
400. Remington, T. P. *et al.* Spall strength dependence on grain size and strain rate in tantalum. *Acta Mater.* **158**, 313–329 (2018).
401. Farbaniec, L., Williams, C. L., Kecskes, L., Ramesh, K. T. & Becker, R. Microstructural effects on the spall properties of ECAE-processed AZ31B magnesium alloy. *Int. J. Impact Eng.* **98**, 34–41 (2016).
402. Fensin, S. J. *et al.* Dynamic damage nucleation and evolution in multiphase materials. *J. Appl. Phys.* **115**, (2014).
403. Jones, D. R. *et al.* Spall fracture in additive manufactured tantalum. *J. Appl. Phys.* **124**, (2018).

404. Jones, D. R. *et al.* Spall fracture in additive manufactured Ti-6Al-4V. *J. Appl. Phys.* **120**, (2016).
405. Brown, A. D. *et al.* Dynamic mechanical response of additive manufactured Ti-6Al-4V. *AIP Conf. Proc.* **1979**, 1–6 (2018).
406. Escobedo, J. P. *et al.* Effects of grain size and boundary structure on the dynamic tensile response of copper. *J. Appl. Phys.* **110**, (2011).
407. Nguyen, T., Luscher, D. J. & Wilkerson, J. W. The role of elastic and plastic anisotropy in intergranular spall failure. *Acta Mater.* **168**, 1–12 (2019).
408. Francis, T. *et al.* Multimodal 3D characterization of voids in shock-loaded tantalum: Implications for ductile spallation mechanisms. *Acta Mater.* **215**, 117057 (2021).
409. Hahn, E. N., Fensin, S. J. & Germann, T. C. The role of grain boundary orientation on void nucleation in tantalum. *AIP Conf. Proc.* **1979**, (2018).
410. Bronkhorst, C. A. *et al.* Local micro-mechanical stress conditions leading to pore nucleation during dynamic loading. *Int. J. Plast.* **137**, 102903 (2021).
411. Gray, G. T. Shock wave testing of ductile materials. in *ASM Handbook Vol. 8: Mechanical Testing and Evaluation* (eds. Kuhn, H. & Medlin, D.) 530–538 (ASM International, 2000).
412. Jensen, B. J., Holtkamp, D. B., Rigg, P. A. & Dolan, D. H. Accuracy limits and window corrections for photon Doppler velocimetry. *J. Appl. Phys.* **101**, (2007).
413. Gluzman, V. D. & Kanel, G. I. Measurement of the tensile stresses behind a spalling plane. *J. Appl. Mech. Tech. Physics1* **24**, 582–585 (1983).
414. Kanel, G. I. Distortion of the Wave Profiles in an Elastoplastic. *J. Appl. Mech. Tech. Phys.* **42**, 358–362 (2001).
415. Song, S. G. & Gray, G. T. Influence of temperature and strain rate on slip and twinning behavior of zr. *Metall. Mater. Trans. A* **26**, 2665–2675 (1995).
416. Knezevic, M., Zecevic, M., Beyerlein, I. J., Bingert, J. F. & McCabe, R. J. Strain rate and temperature effects on the selection of primary and secondary slip and twinning systems in HCP Zr. *Acta Mater.* **88**, 55–73 (2015).
417. Cochrane, C., Skippon, T. & Daymond, M. R. Effect of rate on the deformation properties of metastable β in a high Sn content zirconium alloy. *Int. J. Plast.* **119**, 102–122 (2019).

418. Kaschner, G. C., Gray, G. T. & Chen, S. R. The influence of texture and impurities on the mechanical behavior of zirconium. **31**, 435–438 (2008).
419. Arul Kumar, M., Beyerlein, I. J. & Tomé, C. N. Grain size constraints on twin expansion in hexagonal close packed crystals. *J. Appl. Phys.* **120**, (2016).
420. Chen, Y. J., Meyers, M. A. & Nesterenko, V. F. Spontaneous and forced shear localization in high-strain-rate deformation of tantalum. *Mater. Sci. Eng. A* **268**, 70–82 (1999).
421. Kiran Kumar, M. *et al.* Explaining absence of texture development in cold rolled two-phase Zr-2.5 wt% Nb alloy. *Acta Mater.* **51**, 625–640 (2003).
422. Cai, S., Daymond, M. R., Khan, A. K., Holt, R. A. & Oliver, E. C. Elastic and plastic properties of βZr at room temperature. *J. Nucl. Mater.* **393**, 67–76 (2009).
423. Follansbee, P. S. The HEL and Rate-Dependent Yield Behavior. in *Proceedings of the 1989 Topical Conference on Shock Compression of Condensed Matter* (Los Alamos Nationall Laboratory, 1989).
424. Smith, J. A., Lacy, J. M., Lévesque, D., Monchalin, J. P. & Lord, M. Use of the Hugoniot elastic limit in laser shockwave experiments to relate velocity measurements. *AIP Conf. Proc.* **1706**, (2016).
425. Chen, X., Asay, J. R., Dwivedi, S. K. & Field, D. P. Spall behavior of aluminum with varying microstructures. *J. Appl. Phys.* **99**, (2006).
426. Baeslack, W. A. & Mahajan, Y. INTERGRANULAR FRACTURE OF HEAT-TREATED WELDMENTS IN A HIGH-STRENGTH ALPHA-BETA TITANIUM ALLOY. *Scr. Metall.* **13**, 959–964 (1979).
427. Rudd, R. E. & Belak, J. F. Void nucleation and associated plasticity in dynamic fracture of polycrystalline copper: An atomistic simulation. *Comput. Mater. Sci.* **24**, 148–153 (2002).
428. Fensin, S. J., Valone, S. M., Cerreta, E. K. & Gray, G. T. Influence of grain boundary properties on spall strength: Grain boundary energy and excess volume. *J. Appl. Phys.* **112**, (2012).
429. Fensin, S. J. & Hahn, E. N. Towards predicting susceptibility of grain boundaries to failure in BCC materials. *AIP Conf. Proc.* **1979**, 3–8 (2018).
430. Burgers, W. G. On the process of transition of the cubic-body-centered modification into

the hexagonal-close-packed modification of zirconium. *Physica* **1**, 561–586 (1934).

431. Pilchak, A. L., Williams, R. E. A. & Williams, J. C. Crystallography of fatigue crack initiation and growth in fully lamellar Ti-6Al-4V. *Metall. Mater. Trans. A Phys. Metall. Mater. Sci.* **41**, 106–124 (2010).
432. Savage, M. F., Tatalovich, J., Zupan, M., Hemker, K. J. & Mills, M. J. Deformation mechanisms and microtensile behavior of single colony Ti-6242Si. *Mater. Sci. Eng. A* **319**–**321**, 398–403 (2001).
433. Sui, H. *et al.* Theoretical models of void nucleation and growth for ductile metals under dynamic loading: A review. *Matter Radiat. Extrem.* **7**, (2022).
434. Arrieta, H. V. & Espinosa, H. D. The role of thermal activation on dynamic stress-induced inelasticity and damage in Ti-6Al-4V. *Mech. Mater.* **33**, 573–591 (2001).
435. Capolungo, L., Marshall, P. E., McCabe, R. J., Beyerlein, I. J. & Tomé, C. N. Nucleation and growth of twins in Zr: A statistical study. *Acta Mater.* **57**, 6047–6056 (2009).
436. Yoo, M. H. Slip, twinning, and fracture in hexagonal close-packed metals. *Metall. Trans. A* **12**, 409–418 (1981).
437. Tyler, C., Millett, J. C. F. & Bourne, N. K. Spallation in Ti-6Al-4V: Stress measurements and recovery. *AIP Conf. Proc.* **845 I**, 674–677 (2006).
438. Appleby-Thomas, G. J. *et al.* On the dynamic tensile strength of Zirconium. *J. Phys. Conf. Ser.* **500**, 2–7 (2014).
439. Jonsson, J. C. *et al.* Effect of texture on elastic precursor decay in magnesium alloy AZ31B. *AIP Conf. Proc.* **2272**, (2020).
440. Kanel, G. I. *et al.* Shock response of magnesium single crystals at normal and elevated temperatures. *J. Appl. Phys.* **116**, (2014).
441. Pope, L. E. & Johnson, J. N. Shock−wave compression of single−crystal beryllium. *J. Appl. Phys.* **46**, 720–729 (1975).
442. Pedrazas, N. A. *et al.* Effects of microstructure and composition on spall fracture in aluminum. *Mater. Sci. Eng. A* **536**, 117–123 (2012).
443. Achenbach, J. D. *Wave Propagation in Elastic Solids*. *Wave Propagation in Elastic Solids* (Elsevier Science Publishers B.V., 1999). doi:10.1016/c2009-0-08707-8.
444. Graff, K. F. *Wave Motion in Elastic Solids*. (Dover, 1991).
445. Nayfeh, A. H. *Wave Propagation in Layered Anisotropic Media with Applications to*

Composites. (Elsevier B.V., 1995).

446. Jones, J. P. Wave Propagation in a Two-Layered Medium. *J. Appl. Mech.* 213–222 (1964) doi:10.4064/ap-3-2-213-217.
447. Verbis, J. T., Tsinopoulos, S. V., Agnantiaris, J. P. & Polyzos, D. Wave Propagation in Composites. *Recent Adv. Compos. Mater.* 35–46 (2003) doi:10.1007/978-94-017-2852-2_4.
448. Moon, F. C. *A Critical Survey of Wave Propagation and Impact in Composite Materials*. (1973).
449. Kong, Z., Qiang, F. W., Wei, P. J. & Tang, Q. Surface effects on the wave propagation in composites with random dispersive parallel cylindrical nanofibers. *Arch. Mech.* **67**, 355–370 (2015).
450. Heelan, P. A. On the Theory of Head Waves. *Geophysics* **18**, 871–893 (1953).
451. Nayfeh, A. H. The general problem of elastic wave propagation in multilayered anisotropic media. *J. Acoust. Soc. Am.* **89**, 1521–1531 (1991).
452. Datta, S. K. & Shah, A. H. *Elastic Waves in Composite Media and Structures*. *Mechanical Engineering Series* (Taylor & Francis, 2009).
453. Barker, L. M. A Model for Stress Wave Propagation Composite Materials. *J. Compos. Mater.* **5**, 140–162 (1971).
454. Sun, C. T., Achenbach, J. D. & Herrmann, G. Time-harmonic waves in a stratified medium propagating in the direction of the layering. *J. Appl. Mech. Trans. ASME* **35**, 408–411 (1968).
455. Munson, D. E. & Schuler, K. W. Steady Wave Analysis of Wave Propagation in Laminates and Mechanical Mixtures. *J. Compos. Mater.* **5**, 286–304 (1976).
456. Voelker, L. E. & Achenbach, J. D. Stress Waves in a Laminated Medium Generated by Transverse Forces. *J. Acoust. Soc. Am.* **46**, 1213–1222 (1969).
457. Peck, J. C. & Gurtman, G. A. Dispersive pulse propagation parallel to the interfaces of a laminated composite. *J. Appl. Mech. Trans. ASME* **36**, 479–484 (1964).
458. Scott, R. A. Wave propagation in a layered elastic plate. *Int. J. Solids Struct.* **8**, 833–845 (1972).
459. Hu, M. Z. & Ting, T. C. T. Wave Propagation Parallel to the Layers in Elastic or Viscoelastic Layered Composites. *J. Struct. Mech.* **11**, 13–35 (1983).

460. Farnell, G. W. & Adler, E. L. *Elastic Wave Propagation in Thin Layers*. *Physical Acoustics* vol. 9 (ACADEMIC PRESS, INC., 1972).
461. Mengi, Y. & McNiven, H. D. Analysis of the Transient Excitation of a Transversely Isotropic Rod. *J. Acoust. Soc. Am.* **50**, 258–265 (1971).
462. Armenakas, A. E. Propagation of Harmonic Waves in Composite Circular-Cylindrical Rods. *J. Acoust. Soc. Am.* **47**, 822–837 (1970).
463. Whittier, J. S. & Jones, J. P. Axially symmetric wave propagation in a two-layered cylinder. *Int. J. Solids Struct.* **3**, 657–675 (1967).
464. Scott, R. A. & Miklowitz, J. Transient Elastic Waves in Anisotropic Plates. *J. Appl. Mech.* **34**, 104–110 (1967).
465. Scott, R. A. TRANSIENT COMPRESSIONAL WAVE PROPAGATION IN A TWO-LAYERED CIRCULAR ROD WITH IMPERFECT BONDING. *J. Sound Vib.* **26**, 321–335 (1973).
466. Folk, R., Fox, G., Shook, C. A. & Curtis, C. W. Elastic Strain Produced by Sudden Application of Pressure to One End of a Cylindrical Bar. I. Theory. *J. Acoust. Soc. Am.* **30**, 552–558 (1958).
467. Sve, C. Propagation of a Shear Pulse Parallel to the interfaces of a Periodically Laminated Medium. *J. Appl. Mech.* 203–205 (1970).
468. *Modern Global Siesmology Chapter 3: Body waves and ray theory*. *International Geophysics* vol. 58 (1995).
469. Gebbie, J. & Siderius, M. Head wave correlations in ambient noise. *J. Acoust. Soc. Am.* **140**, EL62–EL66 (2016).
470. Callaway, E. B., Christodoulou, P. G. & Zok, F. W. Deformation, rupture and sliding of fiber coatings in ceramic composites. *J. Mech. Phys. Solids* **132**, (2019).
471. Meyers, M. A., Andrade, U. R. & Chokshi, A. H. The effect of grain size on the high-strain, high-strain-rate behavior of copper. *Metall. Mater. Trans. A* **26**, 2881–2893 (1995).
472. Boakye-Yiadom, S. & Bassim, N. Microstructural evolution of adiabatic shear bands in pure copper during impact at high strain rates. *Mater. Sci. Eng. A* **711**, 182–194 (2018).
473. Gilman, J. J. Mechanism of ortho kink-band formation in Compressed Zinc Monocrystals. *Jom* **6**, 621–629 (1954).

474. Barsoum, M. W., Zhen, T., Kalidindi, S. R., Radovic, M. & Murugaiah, A. Fully reversible, dislocation-based compressive deformation of Ti 3SiC2 to 1 GPa. *Nat. Mater.* **2**, 107–111 (2003).
475. Barsoum, M. W. & El-Raghy, T. Room-temperature, ductile carbides. *Metall. Mater. Trans. A Phys. Metall. Mater. Sci.* **30**, 363–369 (1999).
476. Jones, N. G. *et al.* On the relevance of kinking to reversible hysteresis in MAX phases. *Acta Mater.* **69**, 149–161 (2014).